DNA Origami Nanopores for Protein Biosensing

Genevieve Claire Pugh

University College London

This dissertation is submitted for the degree of
Doctor of Philosophy

Supervisor: Professor Stefan Howorka

August 2018

Declaration

I, Genevieve Claire Pugh, confirm that the work presented in this thesis is my own. Where information has been derived from other sources, I confirm that this has been indicated in the thesis.

.....

Abstract

There is an increasing demand in biomedicine for rapid diagnostic testing. This is fuelled by the improved knowledge of the proteome and genome and a drive towards personalised medicine. Furthermore, many new potential biomarkers for diseases are being identified. Portable, point-of-care biosensors can meet these demands and take advantage of the recent biomedical developments. In this thesis, we investigate the creation of a biosensor element, including a design that allows the detection of protein biomarkers via an electrical label-free method.

The use of nanopores for single molecule sensing has led to the development of commercially viable, portable, label-free DNA sequencing devices.[1] However, the use of nanopores for detection of protein analytes is yet to reach the same viability. A reason for this is the inability for current nanopore materials to combine both atomically precise structural definition and tuneable nanopore size of the widths needed to accommodate protein analytes. In this thesis's main project a route to overcome these limitations is described, by using the DNA origami technique. Multiple layers of DNA duplexes are interlinked to form a nanopore structure with a defined, predetermined central channel. The pore described can transport proteins with a higher fidelity than previously published work.

Small DNA nanopores have shown promise for the transport of some small molecule analytes[2,3,4]. A secondary project looks at the use of a single loop of duplex associated with a lipid bilayer as a simplistic nanopore to induce ion transport through a membrane. Although consistent current steps were not demonstrated, the DNA loop was shown to associate with and cause some disruption and ion transport through the bilayer.

Large DNA origami rings have been shown to template the formation of liposomes of a defined size[5]. These rings, initially functionalised with lipid nucleation sites, were hypothesised to be adaptable for bilayer association and use in a nanopore sensing set up by replacing lipid nucleation sites with cholesterol molecules (lipid

anchors) to induce bilayer association. Out of several anchor arrangements investigated one arrangement, with anchors located on the outside of the ring in the plane of the ring, was shown to be the most viable. By and large, only conductance values of a small magnitude were observed when single channel current recordings were conducted with the DNA origami rings in a Dphpc membrane. This suggested that association of the rings with the bilayer does not lead to the formation of a channel of the desired size.

The origami funnel nanopore designed as the main aim of this thesis is of a form which is robust and versatile for further use. The DNA nanopore designed can be easily modified with additional functionalizations and is shown to associate with, and span, lipid bilayers. The nanopore can be used as a template from which further applications and advances in nanopore sensing research can be established.

Impact Statement

The work in this thesis, funded by Oxford Nanopore Technologies (ONT), describes the construction of DNA nanopores for use as biosensors. Nanopore biosensing devices commercially sold by ONT have been used for DNA sequencing. The DNA origami nanopore constructed in this project demonstrates the potential feasibility for the use of nanopore-based biosensors to detect a wider range of analytes, such as proteins, if a DNA origami nanopore is used in the set up.

The work conducted as part of the PhD project contributes to the advancement of the fields of both nanopore sensing and DNA nanotechnology. The work shows a step change in the size of analyte which can be detected reproducibly with DNA nanopores and contributes to the knowledge base of the field.

For my mother,

Beverley Ann Pugh

Thank you for 26 years of love, support and excessive proof-reading

In Loving Memory of Betty Margaret Storkey

1931 – 2017

and

Alastair Tarrant Pugh

1928 – 2019

Acknowledgements

First and foremost, I would like to thank my supervisor, Professor Stefan Howorka, for giving me the opportunity to work on such an interesting and interdisciplinary project. Thank you for your passion, guidance and patience with a chemistry undergraduate figuring out a biology based PhD.

I would like to thank the post-doctoral researchers from the Howorka group. Thank you to Dr Jon Burns for your help with various elements of my PhD work and for your initial design of the box and triangle sequences. Also thank you to Dr Yongzheng Xing for your help and advice with operating the Transmission Electron Microscope at UCL.

I would also like to thank Dr Alice Pyne and Dr Richard Thorogate at the LCN for your training in Atom Force Microscopy and your help and advice for operating and processing AFM data.

A special thank you goes to the members of the Chenxiang Lin group at Yale University. Thank you for letting me spend time in your laboratory, use your equipment and benefit from all your tips and tricks of the trade. My time at Yale has proved invaluable to my PhD. I'd like to give a huge thank you to Dr Yang Yang. Thank you for giving up so much time to teach me and train me in TEM.

I would also like to thank Oxford Nanopore Technologies for funding my PhD.

I would like to thank all the members of the Howorka group, past and present, for making every day a little more enjoyable. Thank you to Hafi, Jo, Dan, Patrick, Conor, Katya, Yongzheng and Helena. I wish you a productive, data filled future.

Thank you to my family for your unwavering support. I couldn't have done it without you. Especially to my mother, Beverley Pugh, who has proofread every report and project I have written for the last 20 years. This wouldn't have been possible without you and this achievement is as much yours as mine. I promise

this is the last report you will have to read!

To Alex, thank you for being with me for every step of this journey. Thank you for helping me through the difficult days and celebrating with me on the good days. Your love, support and endless patience has meant everything. I'm looking forward to both of our next steps and sorry about the hexagons.

Table of Contents

Acronyms

PFT – Pore forming toxin

α-HL – Alpha haemolysin

phi 29 - Bacillus phage phi29

DNAP – DNA phi29 polymerase

MspA – Mycobacterium smegmatis porin A

OmpG – Outer membrane protein G

ELISA – Enzyme-linked immunosorbent assays

HIV – Human immunodeficiency virus

PSA – Prostate-specific antigen

DNA – Deoxyribonucleic acid

RNA- Ribonucleic acid

ssDNA – Single stranded DNA

ddDNA – Double stranded DNA

dsLNA – Double stranded locked nucleic acid

PEG – Polyethylene glycol

KOH – Potassium hydroxide

HPLC – High-performance liquid chromatography

SEC – Size exclusion column

AFM – Atom force microscopy

DLS – Dynamic light scattering

PAGE - Polyacrylamide gel electrophoresis

SDS – Sodium dodecyl sulfate

FIB – Focused ion beam

UV-Vis – Ultraviolet–visible spectroscopy

IgG – Immunoglobulin G

BSA - Bovine serum albumin

pH – logarithmic scale of H+ ion concentration

pI – Isoelectric point

CNTs – Carbon nanotubes

bp – Base pair

3’ – 3 prime carbon on DNA sugar backbone

5’ – 5 prime carbon on DNA sugar backbone

A – Adenine

T – Thymine

G – Guanine

C - Cytosine

2D – Two-dimensional

3D – Three-dimensional

DX – Double crossover motif

PX – Parameic crossover motif

PCR – Polymerase chain reaction

M13mp18 – Single-stranded DNA isolated from the M13 bacteriophage

SELEX – Systematic evolution of ligands by exponential enrichment

SUV – Small unilamellar vesicles

GUV - Giant unilamellar vesicles

SRB - Sulpho-rhodamine B

CF - Carboxyfluorscein

.json - Javascript object notation file (CaDNAno files)

T_m – Melting temperature

KCl – Potassium chloride

HEPES – 4-(2-hydroxyethyl)-1-piperazineethanesulfonic acid

OPOE – n-Octyl-oligo-oxyethylene

DphPC – 1,2-diphytanoyl-sn-glycero-3-phosphocholine

PPT– Phosphorothioate

Mer – Oligonucleotide length

DMF – Dimethylformamide

Tris - Trisaminomethane

Nt - Nucleotide

^oC – Degrees celsius

TEAA – Triethylammonium acetate

ACN – Acetonitrile

HPA – 3-hydroxypicolinic acid

THAP – 2,4,6-Trihydroxyacetophenone

PEPC – Mix of DOPE and DOPC lipid.

DOPE – 2-dioleoyl-sn-glycero-3-phosphoethanolamine

DOPC – 1,2-dioleoyl-sn- glycero-3-phosphocholine

Chol – Cholesterol

H0 – Helix 0

H3 – Helix 3

H4 – Helix 4

H105 – Helix 1, 0 and 5

H234 – Helix 2, 3 and 4

EDTA – Ethylenediaminetetraacetic acid

MECA – Multielectrode-cavity-array

Mg^{2+} – Magnesium cation

Ni^{2+} – Nickle cation

PTFE – Polytetrafluoroethylene

Min – Minute

Sec – Second

nS – Nanosiemens

nm^2 – Nanometre squared

µs – Microsecond

µm – Micrometre

nm - Nanometre

ms – Millisecond

pA – Picoampere

mV – Millivolts

µM - Micromolar

M – Molar

Nmol - Nanomolar

Hz – Hertz

kHz - Kilohertz

µL – Microliter

pN – Piconewton

Da – Dalton

kDa – Kilodalton

UCL – University College London

LCN – London Centre for Nanotechnology

Current publications from work presented in this thesis:

- Pugh, G. C., Burns, J. R. & Howorka, S. Comparing proteins and nucleic acids for next-generation biomolecular engineering. *Nat. Rev. Chem.* **2,** 113–130 (2018).

- International (PCT) Patent Application No. PCT/GB2017/052089 Titled: Wide DNA Nanopores, Inventors: Howorka, S., Pugh, G.C., Burns, J.R., Applicant: UCL Business

1. Introduction

The main project described in this thesis involves the design and fabrication of a DNA origami nanopore for use in biosensing of protein biomarkers. This introductory section firstly provides an overview of the uses and importance of biosensors and, in particular, the detection of protein biomarker targets. It then explores in more detail the two main elements of the project: the technique of nanopore sensing, and the suitability of DNA nanotechnology to expand the current scope of this sensing technique.

The advantages of label free, real-time sensing devices (such as those based on nanopore technology), is discussed, and the mechanism of nanopore sensing is explained. The literature of the two most well-established nanopore sensing types (biological nanopores and solid-state nanopores) is then reviewed, and their drawbacks examined. Some more recently explored hybrid approaches, which have aimed to overcome some of the drawbacks of both nanopore types, are then also discussed.

Next, the suitability of DNA as a building material for the next generation of nanopores used in sensing is established. The large variety of shapes and sizes of nanoscale objects that can be constructed and simulated to self-assemble with DNA is demonstrated. The functionalization of DNA structures with additional moieties with atomic level precision is then reviewed. This is important for the design of DNA nanopores, which must be chemically functionalised to associate with lipid bilayers. Additional receptors to bind targets may also be added.

The concepts and rules used to build DNA objects are then explained in detail. This includes the manipulation of Holliday junctions, duplex formation and base stacking interactions, as well as considerations that ensure high fidelity folding of large DNA origami structures such as annealing temperature protocols and salt concentrations.

A full review of the literature landscape of previously fabricated DNA

nanostructure and origami nanopores is examined, and the novelty of a multi-layered origami nanopore which can reliably sense protein targets is demonstrated.

Finally, the aims of each sub-project of the thesis are set out in full.

1.1 Biosensors

The concept of a biosensor was first introduced by Leland C. Clark, Jr. in 1956[6]. Since this point the development of increasingly sensitive and compact biosensors has led to extremely wide reaching applications in industries ranging from health care to environmental monitoring[7,8]. Some examples include the monitoring of everything from fruit ripening,[9] or biowarfare agents[10] to the currently most successful embodiment of biosensing: glucose sensors[11].

Glucose sensors and pregnancy tests show the potential of biosensors to provide rapid point of care diagnostics in the form of an easy-to-use test.[12] Dependence on expensive, time-consuming laboratory tests is being replaced by portable, low-cost devices that have the potential to allow patients to take more responsibility for their own health care from home[13]. The ability to track analytes in real time means medicine can be personalised so that patients receive 'the right drug at the right time' and ultimately are provided with better care.

The research field of biosensing has grown significantly over the last 20 years and is now a multidisciplinary research area[14]. The types of biosensors in development and on the market are now expansive and take advantage of many different areas of science to detect their targets, from fibre optics[15] to acoustic waves[16]. Figure 1 summarizes some key types of biosensors in current use. Research is aimed at expanding the range of targets which can be sensed and developing tests where analytes can be detected rapidly, without the need for extensive sample preparation.[14] It is also very desirable to develop tests which will detect various analytes at the same time or that can be adapted for use with multiple analytes.[17]

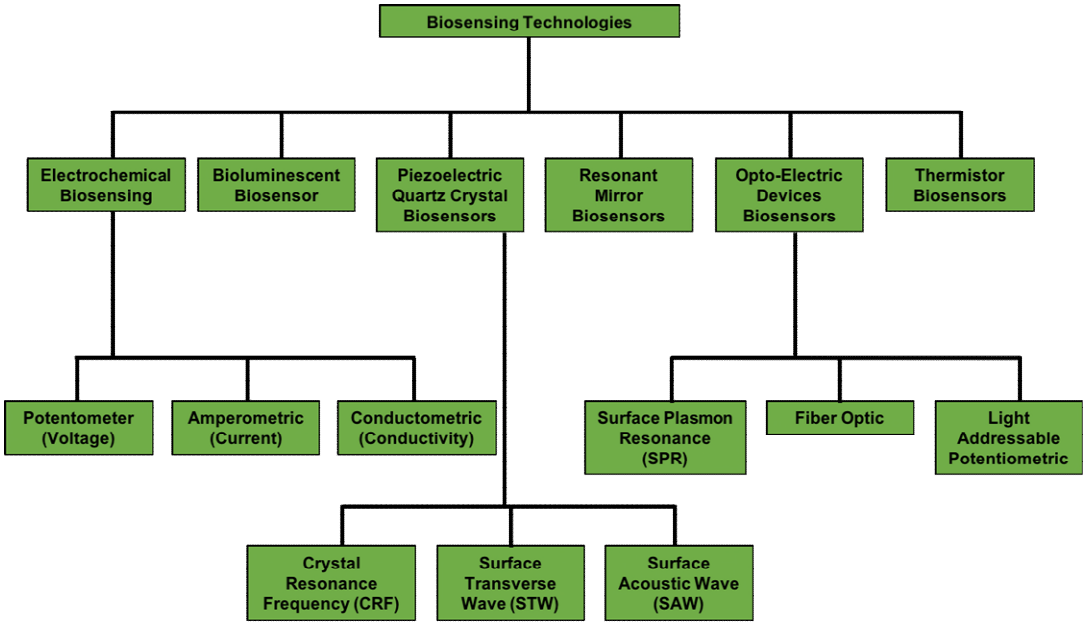

Figure 1 *– Different types of Biosensing technologies*

1.1.1 Types of Sensor

A sensor can be defined as a device that registers an input and then converts that input into a measurable output signal. As shown in Figure 2, sensors can further be broken down into three main elements:

A) a recognition element that interacts exclusively with the analyte, or group of analytes, to be detected,

B) a transducer which converts the recognition event into a signal, and

C) a signal processer that amplifies and converts the signal into a readable output[18].

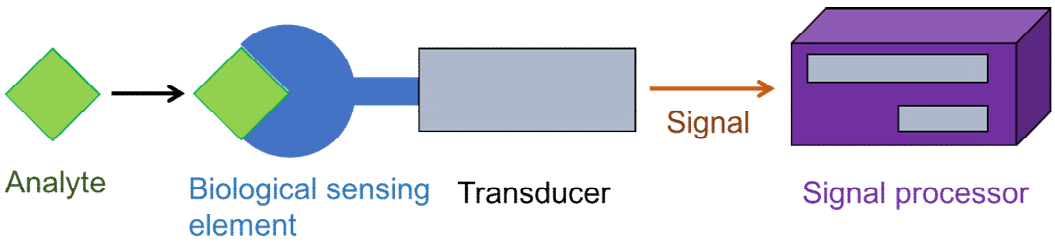

Figure 2 - *Structure of a biosensor. Biosensors are made up of a transducer, signal processor and biological material based sensing element.*

Sensors fall into three main categories: physical, chemical and biosensors. Physical sensors measure physical properties such as mass, pressure or temperature, whereas chemical sensors transform chemical information into a readable output signal[19]. Biosensors (sometimes classified as a subset of chemical sensors), use a recognition element which is formed of a biologically derived material[14].

Biological recognition elements can be biological materials such as protein, nucleic acid, cells or tissues, which can interact selectively with an analyte. Transducers used in biosensors can also take several forms: optical, thermometric, magnetic, electrochemical or electrical. Table 1 summarises some examples of biosensors for known biomarker analytes seen in literature.

Target/ biomarker	*Disease*	*Biorecognition element*	*Transduction*	*Ref*
BRCA1 gene	Breast cancer	DNA	Electrochemical	Castaneda et al. 2007[20]
Cardiac troponin T (cTnT)	Acute myocardial infarction	Antibody Direct assay	Optical (SPR)	Fireman et al. 2007[21]
C-reactive protein	Inflammation Cardiovascular diseases	Antibody Sandwich assay	Magnetic	Centi et al. 2009[22]
L1 viral region	Human papilloma virus	DNA	Acoustic (QCM)	Dell'Atti et al. 2007[23]
a-fetoprotein (AFP)	Cancer	Antibody Competitive assay	Electrochemical (array)	Wilson & Nie 2006[24]

Table 1*- biosensors found in literature for various biomarkers*[25]

The biosensor described in this project uses an electrochemical-based transduction element. Biosensors with electrochemical transduction elements require low power and can be miniaturised with relative ease, consequently leading to low cost sensors applicable for point of care diagnostics.[26]

1.1.2 Biomarkers as Targets

A biomarker is a biomedically important measureable indicator of normal biological processes, pathogenic processes or pharmacological responses to a therapeutic intervention.[27] For example, PSA (prostate specific antigen) is a commonly used protein biomarker. In healthy patients, low levels of the protein are found in the blood. An increase in PSA concentration indicates abnormalities in the prostate gland, which can indicate prostate cancer. The level of PSA increases with advancing clinical stage, giving valuable information about the progression of the cancer.[28]

Biomarkers can be used as a predictive measure or to diagnose the progression or the severity of a disease, as well as helping to identify the most appropriate treatments for diseases ranging from cancer or cardiovascular disease to infections such as HIV.[29] Due to their biomedical importance, protein biomarkers found in blood, urine and other bodily fluids can be essential early indicators of a disease. Although biomarkers can take various forms, with DNA methylation studies and transcriptional profiling showing potential for sensing cancer, proteins are a more closely associated indicator of the current disease state.[30,31]

1.1.3 Label vs. Label Free Biosensors

Many assay-based biosensors need a label to function. The amount of label is detected and is then used as an indication of the bound target[26]. Labels normally fall into four main categories: fluorescence, chemiluminescence, radioactive and enzymatic labelling[32]. Labelling biomolecules however leads to complications, as labelled detection needs the attachment of a secondary molecule which can change the biomolecules' binding properties. Amplification steps can be time consuming and the yield of the target-label attachment can be extremely variable. These variables can affect the results obtained and can be especially problematic when using protein targets.[33,34]

To avoid modification of the binding properties of the assay's probe molecules by the attachment of label molecules, sandwich assays, such as ELISA (enzyme-linked immunosorbent assays), use several probe molecules (Figure 3). Probe one immobilises the analyte, a second labelled probe is introduced after washing, a third probe is then bound to the secondary probe allowing detection. The benefit of this is an increase in selectivity of the assay, however, it also increases the cost and time needed to gain a result, making the technique unsuitable for real time

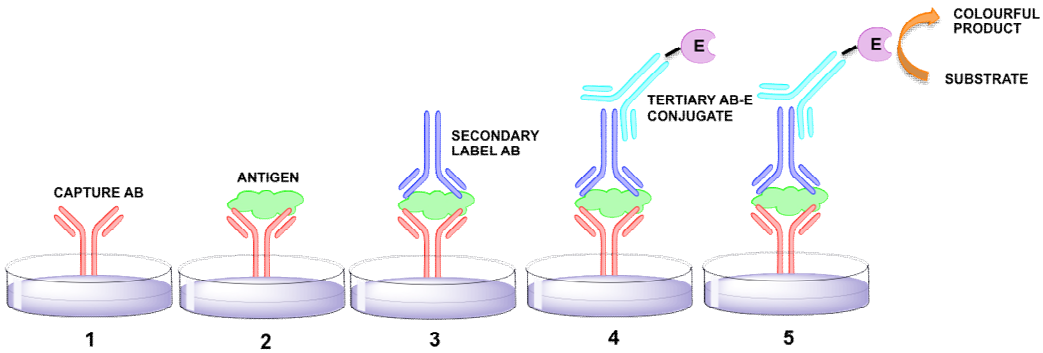

***Figure 3** - ELISA Sandwich Assay – detection requires successive binding of several antibodies making the technique unsuitable for real time analysis*

detection.

Removal of the need for labelling reduces handling, analysis time and costs. Direct detection allows detection of the protein target in real time, (which is not possible with labelled systems) with high sensitivity, low sample consumption and minimal damage to the analytes.[32] Extra information can also be obtained, such as

the average binding event and the generation of affinity constants to a receptor.

Nanopore sensing is a label-free biosensing technique with an electrochemical transducing element. It involves the detection of the passage of the analyte through the pore as opposed to surface binding. Nanopore sensing only requires very low sample volumes that exclude the need for sample preparation or amplification[35]. The technique has been carried out in the presence of many contaminants. Its popularity as a sensing mechanism can be seen by the 900+ publications from Pubmed relating to nanopore sensing.[35]

1.1.4 Nanopore Sensing

Modern nanopore sensing methods can be traced back to the hybridisation of two techniques: the Coulter counter, developed in the 1950s,[36,37] and single channel current recordings, first developed in the 1970s[38,39].

Coulter Counters

Coulter counting involves the passing of microscale objects through an aperture. Periodic reductions in the ionic current flowing through the aperture can be used to look at the mobility, surface charge and concentration of the analytes.[40] Coulter counters are typically composed of two chambers filled with electrolyte, separated by a membrane containing the microscale aperture. (Figure 4) Electrodes immersed in the electrolytes and a potentiostat set a potential across the membrane, which drives the ionic current through the aperture[41]. Pulsewise changes in the conductance of the pore are detected as particles pass through the aperture, replacing a volume of electrolyte corresponding to the particles' volume.[42] The height, pulse frequency and pulse duration can be used to measure the target's volume, concentration and translocation velocity, respectively, in a label-free and calibration-free manner. Commercially sold Coulter counters are frequently used for blood cell counting in hospitals and paint production, among other uses.

Coulter counter apparatus usually allows the detection of species with a size range of 2 – 60% of the aperture's diameter. Therefore, by reducing the size of the aperture to the nanometer scale, the technique can be extended to detect species of this smaller magnitude. Constructing consistently-sized holes of this size range is not necessarily straightforward, however; research in nanopore sensing is focused on different methods to construct these apertures in different membrane materials.[42]

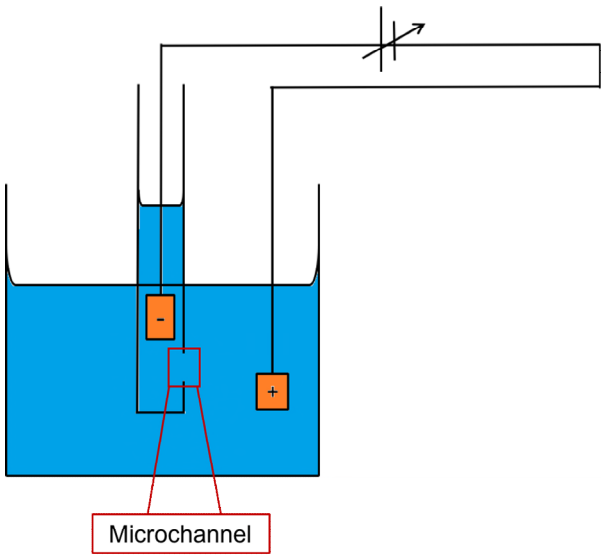

Figure 4 – *Diagram of a simple Coulter counter. Microparticles are counted as they pass out of the test tube, through the microchannel and into solution.*

Single Channel Current Recordings

Single channel current recording is a method originally developed to investigate biological ion channels embedded in a natural lipid bilayer. The flow of ionic current through a channel was used to look at how a channel's conformation could change in response to an external stimulus. For example, acetylcholine was detected by looking at the conformational change and corresponding current fluctuations of the acetylcholine receptor ion channel.[43,44] The use of protein channels as sensors was demonstrated by Kasianowics and Bezrukov in the 1990s[45,46]. Nanopore sensing with biological channels differs from the initial single channel experiments, as channels for sensing applications are reconstituted in membrane of varying types including non-biological membranes composed of organic and inorganic polymer materials[47].

The work of the 1990s led to the development of "stochastic sensing" which allows detection at a single molecule resolution with biological nanopores, most notably shown by the work of the Bayley group.[48,49] Sensing with "Solid-state" nanopores followed as an alternative. This avoided some of the drawbacks of biological pores, however, solid-state nanopores have their own set of issues.

Recent literature has also reported hybrids of these two types of nanopores (to take advantage of the properties of both[50]), and the production of DNA nanopores[51] which will be reviewed in more detail later.[41]

By reducing the size of the aperture to a nanometer scale, the same resistive pulse sensing technique used in Coulter counters can be used to observe nanometer scale or single molecular analytes. Figure 5A shows an idealised representation of a nanopore sensing set up. Either a biological nanopore or a solid-state nanopore can be used as the nanoscale aperture in a membrane between two electrolyte (typically NaCl or KCl) filled chambers. A non-polarisable electrode is placed in each of the electrolyte filled chambers and a potential difference is applied across the electrodes. The potential difference leads to the generation of an ionic current through the nanopore due to the exchange of ions between the chambers either side of the pore[52,53].

For the case of an idealised cylindrical solid state nanopore in a KCl solution of a high ionic strength, the idealised current can be represented mathematically using the following equation[54]:

$$i_o \approx (\mu_k + \mu_{Cl}) n_{KCl} e \left(\frac{4l}{\pi d^2} + \frac{1}{d}\right)^{-1} V_{bias}$$

Equation 1 - *Open current for an idealised cylindrical nanopore*

where i_o is the open current, μ_k and μ_{cl} are the electromobility of K^+ and Cl^- respectively, n_{KCl} is the number density of the salt ions, l is the nanopore's length, d is the diameter of the pore and V_{bias} is the potential difference applied.

Charged analytes can also be driven through the nanopore by the potential difference leading to "translocated events" which cause transient changes in the current (resistive pulse). When no analyte is present, the ionic current remains relatively constant. However, the passage of analytes through the confined volume of the nanopore leads to a detectable increase or decrease in current. Analytes of different sizes and charges will lead to different characteristic current changes (Figure 5B, with both the duration and the amplitude of the event being affected.

The translocation process can be affected by a range of effects including diffusion, electrophoresis and electroosmosis[55].

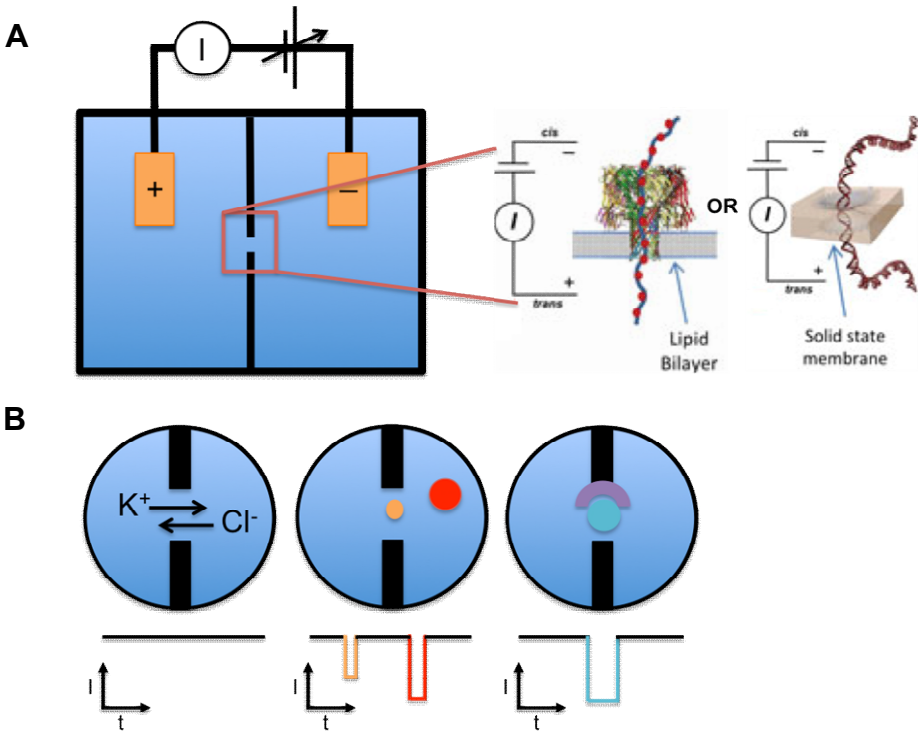

Figure 5 – *A) The set-up of a nanopore sensing device. Analytes travel through the pore in the aperture between 2 chambers, producing a characteristic change in the ionic current. The pore can be of biological origin or an artificial solid-state pore. B) Characteristic reductions in current are seen due to the passage of an analyte; larger analytes will displace a larger volume so will cause a larger reduction in the ionic current. Molecular receptors lead to longer events by increasing the time the analyte spends in the pore.*

The shape and length of a nanopore's channel will contribute significantly to the translocation signal observed. A nanopore with a short length will lead to a larger signal amplitude. This has led to the investigation of increasingly thinner materials for nanopore fabrication, including membranes a single atomic layer in thickness[56]. However, a short nanopore will also have a short translocation signal. Therefore, the minimisation of current noise and the maximisation of the signal bandwidth has become more and more important to ensure high signal sensitivity and reliability.

The bandwidth determines how accurately changes in the current signal can be

detected. The bandwidth needs to be large enough to resolve the full current translocation signal (the full width of the resistive pulse) if meaningful information is to be derived from the current signal. However, noise levels rise steeply with increased bandwidth[57].

Noise in nanopore records affects the sensitivity of the data that can be collected during a nanopore sensing experiment. Current signals need to be of a greater magnitude than current noise to be able to be detected. High signal sensitivity is achieved when there is a high "signal-to-noise ratio". Sources of noise in a nanopore sensing system include those associated with the electronics used for measurement, the membrane material, the membrane thickness, the architecture of the chip supporting the membrane and the fluidic cell used[58]. For solid state nanopores, noise can also be caused by parasitic capacitance of the membrane's support and its surface chemistry[53].

1.1.5 Biological Nanopores

The advancement from devices with micro-apertures to those with nanometer scale apertures was first demonstrated by the manipulation of biological channels naturally adapted to the purpose, Pore forming toxins (PFTs)[40]. Pore forming toxins are secreted in water-soluble form by bacteria such as Staphylococcus aureus. Toxin monomers then oligomerize to form nanopore structures, which can perforate lipid bilayers and cause ionic imbalances in cells or allow secondary toxins to pass in or out of cells.[59,60] The nanopores' abilities to spontaneously insert into lipid membranes makes them ideal for use in sensing apparatus.[61]

The most widely cited biological pore for nanopore sensing is α-haemolysin (αHL). However, work has been carried out with MspA, OmpG, gramicidin, alamethicin and other protein pores to detect the presence of various analytes, including small molecules,[62,63] proteins[64,65] and different conformations of nucleotides.[41,66,67] Table 2 shows the structure and uses of different biological pores seen in literature.

αHL is mushroom-shaped and formed of seven identical polypeptide monomers, which self-assemble to form a heptameric pore. The pore has a minimum constriction of 1.3 nm, and diameters at the cis and trans entrances of 2.9 nm and 2 nm, respectively. The pore has external dimensions of approximately 10 x 10 nm, and consists of a transmembrane β-barrel with a large cap region.[41] When the pore is embedded in a lipid bilayer and a voltage of 100 mV is applied across the membrane, a current of approximately 100 pA can be observed[61]. αHL was used in a nanopore sensing set up for the first detection of different ions and nucleotides[46,68]. The authors were able to directly correlate the concentration of the analyte solution to the frequency of translocation events caused by the analyte, and the length of current blockages were shown to be proportional to the length of the translocating analyte molecules[69].

Pore Name	*Structure*	*Critical Dimensions*	*Types of Analytes*
αHL	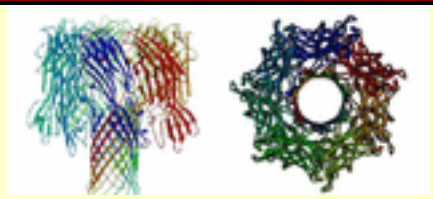	1.4 nm	ssDNA, dsDNA, RNA, protein, small molecules
OmpG	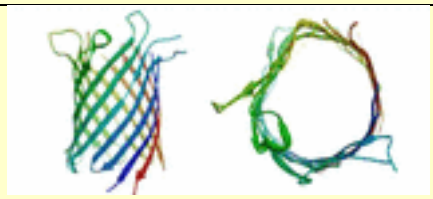	1.3 nm	Protein, small molecules
MspA		1.2 nm	ssDNA, dsDNA
AeL	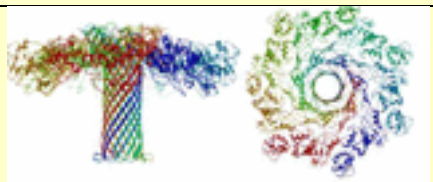	1.0 nm	ssDNA, proteins
Phi29 Motor	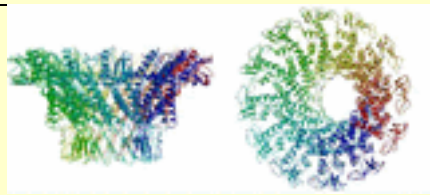	3.6 nm	ssDNA, dsDNA, small molecules, protein
ClyA	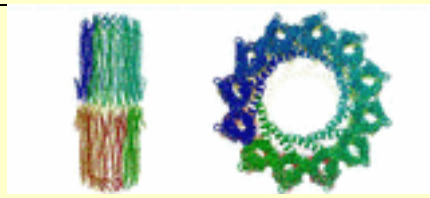	3.3 nm	dsDNA, proteins

Table 2 *– Details of biological nanopores commonly used in sensing applications.*

Since the 1990s sensing with biological nanopores has expanded rapidly. The technique has shown the most success as an alternative to traditional chain-terminating DNA sequencing methods. The main challenge has been to control the translocation speed of nucleotide strands passing through the pore, to allow the resolution and decoding of the DNA bases' current signatures. Approaches have including the engineering of pores to contain recognition sequences[70], or "exo sequencing" where bases are cleaved from a DNA strand by an immobilised enzyme at the mouth of a modified pore [49,71]. However, the most successful approach has involved the use of a DNA phi29 polymerase (DNAP) in conjunction with a biological pore. The DNAP is used to "ratchet" the DNA through the pore, leading to much slower nucleotide translocation speeds and longer current level durations of approximately 28 ms per base, compared to the 1-10 μs of non-ratchetted ssDNA.[49,72]. This technique has been successfully commercialized by Oxford Nanopore Technologies to produce devices aimed at sequencing the human genome for under $1000. Devices such as the MiniION, which are less than 100 g in weight and plug into a computer or laptop via a USB port, have been used to sequence an entire Escherichia coli genome for example.[73]

Sensing of Proteins

Detection of larger analytes, such as proteins, has proved more challenging than DNA detection[74]. The diameter of the pore is generally too small to allow intact proteins to pass through the pore's lumen. However, biological pores can be genetically engineered to allow chemical modification at specific locations in the pore.[75] Receptor molecules linked to the pore via PEG chains[76,77], or aptamers[65], allow detection of the analyte outside the pore (Figure 6). However, this produces a less well-defined signal than when molecules pass through the lumen of the pore. Other indirect methods to allow detection have included the detection of current modulation caused by the analyte's digestion products[78], or the enzymatic cleavage of the analyte protein into peptide fragments prior to translocation.[79] Unfolded proteins can also be passed through the pore after mechanical[80], chemical[64], enzymatic[8182] or thermal denaturation[83]. However, this does not enable information about the globular protein to be collected.

Biological nanopores have the benefit of well-defined geometries and chemical structures, known with atomic precision. Each protein pore is exactly the same, assuring reproducibility in experiments. However, the size and shape of a nanopore is limited to what can be found in nature, which places a limit on the analytes that can be sensed. Although the pores can be modified to add additional chemical groups, modification of the pore is not simple, requiring genetic engineering. The pores also have limited stability when exposed to more extreme temperature, pH or ionic strengths. Solid-state nanopores have been developed as an alternative to biological nanopores, which can overcome some of the limitations of natural pores.

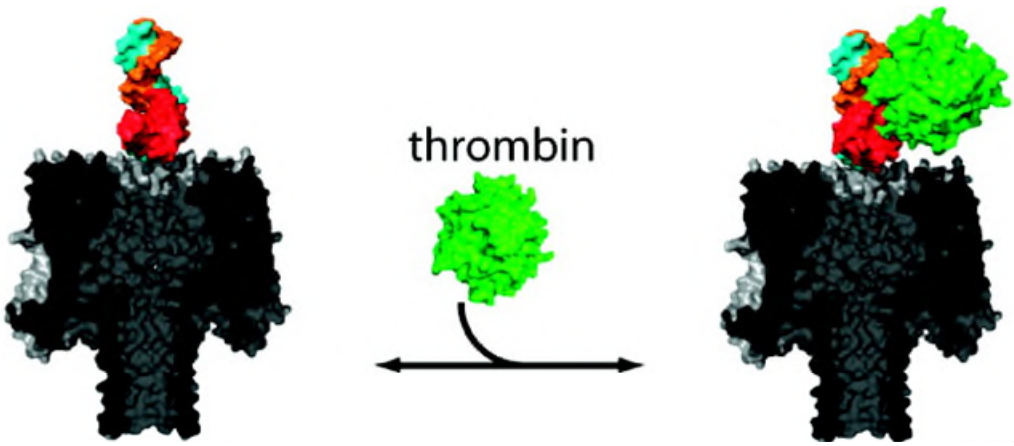

Figure 6 – *An alpha Haemolysin protein pore, equipped with an aptamer at the mouth of pore. When thrombin binds to the aptamer the current flowing through the pore is modulated and the change detected. The aptamer is attached to the pore via an oligonucleotide bound to a cysteine disulphide.*[65]

1.1.6 Solid-State Nanopores

Solid-state nanopores for sensing at the single molecule level were first produced in silicon nitride using ion-beam etching.[84] Other fabrication materials for creating nanopores include silicon dioxide[85], aluminia[86] or polymers, such as polyesters and polyimides (Figure 7A). Some additional fabrication techniques include electron beam etching[85], asymmetric etching,[87] anodic oxidation[86] and track etching[88,89]. Currently, the diameter of pores can be controlled accurately in the 100 to 10 nanometer scale, as described in more detail in the following reviews.[35,41,61]

Ion and electron-beam lithography has been widely used with silicon nitride or silicon oxide membranes to produce nanopores in the sub 5 nm range for biosensing applications.[61,85] However, low sample throughput, expensive instruments and complicated fabrication methods have restricted the productiveness and reproducibility of these techniques.[52,90] Modern focused ion beam (FIB) machines, with electron beams for imaging, can be used to guide the drilling of channels to increase accuracy and allow the patterning of multiple chips with high resolution[40,52,91]. More recently, atomically thin membrane materials have been investigated for nanopore sensing, including hafnium oxide[92], molybdenum disulphide[93], boron nitride[56] and graphene[94,95,96,97]. (Figure 7B) The thinness of these 2D materials allow a higher current to flow through the pore[53]. These materials have potential applications in the production of nanopores with high enough resolution to sense the difference between single DNA bases.[98,99]

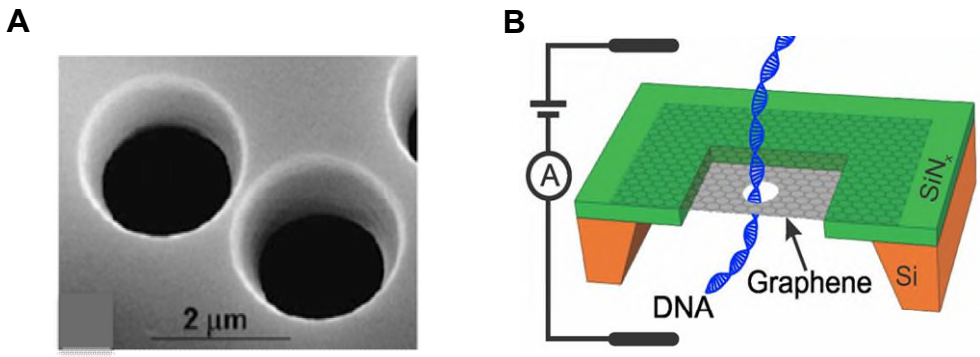

***Figure 7** - A) TEM image of conical poly(ethylene terephthalate) nanopores in a 12 µm thick foil. The pore was fabricated using the track-etching technique.[41] B) Diagrammatic representation of a 2D graphene nanopore mounted on a SiN_x frame.[97]*

Sensing of Proteins

As discussed in the previous section, the narrow lumen size of most commonly used biological nanopores limits their ability to translocate large protein analytes in their folded native state. Solid-state nanopores can be prepared with arbitrary dimensions and are a potential alternative platform for the analysis of native state proteins.[55,100] However, the main problem with solid-state nanopore detection to date has been the poor resolution of analyte translocations. Protein molecules can translocate through the >10nm diameter solid-state pores at an approximate rate of 1 protein per μs. Due to a poor signal to noise ratio, partly due to interactions of the protein molecules with the pore's wall, current amplifiers with a 10 kHz bandwidth tend to be used for experiments.[52,101] It was shown by computer simulation that for sub 100 kDa proteins only the slowest 0.1% of translocations can be observed, and a significant amount of the protein signals are undetected.[102]

Several methods have been investigated to either increase the detection limit of the nanopores or slow the transport of the protein analytes. Protein analytes such as IgG and avidin have been detected using glass nanopores. Glass nanopores have lower electrical noise compared to silicon nitride pores, so 100 kHz filters can be used during experiments[100]. Meller et al. have also detected a small protein, ubiquitin, by reducing the electrophoretic mobility of the protein analyte by keeping the electrolyte solution pH at the isoelectric point of the protein analyte[103]. Bovine serum albumin (BSA) was also detected using a conical PET nanopore, which had an atom thick layer of Al_2O_3 deposited on its surface. This both reduced the pore size and gave the pore surface positive charge. The attraction between the Al_2O_3 surface and the negatively charged BSA molecules slows the transport of the protein through the pore[104]. Edel et al. used DNA carrier strands containing aptamer sequences to bind specific protein analytes before translocation through a quartz nanopipette nanopore[105]. This allowed the detection of the specific proteins by observation of sub peaks in the ionic current reduction produced when DNA strands translocated through the pore. This allowed the identification of the target proteins at low concentrations and in the presence of serum proteins. Keyser et al. employed a similar technique by functionalizing a

translocating DNA strand at certain locations with antigens which bound specific antibodies[106].

Receptor Attachment

Receptors attached to the surface of nanopores can be used to slow protein analyte translocation and also provide selectivity. Metal-chelating ligands have been added to polymeric membranes to detect lactoferrin and his tag proteins[107] (Figure 8). Locked nucleic acid (dsLNA) has also been connected to silicon nitride pores for detection of Nuclear Factor-kappa B proteins[108]. Wei et al. detected single proteins using silicon nitride pores modified with single biological receptors, which is difficult to achieve with solid-state fabrication techniques[109,110] (Figure 9). Conical-shaped pores had a gold layer deposited on their surface, this layer was then modified with a monolayer of ethylene glycol chains. A fraction of the chains was then subsequently modified to show a nitrilotriacetic acid (NTA) tag. The NTA tags were able to bind to receptor proteins modified with His_6 tags via a Ni^{2+} chelate complex. By tuning the ratio of NTA, a single NTA tag and, subsequently, a single receptor protein was added to each pore. IgG was detected however, the pore was unable to differentiate between different types of IgG and was able to recognise one analyte only. There was also no control as to where on the pore's surface the receptor complex was bound, limiting the consistency of the results.

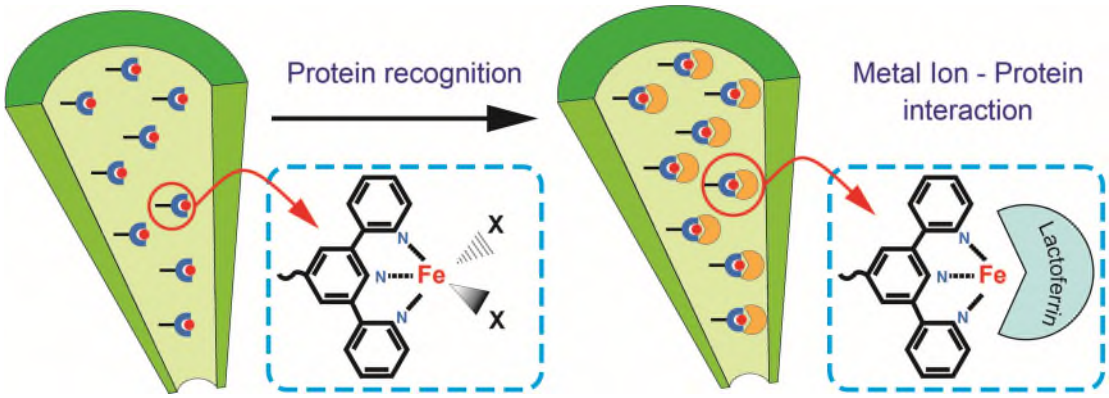

Figure 8 - *Detection of lactoferrin via polymers nanopores modified with a monolayer of amine-terminated terpyridines.*[107]

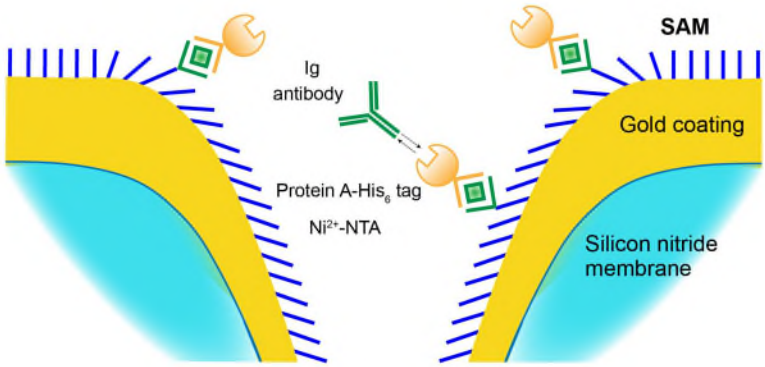

Figure 9 – *One protein A molecule is bound to the solid-state nanopore within the pore to capture IgG reversibly*[110]*.The binding site attached at several different locations on the pores surface.*

The benefits of solid-state nanopores include high stability, allowing recordings to be made over a large range of parameters and easy integration into sensing devices[35,41]. The walls of solid-state nanopores can be modified to display receptors for specific analytes for protein detection[74,110]. However, due to the continuous composition of solid-state pores, attaching a single receptor with precise positioning inside the pore with the correct directionality is difficult[109].

1.1.7 Biological vs. Solid-State Nanopores

Biological nanopores, in general, have a high tolerance for a range of experimental conditions. However, the lipid bilayers that the pores are reconstituted in can be very fragile and limit platform stability[35]. Solid-state nanopores prepared from synthetic polymer such as silicon based materials have much greater durability and stability[111]. Solid-state nanopores can also be tuned to a size range to match the detection of a desired analyte, whereas biological nanopores are fixed and difficult to modify.

Solid-state nanopores however lack the atomic level reproducibility possible when using biological pores. Each biological pore will have the exact same geometry, size and surface properties. These can also be modified by site-directed mutagenesis with precision. Solid-state nanopore technology can currently not replicate this precision, either in the exact sizing of different pores or in the placements of molecular receptors inside pores. This variation can lead to disparity between signals in different experiments and limits the accuracy of sensing set-ups.

Hybrid nanopore set-ups, which combined elements of both biological and solid-state nanopore sensing, have been developed to exploit the benefits and avoid the drawbacks of both solid-state and biological nanopores.

1.1.8 Hybrid Nanopores

Hall et al. tackled the issue of limited stability of biological nanopore set-ups by substituting the traditional lipid bilayer membrane with a durable silicon nitride membrane. A pre-assembled α-HL pore was then inserted into a SiN_x pore, with the coaxial arrangement of the protein pore ensured using a DNA oligo. The oligo was attached to the lumen of the α-HL pore and pulled the α-HL pore into the correct position as it passed through the SiN_x pore, when a potential difference across the membrane was applied[50,52]. Another hybrid approach has involved substituting a biological nanopore with a carbon nanotube (CNT) pore. If the length of the CNTs are of similar size to the thickness of the lipid bilayer, the nanotubes will spontaneously insert into the bilayer. This has been verified in cells using patch clamp measurements and has been used in a sensing set-up to translocate single-stranded DNA[112].

One approach to overcoming the limited variety of biological nanopores has been the de novo design of small peptide nanopores. These could be created synthetically using solid phase synthesis, allowing the inclusion of non-standard amino acids if required[113,114]. Thomson et al. designed an artificial bundle of five to seven water soluble α-helices with an enclosed channel lumen[115], and Joh et al. showed that a de novo four helix bundle could selectively transport Zn^{2+} ions but not Ca^{+} ions[116]. However, it is difficult to design and predict the folding of larger, more complex nanopore structures[117]. A recent hybrid approach to expand the size range and potential of peptide pores involves using DNA as a scaffold to support the formation of the peptide pore[118]. A DNA ring has also been used to arrange a group of PFT (Pore forming toxin) monomers leading to the creation of an artificial protein pore with controllable diameter[119] (Figure 10).

Using the DNA origami approach to make nanopores solely from DNA has shown potential for the development of nanopores for biosensing applications, making possible the design of a large variety of sizes of nanopores. DNA origami combines the properties of both controllable size and dimensions of solid-state nanopores, while maintaining the atomic precision of biological nanopores, and

offers much versatility. DNA origami nanopores will be reviewed in detail in a later section.

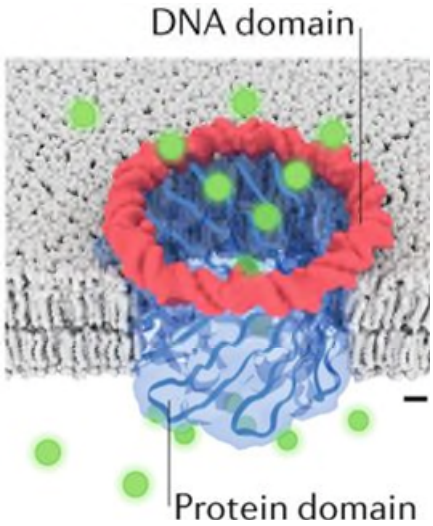

Figure 10 - *Hybrid Peptide-DNA Nanopore. The ring like DNA domain stabilizes the membrane spanning peptide section of the pore*[119,210].

1.2 DNA Nanotechnology

Nanopores built using DNA nanotechnology overcome some of the limitations of more traditional nanopores[75]. In DNA nanotechnology, deoxynucleic acid is used as a nanoscale building material instead of as a carrier of genetic information. Designs take advantage of the physical and chemical properties of DNA to form self-assembling, non-canonical shapes with atomic scale accuracy.

1.2.1 DNA Structure

DNA (deoxyribonucleic acid) is one of nature's most important polymers. The sequence of bases inside the helical dimer contains a code that programmes who we are and is vital for the creation and continuation of life. Its structure has evolved to suit this purpose. DNA's duplex structure is durable and resistant to degradation and modification, yet it is also malleable due to the ability of the structure to reversibly zip and unzip to expose single-stranded sequences under the correct conditions. These properties allow proteins to be coded for, and the code to be copied, while preserving the stability of the original DNA dimer molecule.

The characteristics that make DNA such an efficient, well-evolved information store can be adapted however for the new purpose of nanoscale structural design. DNA's Watson-Crick base pairing, where bases form unique patterns of hydrogen bonds between strands in a duplex, are highly predictable and specific. Adenine (A) bonds to thymine (T) via two hydrogen bonds, whereas cytosine (C) bonds to guanine (G) via three hydrogen bonds. (Figure 11B) This specific, consistent arrangement makes DNA a highly programmable molecule[120,121].

π-π stacking interactions take place between the aromatic rings of adjacent bases in a DNA duplex. The resulting attractive forces contribute significantly to the stabilisation of the double helix structure. Due to the presence of π bonding, aromatic rings possess negatively-charged clouds of delocalised electrons above and below the positive sigma framework of their carbon ring structures. In a DNA duplex the π clouds of neighbouring bases do not sit directly above each other. π

stacking stabilisation is caused by electrostatic attraction between the π cloud of one base and the sigma framework of the adjacent base. These interactions outweigh the repulsion of like charged π clouds and lead to an overall stabilization of the double helix.[122]

DNA in its double helical form consists of two anti-parallel polynucleotide chains, one running in the 5 prime to 3 prime direction, the other running in the 3 prime to 5 prime direction. (3 prime and 5 prime refers to the carbon number in the DNA's pentose sugar backbone). Naturally occurring B-DNA consists of a right-handed double helix with the strands winding around a common central axis. Hydrophobic bases sit on the inside of the structure, while the negatively-charged backbone is exposed to the water-based solvent. The structure and conformation of naturally found B-type DNA is well understood, allowing the planning and building of predictable nanoscale structures. A typical B-type helix has a diameter of approximately 2nm and a length of approximately 3.4 nm per helical turn (10.5 base pairs (bp) per helical turn). The twist of the helix is approximately 34.6^{o} per bp[123].

Another factor that makes DNA an attractive molecule to build with is the relative ease and low cost at which synthetic DNA oligomers can be produced in the laboratory or purchased commercially. Solid Phase Oligonucleotide synthesis is now largely automatic and allows the efficient production of many different oligos in a short time period. A 30 nucleotide length sequence will cost less than \$0.6/nmol[124]. Synthesis is conducted in a cyclic process of several steps, repeated with each nucleotide addition with the use of orthogonal protecting groups. Because synthesis of each strand takes place on a solid support, each reagent can be added in excess leading to typical yields of 99% per step, and consequentially approximately 80% yields for a 20 base sequence. However, although each individual step is high in yield, the decrease in overall yield becomes more significant as the DNA chain length increases. This limits the length of strands that can be efficiently synthesised to approximately 80 base pairs[125].

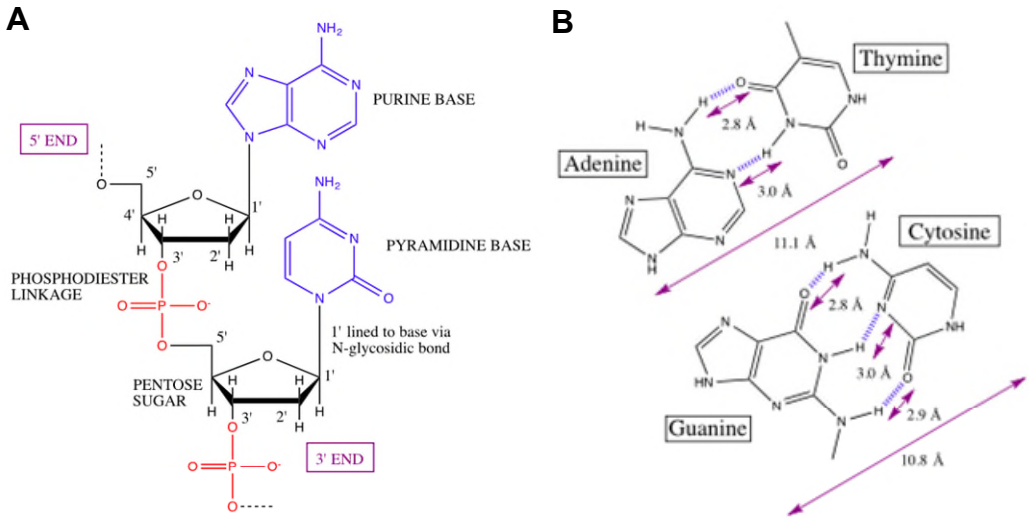

Figure 11 - *A) The structure of two DNA nucleotides showing one purine and one pyrimidine base, pentose ring and phosphate backbone chemical structure. B) The hydrogen bond pairing of the DNA bases. A bonds to T via two hydrogen bonds and G bonds to C via three hydrogen bonds*

1.2.2 Holliday Junctions

DNA nanotechnology is based on the principle that DNA can be manipulated to form "immobilised Holliday junctions" and deriving motifs.[126] The Holliday junction structure, named after Robin Holliday, was first proposed in 1964.[127] In nature Holliday junctions are transient, intermediate structures, connecting DNA strands with similar base sequences or "high sequence symmetry"[128] in recombinant processes.[129] These structure formations are enzymatically controlled and are mobile down the DNA duplex, with structures then collapsing back into double helices. The double helical structure has a greater thermodynamic stability due to complementary base pairing between strands, allowing the quick reformation of the duplex. However, for the formation of synthetic DNA nanostructures, duplex reformation is undesirable. By minimising the symmetry between DNA strands connected in the junction (i.e. using strands which do not have similar base sequences in duplex form), the more complicated multi-strand structure becomes the most stable DNA form and the structure will not collapse into double helices. This allows the formation of complex DNA motifs. The technique of creating artificial "immobilised junctions" was first developed by Seeman et al. in 1982.[126] Seeman et al. were also able to assemble more highly branched junctions including 5, 6, 8, and 12-armed junctions.[130,131]

Figure 12 - *Model of recombination protein ruvA and its square planar arrangement linking 4 ssDNA strands in a DNA Holliday Junction.*[258]

1.2.3 DNA Nanostructures

Using immobilised Holliday junctions and sticky end cohesion techniques it has been possible, over the last 15-30 years, to build a range of DNA nanostructures.[132] Sticky ends are stretches of unpaired nucleotide overhangs extending from the end of a double-stranded DNA molecule, which match up with complementary overhangs on another DNA molecule.[133] Nanostructures will self-assemble into pre-designed structures under the correct conditions, to produce the predicted shape and size of structure with nanometer scale accuracy.

The first DNA nanostructure, a DNA cube[134], was designed and synthesised by Ned Seeman in 1991 (Figure 13). The structure was formed from a series of Holliday junctions connected via sticky end overhangs. 10 single-stranded oligonucleotides were ligated together, to produce two square DNA structures which were then further ligated together into the final 3D cubic structure.[134] Each side of the cube contained two helical turns between the vertices, with each vertex consisting of a Holliday junction branching point.[134,135] Since 1991 many other small DNA nanostructures have been formed, including a truncated octahedron[132] and a DNA tetrahedron[136,137].

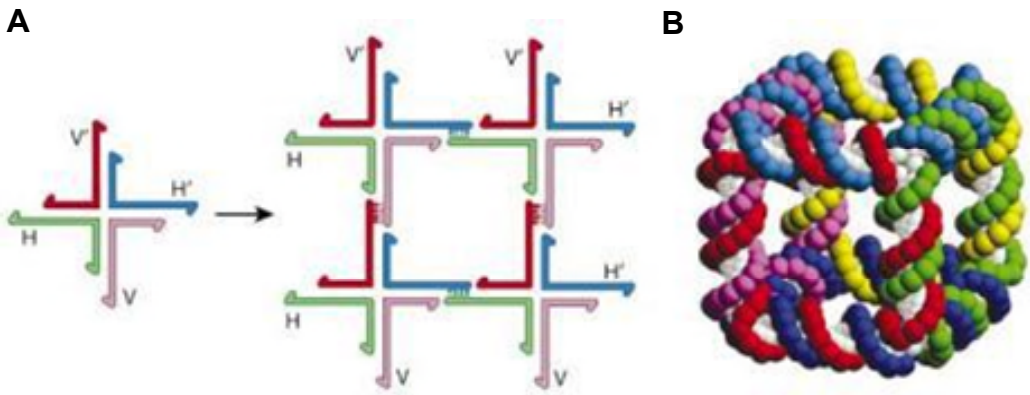

Figure 13 - *Seeman's nanostructure cube[134]. Each edge is constructed of a double helix and every vertex corresponding to the branching points of a Holliday junction. A) the cube's 4 way junctions represented in 2 dimensions. B) A three-dimensional model of the cube.*

To produce small DNA nanostructures, oligonucleotides are required to be combined in precise equimolar concentrations which can lead to multiple product formation, needing purification to separate, and low yields.[138] The structures

produced are generally small in size (in the $1x10^2$ nm^3 range)[139] and have limited complexity. However, larger structures (in the size range of $8x10^3$ nm^3) can be made by a technique known as DNA origami.[124,139]

1.3 DNA Origami

DNA origami was introduced by Rothemund et al. in 2006[124]. The technique involves the folding of a long "scaffold strand", most commonly the M13mp18 genome, with many short oligonucleotide "staple strands"[140]. The technique comes with the added benefit of alleviating the need for stoichiometric conditions, as the oligonucleotide strands are not required to bind to each other but instead bind to a long scaffold strand (Figure 14).

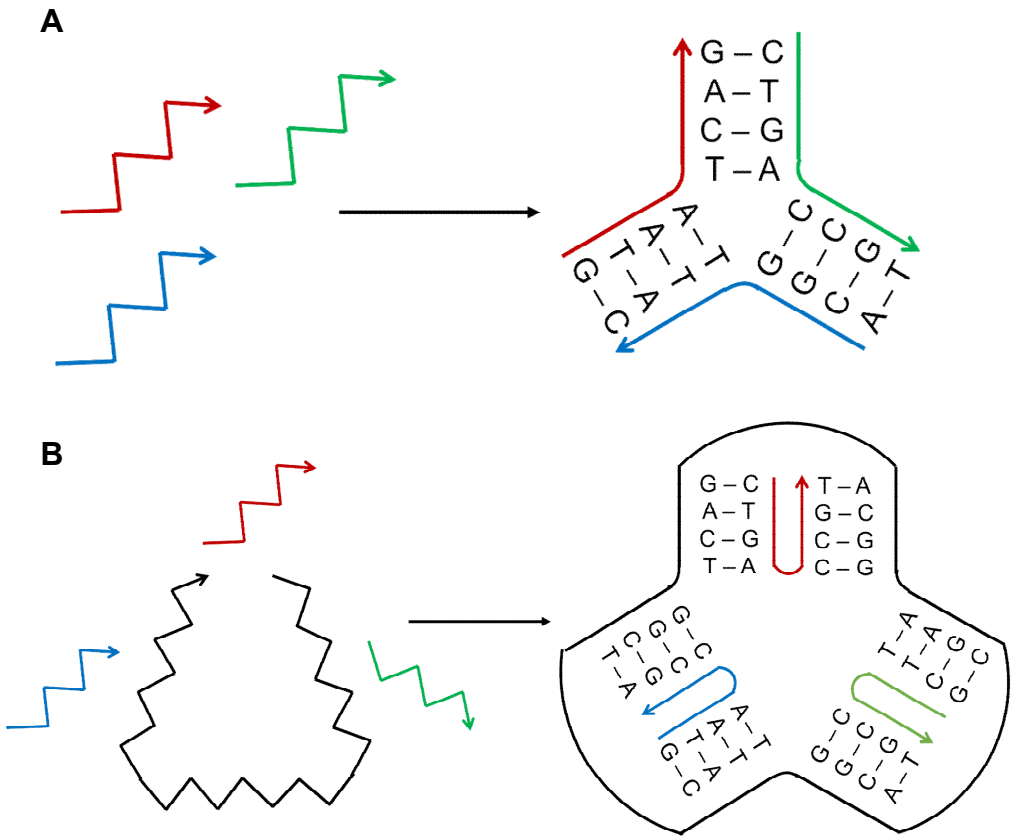

Figure 14 - *A) A multi-stranded approach where DNA strands are combined in equimolar concentrations to build DNA nanostructures. B) The DNA origami approach where short oligonucleotides bind to one larger scaffold strand. The need for equimolar concentrations of strands is elevated in this case.*

It is preferable to use a viral genome with a known sequence as a scaffold strand, as the genomes are thousands of bases long and can be propagated in bacteria and then purified. Staple strands are used in a 100 to 10 fold excess to maximize the yield of the procedure[124]. The elimination of the stoichiometric dependence is also favourable, as it eliminates the need for purification of the oligonucleotides and

reduces the time required for synthesis. With the DNA origami technique it is possible to build up much larger structures than those possible by conventional DNA nanotechnology, with 2D origami tiles formed from single scaffolds reaching sizes of approximately 8500 nm^2, and at much higher yields than Seeman's original nanostructures.[139]

1.3.1 DNA Origami Motifs

For DNA origami design, motifs more complex than standard Holliday junctions tend to be used, such as the anti-parallel crossover (a DX motif). This allows DNA helices to be aligned in parallel orientations with multiple crossovers on the same side[140,141]. There are 3 major variations of branched DNA junction motifs used in DNA nanotechnology:

(1) The double cross over DX motif, consisting of 2 juxtaposed 4-way junctions joined by 2 helical domains. This is the most popular motif and is therefore used extensively in DNA origami structures.

(2) The parameic crossover PX motif, where DNA strands of the same direction are exchanged at every possible site between 2 adjacent double helices. This motif is useful as it joins 2 cyclic DNA strands without opening them.

(3) The JX_2 motif. It is possible for the PX motif to isomerize to the JX_2 motif. The relative positions of the ends of the PX and JX_2 motifs are 180° to each other (Figure 15). This isomerisation can be triggered by exchange of the 2 component strands making the PX motif conversion to the JX_2 useful in nano-mechanical devices.[139]

In DNA origami, DX motifs are usually formed between the staple strands and the long scaffold strand. For staple strands with a helical domain that needs to start and end on the same side of the scaffold strand helix, an integer number of turns is transversed by the staple strand. For any helical domain where the staple strand needs to start and end on opposite sides of the helix, the staple transverses an odd number of half turns[124].

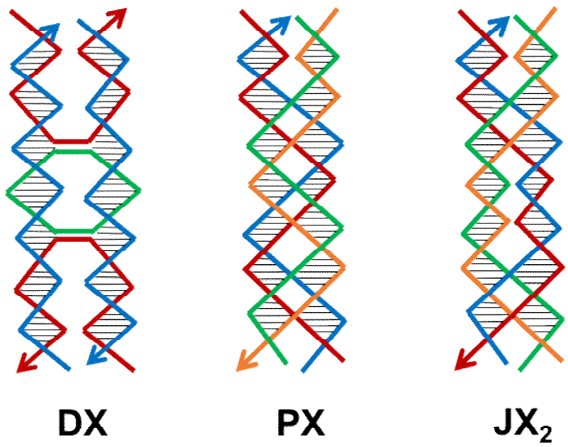

Figure 15 - *Different types of DNA origami motifs that are found in DNA Nanotechnology. The DX, PX and JX_2 motif*

In the seminal publication introducing the origami technique, Rothemund et al. were able to assemble a range of 2D origami shapes, including a DNA smiley face, by placing crossovers with oligonucleotide staples and a scaffold strand every (n + 0.5) helical turns (Figure 16A). The scaffold strand was folded back and forth through the DNA structure, so that it comprised one of the 2 strands in every helix. Staples were then determined to complement the routing path of the scaffold strand[121]. Crossovers were anti-parallel (DX motif), as staples reverse direction as they cross over the scaffold strand[124]. Gothelf et al. later expanded the origami technique to form an origami box where each side was constructed of a 2D origami sheet (Figure 16B) [142]

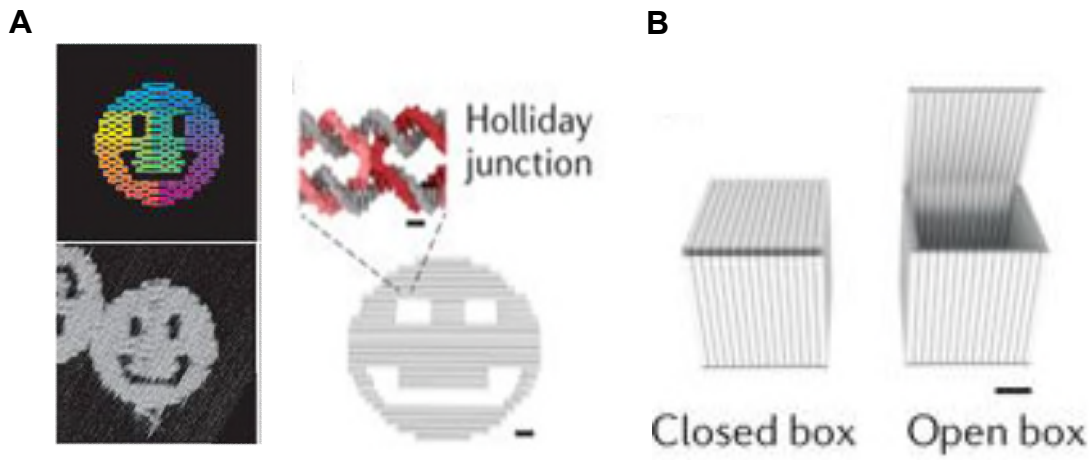

Figure 16 - *Rothemund's 2D origami smiley face with its corresponding AFM image[124]. The structure is formed by DNA origami where a long DNA scaffold strand is linked together by short staple strands. In the inset the staple strands are showed in colour and the scaffold strand in grey. B) An open and closed DNA origami box; duplexes are represent as cylinders[142].*

1.3.2 2D Origami

Originally, origami structures produced were limited to two dimensions. Rothemund et al. demonstrated the formation of a smiley face, five-pointed star and triangle[124]. Since this point, a 2D DNA origami map of China[143] and a dolphin[144] has been produced among a large array of diverse structures.

Curvature can be incorporated into designs by adding single base insertions or deletions to the design of a structure. Addition of bases leads to a local under-winding, resulting in a right-handed torque. Deletion of bases results in a local over-winding and an increase in tensile strain in a DNA strand in a DNA origami bundle. This results in a left-handed torque[145]. By employing a gradient of deletion and insertion into designs a curve can be added, with the steepness of the gradient affecting the degree of curvature. Curvature has been demonstrated of up to 180°, with structures being formed in high yields with up to 120° curvature.[145] Periodic base insertions and deletions have been used to construct concentric DNA rings[146] and a Mobius strip origami structure[147] among other structures (Figure 17).

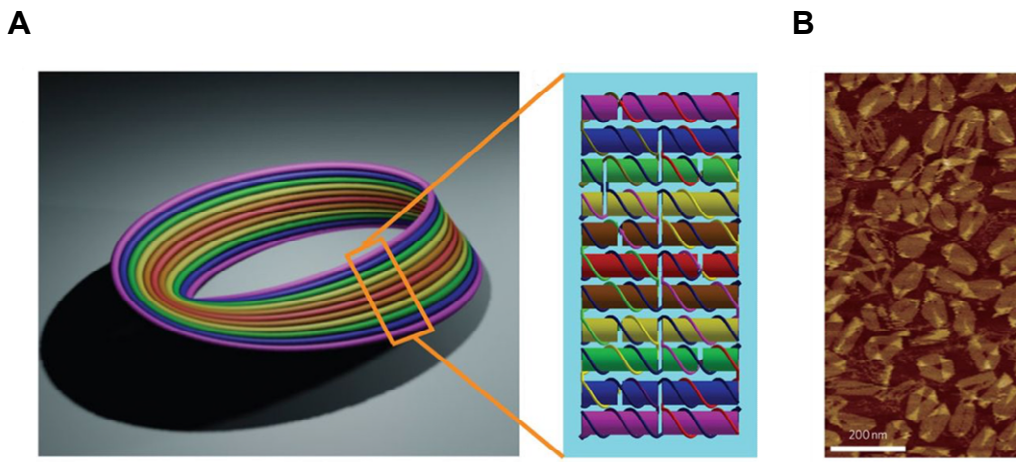

Figure 17 - *A) A model of the Mobius strip DNA origami created by Yan et al. introduces curvature into the origami's design. Each colour in the model represents a different DNA helix. B) AFM images of the Mobius strip origamis*[147]

`

1.3.3 3D Origami

Initial three-dimensional objects involved the formation of planar 2D origami structures, which could then be subsequently folded in additional steps into 3D shapes. Gothelf et al. used this methodology to construct a DNA cube, with planar sides and a lid which could open and close.[142] Step-wise folding methods were also used to construct a DNA prism[148] and a tetrahedral container.[149] Douglas et al. were also able to follow similar methods, but with the addition of base deletions and insertions, to construct a 3D spherical football and nanoflask.[146]

More recently, it has been shown that 3D origami structures can be designed by stacking layers of origami on top of each other. This has the added benefit of increasing the rigidity of designed` structures. Douglas et al. described stacked structures which involved a six-helix bundle basic unit. These units were then built up into 3D blocks with a "honeycomb lattice" cross-section. A monolith, slotted cross and square nut were constructed using this cross-section[145] (Figure 18).

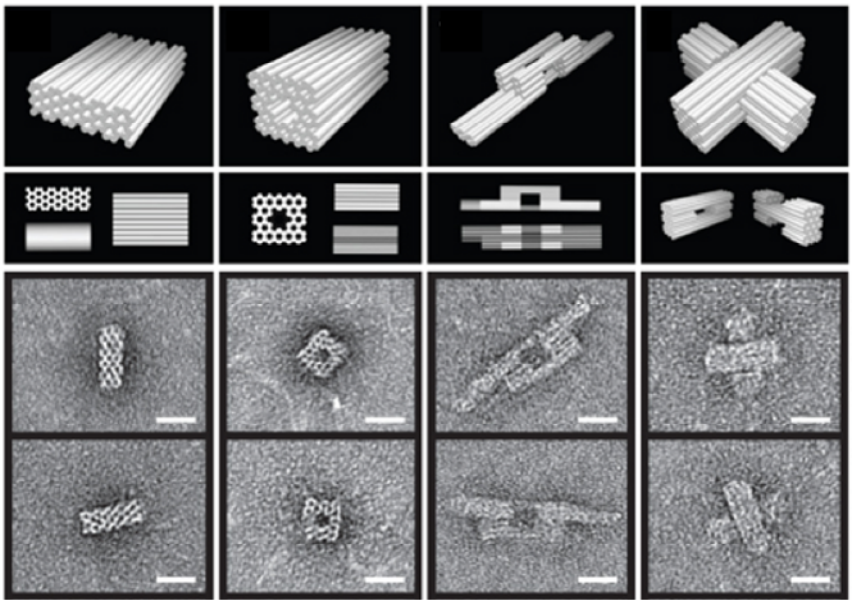

Figure 18 - *Each column shows the model view and TEM imaging of one of 4 3D origami objects: a Monolith, Square Nut, Railed bridge and slotted cross origami.*[145]

Ke et al. and Dietz also reported an alternative to this approach using a "square lattice" as opposed to a honeycomb, which led to the production of a more densely packed origami structure which could also be programmed to contain twists and curvature.[150151] Although multilayer structures increase the rigidity of structures, much care is needed in the routing of scaffold and staple paths to maintain high structural yields. Long folding protocols are also needed to avoid kinetic traps.[152] High concentrations of magnesium ions are needed in folding buffers to counteract the electrostatic repulsion of neighboring negatively-charged DNA backbones.[153] Folding of multilayer objects can be simplified significantly by the use of DNA origami modeling software and programs such as CaDNAno and CanDo.[154]

1.3.4 CaDNAno

Objects designed using the DNA origami technique involve the use of hundreds of staple strands and the hybridisation of thousands of base pairs. Hybridisation between neighbouring strands is only possible at points where the helical twists bring helices into contact in appropriate orientations. This can make designing of origami structures by hand extremely difficult.

CaDNAno is an open source software created by Shawn Douglas at the University of California[154], which vastly simplifies the design process of DNA origami. The software works using a reduced representation of the DNA structure, which breaks down the design of structures to a set of rules to be followed. In DNA origami, a long strand is routed back and forth to develop a scaffolded version of the structure to be built. The scaffold strand runs back and forth through adjacent helices. These helices are then held together by staple strands, which cross over between different sections of scaffold helices. Crossovers can only take place where adjacent helices touch, with one section of scaffold running in the parallel direction and one section of scaffold running in the anti-parallel direction. As a DNA duplex is arranged in a helix, adjacent duplexes only touch at certain points and can therefore only form crossovers at certain points. CaDNAno routes scaffold through a DNA origami object, using either the honeycomb lattice or square lattice arrangement. Crossover locations can be predicted, assuming B type DNA with geometric parameters of 2.5 nm diameter, 10.5 bp per turn.

Honeycomb Lattice

The honeycomb lattice allows each helix to touch 3 neighbouring helices, at 0^o, 120^o and 240^o to the helix. The helix twists through 240^o every 7 bp, therefore a crossover can be made in one of the 3 possible crossover positions at every 7 base pairs. To make a second crossover between the same 2 adjacent helices a distance of 21 bp needs to be traversed; this is equivalent to two full helical turns. Therefore crossovers can take place every 0 + 21n bases, 7 + 21n bases, or every 14 + 21n bases to the 3 adjacent helices[146].

Square Lattice

The square lattice arranges a 33.75° per bp average twist instead of the normal 34.3° per base pair. This leads to a slight under winding of the DNA helix, which can lead to an overall global twist in the structure. However, by assuming 10.67 bp per turn, neighbouring helices can be arranged with 4 neighbouring helices at 0°, 90°, 180° and 270° to the top of the central helix. This arrangement allows the formation of more densely packed DNA origami structures, which is useful for nanopore design as less residual current can pass through the DNA origami framework. The helices in this model twist through 270° every 8 base pairs, allowing crossovers between neighbouring helices every 8 base pairs (at 0 + 32n base pairs, 8 + 32n base pairs, 16 + 32n base pairs and 24 + 32n base pairs). This makes crossovers between a pair of adjacent helices possible at every 32 base pairs[150].

1.3.5 CanDo

When designing DNA nanopores for use in sensing apparatus the rigidity of the pore, especially the lumen of the pore, is important for achieving consistent, stable recordings. The stability of a structure can be qualitatively assessed using an open source program called CanDo (Computer-aided engineering for DNA origami). https://cando-dna-origami.org/ CanDo uses the CaDNAno .json files to provide coarse and fine grain modelling of flexibility and strain in the origami nanopores. CanDo models base pairs as "two-node beam finite elements". The coarse model denotes isotropic elastic rods, which are constrained to their nearest neighbours at crossover positions. The fine grain model calculates the shape and flexibility of single base pairs in the design, assuming length and width of 0.34 nm and 2.25 nm and stretch, bend and twist moduli of 1,100 pN, 230 pN nm^2 and 460 pN nm, respectively[155]. It uses the finite element method to generate a 3D DNA shape from the CaDNAno design, which is disrupted by external forces modelling thermal fluctuations. The application of these forces deforms adjacent helices so a qualitative assessment on the rigidity of the structure can be made[152].

CanDo outputs picture and video heatmaps displaying the DNA's response to thermal fluctuations, which can be downloaded and retained. (Figure 19) Successive cycles of CaDNAno design and CanDo assessment can be employed until rigidity of the structure is within desired limits.

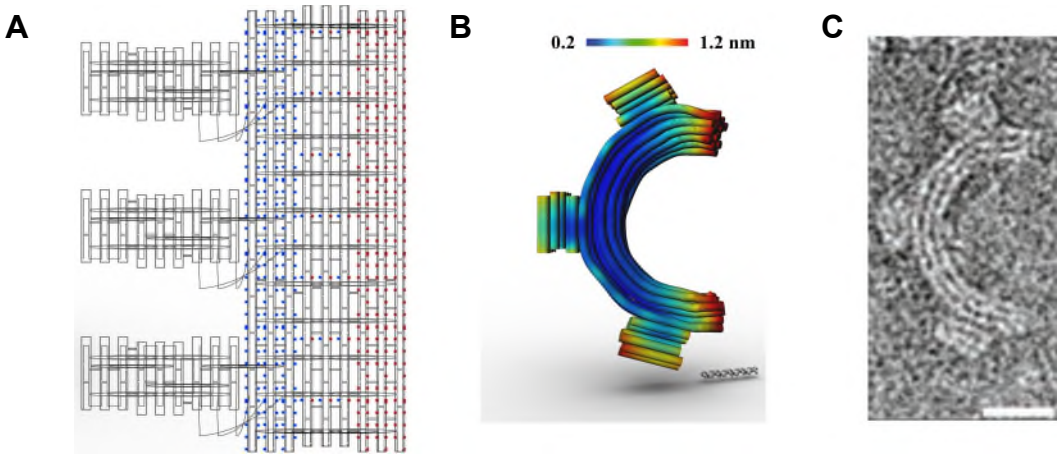

Figure 19 - *DNA origami gear[151] formed of 3 by 6 helix bundles and designed using the honeycomb lattice in CaDNAno. A) Shows the CaDNAno strand map. Red and blue dots represent base insertions and deletions respectively which introduces curvature into the object. B) The CanDO 3D representation of the gear. Red represents areas of high flexibility and blue areas of low flexibility with the scale bar shown at the top of the image. C) TEM image of the origami gear. The scale bar represents 20 nm.*

1.3.6 Base Stacking

Larger DNA origami structures can be formed by linking several DNA origami "tiles" together, with each tile consisting of a fully hybridised DNA scaffold. Tiles can be joined together by either using DNA sticky ends, which "stick" the tiles together via base pairing[156,157,158], or by manipulating the non-sequence specific base stacking interactions at the edges of helices.[159,160] Both of these interactions contribute to a lower enthalpy which allows the lower entropy of the larger, more organised structures to be compensated for.

Base stacking interactions are important to consider when designing DNA origami structures so they can either be prevented or manipulated[161]. π-π stacking contributions provide considerable stabilisation to a duplex and, at "blunt-ends" of DNA helices in the structures where the helix changes direction, base stacking can lead to assembly of multiple DNA objects[121]. Unwanted stacking between origami units can be prevented by leaving single-stranded sections of sequence at the edges of origami designs, as stacking is not possible with ssDNA.

Dietz et al. showed that by varying the Mg^{2+} concentration and temperature of solutions containing DNA origami, the relative forces of blunt end stacking and the repulsion of negatively-changed origami units could be controlled. They demonstrated the importance of stacking contributions by assembling a multi-unit nanorobot, which was shown to reversibly assemble and change its arm conformation when salt concentrations were varied[162] (Figure 20).

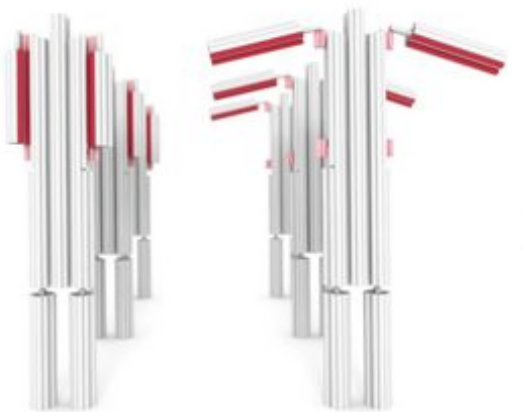

Figure 20 - *DNA robots by Dietz et al. [210] The arms of the robot sit in an open or closed conformation by changing the concentration of Mg^{2+} in the origami buffer from 30 mM to 12.5 mM.* [162]

1.3.7 Folding Origami

The components of a fold reaction normally consist of:

- The DNA scaffold strand
- The DNA staple strands (typically in a x10-x100 excess)
- pH controlling buffer
- mono or divalent cations such as Na^+ or Mg^{2+}

The fold reaction is then heated up to melt the DNA strands, and cooled slowly using an optimised protocol.

The presence of a concentration of cations helps stabilise the secondary and tertiary structures of the DNA origami structures, by reducing the electrostatic repulsion between neighbouring strands. Divalent Mg^{2+} is most commonly added to origami folding solutions as $MgCl_2$. Multi-layered structures can be extremely sensitive to $MgCl_2$ concentrations, and screening of salt concentration is often required to optimise fold reactions and maximise yield.[152,163]

Although DNA origami techniques have been used to build a plethora of nanoscale objects, the mechanism by which assembly takes place is still not fully understood. Recent work into the mechanism of staple and scaffold hybridisation has allowed more rational design of folding protocols, and therefore higher yields of correctly formed DNA structures.[164,165] Dietz et al. looked at the folding and unfolding temperatures of origami using real-time fluorescence monitoring and cryogenic reaction quenching. It was shown that, both in folding and unfolding, there was a narrow transition temperature, suggesting strong cooperativity of folding. Dietz was able to demonstrate that some origami objects can be rapidly folded with an almost 100% yield by holding the origami solution at a fixed optimized temperature.[166] This has been confirmed by other groups and is now common practice for the folding of some origami structures.[167,168]

However, DNA folding is thought to be as complex as protein folding.[121] Simply changing the routing of the scaffold strand can change the kinetics and thermodynamics of an origami object's folding significantly.[169] The presence of

incorrectly folded DNA origami structures in final annealing products suggests that there are multiple folding pathways available during folding, and that there are multiple topological or kinetic traps present.

Many origami object folds, especially those of multi-layered objects, require "ramp" protocols, where the temperature is decreased at defined rates, to fold in high yields. Incorrectly folded structures can be prevented by extending the time and slowing the rate of annealing, allowing reversibility in staple binding steps.[170,171]

1.3.8 DNA Origami Functionalisation

When choosing an alternative building material for nanopore production a desirable characteristic is a material which can not only form structures with atomic level specificity, but also a material which will allow the positioning of additional functional groups with the same level of precision. DNA origami has been shown as a tool for atomic level organization of a range of nanomaterials, including protein[172,173], metal nanoparticles[174,175,164], quantum dots[176,177,178], carbon nanotubes[179] and fluorophores.[180]

Origami Functionalized with Protein

Incorporation of modified nucleotides with additional functional groups to staple oligomers during solid phase synthesis allows the addition of functionality to DNA objects at predetermined positions. Nanoscale precision is possible to a degree beyond what is possible through top down synthetic approaches. For example, origami structures have been used to produce an effective "nano-breadboard" for chemical reactions[181]. Voigt et al. demonstrated that biotin could be conjugated to nucleotides in staple strands via a range of chemistries. Biotin-conjugated nucleotides could then be used to non-covalently attach larger protein streptavidin free in solution[181]. More recently, three-dimensional functionalized structures have been designed, such as Kostiainen et al.'s enzyme cascade nanoreactor. The origami structure is functionalised with glucose oxidase (GOx) and horseradish peroxidase (HRP) via avidin-biotin interactions. The structure was shown to demonstrate an efficient GOx/HRP enzyme cascade reaction[182]. Sacca et al. were also able to demonstrate the orthogonal attachment of proteins to an origami face. As well as a biotin-streptavidin interaction, fusion proteins containing snap-tags (O6-alkylguanine-DNA-alkyltransferase (hAGT)) and halo-tags (haloalkane dehalogenase) were bound to the origami face via benzylguanine (BG) and chlorohexane (CH) groups on staple oligonucleotides[183].

TEM and Cryo-EM has been shown as a powerful method to image both DNA origami and protein structures[184,185]. The binding of protein to a DNA origami

lattice has been suggested as a technique to allow high resolution determination of protein structure. Martin et al. showed that the transcription factor p53 could be imaged at an approximately 15 Å resolution by binding to a duplex crossing an origami structure.[173] The orientation of the protein could be controlled by shifting the binding domain along the DNA's helix.

DNA origami functionalised with the intrinsically disordered proteins FG-Nups has also been used to model nuclear pore complexes (NPCs). NPCs control the molecular exchange between the cell cytoplasm and the nucleus in eukaryotic cells. However, how the NPC allows transport of macromolecules is not fully understood. In two studies different types and copy numbers of FG-Nups were attached to DNA origami rings to investigate how the protein's density affected the NPC's transport properties.[186,187]

Origami Functionalized with Nanoparticles

Metal nanoparticles with plasmonic properties are becoming vital tools in nanotechnology, with possible applications in miniaturized optical sensors[188], electronic devices[189] and photonic circuits[188]. However, the plasmonic properties of structure are strongly dependent on the orientation and distances between particles. Assembling nanoparticles into plasmonic structures requires a considerable degree of control on a small scale, which can be difficult with traditional fabrication methods[188]. DNA has proved to be an extremely promising linker, capable of reversible assembly[190]. Gold nanoparticles can be functionalised with single-stranded DNA via terminating alkanethiol groups at the 3 prime and 5 prime positions[191,192]. A 2D triangular piece of origami was used by Ding et Al. to organize different sized gold nanoparticles into a precisely controlled linear sequence.[193,194] Gold nanoparticles have also been positioned in 3-dimensional arrangements around DNA origami nanorods[195], rings, and tetrahedral scaffolds[196].

Origami Functionalized with Aptamers

DNA aptamer sequences can be added to the sequences of DNA staple strands, so that they protrude from specific locations on a DNA origami object's surface. DNA aptamers are DNA strands selected by SELEX (systematic evolution of ligands by exponential enrichment) to bind to targets. Aptamers have been shown to bind proteins, small molecules, viruses and cells[197]. Yan et al. used a DNA tile, with precisely placed aptamers, to show distance dependent aptamer-thrombin binding[198]. Low affinity of the two aptamers to the protein were seen when the aptamers acted alone, but a much higher binding constant to the thrombin protein was observed when the 2 aptamers were at a precisely defined closer distance (5.8 nm). Douglas et al. also used DNA origami with integrated aptamers to build a locked DNA nanorobot, containing five antibody fragments active against human leukocyte antigens. The box would only open when correct "keys" bound to the aptamer locks[199]. (Figure 21A)

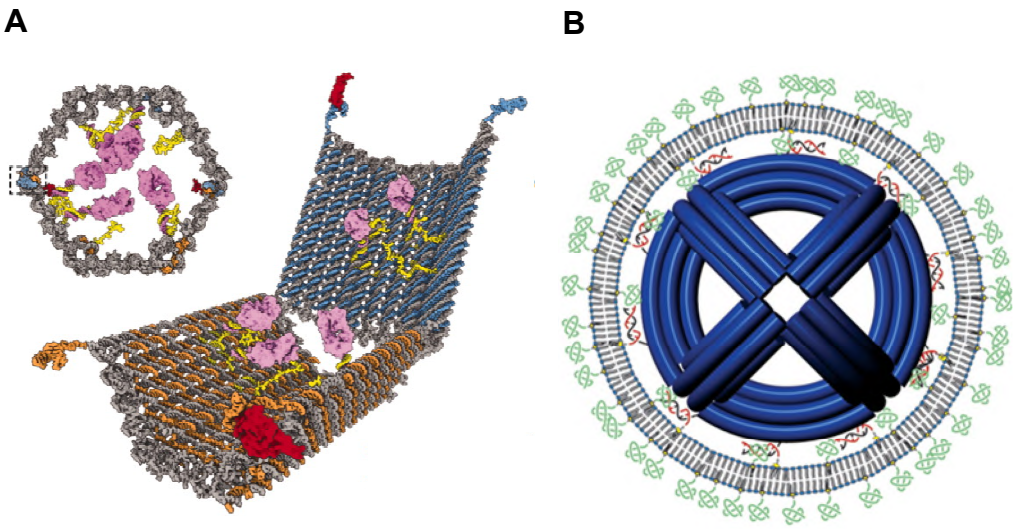

Figure 21 - *A) A Nanorobot which can open and close using aptamer binding[199]. B) PEGylated-lipid bilayer coated DNA nanostructure[202].*

Origami Functionalised with Lipid

Importantly for the production of DNA nanopores, DNA origami can also be functionalised with organic molecules, such as cholesterol[200,201], or lipids[5,202] which allows the structures to associate with lipid bilayers. Rectangular[203,204], brick[205] and star[206] shaped origami rafts have been built which can associate with and shape lipid bilayers[207,208].

Shih et al. coated a DNA origami sphere in PEGylated lipid to improve the pharmacokinetics and immune response to the origami[202]. (Figure 21B) Lin et al. used a DNA ring, functionalised with lipid molecules, to guide the formation of liposomes with a narrow size distribution[5]. More complicated membrane morphologies such as rings, tubes and spirals were also templated using a similar approach and multiple interconnected cylindrical or square shaped nanocages[209,210]. Ding et al. also used a cuboid DNA origami, which was conjugated via poly A sticky ends to a poly T functionalised poly(aryl ether) dendron, and had a hydrophobic core possessing eight hydrophilic oligo(ethylene glycol) to template cubic vesicles[211] Ethane capped residues[212] and porphyrin[213] molecules have also been used as "lipid anchors" in DNA nanopore designs, discussed in detail below.

For DNA origami to be used as a potential building material for nanopores capable of biosensing it is essential that the origami structure can be functionalised with hydrophobic moieties, that can allow interaction between the nanopore and lipid membranes.

1.4 DNA Nanopores

It can be seen from the previous sections that, as a building material, DNA possesses many properties that make it a versatile and suitable material for nanopore fabrication. DNA has been programmed to construct nanopores with a large variety of structures and shapes, but with atomic level precision. The first nanopores constructed from DNA were published in 2011[214]. DNA nanopores can be separated into two groups: (1) DNA nanostructure pores, and (2) DNA origami pores. DNA nanostructure pores are much simpler and smaller in size, and are assembled using a few oligonucleotides in equimolar concentrations. Whereas DNA origami nanopores are assembled using the DNA origami technique, and are generally much larger in size and of more complex design. Their larger size allows the potential detection of much larger analytes.

1.4.1 DNA Nanostructure Pores

Burns et al. published small nanostructure pores in 2013, consisting of 6 duplexes, with a lumen diameter of 2 nm, similar to the minimum constriction of αHL (1.4 nm) (Figure 22). Pores were inserted into bilayers in a similar set-up to that used for biological pore sensing. The main concern when building DNA nanopores is the insertion of the negatively-charged, hydrophilic, DNA phosphate backbone into the hydrophobic layer of the membrane bilayer[75]. A region of negative charge must be masked for insertion. This has been done in several ways. Firstly, Burns et al. modified 72 nucleotides in the nanopore structure to possess PPT (phosphorothiolates) groups, by incorporating the groups during the solid phase synthesis of the 14 oligonucleotides making up the structure. The PPT groups were then further reacted with iodoethane to produce charge-capped ethyl-PPT groups. This produced a "hydrophobic belt" around the centre of the nanopore[212]. (Figure 22A) The ethyl-capped pores were then shown to insert into cell membranes as well as synthetic membranes, suggesting potential in cytotoxic applications. The pores were able to interact with the membranes of cervical cancer cells and trigger cell death[215].

`

Secondly, Burns et al. described nanopores of the same type, but with two tetraphenyl porphyrin tags as lipid anchors. The DNA strands were linked to the tags via a sonogashira coupling reaction[3]. Only two copies of the lipid anchors were needed, instead of a full ring of ethyl modifications. The fluorescent properties of the tags were used to visualise the structures inside giant unilamella vesicles[3]. The monomeric nature of both nanopores was confirmed by AFM and DLS analysis. Constant flow was seen through the pores at a potential of +100 mV and -100 mV[3,212]. A channel conductance, in the order of magnitude of 0.4nS in 1 M KCl, 50 mM tris (pH 5), was seen for both pores.[75]

Seifert et al. demonstrated that there were 2 conductance states seen for the pores[4]: a stable high conductance level at low voltages, and a lower conductance level at high voltages, caused by changes in conformation or orientation of the DNA. Seifert et al. showed the translocation of PEG molecules through the nanostructure pore[4]. However, it is unlikely that translocation of DNA is possible with a pore of this diameter, due to the strong electrostatic repulsion between the strands[75].

Göpfrich et al. also demonstrated that a single DNA duplex could act as a nanopore when functionalised with porphyrin anchors. The 19-nucleotide long duplex had 6 porphyrin tags attached at modified T bases, so that the duplex spanned a lipid bilayer. The duplex lacked a central channel, however, the lipid around the duplex formed a “toroidal” pore which was permeable to the passage of ions. When monitoring the pore via ionic current traces the duplex showed insertion, closing and gating steps, with a conductance of approximately 0.06 nS observed. This set-up, however, is not viable for the conductance of any larger analytes.[213]

A progressively more popular anchoring method for nanopore production is the use of cholesterol as a hydrophobic anchor. Göpfrich et al. used cholesterol anchors in small DNA nanopores consisting of only 4 duplexes, leading to a pore lumen diameter of 0.8 nm and an external diameter of 4nm. Two of eight DNA single strands used to make the pore carried terminal cholesterol modifications, which acted as membrane anchors.[216] Burns et al. also used cholesterol anchors in several publications, with a variation of the previously published 6 helix pore.

Cholesterol anchor possessing pores were inserted into the membrane of polymersomes containing the enzyme trypsin. It was shown that the enzyme substrate (Boc-Gln-Ala-Arg-7-amido-4-methylcoumarin) was able to enter the polymersome, and the fluorescent product AMC (amido-4-methylcoumarin) was able to leave the polymersome via the DNA nanopores.[217]

Another study used a cholesterol-anchored, 6 helix pore, which also possessed an additional "lock" strand that could control the selective movement of analytes across a bilayer. When a "key" strand was not present the pore remained closed, however, when the key strand was provided the pore was able to open and allow the translocation of analytes[2]. (Figure 22B) The selectivity of the DNA nanopore was also shown in this study by looking at the passage of two analytes, SRB (sulpho-rhodamine B) and CF (carboxyfluorscein). SRB, which possesses a positive charge and two negative charges, translated at a 13-fold higher selectivity than CF, which possessed three negative charges. This was suggested to be due to the negative charge of the DNA nanopore[117].

Further studies using the Burns et al. 6 helix nanopore as a model have been carried out to gain a deeper understanding into the dynamics of pore insertion and interactions with lipid bilayers[218,219]. In one study, different numbers of cholesterol anchors were used to study the mechanism of nanopore insertion. It was shown that insertion of the nanopores tended to happen in two steps. The first step involves the fast tethering of the pore to the membrane via a single anchor, which is then followed by a slower reorientation and puncturing step involving multiple anchors. It was also observed that insertion was more efficient in curved bilayers compared to flat bilayers, potentially due to the lipid misalignment and therefore lower energy barriers for pore insertion[218]. Molecular dynamics simulations have also been conducted with the 6 helix pore to look at how the pore interacts with ions and water in solution, the causes of conductance gating steps[220] and the stability of the hydrophilic nanopore in hydrophobic lipid bilayers[221]. It was shown that gating is caused by motion at the openings of the DNA nanopores, and that the lipids near the nanopore rearrange to interact closely with the membrane-spanning portion of the DNA nanopore.

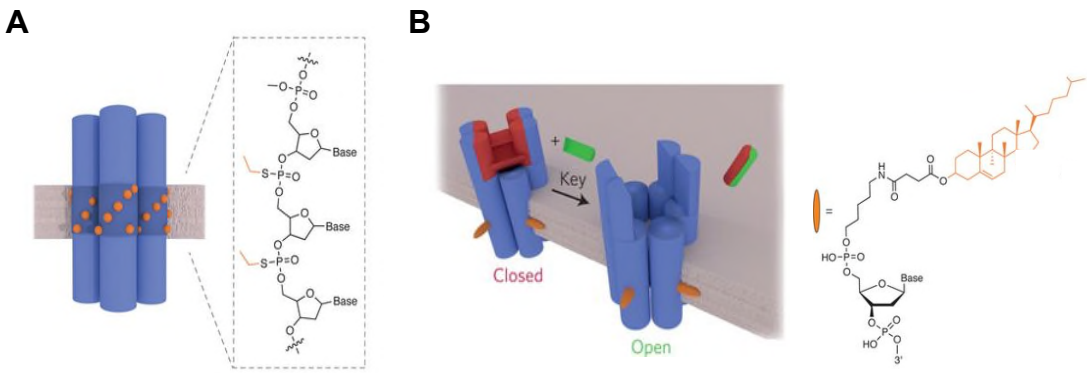

Figure 22 *- A) A Six duplex nanopore anchored in the lipid bilayer by charge masking ethyl phosphorothioate residues.*[212] *B) A DNA nanopore which is anchored in the membrane by cholesterol residues. The design also features a lock strand (red) which is removed by hybridisation of a key strand (green)*[2,117]

1.4.2 DNA Origami Pores

Although DNA nanostructure nanopores have been shown to be useful over a range of applications, the size of the pores limits the size of the analytes which can be efficiently detected. In this sense nanostructure pores have not overcome the limitations of biological pores. The flexibility of DNA origami design has led to the creation of de novo molecular nanopores with a diversity of pore architectures. DNA origami enables the design and fabrication of nanopores of size ranges larger than that possible for protein pores, while maintaining exact structural specificity not currently possible with solid-state nanopores. To date origami nanopores have been designed both to associate with prefabricated solid-state nanopores, as well as to associate with lipid bilayers in a similar way to biological pores.

Wei et al. and Bell et al. described using larger DNA origami structures as nanopores in a hybrid arrangement with solid-state pores[214,222]. (Figure 23) In both designs, DNA nanopores were inserted into larger solid-state nanopores using electrophoretic force[75], similar to the insertion of α-HL into solid-state nanopores by Hall et al. in 2010[50]. Wei et al.'s origami structures are simple origami nanoplates of 6 nm thickness and pore diameters of 9 x 14 nm and 5 x 7 nm[222] (Figure 23B). Evidence for correct trapping of the origami was shown by the decrease in current with decreasing lumen size[75]. Hernández-Ainsa et al. showed that these nanoplates could be combined with nanocapillaries, by laser-assisted capillary pulling[223]. When trapping the origami, the current drop was of a different magnitude depending on the voltage applied during trapping. This suggested a distortion of the origami nanoplate's structure when larger voltages were applied. In this study, a difference was seen in the translocations of DNA strands possessing hairpins for a 5 nm x 7 nm pore and a 14 nm x 15 nm pore.[223] The nanopore was also used to observe the passing of streptavidin, in comparison to IgG; IgG was too large to pass through the aperture of the DNA nanopore. The recordings however were extremely noisy compared to the solid-state nanopore, making events corresponding to individual translocations difficult to identify.

Bell et al. reported a more complex origami design of a DNA nanofunnel. The nanopore was based on the 8613 base pair scaffold, and involved progressively larger "skirts" of origami arranged in a square lattice format. Each skirt overlapped with the previous skirt in an 8 bp-16 bp double layered section, with the rest of the structure being a single duplex layer thick. (Figure 23A). Hybridisation with the solid-state pore with the correct orientation was ensured by directed trapping by an attached 2.3 kilo base pair DNA tail[214]. After hybridisation, the narrowest width of the nanopore was reduced to 7.5 nm x 7.5 nm. The funnel was able to detect the passing of double-stranded λ-DNA, however, the quality of the recordings were again very noisy compared to the solid-state pores alone. The pore was also not shown to be able to translocate protein analytes.

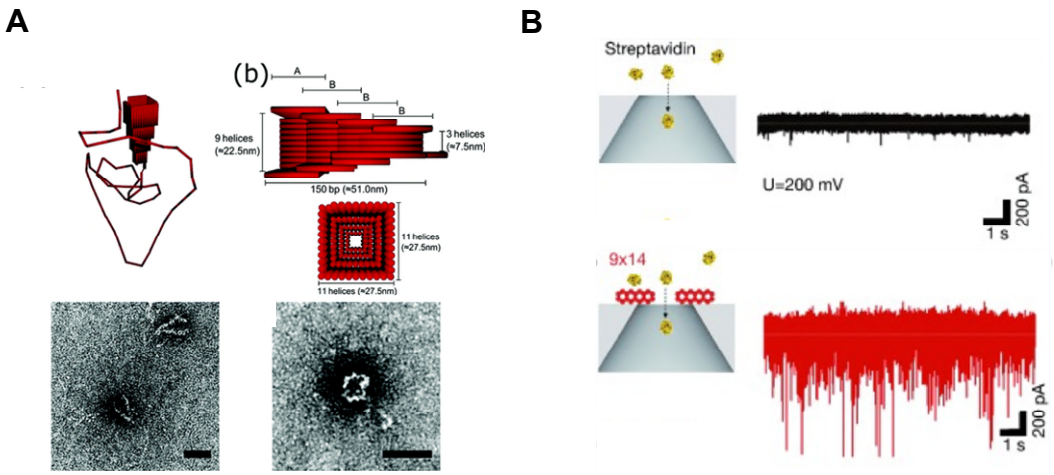

Figure 23 - *A) DNA nanofunnel design and TEM imaging.[214] B) Wei et al. hybrid nanopore[222]. More noise was seen when using the origami nanoplate compared to the naked solid-state nanopore.*

In both plate and funnel designs the hybrid systems showed substantially higher than expected ionic current due to leakage through the nanopore structures, reducing the translocation signals[75,222]. There is a significant increase in ionic current noise in the hybrid solid-state-origami pores compared to the solid-state pores alone, formed by the fluctuations of the DNA origami structures. Plesa et al. investigated the leakage further by looking at the current flow through origami structures with varying layers and without any apertures. It was found that the nanoplates had a significant ionic permeability and a non-linear current voltage

curve was seen for the origami structures, indicating mechanical buckling of the origami at increased voltage[224].

An advantage of using DNA pores inserted directly into the lipid bilayer is the ability to use both positive and negative voltages. Pores hybridised with larger solid-state nanopores are inserted using a positive voltage; applying negative voltage leads to the escape of the origami structures[75]. Langecker et al.[225] introduced a large DNA nanopore for insertion into a lipid bilayer. The structure was anchored via 26 cholesterol-tagged oligonucleotides. The pore had dimensions of 2 nm wide and 42 nm in length and was visualised puncturing and spanning lipid vesicles by TEM imaging. (Figure 24) Single channel current recordings showed a unitary conductance of 0.87 nS in 1M KCL, 10 mM Tris (pH 8), 2 mM $MgCl_2$ buffer. The pore was used to show the translocation of DNA hairpins and G quadraplexes showing characteristic blockage events[75,225]. The pores showed variable noise in a similar range to that observed in the solid-state hybrid pores by Bell et al. and Wei et al. Several sub-conductance states were observed, which was indicated to be due to the movement of staple strands[225]. The minimum constriction of 2 nm of this nanopore meant that this design was not suitable for use with larger protein analytes.

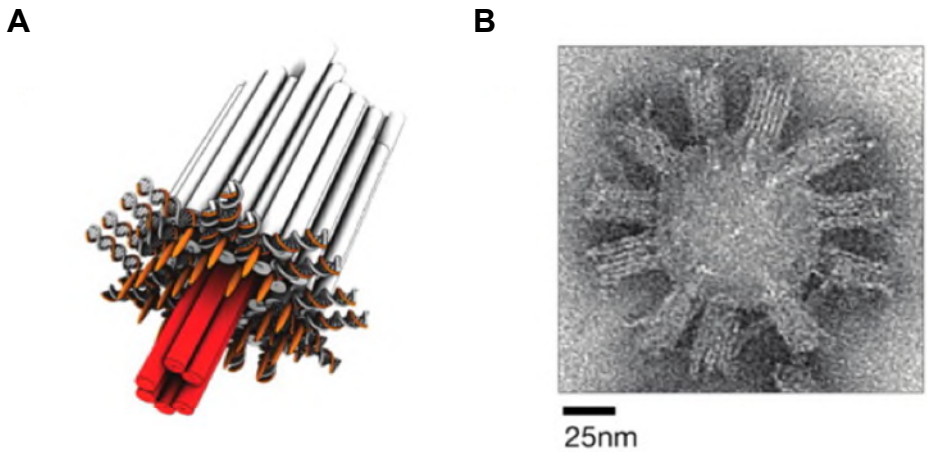

Figure 24 *- A) Model of Langecker et al. DNA nanopore. Orange rods indicate cholesterol molecules which anchor the pore in membrane bilayer. B) TEM image of pores inserting into a lipid vesicle.*[225]

More recently Krishnan et al. have shown the development of a T shaped DNA origami pore with a lumen diameter of 4 nm[226]. The T shape pore comprises 2 parts: (1) a double layered plate (46 x 51 nm in diameter) and (2) a perpendicular rectangular aperture section with dimensions of 3.7 x 8.4 nm. Hydrophobic anchors were added to the bottom of the double layered plate to allow a large contact area with the lipid bilayer. 57 tocopherol molecules were used, as tocopherol interacted well with the disordered membrane phase of phosphatidylcholines used in the experiments.[227,228] Ohmic behaviour was observed with a conductance of around 3 nS and no second gating level was seen at the voltages measured. The translocation of double stranded DNA was shown to be successful by single channel current recordings as well as the transport of the dye Atto 663 into GUVs. However, no sensing of larger proteins was performed. A T pore design, which was linked to the bilayer via streptavidin-biotin interactions, was also investigated.

Gopfrich et al. have recently published a version of the DNA nanofunnel, previously presented by Bell et al., which could penetrate lipid bilayers via 19 cholesterol anchors[229]. The conductance of the pore was calculated from steps down in conductance caused by the escape of the DNA pores from the lipid bilayer. Conductances in the 10s of nS range were seen, however, a logarithmic scaled histogram of conductance showed a very broad range of conductance steps. This was suggested by the authors to be potentially due to multiple pores and membrane pressure effects. The conductance histogram showed a mean value of approximately 30 nS, and an IV plot of 6 pores showed a conductance of approximately 20 nS in the -50 mV to 50 mV voltage range where more ohmic behaviour was observed. No translocation with either DNA or protein were attempted with this nanopore design, possibly due to the large variation in conductance from pore to pore. A molecular dynamics simulation study of the pore was also performed, which included the DNA porin, water molecules, ions and a Dphpc lipid bilayer. The simulation suggested the pore should have a mean conductance in the range of 46.6 nS and showed that lipid molecules rearranged around the membrane spanning part of the pore, similar to the effects seen by Howorka et al[221].

In this section, the importance of biosensors and the benefits of label free sensing devices has been shown. Nanopore sensing facilitates the sensing of analytes with high accuracy and the need for only low sample concentrations. The potential of this sensing method has been demonstrated by the high accuracy with which devices, such as those commercially produced by Oxford Nanopore Technologies, are able to sequence DNA.

Although much has been achieved with the current more traditional forms of nanopores, biological nanopores and solid-state nanopores, both have their drawbacks which either limit the range of analytes or the resolution of the technique. DNA structures constructed using DNA origami show potential to overcome some of the current limitations to nanopore sensing. DNA nanopores can be built in an array of controllable sizes and additional functionalization can be added with atomic scale resolution.

However, pores of a design and size which can sense larger cargos with accuracy, such as protein biomarkers, have not yet been demonstrated. Issues with currently published pores include ionically leaky walls and instability in the pores' structures, leading to inconsistency in nanopore recordings taken with the pores[117]. A DNA origami nanopore designed to have a larger lumen, which is supported by thicker, less flexible duplex walls, has the potential to sense larger analytes with a potential consistency not seen in current literature.

1.5 Project Aims

This thesis describes three separate projects worked on during the PhD period. Firstly, the project which is the main subject of this thesis involves the design and generation of a multi-layered DNA origami nanopore for sensing specific protein biomarkers. Secondly, the attempted formation of a simple DNA nanostructure nanopore, constructed of a single DNA duplex modified with two lipid anchor types, is described. Finally, a collaboration project with the Lin group at Yale University involving the assembly and adaption of a previously published curved DNA origami ring to nanopore sensing applications.

1.5.1 Multi-layered DNA Origami Nanopores

Hypothesis: The main aim of the work is to rationally design a DNA nanopore which can be used as a biosensor element to detect protein biomarkers. Currently published nanopores used in biosensing have been unable to detect protein biomarkers with high fidelity.[223,225,229] The pores will be made with DNA as a building material as this can overcome some of the disadvantages associated with both solid-state and biological nanopores, including ease of design, assembly, the atomic precision of the assembled nanostructure and the larger size range of DNA origami nanopores compared to biological pores. The origami building technique will be used to produce a large, layered origami structure with greater structural stability than currently published designs and therefore allow for more reliable biosensing. The resulting DNA nanopore-based sensors will help to facilitate the development of low cost, rapid biosensing devices. (Figure 25)

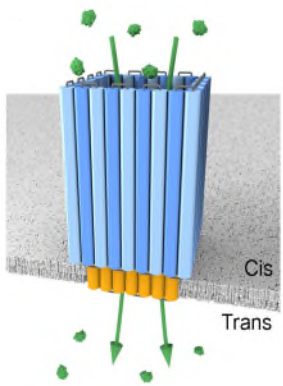

Figure 25 - *Model of the multi-layered DNA origami nanopore to be used to translocate protein biomarkers*

1.5.2 Simple DNA Nanostructure Nanopore

Hypothesis: The main aim of this project is to mimic and improve on the properties of published small DNA nanopores[3,4,215] using a simplified design. The pore again is to be used as part of a biosensing device. Although the nanopore is not aimed at any type of analyte specificity, the formation of a nanopore from a single duplex of DNA, threading parallel to the bilayer, is novel in its simplicity. The pore design consists of only two lipid anchor modified strands. The pore aims to be less susceptible to gating compared to the previously published DNA six helix nanopore[4]. (Figure 26)

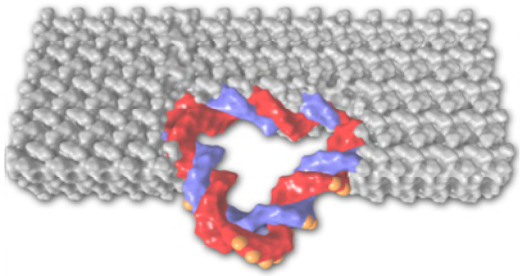

Figure 26 - *A representation of the DNA nanostructure nanopore (DNA triangle) The triangle sits parallel to the membrane forming a pore using only a single DNA double helix.*

1.5.3 Adaption of DNA Origami Rings

Hypothesis: The aim of this project is to adapt DNA origami rings, designed by the Lin group to template the growth of liposomes, for use in a nanopore sensing set up. The lipid nucleation points on the rings are to be substituted with cholesterol lipid anchors, leading to the potential association of the rings with a bilayer. The membrane association of the ring is to be looked at using rings with different orientations of anchor positions to find an arrangement which leads to the best membrane puncturing and nanopore characteristics. (Figure 27)

Figure 27 - *DNA origami rings designed by the Lin group. The lipid anchor positions on the six-helix bundle will be varied and the membrane puncturing fidelity observed.*

2. Results and Discussion

2.1 Multi-layered DNA Origami Nanopores

DNA origami nanopores, which incorporated all of the criteria necessary to achieve the project's aims, were designed. These criteria included:

1. A nanopore with a lumen which is large enough in size to accommodate protein biomarker analytes.
2. A nanopore with a pore lumen which is robust and designed to remain as static as possible, so it can function as an efficient sensing device.
3. The nanopore must remain stable where possible when a voltage in ranges needed for sensing is applied (-50 mV to +50 mV).
4. The pore must have functionality which allows it to associate with and span a lipid bilayer.

To achieve these goals two multi-layered DNA nanopore designs were suggested – a "box" and a "funnel" nanopore.

Design 1 – Box Nanopore

Design 1, labelled a DNA box nanopore, contained two layers of stacked helix. The design has 7 x 7 duplexes and dimensions of 28 nm x 17.5 nm x 17.5 nm. (Figure 28) The pore is relatively small in size for a DNA origami object, with only approximately half of the standard M13mp18 DNA origami scaffold strand in use in the design. Cholesterol molecules are attached to staples in the second, outer layer of the bottom section of the pore to allow the pore to penetrate lipid bilayers (labelled in yellow in Figure 28). The pore lumen has a constant diameter of 7.5 nm x 7.5 nm, assuming idealised B-DNA conditions with a rise of 0.34 nm per base pair and a 2.5 nm helix diameter.

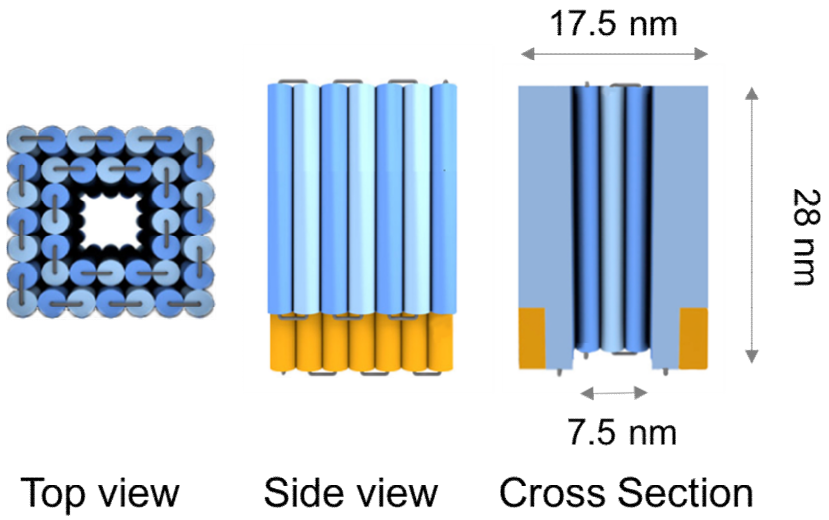

Figure 28 - *DNA "Box" Nanopore design*

Design 2 – Funnel Nanopore

Design 2, termed a DNA funnel nanopore, was designed to use the full 7429 base pairs of the M13mp18 DNA scaffold strand, has dimensions of 46 nm x 22.5 nm x 22.5 nm and is 9 x 9 duplexes across. The majority of the pore has three layers of cross-linked duplex to facilitate maximum rigidity of the pore. However, the number of layers of duplex were progressively reduced inside the top "cap" region of the pore design, to create a graduated lumen which is largest at the pore's opening. The graduated lumen allows a single pore design to be adapted for the detection of a range of potential analyte sizes. Larger analytes which can associate with the pore opening could be detected using a similar strategy to that suggested by Bayley et al. for the αHL pore, where analytes are detected by association with aptamers[65] or PEG chains with molecular receptors[76] at the mouth of the nanopore. The third layer of duplex is again graduated at the bottom of the design to expose a two-layered, membrane-puncturing section of the pore. Staple strands functionalised with cholesterol are incorporated into the second layer of duplex at the bottom of the pore design. The pore lumen has a minimum constriction diameter of 7.5 nm x 7.5 nm.

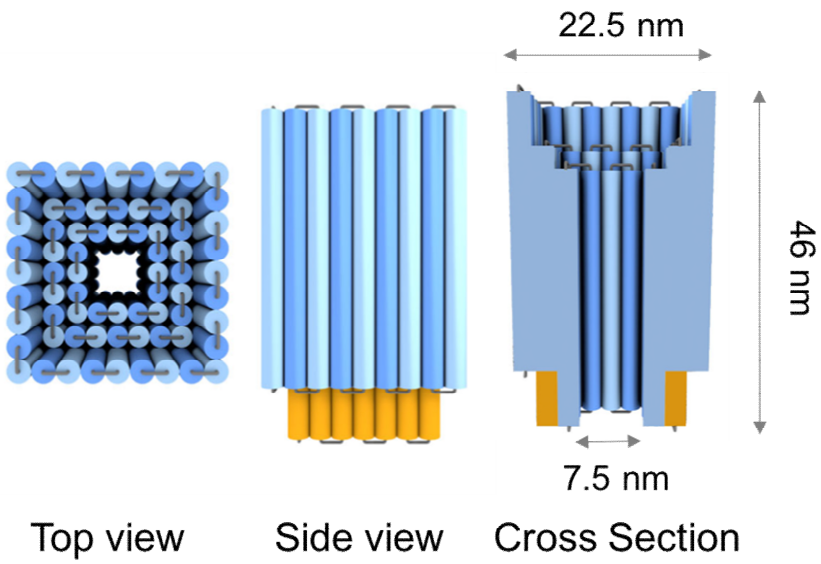

Figure 29 - *DNA "Funnel" Nanopore Design*

2.1.1 Computational Design of Origami Pores

Design with CaDNAno

CaDNAno software was used to design the DNA origami nanopores. CaDNAno uses a reduced representation of DNA to allow the production of stable DNA objects. The program represents the DNA structures over three views: the "slice panel", the "path panel" and the "render panel"[154]. (Figure 30) The program was used to help template the origami nanopore and route the m13mp18 scaffold strand. The strand map seen on the path panel view allows the user to schematically route the scaffold strand through the desired nanopore shape in two dimensions. The scaffold passes through antiparallel crossovers between neighbouring helices. The program was then used to generate an initial pattern of the 242 staple strands needed to form the nanopore. The staples were then further manually adjusted to produce the most stable structure.[140,154]

The "square lattice template" was used, as it allows dense packing of DNA helices and therefore more structural rigidity.[150] Using this template, cross overs between helices of the nanopore can only be made between neighbouring strands every 8 base pairs, where it touches one of the four neighbouring helices.[150] It was also ensured that cross over positions of staples were at least five base pairs away from antiparallel cross overs between scaffold helices. This ensures the canonical structure of the DNA is maintained[154]. DNA staples were adjusted to between 18 and 49 bps long. The staples' minimum length limit ensures the staple has a melting temperature above room temperature; the maximum lengths ensure the staple is an appropriate length for cost-efficient solid phase synthesis.

The pores were modelled in CaDNAno to have the desired dimensions of 28 nm x 17.5 nm x 17.5 nm for the box. (Figure 31) and 46 nm x 22.5 nm x 22.5 nm for the funnel. (Figure 32) The DNA box used 4204 bp of the 7249 bp M13mp18 scaffold strand. The full M13mp18 scaffold was enzymatically digested to yield the desired fragment. For the larger origami funnel design the entire length of the M13mp18 scaffold strand was routed through the structure.

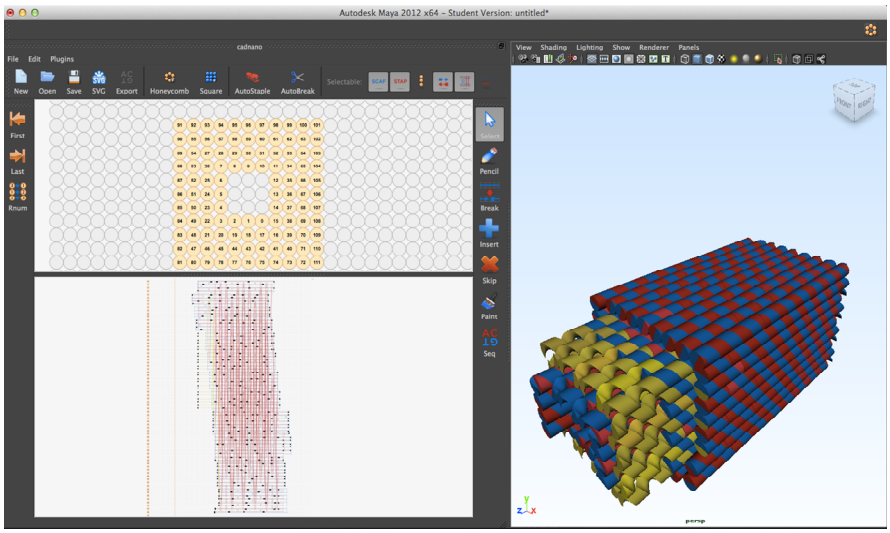

Figure 30 - *CaDNAno user view. The user uses 3 panels to help with object construction. The slice view (top left) shows the active helices. Numbering of the helices correspond to the number running down the left-hand side of the path panel. The path panel (bottom left) shows a 2D representation of the routing of the scaffold and staples. Editing of staple paths is done in this panel . The render panel shows a 3D representation of the object as it is being built.*

The CaDNAno designs were further manually modified to accommodate hydrophobic anchors. A layer of staple strands was extended in both designs to leave a belt of single stranded DNA regions to act as "sticky ends" (labelled in yellow in Figure 31 & 32). These regions' sequences were modified to complement short oligonucleotides, possessing cholesterol modifications at either their 3 prime or 5 prime termini (Table 9 & 10, Appendix). Hybridisation of these strands to the single stranded sticky ends on the origami forms a belt of 24 cholesterol molecules. These cholesterol molecules are then used as "lipid anchors" to help associate the DNA nanopore with the membrane bilayer. Due to the antiparallel arrangement of the DNA helices in the nanopore design, helices run alternatively in the 3 prime and 5 prime directions. Adding only 3 prime cholesterol modified strands, or only the 5 prime cholesterol modified strands, leads to a halving of the quantity of lipid anchors while maintaining the anchors' equal distribution around the nanopore structure. This allows the extent of hydrophobicity of the origami to be controlled. The full list of DNA sequences and "structure strand maps" are shown in the Appendix. (Figures 97, 98, Tables 9 & 10) CaDNAno rendered images of Design 1 and Design 2 are shown in Figure 31 & 32. The scaffold strand is shown in blue, structural staples in red and staples with sticky ends for cholesterol strand attachment in yellow.

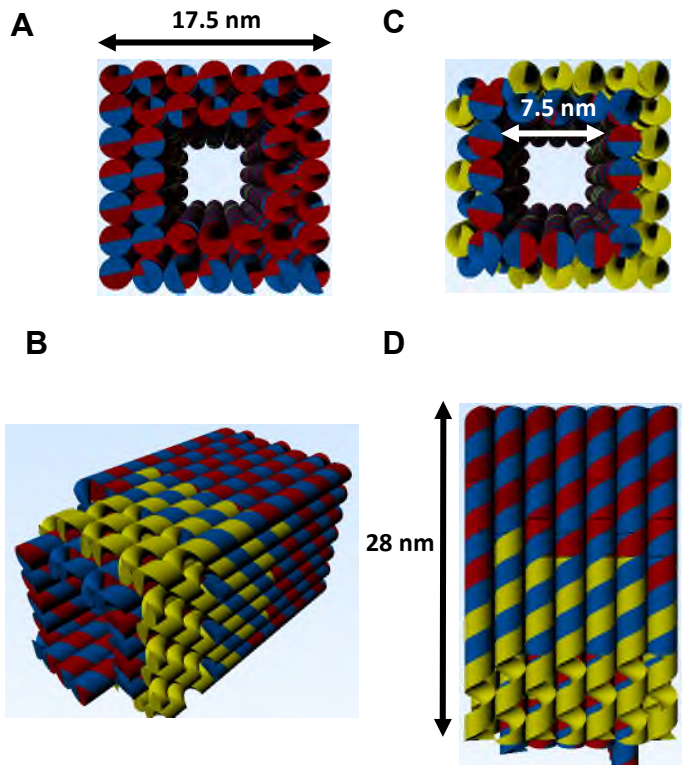

Figure 31 - *CaDNAno generated model of DNA Box Nanopore. A) Top view, B) Diagonal view C) Bottom view D) Side view. The scaffold is represented in blue, staples in red and hybridisation points for cholesterol functionalised strands in yellow.*

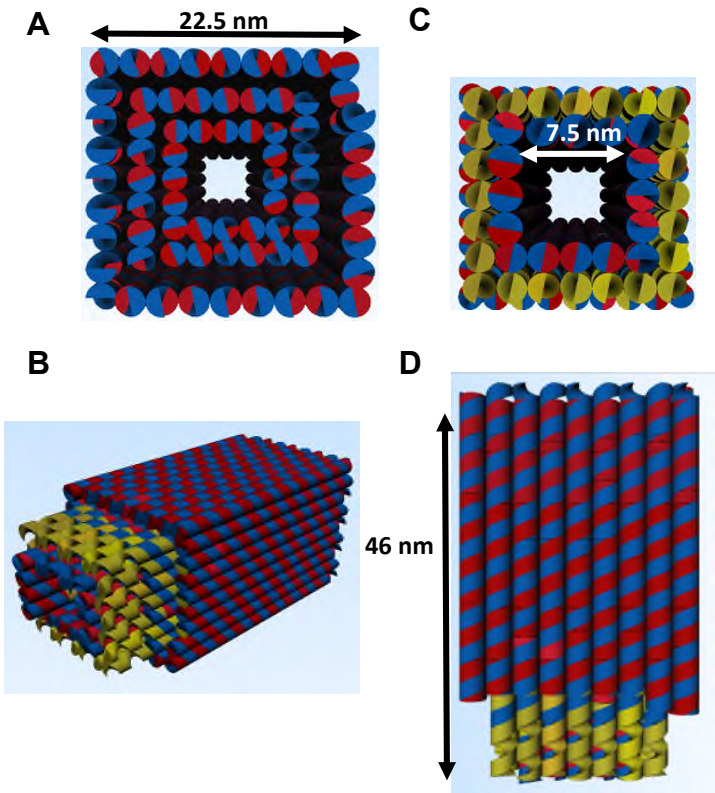

Figure 32 - *CaDNAno generated model of DNA Funnel Nanopore. A) Top view, B) Diagonal view C) Bottom view D) Side view. The scaffold is represented in blue, staples in red and hybridisation points for cholesterol functionalised strands in yellow.*

Modelling with CanDO

The robustness of nanopore designs was assessed qualitatively using the program CanDo (Computer-aided engineering for DNA origami).[152] CanDo uses the CaDNAno design files to provide coarse-grain modelling of flexibility and strain in the origami nanopores.[230] It uses the finite element method to generate a 3D DNA shape from the CaDNAno design, which is disrupted by external forces modelling thermal fluctuations. The application of these forces deforms adjacent helices so an assessment on the rigidity of the structure can be made[152]. Short movie files showing fluctuations of the objects, with the flexibility of regions of the nanopore denoted using a colour scale running from blue (least flexible) to red (most flexible), were used to help assess where to edit stapling crossover positions of the structures to provide the most stable result. (Figure 33) Progressive cycles of design modification in CaDNAno and modelling in CanDo were used to generate structures with the highest structural rigidity. The three layered funnel showed lower flexibility than the smaller origami box design.

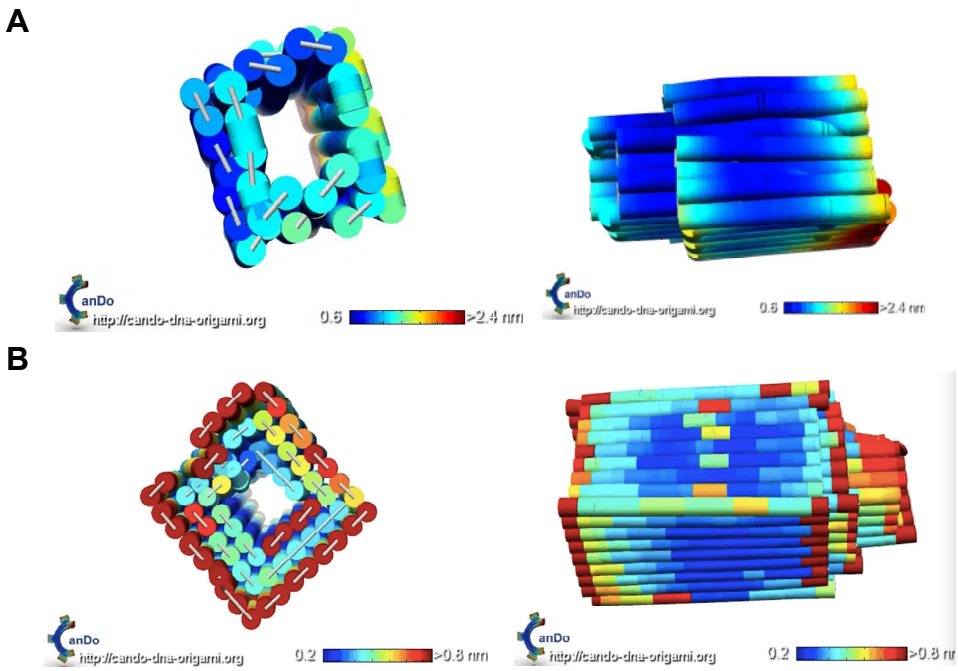

Figure 33 - *CanDo flexibility assessment A) top and side views of the DNA box structure - the most flexibility is seen at the entrance and base of the nanopore. B) top and side views of the DNA funnel structure - again the most flexibility is seen at the top and bottom of the structure. The funnel structure shows less flexibility than the box structure, with the flexibility scale running from 0.2 mm to 0.8 nm, whereas the box has a scale running from 0.6 to 2.4 nm. The funnel structure is more rigid.*

When modelling the flexibility of the nanopore the greatest concern is the rigidity of the pore's lumen, to ensure consistent current travels through the nanopore when it is used in a nanopore sensing set up. CanDo helps model a design with greater rigidity, however, the modelling is only qualitative. It provides information for a reduced representation of the nanopore structure and cannot incorporate the effects of membrane pressure after bilayer insertion, or the effect of the applied voltage during sensing. Although the program is a useful tool for design, it does not provide a quantitative assessment of the stability the synthetic nanopore will possess. The structure's stability needs to be assessed experimentally after assembly.

When structure design and modelling was completed, the modified CaDNAno-generated sequences were ordered commercially and the designed structure assembled. The programmed staple-scaffold arrangement allows the designed nanopore to form by minimising the energy of the structure via Watson-Crick base pairing. Whether the designed structure follows the correct folding pathway to reach its global energy minimum and avoid topological or kinetic traps depends on: (1) the staple-scaffold routing (described above), (2) solvent conditions, (3) the annealment procedure, and (4) the scaffold/staples ratio. These conditions were explored and optimised for both the folding of the box and funnel nanopore designs. Staples are added in at least a 10-fold excess, ensuring scaffold folding is pushed to completion. Excess staples can then be removed in later purification steps.

2.1.2 Multi-layered Box Nanopore

DNA box assembly with full DNA scaffold strand

The DNA box was initially assembled using the full DNA scaffold strand to check the design's validity. The box was annealed using a 12-hour protocol. (Solutions heated to 80ºC were then cooled from 80ºC - 70ºC at 1ºC per min, 70ºC - 50ºC at 1ºC per 10 min, 50ºC – 20ºC at 1ºC per 15 min, 20ºC – 4ºC at 1ºC per 4 min). Scaffold (20 μg, 4.2 nM) and 77 staples (130 nM) were combined in X mM $MgCl_2$ 1xTAE buffer solutions, where X = 12, 14, 16, 18, 20, 22, 24. Solutions were initially annealed in a range of $MgCl_2$ buffer concentrations, as multi-layered structures (such as the origami nanopores) will have repulsion between layers of closely-packed, negatively-charged double helices. By finding the correct concentrations of magnesium-containing buffer repulsion effects can be alleviated, as Mg^{2+} ions are able to co-ordinate to the helix backbone[152].

The successful assembly of the DNA origami pores was initially assessed using agarose gel electrophoresis. The presence of discrete, slow-moving bands indicated the presence of a single DNA object. Immediately after sample annealing, two slow-moving bands were observed for the annealed structure, as well as a much faster moving broad band corresponding to the excess staples (Lane 1, figure 34A). However the top band, a multimeric association of box origami structures[153], dissipated over time to leave only the monomeric box band after 4 days' curing (figure 34B). Over the range investigated (12 mM – 24 mM $MgCl_2$), there appeared to be little difference in the folding of the box with salt concentration. A value of 14 mM $MgCl_2$ 1xTAE was fixed on for the folding buffer. This concentration has been used in literature for annealment of similar sized objects[75].

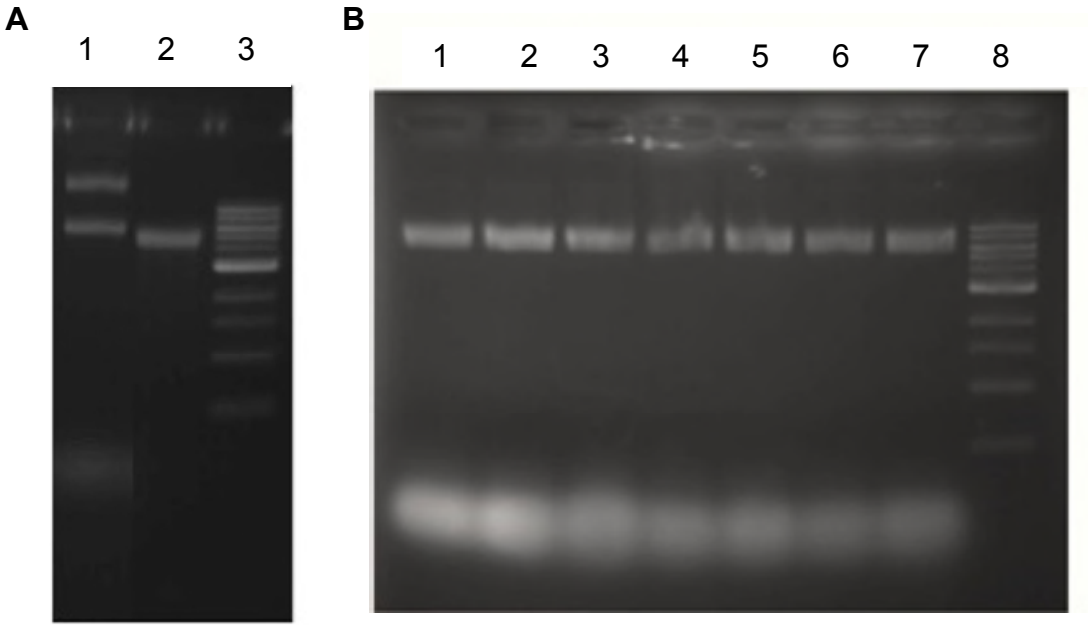

Figure 34 - *1.5% agarose gels run at 70 V for 1 hour. A) Lane 1 – folded box directly after annealment. 2 slow moving bands were seen and a faster running stables band, lane 2 – M13mp18 ssDNA scaffold, lane 3 – 1 kbp DNA ladder. 2 bands are seen in each lane - the first band corresponds to the folded box, the second to excess staple strands. Lane 8 shows 1 kbp DNA ladder. Lanes 1-7 show the box annealed under the same conditions except for differing concentrations of $MgCl_2$ in the 1xTAE buffer. Lanes 1-7 show concentrations of 12, 14, 16, 18, 20, 22 and 24 mM $MgCl_2$, respectively.*

DNA melting analysis, (conducted by heating the origami structure from 20°C to 90°C at 1°C per min), showed a defined transition with a T_m of 55.6°C calculated from the first derivative of the DNA melting profile. (Figure 35) The co-operative transition supports the formation of a single origami structure.

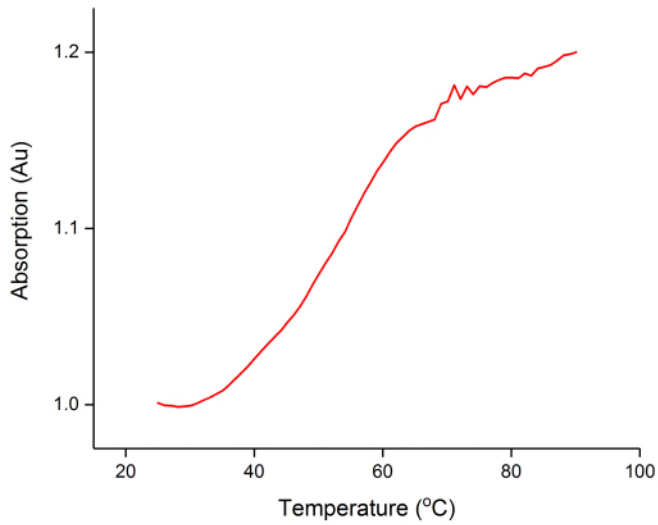

Figure 35 - *Representative DNA melting profile of the box. T_m was found from the first derivative of the curve to be 55.6°C.*

DNA Box Assembly with Digested Scaffold Strand

Following successful assembly of the box with the full scaffold, the box then needed to be assembled with only the required section of the scaffold. The box design requires only a 4204 bp portion of the scaffold. To function correctly the unused section of the scaffold needed to be removed, as excess free negatively-charged scaffold will block the lumen of the pore when voltages are varied during single channel current recordings. This would make the nanopore unsuitable for use in biosensing applications.

Enzyme	*Primer*	*Primer sequence*	*Cut site*	*Primer melting temperature °C*
SnaBI	Primer 1270	TGCCTTCGTAGTGGCATTAC GTATTTTACC CGTTTAATGG AAACTTCCTC	TAC GTA	66.3
BsrBI	Primer 5574	CACTTGCCAG CGCCCTAGCG CCCGCTCCTTTCGCTTTCTT CCCTTCCTTT	CCG CTC	74
DarI	Primer 131	CTTCCAGACA CCGTACTTTA GTTGCATATT TAAAACATGT TGAGCTACAG	TTT AAA	64.1
	Primer 474	TCATTCTCGT TTTCTGAACT GTTTAAAGCA TTTGAGGGGG ATTCAATGAA	TTT AAA	65.2
	Primer 6769	TAACAAAATA TTAACGTTTA CAATTTAAAT ATTTGCTTAT ACAATCTTCC	TTT AAA	6.1.7
	Primer 7076	TACACATTA CTCAGGCATT GCATTTAAAA TATATGAGGG TTCTAAAAAT	TTT AAA	71.8
BamIH HF	Primer 6261	GAATTCGAGCTCGGTACCCG GGGATCCTCT AGAGTCGACC T GCAGGCATG	GGA TCC	71.8

Table 3 – *List of enzymes and primers used to cut the M13mp18 scaffold. The colour of the primer equates to the highlighted colour of the M13mp18 sequence in Appendix section 7.5. The highlighted six residues in each primer sequence correspond to the enzymes' cut site.*

The M13mp18 scaffold is a single stranded circular plasmid. SnaBI and BsrBI restriction endonucleases and the appropriate DNA oligonucleotide "primers" were used to cut the scaffold, to liberate the 4204 bp fragment needed for assembly and a waste fragment of 3045 bp. Short oligonucleotides were hybridised to the scaffold at regions where the plasmid was to be cut to provide

the necessary double stranded sites for enzymatic digestion. The 3045 bp fragment proved difficult to separate during SEC purification procedures, as it was too similar in size to the desired fragment. Therefore, the waste fragment was further cut using two more endonucleases, DarI and BamIH-HF. These enzymes subsequently fragmented the excess scaffold into six smaller fragments of sizes 305 bp, 343 bp, 796 bp, 690 bp, 532 bp and 280 bp. The list of primer sequences can be seen in Table 3, and the subsequent binding and digestion sites of the enzymes on the M13mp18 scaffold can be found in the Appendix section 7.5.

In Figure 36 a star represents the position from which excess scaffold extends from the box design. This loop of DNA was removed using the digestion procedure described above. The two ends of the scaffold meet at neighbouring bases (duplex 39, bases 104 and 105). This can be seen in the box scaffold plan found in the Appendix section 6.1.

Figure 36 – *Cut point of DNA box. The two ends of excess DNA scaffold to be cut meet at bases 104 and 105 of duplex 39.*

The course of the scaffold digestion experiment was followed using a time study, where the enzymatic reactions were terminated using thermal denaturation (Figure 37). An optimised time for the digestion reaction was shown to be approximately three hours. Digestion allowed to run over three hours showed non-specific digestion due to the "star activity" of the SnaBI enzyme[231,232].

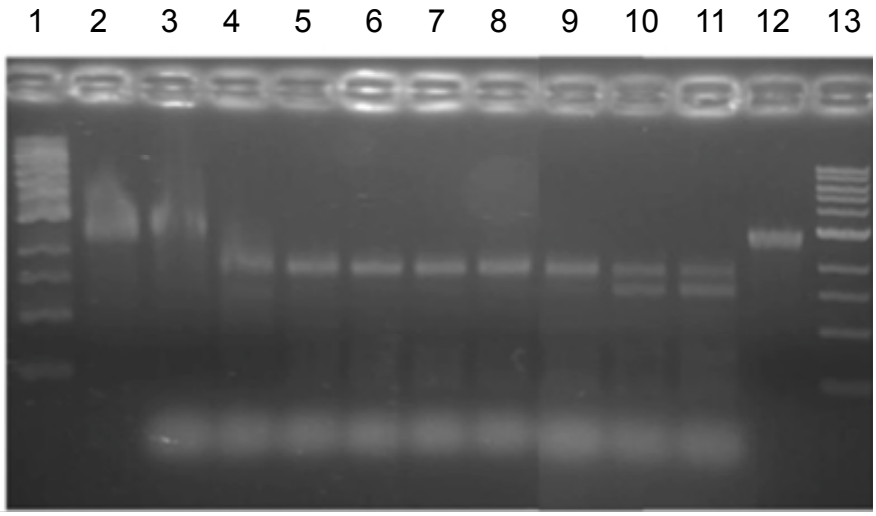

Figure 37 - *Time study showing the fragmentation of progression of enzymatic digestion of the DNA scaffold strand over time. Lane 1/13 1 kbp DNA ladder, Lane 2/12 DNA scaffold. Lane 3 0 min, Lane 4 20 min, Lane 5 40 min, Lane 6 60 min Lane 7 80 min, Lane 8 100 min, Lane 9 180 min Lane 10 4 hours, Lane 14 24 hours.*

Digested scaffold was purified from waste fragments and excess oligos using a size exclusion column (SEC). Elution of the DNA fragments was monitored by absorption at 260 nm. The size exclusion column separates mixtures by size, with larger structures being eluted first. Two peaks were seen in the SEC traces after purification (Figure 38A). The first peak, at 8.40 ml, corresponds to the larger scaffold fragment; the second peak, at 15.74 ml, corresponds to the excess scaffold fragments and the DNA oligo primers. The digestion scaffold eluted at a slightly larger volume than the full scaffold strand, which elutes at 8.19 ml when the same protocol was applied. (Figure 42A) This indicates that the scaffold fragment is smaller in size than the full scaffold. The same peak pattern was seen for each scaffold digestion batch (n=4).

SEC fractions containing the first peak were combined and re-concentrated using 3K spin filters for use in the box assembly. The scaffold fragments were then annealed under the same conditions as used for the non-fragmented scaffold assembly, with the full scaffold strand described above. Results however did not show a clear, defined banded product as seen with the box assembled undigested scaffold (Figure 38B). Lane 2 showed a faint band at a height above the scaffold strand but significant smearing was seen in the lane, suggesting a single structure

was not formed. The annealment protocol was changed to protocols of 24 hours and 72 hours in length, but the smearing was not resolved. The presence of sections of duplexed primer strands may affect the hybridisation of staples to the origami scaffold and the cooperative folding of a single origami product.

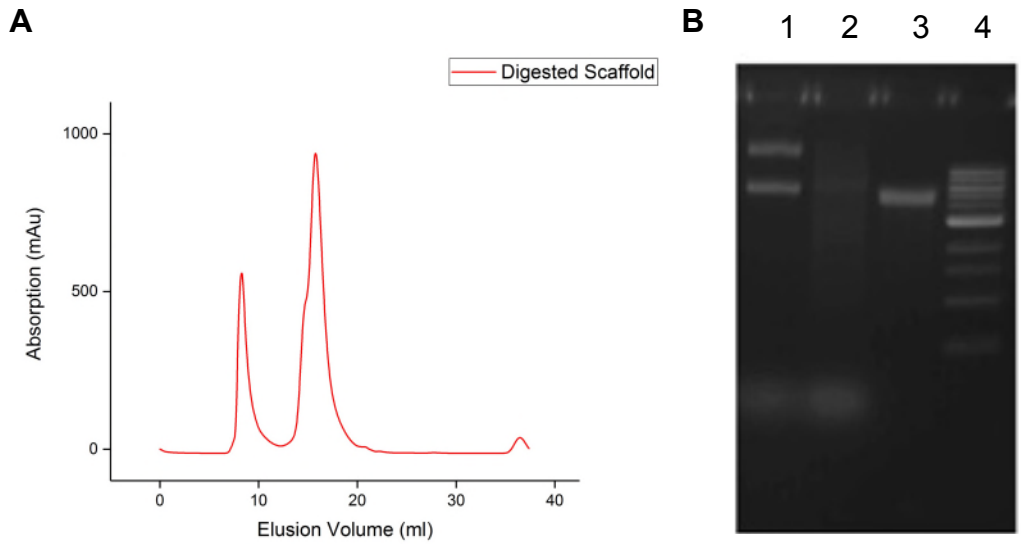

Figure 38 - *A) SEC of digested DNA scaffold. 2 large peaks were seen at 8.40 ml and 14.74 ml. B) 1.5% agarose gel. Lane 1 shows the undigested DNA box directly after annealment, Lane 2 shows assembly of the digested box, Lane 3 shows DNA scaffold strand, Lane 4 1 kbp DNA ladder. Digested box folds with a smear.*

Due to the significant reduction in viability of the formed structure when folding with an enzymatically digested scaffold, attention was focused on moving forward with the more viable funnel pore design (Design 2) for the following steps of the project.

In Design 2, the full length of the M13mp18 scaffold strand was used. This alleviates the need to digest the DNA scaffold strand but also had a more complex shape with some additional structural benefits. The DNA nanopore of design 2 possesses an extra layer of duplex compared to that of design 1. (Figure 39) This additional layering leads to an increased rigidity, as indicated by the CanDO simulations of Figure 33. Both designs have the cholesterol functionalised staples on the second layer of duplex and the minimum lumen constriction is the same (7.5 nmx7.5 nm). However, design 2 possesses an additional graduated cap region.

This cap region extends the usefulness of the origami nanopore, as the pore design can be adapted for use with multiple analyte sizes. Analytes too large to translocate through the pore can cause current blockades by associating with the cap region of the pore. Additionally, the funnel design is longer than the box nanopore. This allows for longer, more easily detectable current blockages.

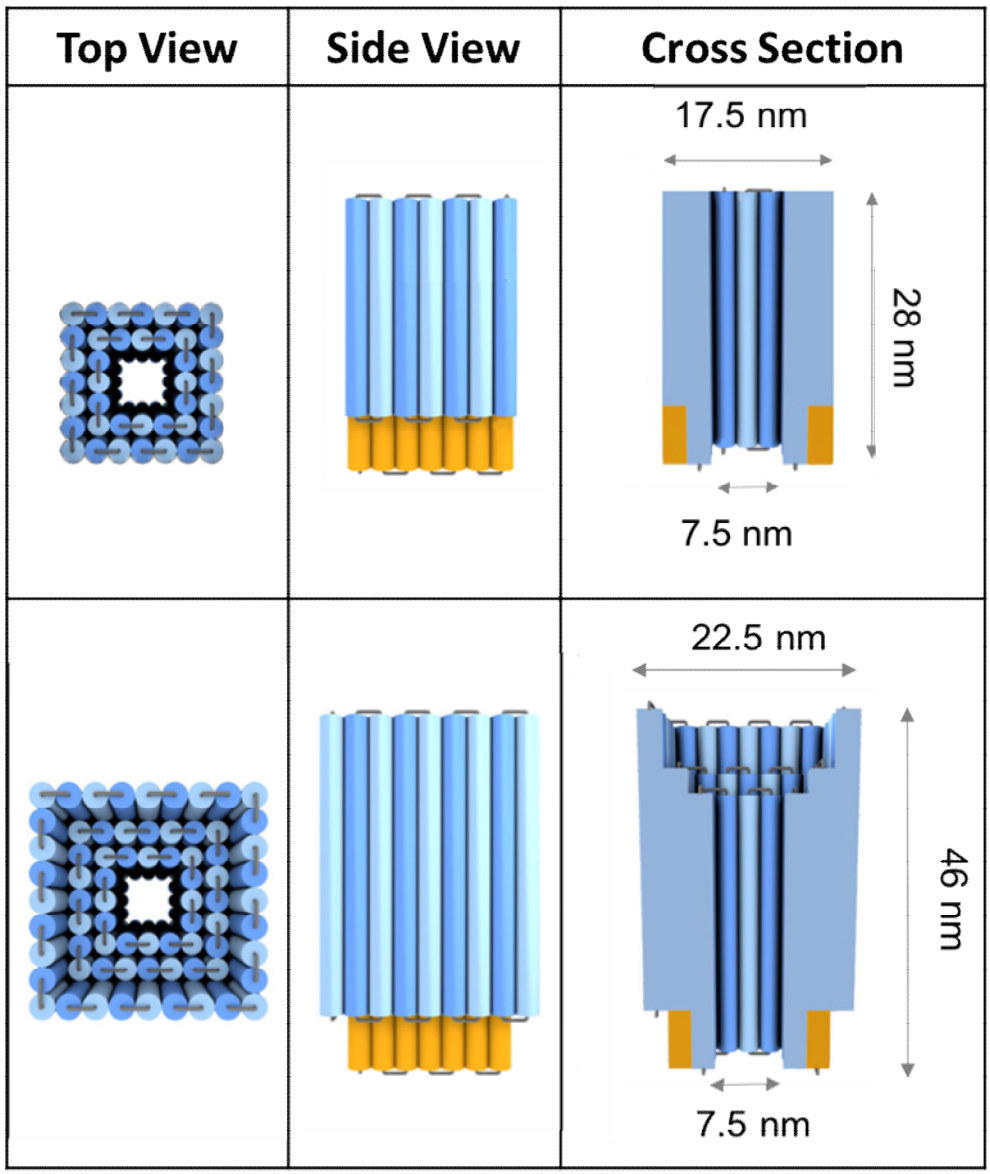

Figure 39 – *Comparison between design 1 (top row) and design 2 (second row) for the DNA orgami nanopore. In design 1 only 4204 bp of the M13mp18 scaffold is used. In design 2 the entire 7429 bp of the M13mp18 scaffold strand is used.*

2.1.3 Multi-layered Funnel Nanopore

For the origami funnel design the entire length of the M13mp18 was hybridised with staple oligonucleotides. Using the full length of the scaffold strand alleviated the need for enzymatic digestion and removed the problem of excess, free-moving scaffold DNA interfering with nanopore recordings. However, the origami funnel pore is a larger, more helically-layered nano-object and therefore requires a more extensive annealing period to form the desired origami object in high quality.

Initial folding of the origami funnel nanopore

Multi-layered origami objects, like the origami nanopores, can follow several energy pathways during folding[170]. Longer thermal denaturation and annealment procedures (where the scaffold and staple solution is heated then slowly cooled) helps prevent partially formed origami structures from becoming stuck in kinetic traps during assembly, ensuring that only the desired minimised energy object is formed[152]. Several annealment procedures were investigated for initial folding of the origami funnel. Firstly, a 24 hour fold based on a protocol by Ke et al[150] was investigated. The fold product was run in lane 4 of the gel. (Figure 40)

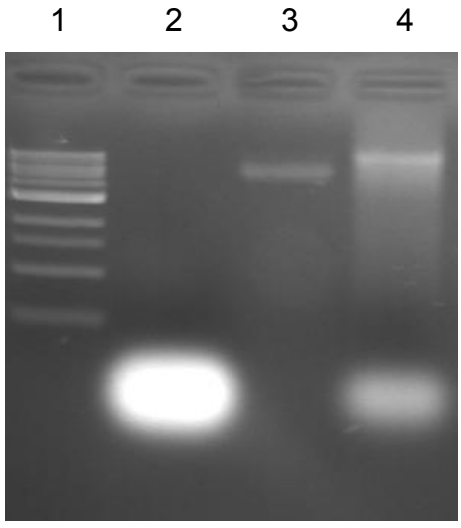

***Figure 40** - 1.5% agarose gel, run at 70 V for an hour, of DNA funnel after 24 hour annealment. Lane 1 1 kbp ladder, lane 2 staples, lane 3 scaffold, lane 4 annealed funnel (24 hours).*

A fast running band was seen, which ran at the same speed to the control staple band (lane 2), and a single slow-moving band was seen, which moved more slowly than the non-hybridised scaffold strand band (lane 3). There was significant smearing in lane 4 around the slow-moving band, indicating that a single origami structure was not formed. To improve the yield of the fully folded origami product, protocols with a much longer annealment time were tested.

The most successful assembly protocol found by purely gel analysis was a 7 day fold protocol based on a protocol by Castro et al.[152], consisting of heating at 80ºC for 5 min, then cooling from 80ºC - 60ºC at 1ºC per 5 min and 60ºC - 25ºC at 1ºC per 300 min (Figure 41A). Scaffold (20 ng, 4.2 nM) and 240 staples (100 nM) were initially combined in X mM $MgCl_2$ 1xTAE buffer solutions, where X = 14, 16, 18, 20.

Similar to the formation of the origami box nanopore, the agarose gel electrophoresis showed two slow moving bands, corresponding to the fully-formed funnel and a multimeric association of the funnels[153]. This multimeric structure dissipated following curing of the structure for three days after annealment. (Figure 39B) 14 mM $MgCl_2$ was again selected for the salt concentration of the buffer, after gel analysis of different $MgCl_2$ concentrations.

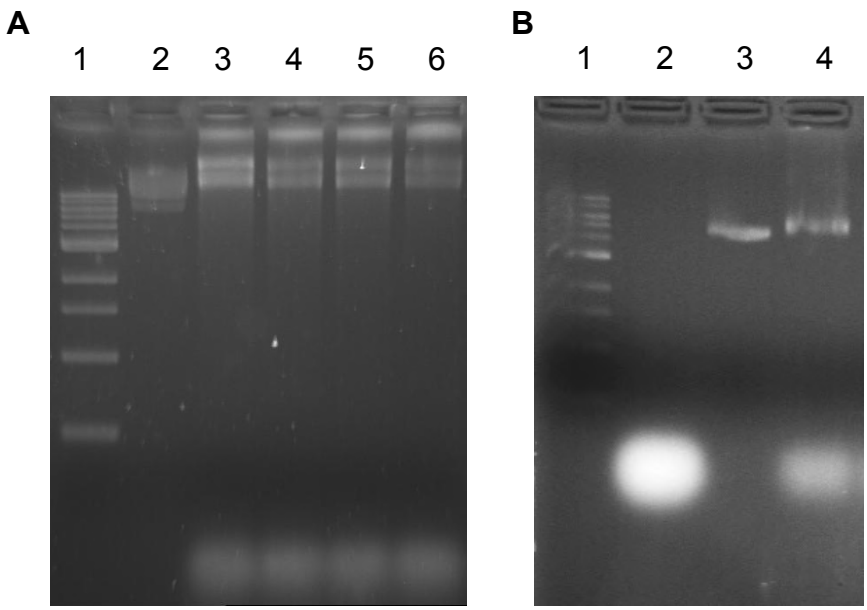

Figure 41 - *A) 1.5% agarose gel run at 70 V for an hour of DNA funnel directly after 7 day annealment. Lane 1 1kbp ladder, lane 2 scaffold, lane 3-6 annealed funnel with $MgCl_2$ concentrations of 14, 16, 18, 20 mM respectively. B) 1.5% agarose gel run at 70 V for one hour after 3 days of curing. Lane 1 1kbp ladder, Lane 2 staples, Lane 3 scaffold, Lane 4 funnel.*

The assembled funnel structures were purified by SEC (Size exclusion column). The SEC traces of the funnel showed two peaks: the first at 7.88 ml, corresponding to the folded DNA funnel; and a second large peak at 16.13 ml, corresponding to excess staples which were added at a 20x ratio (Figure 42A). The funnel peak is seen at a quicker elusion volume than the scaffold strand (8.19 ml), which indicates the funnel is a larger structure and corroborates the gel analysis. The second peak in the funnel traces has a similar elusion volume as the peak for the standard trace, showing staples only at 15.86 ml, indicating that this peak is due to excess staples.

Fractions containing the first SEC peak were collected and used for DNA melting analysis. The DNA melting curve shows a defined melting transition, suggesting a single object is present in solution. The melting temperature of the native pore calculated from the first derivative of the melting curve was 52.0°C (Figure 42B).

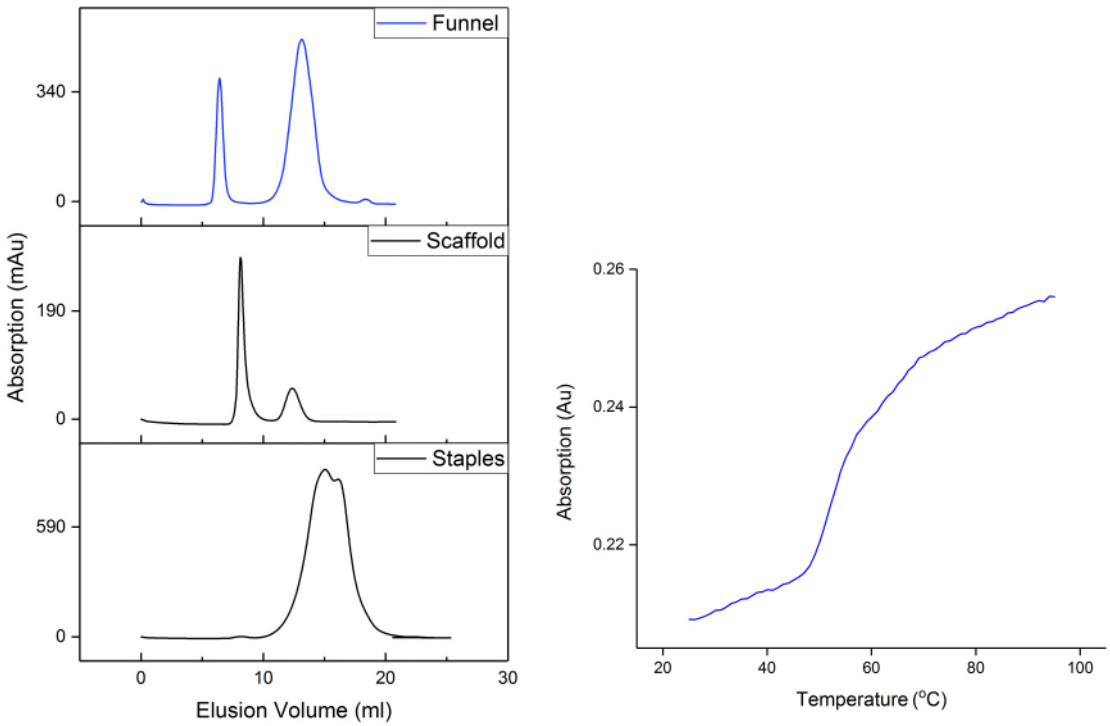

Figure 42 - *A) SEC traces for the folded funnel with peaks corresponding to the scaffold strand and the staples. The two peaks in the funnel SEC are consistent with a peak for the folded scaffold and for excess staples. The second peak in the scaffold SEC corresponds to a portion of the commercially sourced scaffold strand which is linear instead of circular, and therefore runs faster. B) DNA melting profile for the folded funnel. The first derivative of the curve shows a T_m of 52.0°C.*

Folding Optimisation with TEM Analysis

Using the origami melting curves, the folding protocol of the funnel nanopore was further investigated and optimised during a placement in the laboratory of Professor Chenxiang Lin at Yale University.

"Magic Fold" Protocols

It was demonstrated by Dietz et al. that, due to the strong cooperativity of folding or origami objects, it is possible to fold selected origami structures rapidly and in high yield by holding the structures at a constant temperature below the structures' melting temperature (T_m)[166]. These types of folding methods are often referred to as "magic folds". Magic fold test protocols were conducted in a PCR machine with the temperature graduated from the back of the PCR machine to the front. This allowed several different hold temperatures to be investigated in parallel. After annealment, aliquots from each hold temperature were compared on 1.5% agarose gels. (Figure 43) Promising structure bands were then extracted from the gel using the "freeze and squeeze" approach. Structures were then stained with uranyl formate and examined using TEM (Transmission electron microscopy) to investigate the formation of the nanopores. (Figure 44) Fold experiments were repeated with a range of different temperatures and for time holds of up to 32 hours.

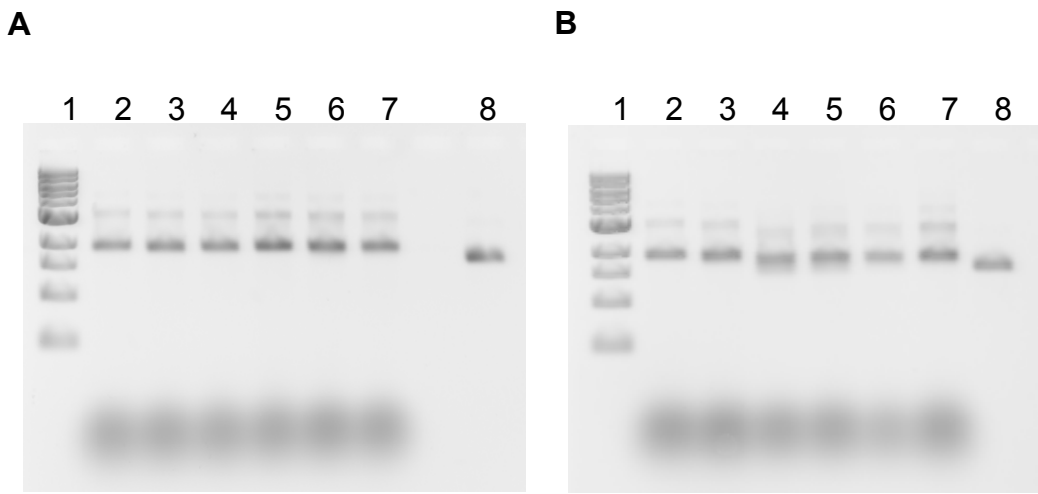

Figure 43 - *8 Magic fold temperature investigation. A) 8 hour fold B) 32 hour fold. Lane 1 – 1kbp ladder, Lane 2 – 48°C hold, Lane 3 – 46°C hold, Lane 4 – 44°C hold, Lane 5 – 42°C hold, Lane 6 – 40°C hold, Lane 7 – 38°C, Lane 8 – Scaffold strand.*

The gels were run in 0.5×TBE buffer containing 10 mM $MgCl_2$ at 60 V for 90 minutes. Each lane containing origami showed a fast-moving staples band and two slower-moving bands. For the 8-hour magic fold protocol there was very little difference in the movement speeds of the origami bands when the DNA was held at different temperatures. The lower slow-moving bands of structures, held at 42ºC and 38ºC, were cut from the gel for further analysis with the TEM, as these were believed to correspond to the monomeric funnel structures. 5 µl of each structure were deposited on glow discharged carbon-coated copper grids stained with 2% uranyl formate for 60 seconds. TEM images were taken of areas of both positive and negative staining. After 8 hours of hold the scaffold strands appeared clustered, but no fully formed funnel structures were observed at any temperature hold. (Figure 44 A&B)

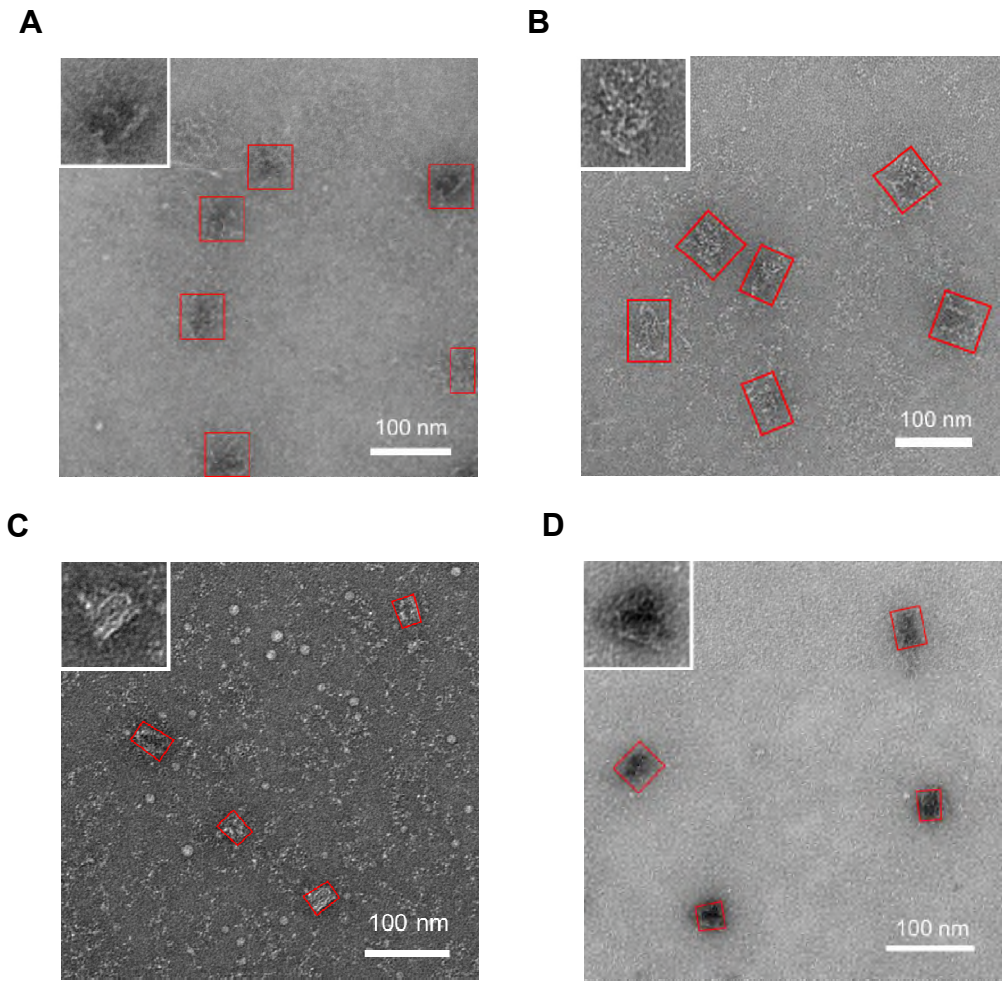

Figure 44 - *TEM images of magic fold temperature investigation. A) 8 hour fold 42ºC, B) 8 hour fold 38ºC C) 32 hour fold 44ºC, D) 32 hour fold 40ºC. After 8 hours no fully folded structures seen. After 32 hours a few folded structures observed.*

After 32 hours of folding a more significant variation was seen in the running speed of bands in the agarose gel with different temperatures. Bands at 44ºC and 40ºC were selected for TEM analysis. (Figure 44 C&D) The structures at both temperatures were more compact than after 8hrs of folding, and some fully folded funnel type structures were observed (approx. 13%) at 44ºC. However, most folded structures appeared with defects.

An investigation was also conducted using an 8,064 bp scaffold strand instead of the 7429 bp scaffold strand. This longer scaffold was produced by the Lin group using E coli. and an M13 derived bacteriophage. It was hypothesised that a longer scaffold could reduce the tension on the origami structure, and therefore lead to a lower energy final structure and a corresponding reduction in folding time. Using the longer scaffold strand a greater difference in the movement of the origami bands with temperature was observed, for both the 8 hrs and 32 hrs fold in gel electrophoresis experiments (Figure 45 A&B). The lower, slow moving bands were once again cut and observed using TEM. Again, temperatures of 42ºC and 38ºC were picked for the 8hr fold (Figure 46 A&B), and 44ºC and 40ºC were picked for the 32 hour fold (Figure 46 C&D).

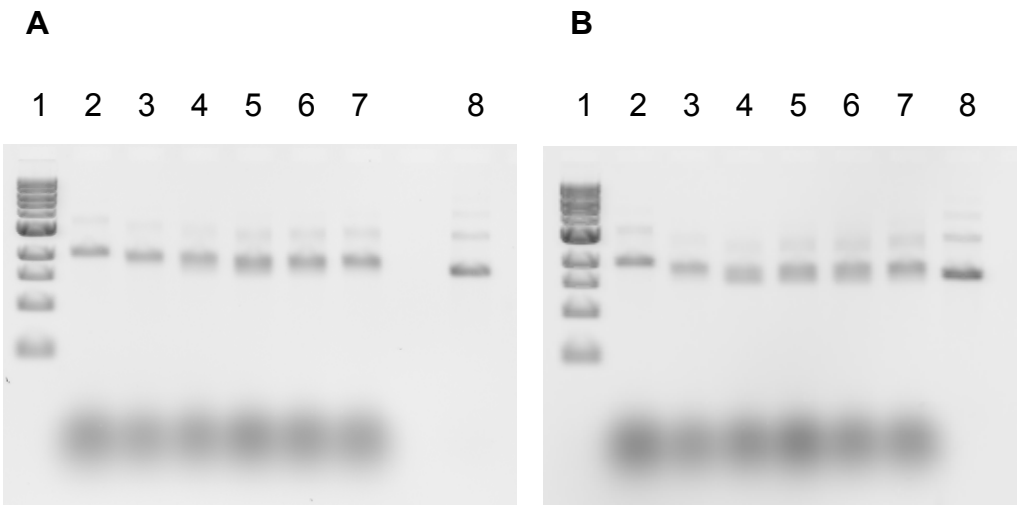

Figure 45 - *8064 bp scaffold magic fold temperature investigation. A) 8 hour fold B) 32 hour fold. Lane 1 – 1kbp ladder, Lane 2 – 48ºC hold, Lane 3 – 46ºC hold, Lane 4 – 44ºC hold, Lane 5 – 42ºC hold, Lane 6 – 40ºC hold, Lane 7 – 38ºC hold, Lane 8 – Scaffold strand*

Better folding was observed at each temperature with fully formed funnel structures seen for the 32-hour magic fold protocol. However, again, some structures had defects. Structures were also observed without gel purification. It was seen that the 8064 bp scaffold produced in the Lin lab was purified to a much higher quality than commercially sourced M13mp18 scaffold strand, which showed some additional debris which was difficult to separate while maintaining a high yield of scaffold. This could also influence the folding fidelity.

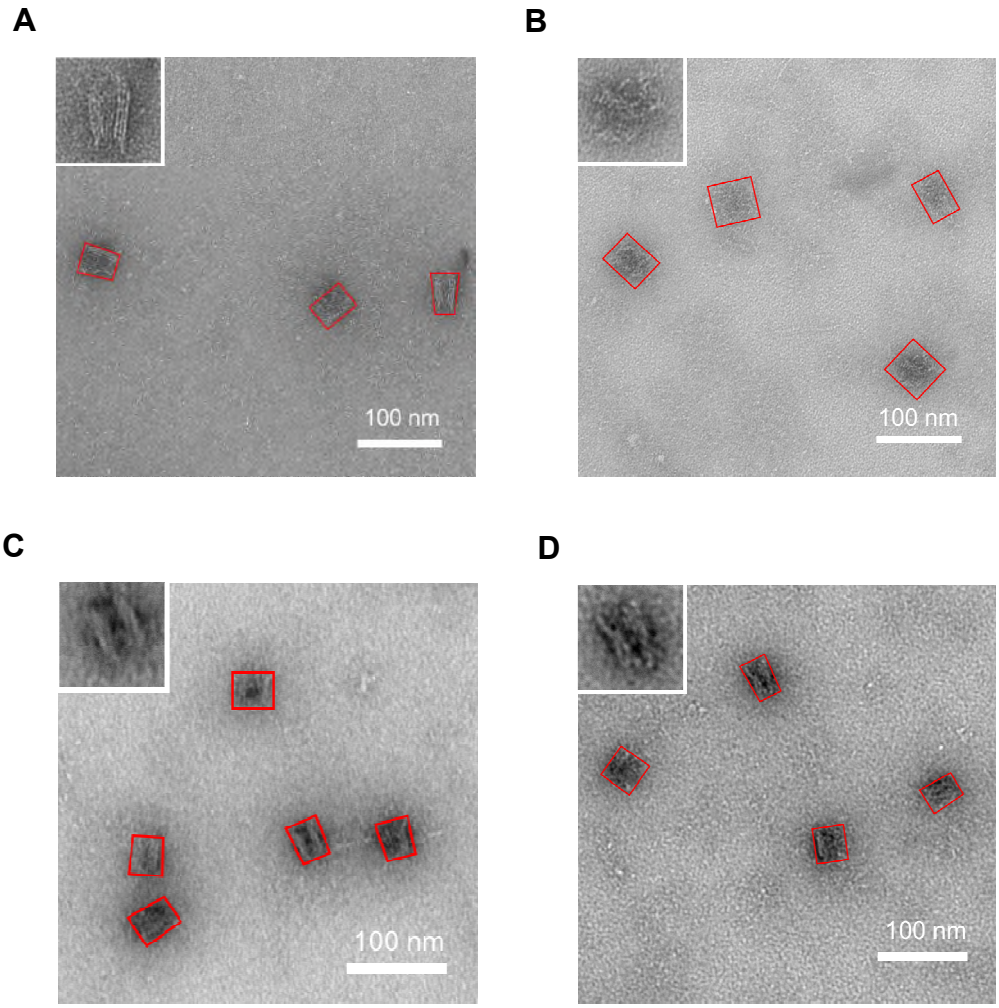

Figure 46 - *8064 bp scaffold TEM images. A) 8 hour fold 42°C, B) 8 hour fold 38°C C) 32 hour fold 44°C, D) 32 hour fold 40°C. Better formed structures at all temperatures although all magic fold products still possessed defects.*

As defects were seen when structures were folded using a magic fold, it was determined that the layered funnel design was not compatible with magic fold protocols and therefore "ramp" protocols (where the temperature is progressively decreased instead of held) were investigated. Ramp protocols are often more favourable for the folding of layered origami objects[169,170].

"Ramp" Fold Protocols

Several lengths of "ramp" protocols were investigated. The first protocol investigated involved the heating of the scaffold to 80ºC, then progressive cooling over 15 hours. (80ºC - 65ºC at 1ºC per 5 min, 64ºC - 24ºC at 1ºC per 20 min, hold at 4ºC). After folding, the success of the folding protocol was examined using agarose gel electrophoresis and TEM analysis. (Figure 47)

Gel electrophoresis showed a fast-moving band corresponding to excess staple strands, a faint origami monomer band at a slower running speed than the DNA scaffold stand (lane 3) and a smear from the height of the lane's well to just above the slow running band (lane 2). (Figure 47A) The smearing on the gel suggests the presence of a range of structure sizes, most likely due to aggregation of the origami, and this was indeed what was observed during TEM analysis. TEM images were captured of the unpurified origami mixture and of the faint faster moving, discrete band in lane 2 which was cut from the gel.

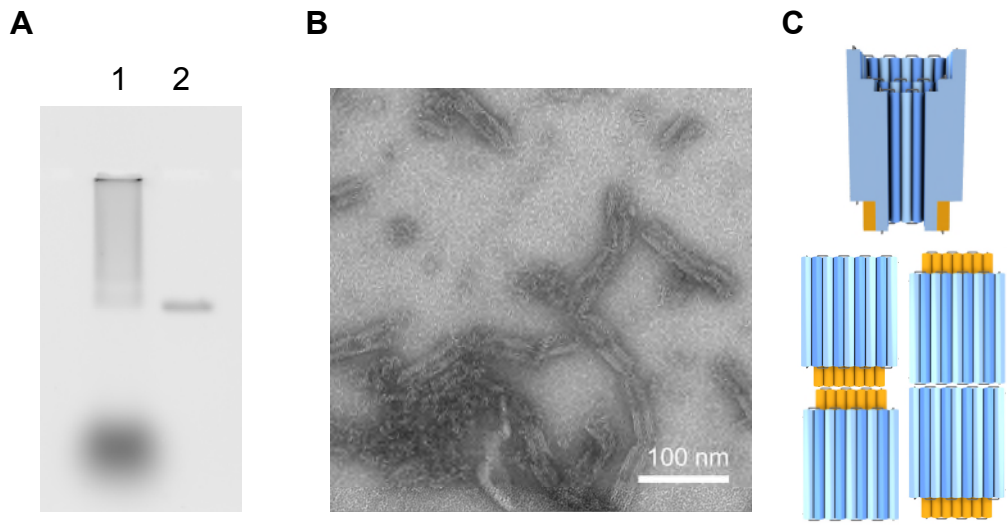

Figure 47 - *A) 1.5% Agarose gel run at 60 V for 1 hr 30 min. Lane 1 Funnel sample after 15 hour ramp. Lane 2 – scaffold strand B) Unpurified funnel TEM showing aggregation and stacking of funnel structures. C) The cross section of the funnel is very visible in the TEM images. Funnels stack head to head and tail to tail.*

After the 15 hour ramp protocol significant aggregation was seen, with long chains of origami funnels forming. The chains are formed due to base-base stacking interactions, which form due to the presence of blunt ends of helix at the top and bottom of the nanopore structures (Figure 47B). The nanopores appear to stack bottom to bottom and top to top, as this maximises the stabilisation energy of the blunt end stacking interaction. In Figure 47B the cross section of the funnel nanopore is clearly visible. In both positively and negatively stained images of the nanopore the inner lumen of the pore appears darker in the TEM images. During negative staining, the heavy metal salt stain (uranyl formate) completely covers the TEM grid surface so that the origami appears light on a dark background. In positive staining, smaller quantities of stain mean that there is only enough dye to form a dark shell around the DNA origami and the background of the TEM grid remains light. In both cases the DNA duplex is light with dye occupying the space between duplexes. Dye is able to enter the hollow lumen of the nanopore and accumulate, meaning that the hollow lumen of the funnel appears darker. This means that we see effectively a cross section of the nanofunnel during TEM imaging.

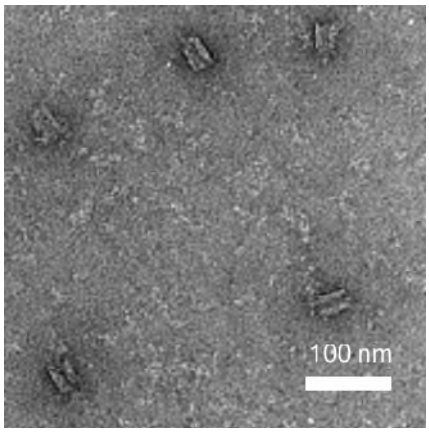

Figure 48 - *TEM of slower moving band cut from 15h ramp agarose gel. Monomer funnels were seen.*

Monomer origami funnels were observed when the faint, lower band was imaged. (Figure 48). This supports the previous hypothesis that the higher band seen in the agarose gels of the funnel after folding, and which dissipates over time, corresponds to origami dimer bands formed by non-specific base stacking interactions.

To improve the folding yield of monomer origami structures, ramp protocols of increased lengths were investigated. The total ramp time was increased to 36 hours, 3 days and 4 days. Agarose gels which were run of samples after each folding protocol showed a very similar band pattern: a fast moving excess staples band, and two slow moving bands above the M13mp18 scaffold strand band. The lower band, corresponding to the funnel monomer, was more prominent than the top band, corresponding to funnel dimers. (Figure 49)

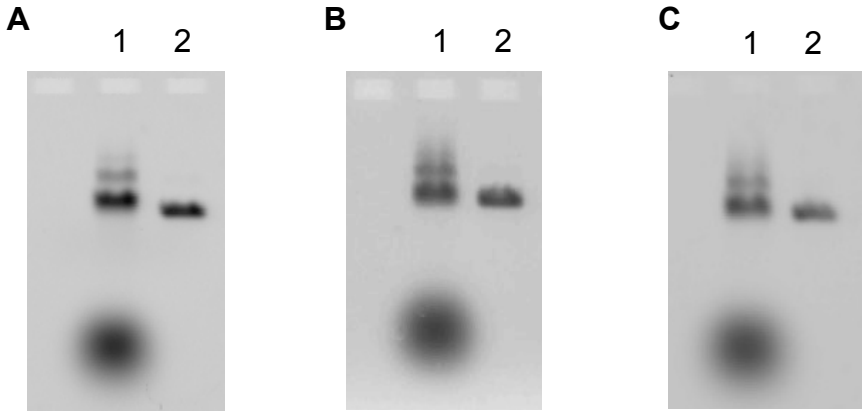

Figure 49 - *1.5% Agarose gel run at 60 V for 90 min. Lane 1 – folded funnel, Lane 2 – Scaffold A) 36 hour ramp fold, B) 3 day ramp fold, C) 4 day ramp fold.*

TEM imaging was performed for samples taken from the annealment mixture, and with single gel bands for the different ramp protocols. (Figure 50) The annealment mixtures showed a mixture of monomer and dimer origami structures. The top gel band showed a high proportion of dimer structures (Figure 50D), and the lower band showed monomer structures only. (Figure 50B)

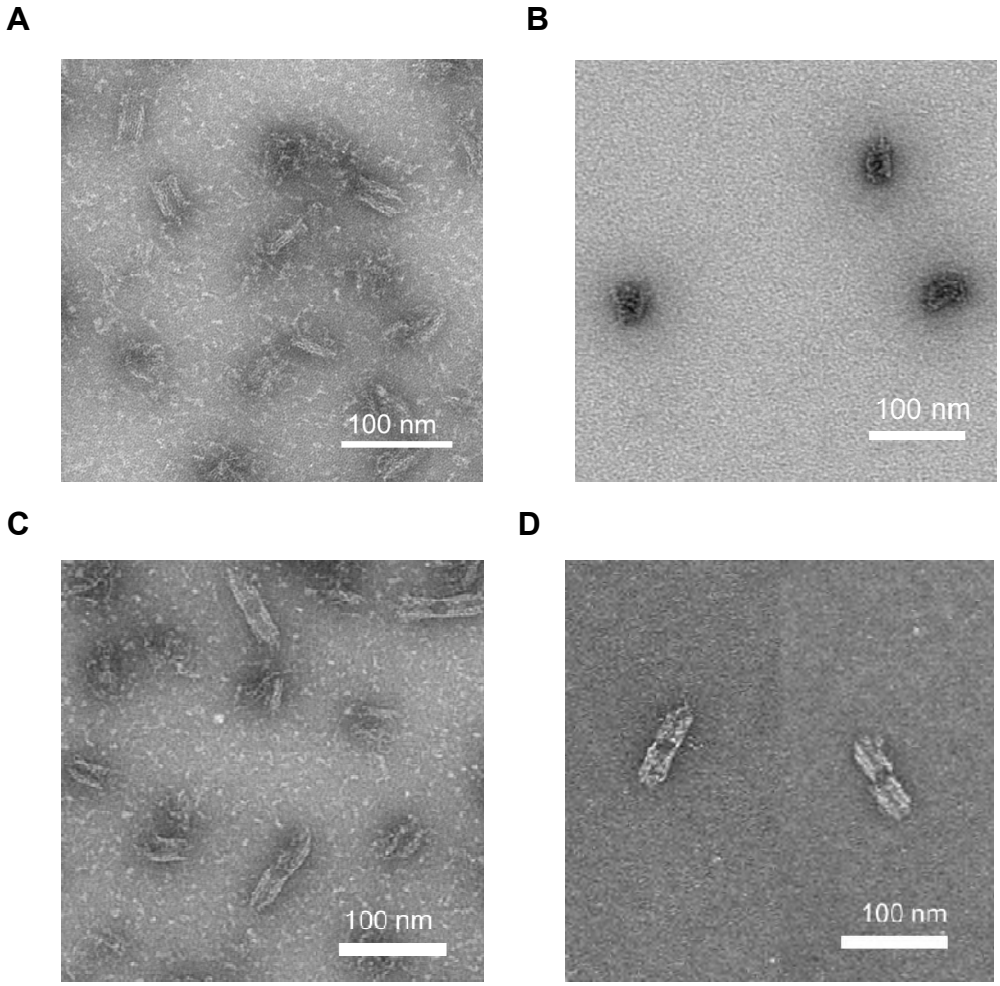

Figure 50 - *A) 36 hr ramp fold, unpurified sample. B) 36 hr ramp fold, cut faster moving monomer band. C) 3 day ramp fold, unpurified sample. D) 3 day ramp fold, cut slower moving dimer band.*

The four-day ramp protocol led to the formation of nanopores with minimal defects (approximately 86% of pores were correctly formed), and therefore this folding protocol was used to produce pores for further experiments. A 4 day protocol decreases the temperature gradually enough to avoid kinetic traps in the folding pathway of the origami funnel. Pores were imaged in areas of positive and negative TEM staining and compiled in Figure 51.

The tapered top section of the cap and two-layered membrane puncturing section are clearly visible in the TEM images. The images show a cross section of the DNA funnel with the central lumen seen as a darker channel through the centre of the pore as dye is able to accumulate in the pore's lumen. The well-formed pores imaged with TEM showed lengths of 38.0 ± 3.4 nm (n=30). This is slightly shorter than the expected 46nm. However, as the top and the bottom of the nanopore consist of fewer duplex layers than the rest of the nanopore this may affect the visibility of these sections. The width of the funnel was seen to be 24.2 ± 1.9 nm (n=30) which is consistent with the theoretical diameter of 22.5 nm, when taking into account helix repulsion and imaging accuracy.

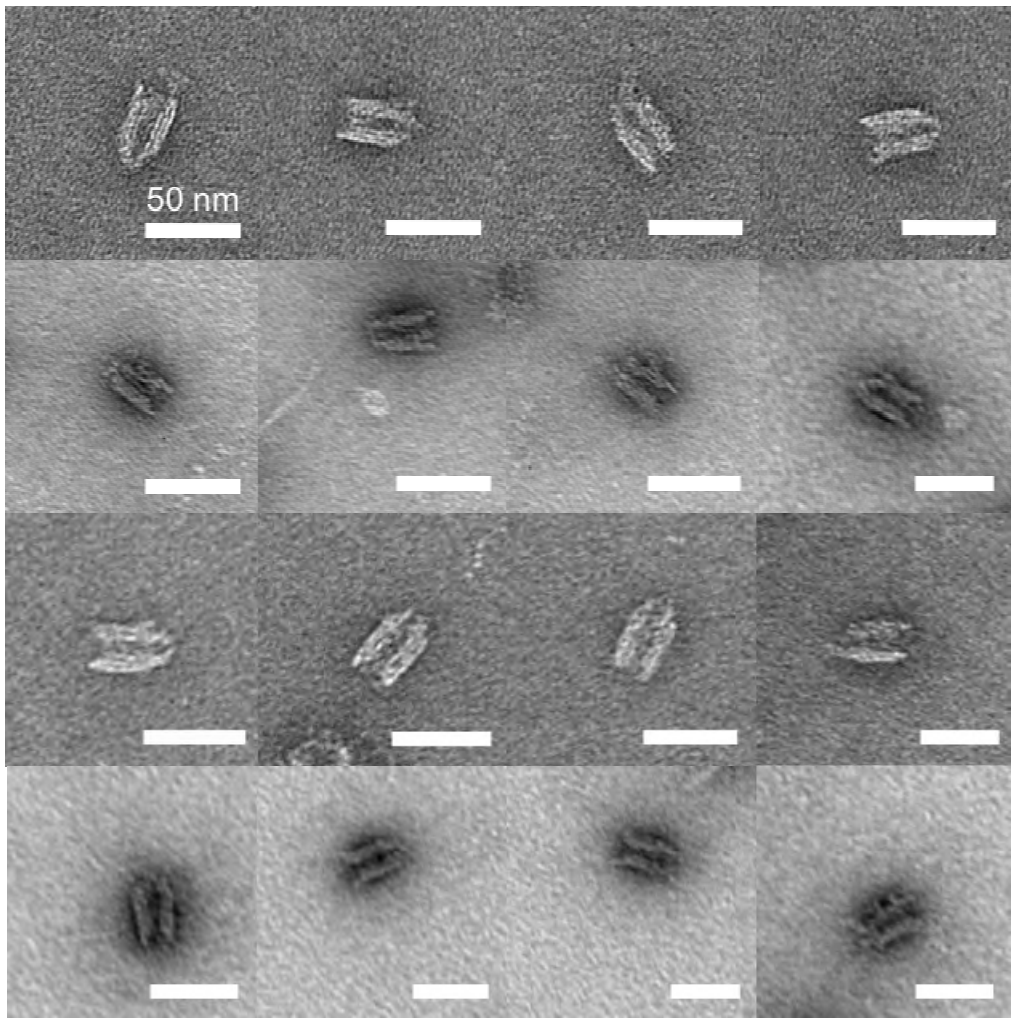

Figure 51 - *Compilation image of 16 fully folded origami funnels after a 4 day fold protocol. TEM images taken in areas of positive and negative staining.*

2.1.4 AFM Imaging with Stacking

Visualisation of the origami nanopores with TEM allows for two-dimensional visualisation of the origami pores. However, information about the three-dimensional height of the nanopore cannot be deduced from TEM images. AFM (Atom Force Microscopy) was performed in liquid in tapping mode. Several AFM protocols were tested to find a protocol which resulted in appropriate coverage of origami structures. The origami objects were allowed to base stack, to allow for easier AFM visualisation and identification. (Figure 52) Due to base stacking interaction of the bases at the top and bottom end of the DNA funnel structure, the DNA origami funnels group themselves into chains. This makes the origami structures more easily identifiable from background debris on the mica surface.

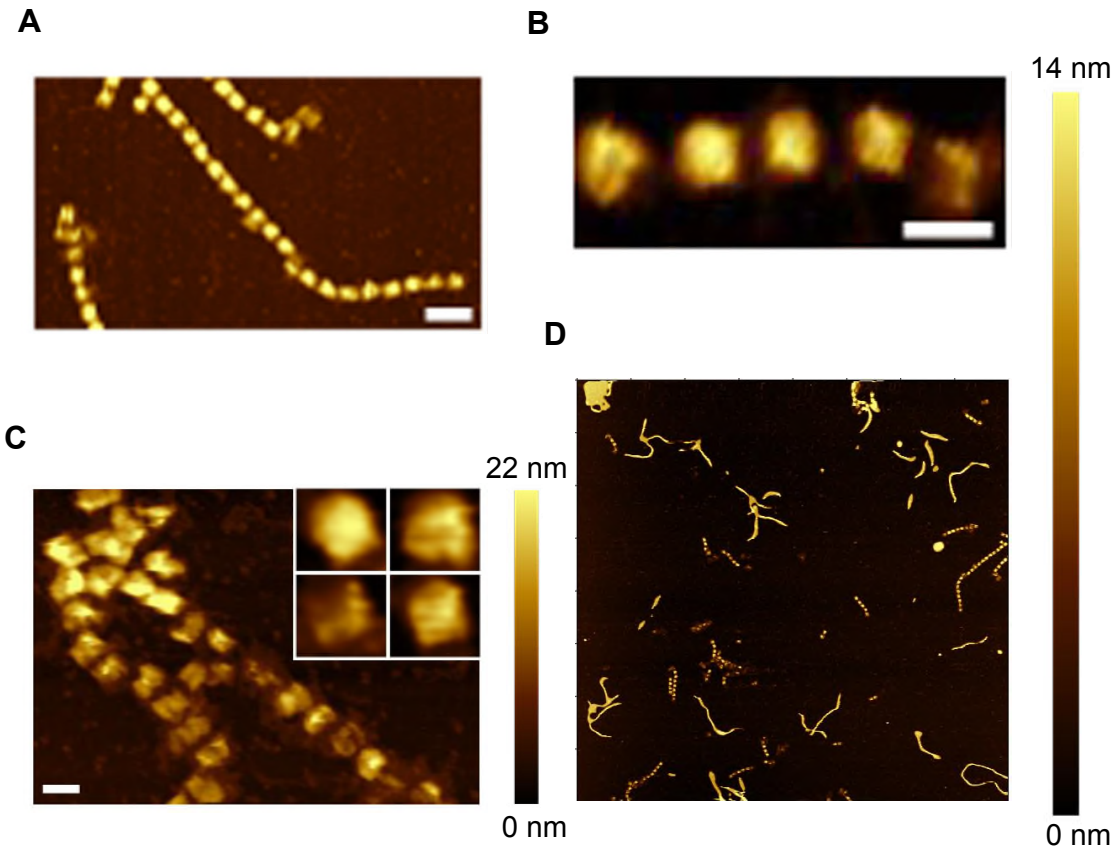

Figure 52 - *AFM micrographs. In the micrographs nanopores appear as squares due to the compression of the hollow DNA nanostructure. A) Scale bar = 200 nm B) group of 5 funnels scale bar = 100 nm C) Application of a higher force set point led to compression of the nanopore and visualisation of a depression caused by the inner lumen. D) 4 µm x 4 µm micrograph shows groups of stacked nanopores, aggregates and some debris from commercially sourced scaffold sample not removed by SEC purification.*

DNA was imaged on mica, incubated first with 100 µL of SEC purified funnel solution in 14 mM $MgCl_2$ 1xTAE folding buffer. This buffer was then wicked off and replaced with 100 µL 14 mM $MgCl_2$ 4 mM $NiCl_2$ 1xTAE buffer. With just $MgCl_2$ buffer, objects may move on the surface. The Ni^{2+} ions help coordinate the negatively-charged DNA nanostructures strongly to the negatively polarised, atomically flat, mica surface[152,233]. Gel cut origami bands did not image well using AFM, potentially due to the deposition of small pieces of agarose which are difficult to differentiate from the origami.

The SEC purified sample showed deposition of debris from the commercially sourced scaffold solution, which was also seen in TEM images of the unpurified structure. (Figure 52D) Allowing the origami to stack allowed the identification of chains of objects with dimensions matching those of the DNA funnels. The observed chains looked similar to the chains observed during TEM analysis. (Figure 47B) The nanopores lie on their sides on the mica surface to maximise the contact between the DNA's negative backbone and the Ni^{2+} and Mg^{2+} cations. Objects are expected to be 47 nm x 22.5 nm x 22.5 nm in size, assuming an idealised B-DNA model with no repulsion between neighbouring helices, lengths per base pair of 0.34nm and helix diameters of 2.5nm.

AFM images showed objects that appeared square in shape. The square shape is most likely caused by tip broadening effects and compression of the hollow origami pores. Tip broadening effects, caused by the elastic deformation of the DNA by the AFM tip, are well known[234]. Compression of DNA origami objects by AFM tips is also well documented in literature[2,142,235] The funnel nanopore is designed so that the top 7 nm of the pore is only a single duplex thick, and the bottom membrane-penetrating section of the pore, 11nm in length, consists of only a single duplex and layer of ssDNA (where cholesterol possessing staples will be hybridised for membrane association). The origami nanopores observed by AFM showed side lengths of 36.0 ± 10.5 nm (Figure 52). This size range encompasses both the expected widths of the origami pore (22.5 nm) and the length of the origami pore's cap region (35 nm). (Figure 39) Considering the tapering of the pore bottom section in the design, the certain compression of the nanopore by the AFM tip and the accuracy of the technique, this range of dimensions supports the

assembly of the designed pore.

Looking at a selection of objects in three dimensions revealed further structural detail (Figure 52C inset). DNA structures show troughs in the middle of their structures; this is consistent with the central region of the structure being more compressible, as the open space of the pore lumen is situated below.

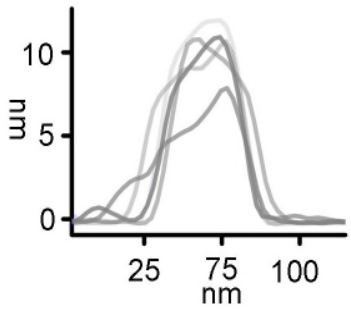

Figure 53 - *AFM elevation profiles shown of the dimensions of the five DNA nanopores in Figure 50B. Measured at a set point force of 0.05 V*

Height profiles showed average heights of 7.88 ± 1.93 nm. This value is significantly shorter than the theoretical height of 22.5 nm. However, the reduced height is likely due to compression of DNA origami structures by AFM tips[142]. Considering that this structure is hollow, a large amount of compression is expected to take place. To assess the compression effect, a group of five structures (Figure 52B) was imaged, using different force setpoints of 0.05 V and 0.01 V. The set point in AFM tapping mode is the amplitude of oscillation that the AFM cantilever is in a negative feedback loop around. The set point value can therefore be used as a measure of the force exerted on the mica surface by the AFM tip. Objects showed an average height of 10.5 ± 0.75 nm at a setpoint of 0.05 V (Figure 53), which was significantly increased to average heights of 14.07 ± 2.09 nm when the force was reduced to 0.01 V. This indicates that the force of the AFM tip significantly affects the height of the imaged structure. Assuming compression, experimental heights of 14 nm are consistent with the correct formation of the funnel structure.

2.1.5 Means to Prevent Base Stacking

To prevent dimer formation due to base stacking interactions and avoid the need for origami "curing time", staple strands at the top and bottom edges of the origami nanopore were replaced with staples possessing four T bases which were to remain single stranded. (Table 4). Blunt end stacking can only take place where a DNA duplex is present. By adding extensions where only single stranded DNA is present, unwanted non-sequence specific association of the DNA nanopore structures can be prevented[121]. (Figure 54)

Duplex Reference	*Staple Sequence*	*Length*
40[190]	TTTTAACGGATTCGCCTGAAACAGTTGATTAACATTTT	38
42[190]	TTTTGAGACCCAATTCTGCAGTACCTTTTACATCTTTT	38
44[190]	TTTTGAAGGGTTAGAACCTTATACTTCTGAATAATTTT	38
46[190]	TTTTGATGGCAATTCATCAATTCCTGAGCCCGAAC	35
48[193]	TTTTTAAATCCTTTTTATCAGATTTT	26
50[193]	TTTTGAAGGTTATCGACAACTCGTTTTT	28
52[193]	TTTTCCACGCTGAGAAAGGAATTGTTTT	28
56[185]	TTTTCATTCTGGCCTCTTTAATTTTT	26
60[185]	TTTTTAATAACATCCAACAGGAAATTTT	28
62[185]	TTTTAATCCTGAGATTCTTTGATTTTTT	28
34[178]	AACTTTTTCAATGTTTAGTACAAACATCACACGGAACGGTACGCCTTTT	49
58[185]	TTTTCGCTCATGGATAATAAAAGGTTTT	28
53[164]	GGCGGTCAGTATTAACACCGTTTTGCGCGA	30
15[69]	TGCTCATTCAGTGAATAAGTTTCATCGGCATTTTCGGTCACAACGTTTT	49
13[62]	TTTTCAAATTAGCCCCCTTATTAGCGTTTGCAGGT	35
12[82]	CAGACGATTGGCCTTGCATTATTTT	25
7[57]	TTTTATGAACGGTGTACAGACTTTGA	26
6[64]	AAGAGGACATTTTGGCGCAGACGGTCAATTACTTAGCCGGAACGATTTT	49
3[64]	TTTTCTCCGTCTATCTTTTTGTTCAGAAAACGAGAATCAAA	41
1[72]	AACGAGGGGGAGATTTGTATCATCTTTTAAAGC	33

Table 4 – *Addition of T bases to nanopore edge staples to prevent base stacking interactions*

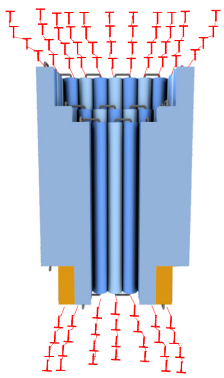

Figure 54 - *Representation of T base addition.*

2.1.6 Lipid Anchor Addition

After full characterisation of the origami nanopore's folding, cholesterol-containing staples were hybridised to the origami nanopore via sticky ends in the second layer of duplex to facilitate membrane association. (Appendix Table 10). Cholesterol functionalised DNA strands were allowed to attach to the fully formed funnel structure by incubating the origami funnel with cholesterol functionalised strands at 30°C for 30 min. This is above the melting temperature of the short cholesterol staple strands and the free sticky ends on the origami, but not high enough to disrupt the extended duplex of the folded origami funnel.

The running of the cholesterol modified funnel in agarose gel was compared to the running of the cholesterol free funnel. (Figure 55) The cholesterol funnel appeared streaky in the agarose gel; this is likely due to hydrophobic interactions between the gel matrix and the cholesterol anchors.[215,225] By adding 0.015% SDS to the agarose gel this streaking was able to be resolved, and a defined slow running band at a similar height to the cholesterol free origami scaffold was seen. (Figure 55) Both the cholesterol free and cholesterol modified funnels showed fast running bands corresponding to excess staples.

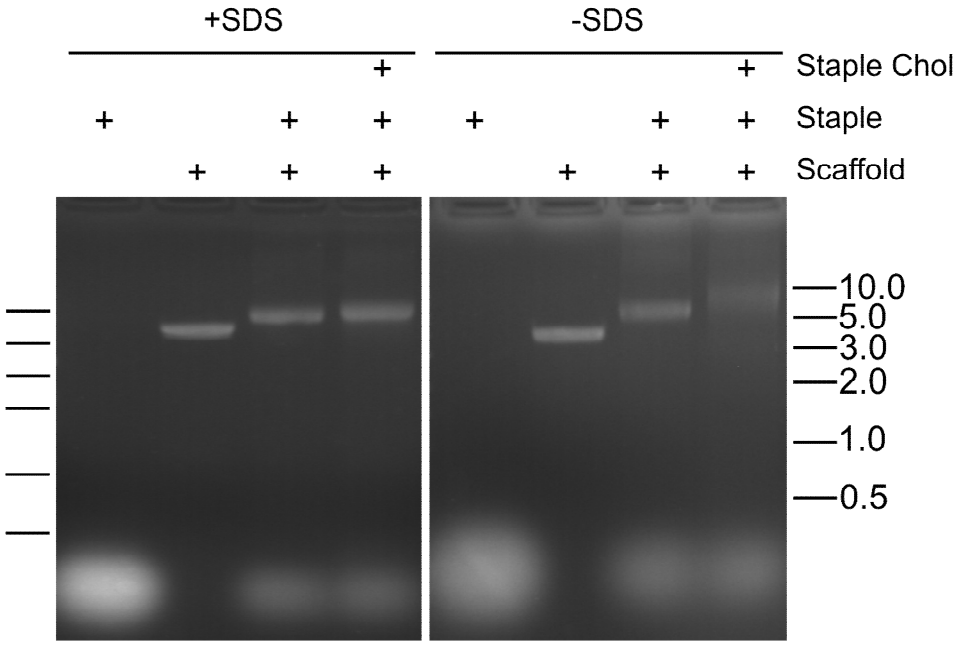

Figure 55 - *Gel electrophoresis of origami funnel with and without cholesterol strand hybridisation. Lane 1 – Staples, Lane 2 – Scaffold, Lane 3 – Cholesterol free funnel, Lane 4 – Cholesterol funnel. LHS gel - without SDS, RHS gel - with 0.015% SDS in gel and run buffer.*

Optimisation of Cholesterol Strand Hybridisation

When adding hydrophobic moieties to DNA structures, the formation of aggregates over time can be a significant problem.[5,236] To maintain a high yield of the cholesterol funnel monomer over time, the ratio of the cholesterol functionalised strands to origami funnel was investigated. A range of stoichiometries were investigated over time to identify the ratio addition which led to the most stable product and the lowest aggregation rate. (Figure 56)

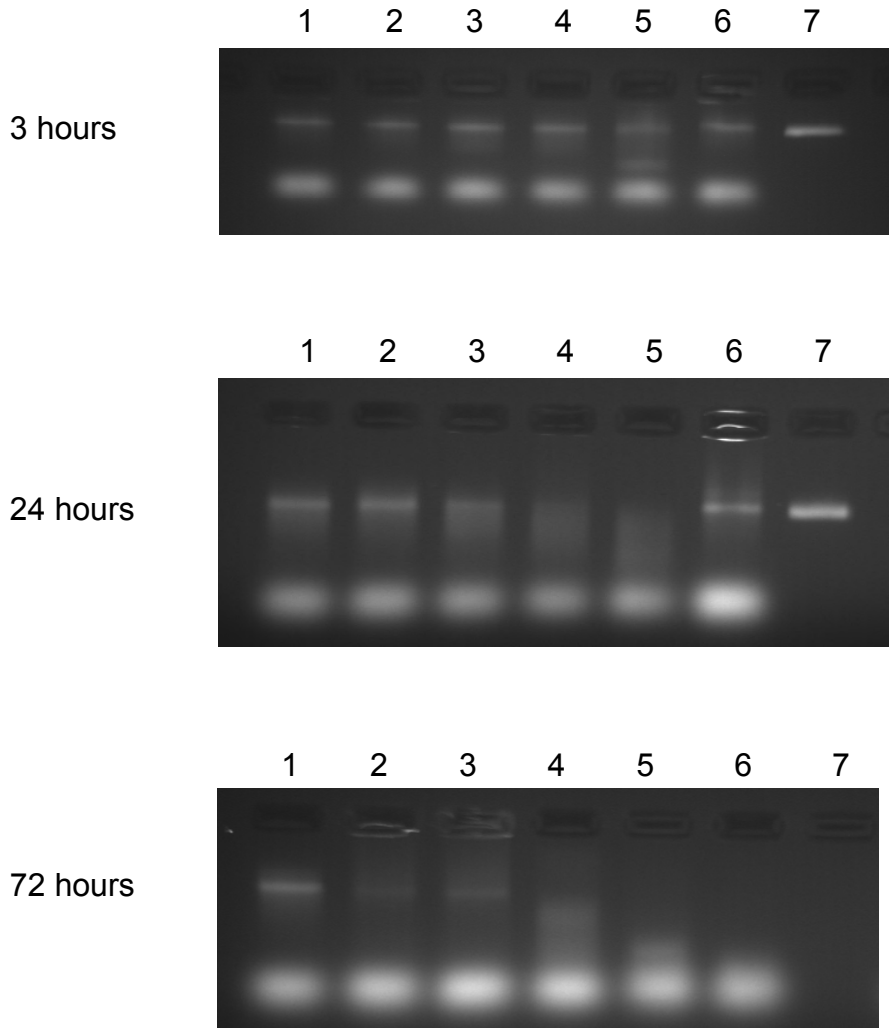

Figure 56 - *Gel investigation into aggregation of origami structures caused by cholesterol DNA strands presence. Funnel was incubated with: Lane 1 – 0x chol, Lane 2 – 1x chol, Lane 3 - 1.1x chol, Lane 4 – 3x chol, Lane 5 – 5x chol, Lane 6 – 10x chol, Lane 7 – Scaffold strand. Aggregation was monitored at 3 hrs, 24 hours and 72 hours.*

DNA funnel samples were incubated with cholesterol strands in an equal stoichiometry and a 1.1x, 3x, 5x, 10x excess. Aliquots of the origami solution were taken, and the extent of aggregation and structure disruption was monitored with agarose gel electrophoresis and compared to the cholesterol free funnel. (Figure 56) After three hours of incubation at 30^{o}C, although some bands appeared less defined compared to the cholesterol free funnel, little aggregation was seen with any ratio of cholesterol functionalised strands. After 24 hours, more streaking was seen in all lanes where cholesterol strands had been added. Extensive streaking and less band definition were seen from a 3x excess of cholesterol strands onwards. After three days, origami bands were significantly weaker in intensity compared to the funnel structure without cholesterol strands. Structures with a 5x excess and above showed no defined origami band. Large aggregate formation most likely led to the precipitation of the origami from solution, and therefore the disappearance of the origami band from the agarose gel. For subsequent experiments, cholesterol functionalised strands were incubated with the funnel at a 1.1x excess for 30 minutes directly before experimentation.

2.1.7 Insertion of DNA Nanopores into Membranes

The association of the cholesterol funnel with lipid bilayers was assessed using gel electrophoresis assay experiments (Figures 57&58) and TEM imaging (Figures 59&60).

Gel Binding Assay

The gel binding assay involved the incubation of the cholesterol nanopore with progressively higher concentrations of PEPC (30:70 DOPE:DOPC) SUVs (small unilamellar vesicles). The SUVs are unable to enter the agarose gel matrix, so remain in the gel wells during the assay. DNA associated with the SUVs remains bound to the SUVs, and therefore does not run through the agarose gel when a voltage is applied. The DNA however is visible as bright features in the gel wells after staining with ethidium bromide. DNA not associated with the SUVs was free to move through the agarose gel, and appears as bands in the gel.

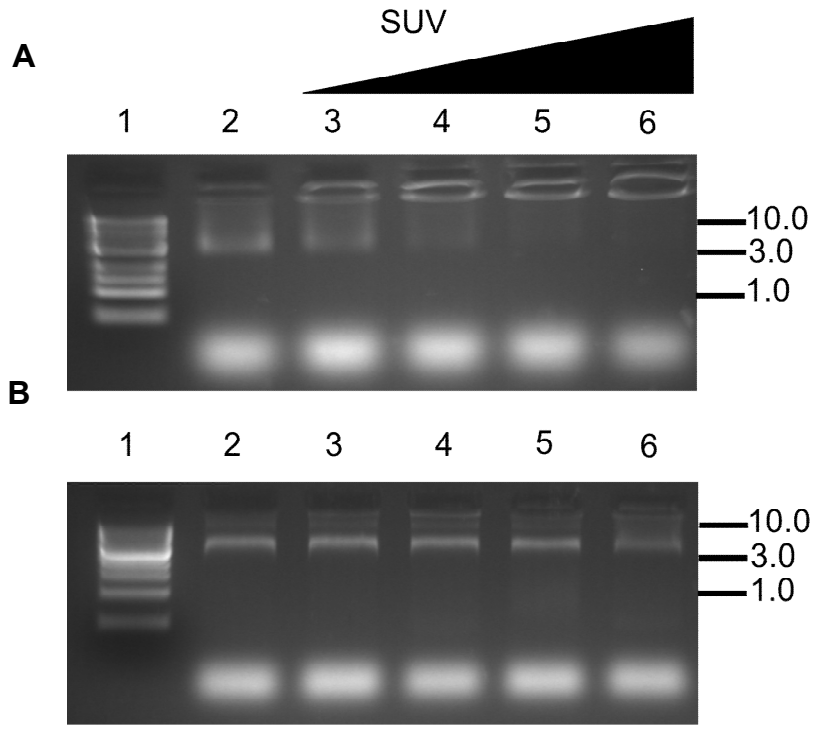

Figure 57 – *Gel electrophoretic assay of the interaction between cholesterol-tagged DNA nanopores and lipid vesicles. A) The DNA nanopores carried the lipid anchor at all 24 possible membrane-spanning duplex positions. B) The DNA nanopore with no lipid anchors. Lane 1 – DNA ladder, Lane 2 – DNA nanopore with no lipid, Lane 3 to lane 6 – 6.9 – 12.5 nM SUVs.*

Assays were performed with the funnel nanopore without cholesterol strands (Figure 57B), with all cholesterol strands added (Figure 57A), with only the 5 prime cholesterol strands added (Figure 58A), and with only the 3 prime cholesterol strands added (Figure 58B). Increasing concentrations of SUVs were added to the funnel solutions (6.9 to 12.5nM), and the samples were incubated at 30^{o}C for 30 min before gel electrophoresis. Increasing concentrations of SUV led to a complete disappearance of the slow-moving funnel band, and increasing brightness in the gel wells.

The control experiment with the cholesterol free funnel showed no movement of funnel band with increasing concentration of SUV. Nanopores possessing only the 5 prime cholesterol anchors or the 3 prime cholesterol anchors showed a lower band disappearance with SUV concentration. Reducing the number of lipid anchors leads to a corresponding reduction in vesicle binding.

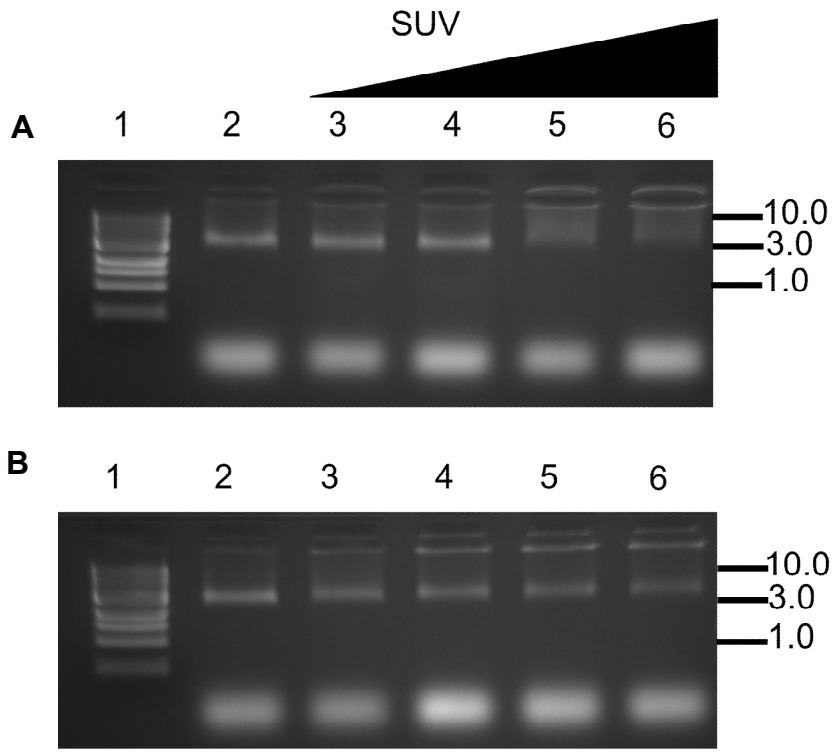

Figure 58 - *Gel electrophoretic assay of the interaction between cholesterol-tagged DNA nanopores and lipid vesicles. A) 12 lipid anchors corresponding to 5 prime-modified anchor strands, and B) 12 lipid anchors corresponding to 3 prime-modified anchor strands. Lane 1 – DNA ladder, Lane 2 – DNA nanopore with no lipid, Lane 3 to lane 6 – 6.9 to 12.5 nM SUVs.*

Vesicle Binding TEM Imaging

The gel binding assay confirmed the association of the DNA origami nanopore with the lipid bilayer, but not the orientation of the pore or whether the nanopore punctured the lipid bilayer. TEM analysis was conducted at UCL with the help of Dr Yongzheng Xing, who operated the TEM. Approximately 10 μM of PEPC SUVs were incubated with 1nM of the cholesterol functionalised origami funnel in 0.3M NaCl 1xTAE buffer for 30 min at room temperature. 6 μL of funnel/SUV sample was added to glow discharged carbon-coated copper grids, and imaged using a JEM-2100 electron microscope.

Clear binding of the origami funnels was observed. The average dimensions of the pore were 28.8 ± 3.1 x 21.1 ± 2.0 (n=30). This reduction in length of the funnel nanopore observed, compared to the TEM images of the vesicle-free nanopore, indicates that the lower section of the pore is embedded within the lipid bilayer and that only the cap region of the nanopore is visible. Multiple pores were seen to bind to each vesicle. (Figure 59, 60)

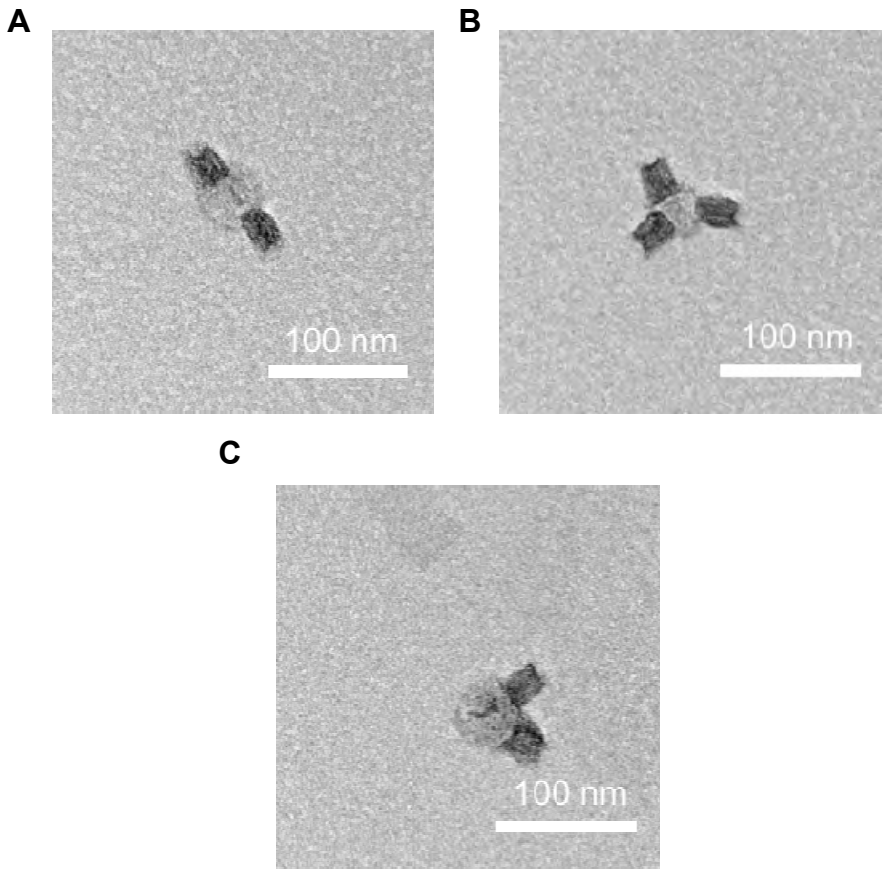

Figure 59 - *Three representative TEM imaged vesicles with nanopores associated*

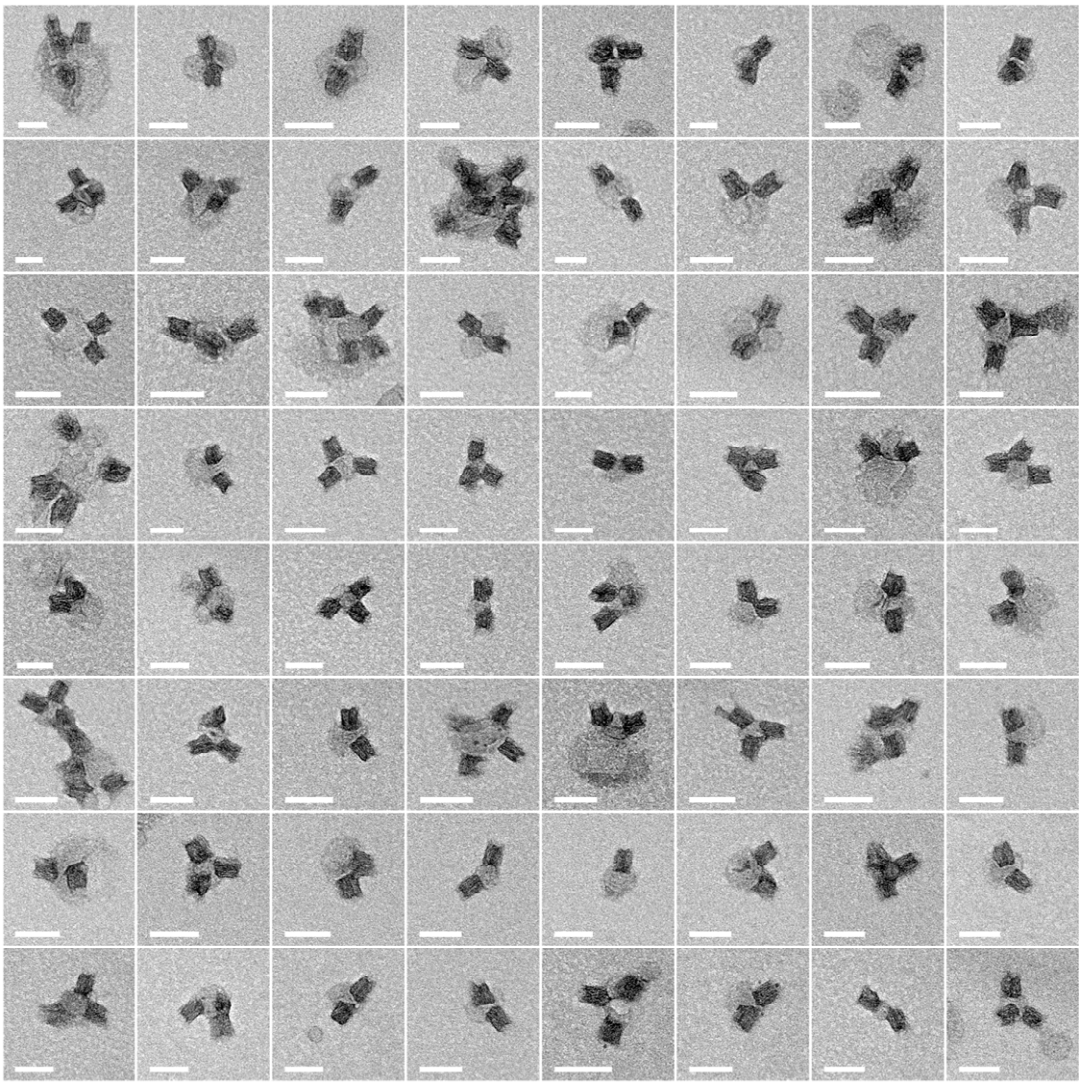

Figure 60 - *Panel of 8 x 8 TEM images each showing SUVs with at least one funnel nanopore associated. Scale bar = 100 nm.*

Gel electrophoresis, TEM and AFM analysis were used to characterise the correct formation of the designed DNA funnel nanopore. The shape of the nanopore is consistent with the theoretical pore's design. The nanopore has also been shown to associate with lipid vesicles. After establishing this, the nanopore's characteristics in a nanopore biosensing set up were examined to assess the viability of the pore for sensing of proteins.

2.1.8 DNA Funnel Nanopore Recordings

Planar lipid bilayer electrophysiological measurements were performed using an integrated chip-based parallel bilayer recording set up, known as an Orbit 16[237] (Figure 61). The chips used in the Orbit 16 set up contain a 4x4 array of less than 1mm^2 channels with embedded microelectrodes (microelectrode cavity array, MECA)[238]. Automatic formation of bilayers is achieved using a PTFE (Polytetrafluoroethylene) coated magnetic stirrer bar, allowing detection and manipulation of multiple nanopore-containing channels simultaneously[239].

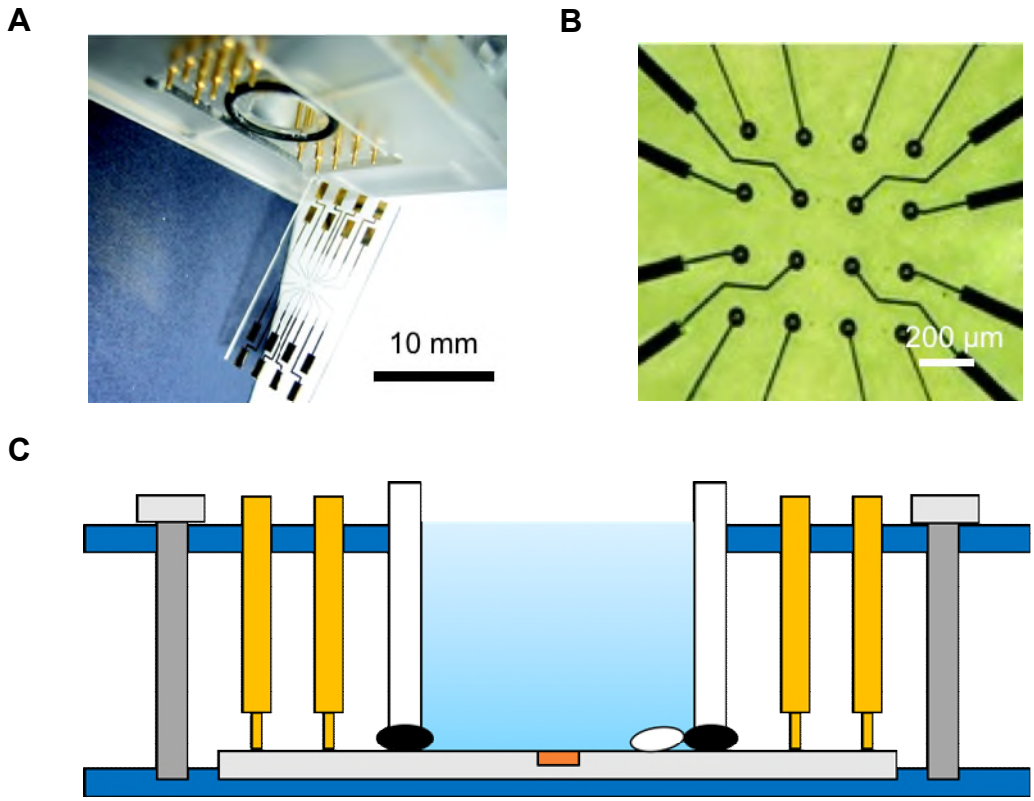

Figure 61 - *Orbit 16 components A) MECA chip, the buffer filled chamber is prevented from leaking on to the contact pads by the black O ring. B) Zoomed in view of the MECA chip. Conductive path ways end at small circular pads below each microscale aperture channel and start at the contact pads. The chip is coated in an insulating polymer[238]. C) Diagram of orbit 16 set up. The MECA chip is shown in light grey, and a PTFE (Polytetrafluoroethylene) containing buffer solution is shown in white. The silicon O ring (black) maintains the seal of the chamber. The upper board (blue) contains several rows of contact pins (yellow) which connect the chip to the amplifier. The PTFE coated magnetic stirrer bar is placed within a chamber (white oval) and stimulated to spread lipid and then sit away from the active channels by a counter magnet below the diagram. The active section of the chip containing the apertures is shown in orange[239].*

Characterisation of Insertion and Current Flow through the Funnel

150µL of a standard electrolyte solution of 1 M KCl and 10 mM HEPES, pH 8.0 was added to the cis chamber, and stimulated to enter the channel using a "micro-plunger". An alternating ± 5 mV voltage protocol was applied to confirm buffer entrance to each of the channels. Bilayers are formed by spreading DPhPC lipid dissolved in octane across the chip's buffer-filled channels, using a miniature magnetic stirring bar coated with the lipid (Figure 61C). When the lipid is covering the channel, no current flow should be seen when the ± 5 mV voltage protocol is applied. A holding voltage of +30 mV relative to the cis side of the bilayer was then applied, and solutions containing the DNA origami funnel were then added to the cis side buffer solution and allowed to diffuse to, and insert into, the lipid bilayer. When no nanopore or perforation of the bilayer is present, no current can travel through the bilayer (Figure 60 (0-4000 ms)). When a nanopore inserts into the bilayer, a current is now able to flow and be detected and can be observed on a distinctive current "step" in the recorded current traces, as shown in Figure 62 (4000 ms onwards).

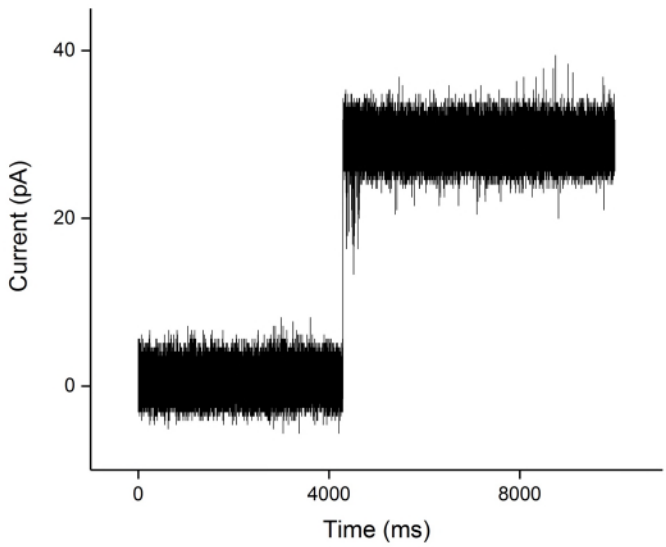

Figure 62 - *Insertion step. No ionic current flow is seen before 4000 ms as no current can pass through the membrane. When a nanopore inserts into a bilayer a "step" is seen where there is a jump in the ionic current flow which is now able to travel through the pore embedded in the membrane.*

Initially, it proved more difficult to stimulate the funnel nanopores to spontaneously insert into the planar bilayer compared to their insertion into SUVs in previous experiments. It is more energetically favourable for the nanopores to insert into curved vesicles.[226] This is likely due to the presence of defect regions caused by the strained lipid arrangement in the curved vesicles, which can favourably accommodate insertion of the nanopores.[218] To facilitate insertion of the nanopore into the planar lipid bilayer it was found that a 2:1 volume ratio of Funnel:0.5% OPOE detergent solution needed to be used. OPOE is a non-ionic detergent and is commonly used to solubilise membrane proteins to help stabilise the proteins outside of a lipid bilayer[240]. The use of OPOE to facilitate DNA nanopore insertion during recording experiments has been shown in previous literature[4]. Individual nanopores were successfully inserted into the lipid bilayer, under standard electrolyte conditions. Figure 63 shows a representative open trace held at an applied voltage of +20 mV relative to the cis side of the pore; a constant current of 49.5 pA was observed.

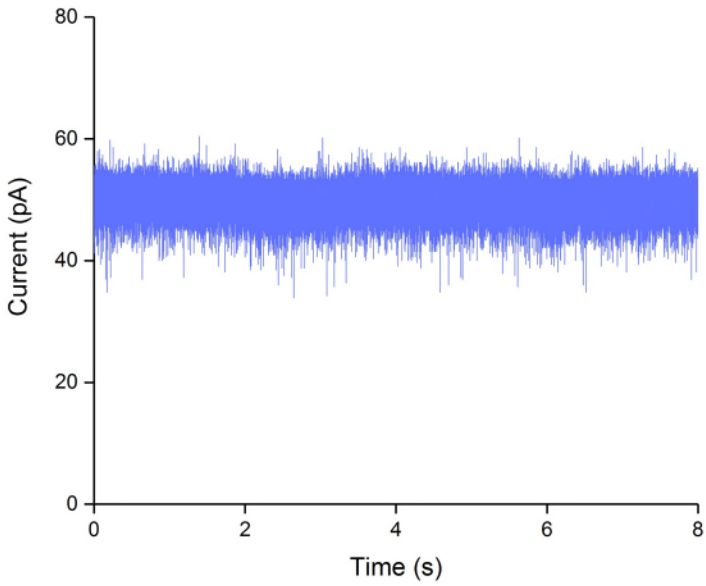

Figure 63 - *Representative "open" ionic current trace of a single funnel pore in 1 M KCl, 10 mM HEPES pH 8.0 and at +20 mV relative to the cis side of the membrane*

Voltage Protocols

Several different types of voltage protocols were used to fully characterise the nanopore's sensing characteristics: a) a hold protocol, b) an IV protocol, and c) a voltage ramp protocol. (Figure 64).

a) *Hold protocols* involved the manual changing of the voltage applied to the nanopore.
b) *IV protocols* involved the application of positive voltages for a time period (T_{pu}), followed directly by the negative voltage of the same magnitude. Three sets of IV protocols were used for characterisation:
    - Protocol 1: 0 mV (0.25 sec), ± 40 mV (1 sec), ± 60 mV (1 sec), ± 80 mV (1 sec) ±100 mV (1 sec), 0 mV (0.25 sec), (V_{fp}=40, V_{step}=20 T_{pu}=1, Tp_e=8, N=4)
    - Protocol 2: 0 mV (1 sec), ± 20 mV (1 sec), ± 40 mV (1 sec), ±60 mV (1 sec), ±80 mV (1 sec), ± 100 mV (1 sec), ± 120 mV (1 sec), (V_{fp}=20, V_{step}=20 T_{pu}=1, T_{pe}=12, N=6)
    - Protocol 3: 0 mV (1 sec), ± 50 mV (4 sec), ± 100 mV (4 sec), (V_{fp}=50, V_{step}=50 T_{pu}=4, T_{pe}=8, N=2)
c) *Voltage ramp protocols* ran from -100 mV to +100 mV, with a 0.8 mV voltage step every 20 ms. (V_{fp}=-100, V_{step}=0.8 T_{pu}=0.02 V_{max}=100)

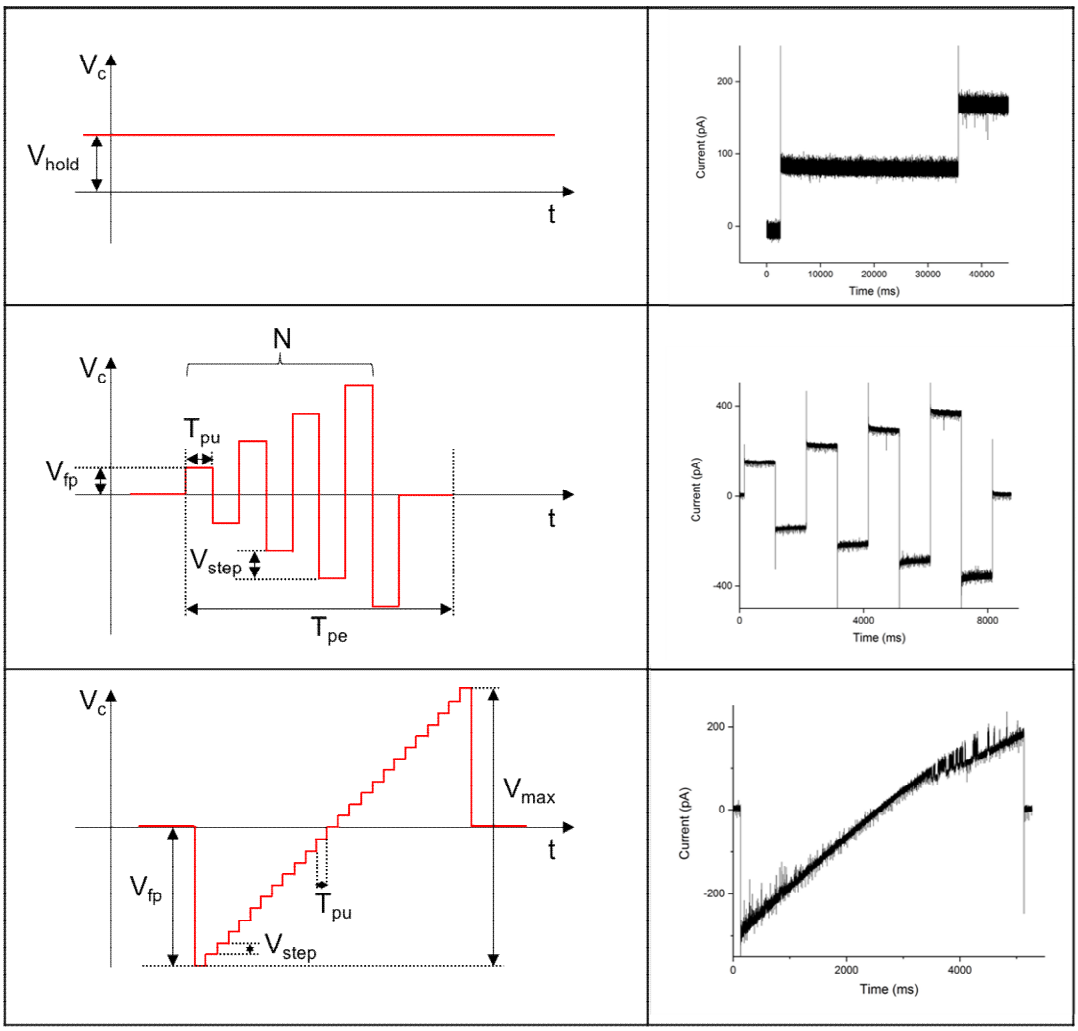

Figure 64 - *Diagrammatic representation and example traces for each type of protocol used to characterise the nanopore. Row 1 - hold protocol, row 2 - IV protocol, row 3 - voltage ramp protocol*

Conductance Distribution

Conductance is the ratio of the current flow to the voltage applied. Conductance during single channel current experiments is dependent on the ion concentration in the buffer used. The conductance seen for nanopores during single channel current recordings in a standard 1M KCl buffer is typically in the nanosiemens nS range.

The conductance of the funnel nanopore was calculated using a basic model, where the nanopore is approximated as a cylindrical resistor with access resistances at the entrance and exit of the pore.[225,241] (Equation 2)

$$G = \kappa \frac{\pi d^2}{4L + \pi d}$$

Equation 2 – *Estimation of the conductance of a cylindrical nanopore.*

G is conductance, d is the diameter of the pore (7.5nm), L is the length of the pore (36nm) and κ is the electrolytic conductivity of 1M KCl at 25°C (10.86 S/m).

Using equation 2, the conductance of the nanopore is estimated as approximately 11nS. A conductance histogram comprising data collected from 177 different DNA funnel nanopores at low voltages (20 mV – 40 mV) showed a double peaked distribution. Peaks were seen at 0.9nS and 2.3nS conductance. (Figure 65) This double peaked histogram indicates that the funnel nanopore has two distinct current confirmations, and that the current that is able to flow through the pore changes due to structural variations in the DNA nanopore. The two peaks were specified as nanopores in a fully "open" state, and in a "closed" state.

Even in the open conductance state, the funnel nanopore's conductance is approximately 5 times less than the theoretical current calculated using the geometry of the pore. This suggests that the lumen of the funnel may be compressed due to the pressure of the lipid bilayer. The low conductance may also indicate a reduction in current leakage through the funnel structure compared to other DNA origami objects[224]. However it is hard to determine whether this is actually the case or whether current leakage is occurring and further offsetting an

even lower overall conductance.[226] The simple model also incorrectly assumes a constant mobility of electrolyte ions in the negatively charged DNA nanopore.

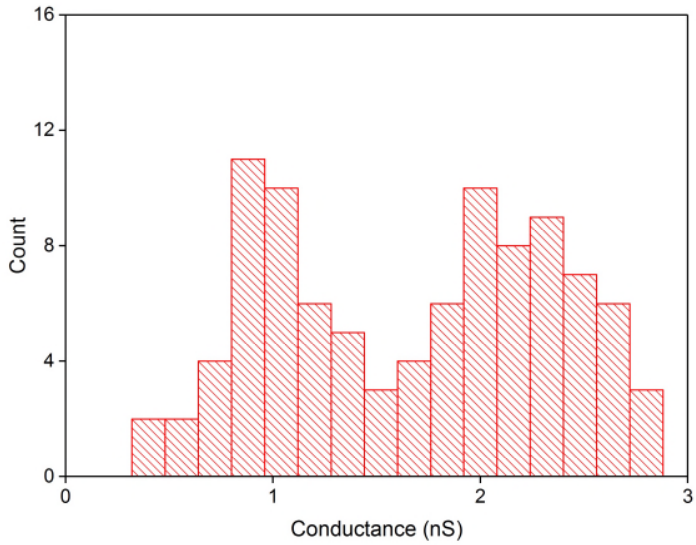

Figure 65 - *Conductance histogram of all active funnel nanopores recorded. Data set comprises 177 nanopores with the conductance recorded at low voltages (20mV-40mV). Traces with a conductance over 3.5 nS were excluded as channels likely possessed multiple nanopores.*

The closed state is likely caused by "gating" or movement or the negatively charged DNA origami structure due to the application of a potential difference. Traces of open nanopores also showed some progressive gating characteristics, with the pores' conductance reducing as the applied voltage was increased. (Figure 65) To investigate the effect of voltage on the conductance of the origami nanopores, the distribution of 51 nanopores at 100mV was collected. (Figure 66) This showed 40% percentage increase in the proportion of nanopores in the closed state, suggesting that the pores' structural integrity is being affected by the applied voltage. Traces with conductance above 3.5nS were ignored, as they most likely correspond to multiple pore insertions in the same channel.

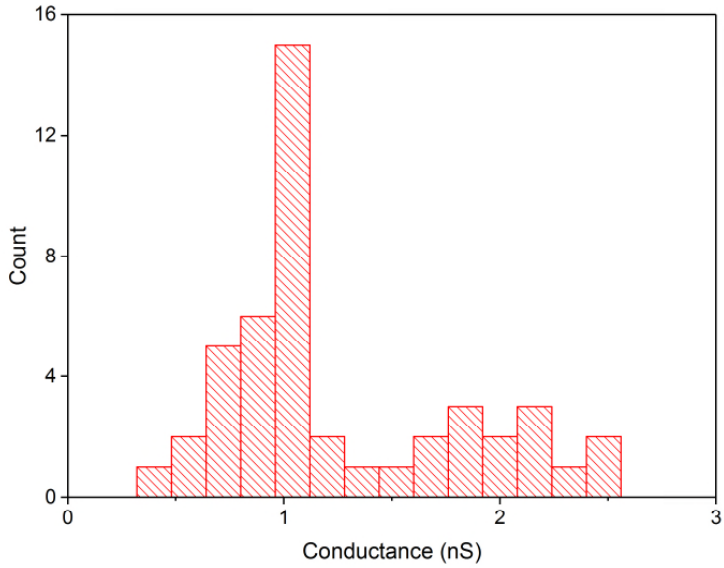

Figure 66 - *Conductance of 55 funnel nanopores collected at 100mV. 70% of nanopores are now in the closed state*

Gopfrich et al.'s DNA origami porin is one of the most similar pores to that of the current study. The origami nanopore is also designed to associate with and span the lipid bilayer using cholesterol molecules as lipid anchors[229]. The minimum constriction of the Gopfrich pore is smaller than the funnel nanopore (6 nmx6 nm) but it has a significantly larger internal volume. The funnel nanopore has an average ionic conductance approximately 17 times lower than the Gopfrich pore, which has an average conductance in the 40 nS range. However, the conductances observed in single channel experiments for the Gopfrich et al's nanopore showed an extremely large range of values. The conductance histogram of the study had a range of over 100 nS compared to a range of 2.2 nS for the nanopore of this thesis.

Krishnan et al. demonstrated a T shaped DNA origami nanopore with a minimum constriction of 4 nm x 4 nm which associated with lipid vesicles.[226] The pore had a large area of surface contact with the membrane bilayer. By using the droplet interface bilayer technique (DIB)[242,243]. Krishnan et al. determined the conductance of the nanopore to be 3.1 nS, higher than the funnel nanopore. Additionally, no secondary conformation state was seen. However, Krishnan et al. did not demonstrate the insertion of the T shape pore in a planer lipid bilayer set

up. Nanopores have been shown to insert more readily in curved bilayers[244], however commercial nanopore sensing devices, such as those manufactured by Oxford Nanopore, use a planar bilayer. The T shaped pore has not been shown to be compatible with a planar bilayer set up. Additionally, the size and dimensions of the pore lumen was not shown to support the translocation of protein analytes.

Gating Characteristics

The gating characteristics of the funnel nanopores were further investigated by looking at the characteristics seen in voltage ramp protocols. (Voltage ramp protocols ran from -100 mV to +100 mV, with a 0.8 mV voltage step every 20 ms. (V_{fp}=-100, V_{step}=0.8 T_{pu}=0.02 V_{max}=100)), Three different characteristics were commonly observed in the voltage ramp traces collected. Examples of the different gating characteristics are shown in Figure 67.

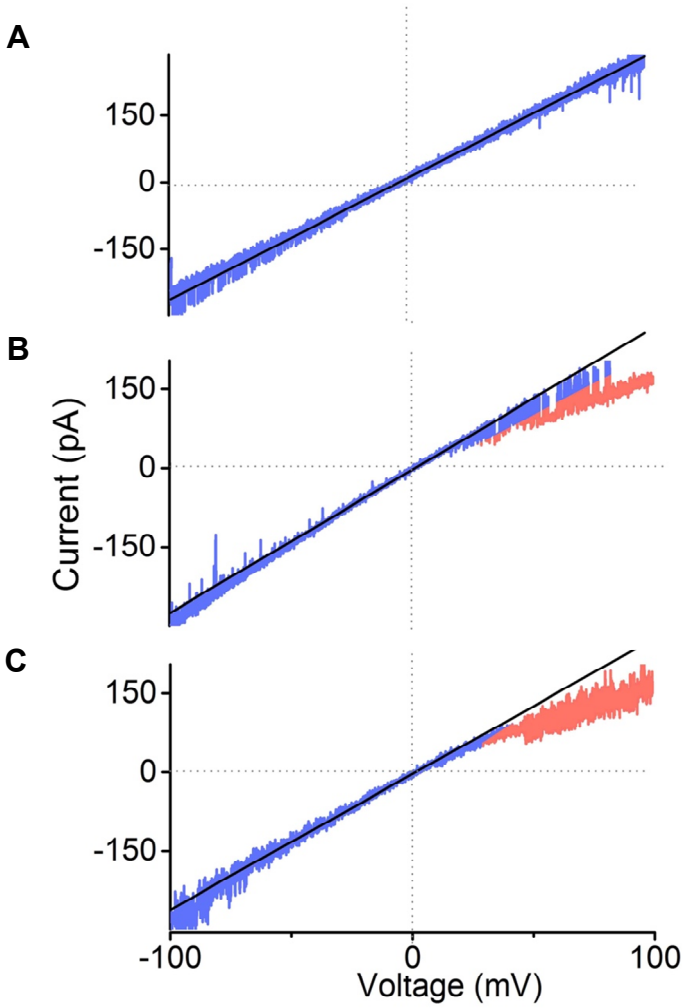

Figure 67 – *Examples of the different gating characteristics observed in voltage ramp traces. The voltage ramp traces of single DNA were recorded at voltages from -100 to +100 mV. The high conductance state is color-coded in blue; the lower conductance state is coded in red. Ohmic conductance is shown in black. A - Some origami pores remained open throughout the full range of voltages applied. B & C – some traces showed gating and a reduction of conductance to a closed state at higher voltages (shown in red). This was either seen as a constant reduction in conductance to a lower conductance level (C), or a switching between the open and closed states (B).*

Some origami pores remained open through all voltages, (Figure 67 A), while others showed gating at higher voltages (shown in red). This was either seen as a constant reduction in conductance to a lower conductance level (Figure 67 C), or a switching between the open and closed states (Figure 67 B).

10 funnel nanopores which initially had an open conductance were selected and their IV characteristics were assessed. The IV plot displaying the averages and standard deviation from single channel current traces of the 10 initially open pores verified that the funnel nanopore had ohmic behaviour when the pore was in the open state (Figure 68). However, at voltages of approximately 40mV magnitude and above the pores could switch to a lower conductance state (shown in red). A distinct difference between the current flow through open and closed state pores can be seen in the graph. The funnel nanopore design is susceptible to conformational change when a relatively large magnitude of voltage is applied. The current-voltage characteristics are relatively similar to those of Gopfrich et al.'s DNA origami porin. Gopfrich saw a largely ohmic behaviour between -50 mV and +50 mV and saw deviation from an open conductance level to a lower conductance outside this range.

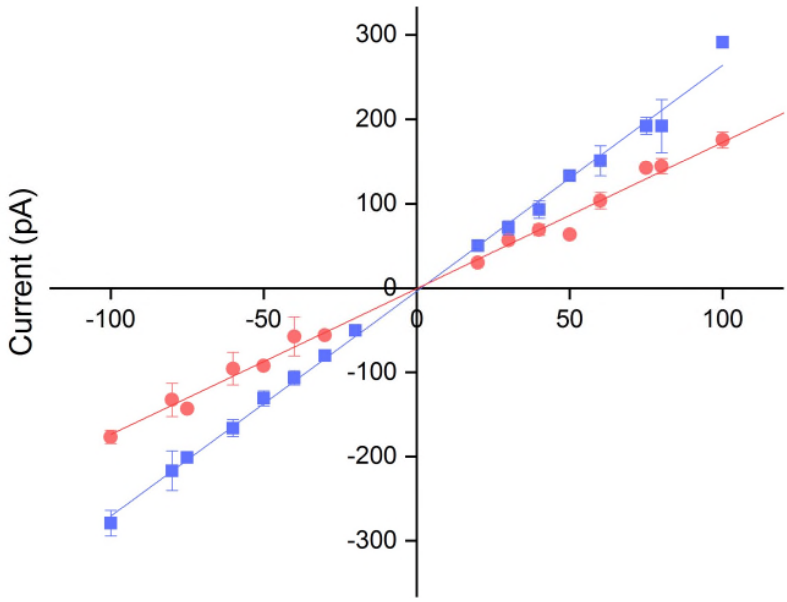

Figure 68 - *IV curve displaying the averages and standard deviation from 10 single-channel current traces.*

The single channel current recordings of the funnel nanopore have shown that the origami nanopore is able to insert successfully, and is stable at low voltages with a narrower conductance distribution than some previously published pores of a similar size[229].

Protein Translocations

The transport of protein through the lumen of the nanopore was investigated using trypsin (a biomarker for pancreatitis), with a molecular size of 4.3 x 3.8 x 2.3 nm (pI 10.1), as a test protein. Upon addition to the cis side, distinctive current blockage events were seen (Figures 69, 70 & 71), showing that the funnel origami nanopore is able to successfully transport and detect the passage of the protein biomarker.

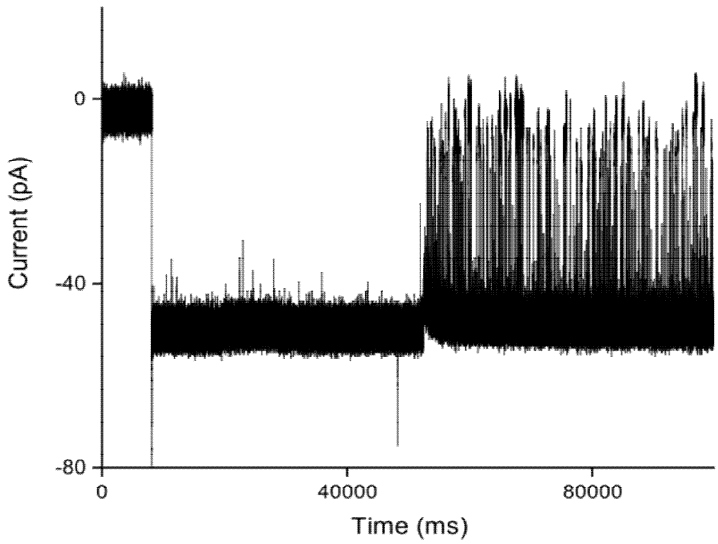

Figure 69 - *Channel with nanopore in bilayer held at -50 mV. Before trypsin addition few events were seen; after trypsin addition, significant translocation events were seen.*

A hold trace was performed where the voltage was held at -50 mV. The trace was held at the voltage for 45 seconds and minimal current fluctuations were seen. 5 µL of 10mM trypsin were added to the cis chamber buffer and mixed. After addition, a significant number of current spikes, (where the magnitude of the current is decreased), were seen. This suggests that trypsin is being successfully translocated through the origami funnel nanopore. The trace was run for a further 115 seconds after trypsin addition.

To further investigate the translocation of trypsin through the origami funnel nanopore, the concentration dependence of translocation events with trypsin addition was tested by adding 5 µL solutions of trypsin of 50 µM, 100 µM and 200 µM concentration, respectively, to the cis side of the bilayer, and mixed with no voltage protocol applied. IV protocol 3 was then run and the translocation events observed (Figure 70).

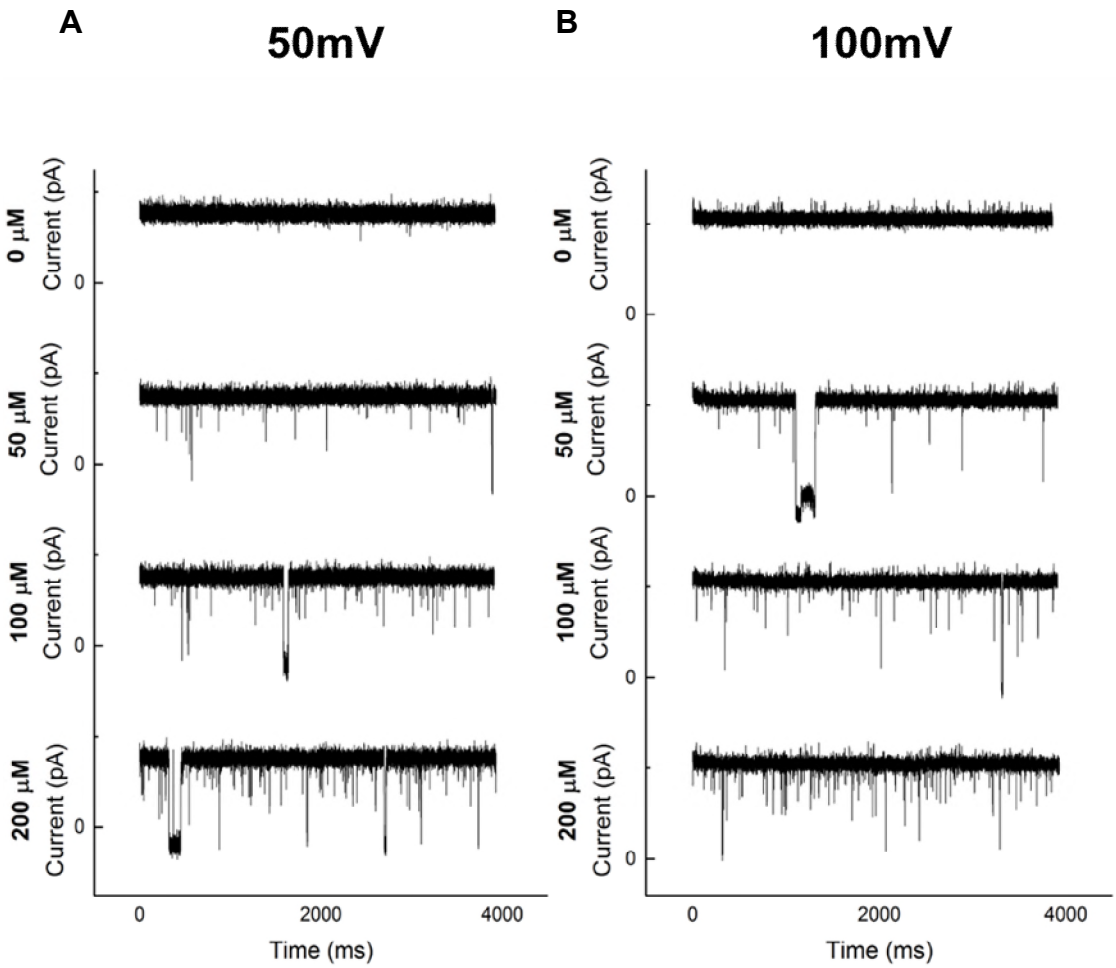

Figure 70 - *Concentration dependence investigation. As the concentration of trypsin is increased, the frequency of translocation events observed is also increased.*

No significant noise or gating was seen in the nanopore traces before protein addition. The frequency of current blockages increased in a linear fashion as the concentration of trypsin solution added was increased, at both 50 mV and 100 mV voltages (Figure 71). The linear increase of frequency of events with protein

concentration confirms that the events are likely due to molecular translocation through the pore.

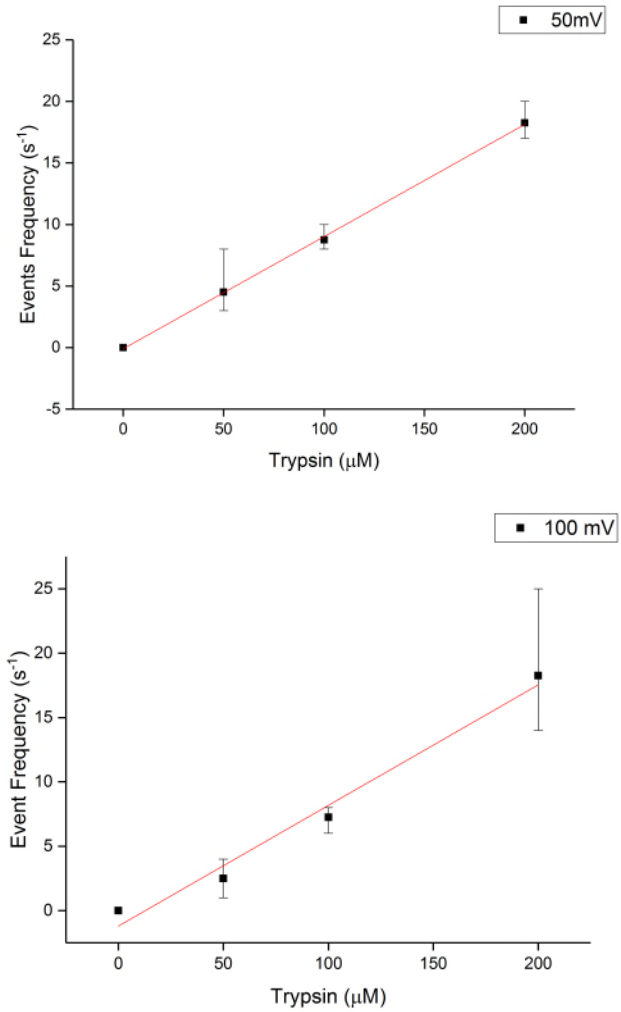

Figure 71 - *Scatter plots showing the relationship between trypsin concentration and event frequency. A linear relationship can be seen from the trend line as concentration of trypsin is increased.*

Traces run with IV protocol 2 showed that translocations were more frequent when a voltage in the positive direction was applied compared to the negative direction (Figure 72). Trypsin's pI is 10.1, so it will have a positive charge in the standard pH 8 electrolyte. Surprisingly, it appears to be more favourable for the positively charged trypsin to travel towards the positively charged trans electrode, which cannot be explained by an electrophoretic effect.

The amplitude of events increased with increased voltage, suggesting that the analytes spend longer in the lumen of the pore when high voltages were applied. Again, this is surprising as it would be expected that electrophoresis would lead to the more rapid movement of the analyte through the pore lumen at high voltages, which does not appear to be the case.

Translocation events of three independent nanopores were collected from three IV traces per nanopore. (Figure 72).

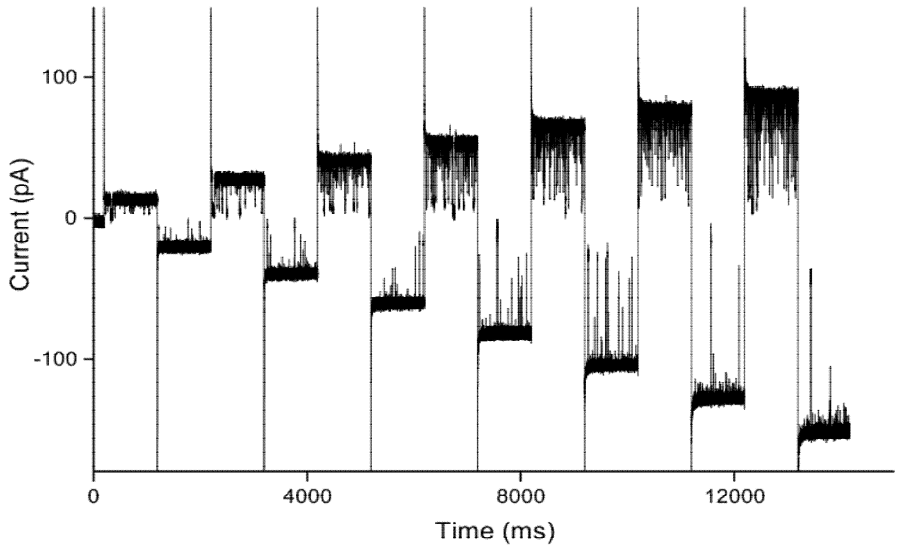

Figure 72 - *Characteristic IV trace after trypsin addition. A greater event frequency is seen when a positive voltage is applied compared to the same magnitude of negative voltage.*

Translocation events were analysed at 100 mV and -100 mV and plotted in Figure 73. The increased frequency of events can be seen clearly in the graph, plotting dwell time against amplitude for both voltages. 212 events were seen over the 9 traces at 100mV, and 19 events at -100mV (Figure 73). A much higher number of events were seen when a positive voltage was applied compared to when a negative voltage was applied. The low pass filtering for the recordings was 3.07 kHz. Therefore, only events over 0.32 ms can be assured to have reached full amplitude. The amplitude of events seen in this time window were between 60% and 90% of the baseline current showing that a large amount of the nanopore's lumen is blocked by the translocating protein.

Protein translocation events were seen in recordings of both nanopores designated as in open and closed states, showing that both states can be potentially used for protein biosensing. The data displayed in this section shows successful transport of a protein using the origami nanopore. However, the results obtained for the translation of trypsin are surprising. A preference for the reverse direction of transport was expected. More experiments need to be conducted with trypsin and experiments with other comparative proteins need to be performed to validate the results collected.

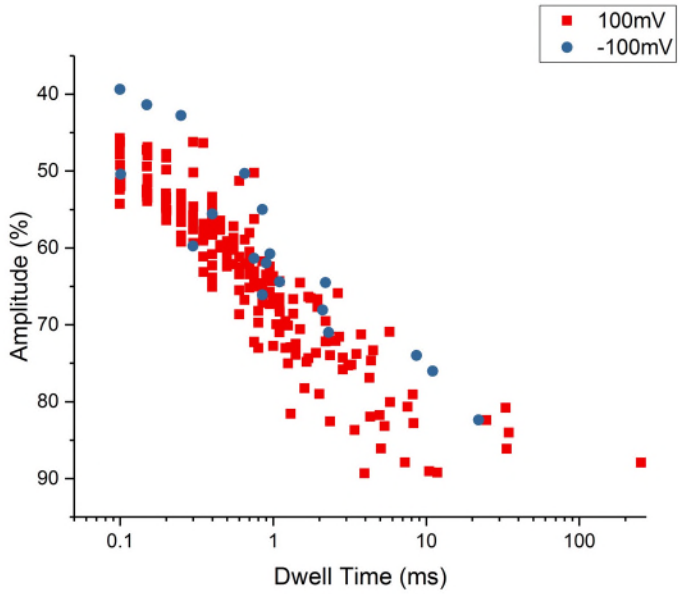

Figure 73 - *Amplitude vs. Dwell Time plot for events seen in 9 IV traces collected from 3 nanopores at +100 mV and -100 mV. Events had amplitudes between 60% and 90% of the baseline current. The majority of events have dwell times between 0 and 10 ms..*

The origami funnel nanopore, although showing gating characteristics, is able to provide more stable and lower noise recordings for protein translocation than has been previously demonstrated in literature for DNA nanopores. [214,222]

2.1.9 Section Conclusion

The aim of this project was to design and build a DNA origami nanopore which could be used for the biosensing of protein biomarkers. The origami nanopore design was shown to successfully translocate a protein biomarker; a key step towards the selective sensing of protein biomarkers.

Two multi-layered DNA origami nanopores were designed: a DNA origami "box" nanopore, and a DNA origami "funnel" nanopore. Protocols to assemble both nanopores from a DNA scaffold strand and a pool of staple strands were found. The origami box nanopore, however, did not assemble effectively after enzyme digestion protocols were used to cut the origami scaffold strand. Therefore, due to the higher fidelity of the design, subsequent experiments were continued solely with the origami funnel.

The folding protocol for the funnel nanopore was further examined and optimised using gel electrophoresis and TEM imaging. The structural characteristics of the funnel nanopores were characterised with AFM and TEM imaging, and showed dimensions consistent with the theoretical dimensions expected for the nanopores.

The funnel nanopores were then successfully functionalised with lipid anchors for association with membranes. The membrane association of the funnel nanopores with small unilamellar vesicles was then demonstrated with gel electrophoresis assays and TEM imaging. Association of the origami funnel nanopores with planar lipid bilayers were then demonstrated using single channel current recording experiments.

The funnel nanopores showed a narrow range of conductance compared to previously published origami nanopores, however, a two-peaked distribution was seen. These two peaks, at 0.9nS and 2.3nS, were designated as nanopores in the "open" or "closed" state when voltage was applied.

An aim of this project was to increase the stability of the DNA origami lumen during nanopore recording experiments by using a multi-layered origami design. The current design was not able to prevent the gating of the negatively charged DNA origami when a voltage was applied, however, recordings collected showed relatively stable characteristics. It was also seen that nanopores were able to successfully translocate and detect the passing of a protein biomarker in both the open and closed state.

However, protein translocation experiments showed translocation characteristics opposite to what would be expected if the translocation of the protein analytes was dominantly controlled by electrophoretic effects. More experiments and control experiments need to be conducted, with a greater range of analytes which have positive, negative and neutral charge in the pH 8.0 buffer, to fully elucidate the mechanism of translocation through the origami pore. It would also be useful to conduct experiments where protein analyte is initially encapsulated in the trans chamber and moved to the cis chamber during single channel current experimentation.

2.1.10 Future Work

Box Nanopore

Experimentation with the box nanopore was halted due to folding errors seen after enzymatic digestion of the scaffold strand. If this design is to be developed further, a better approach would be to use a shorter scaffold strand grown in an in-house laboratory instead of a commercially sourced scaffold strand. This would eliminate the need to digest the scaffold. Lin et al. have shown the formation of origami rings with the p3024 scaffold strand grown in the laboratory.[5]

Funnel Nanopore

The funnel nanopore has shown that it can sense the translocation of a protein biomarker analyte, trypsin. Efflux experiments with the DNA funnel nanopore have recently been carried out by Tim Diederichs of the Tampé group. These have shown that green fluorescence protein (GFP) can also be transported through the funnel nanopore. The GFP was shown also to be selectively transported with respect to the larger rhodomine B. Nanopore recordings with further protein analytes and particularly those of diagnostic significance would demonstrate further the potential of the funnel nanopore for versatile, useful biomarker detection.

To allow the funnel nanopore to selectively detect protein analytes, a molecular receptor (such as a DNA aptamer) needs be added to the pore design. Analytes would then be able to be differentiated from an ensemble mixture by the longer association time of an analyte with the molecular receptor and pore, and therefore the longer, distinctive current blockage.

Further modification to the nanopore design to reduce the proportion of gating events is required. A structure which is more stable to voltage change will allow more reliable detection of analytes.

To adapt a DNA origami nanopore, such as the funnel nanopore, for commercial

use it would be advantageous for the nanopore to be compatible with nanopore sensing devices already on the market. The funnel has been seen to associate with polymer membranes provided by Oxford Nanopore Technologies but no insertion events were seen with the funnel nanopore incubated with a minION device. Adaption of the nanopore design to facilitate insertion into commercially used polymer membranes would expand the biosensing potential of the origami nanopore.

The project described above has shown that nanopores constructed out of DNA are a promising alternative to more traditional nanopore materials, and shows the potential for use of DNA origami nanopores in biosensing devices.

2.2 Small DNA Nanostructure Nanopores

In contrast to the large origami pores (formed of hundreds of DNA strands with thousands of base pairs), this project explores the properties of a DNA nanopore with an extremely simplistic design, consisting of only two DNA strands. The pore is formed of a single ring of duplex, functionalised with lipid anchors to allow the duplex to associate with lipid bilayers. (Figure 74) The use of a single duplex for the formation of a nanopore has been previously demonstrated by Göpfrich et al.[245] This duplex spanned the lipid bilayer in a perpendicular orientation to the bilayer; in the design below the loop of duplex sits parallel to the bilayer.

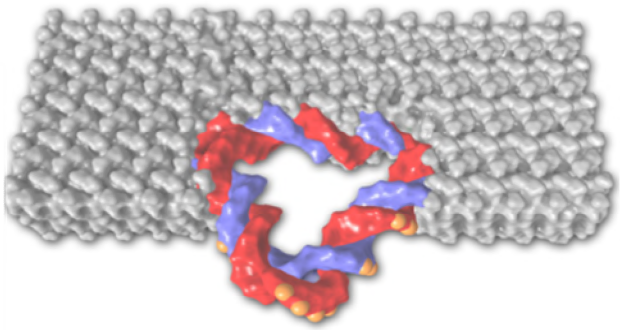

Figure 74 - *Model of triangle nanostructure pore. Orange represents hydrophobic residues for association with the lipid bilayer.*

Two versions of the single duplex DNA pore, labelled "DNA Triangle nanopores", have been worked on, both containing the same sequence. The first, labelled the "PPT Triangle", possesses phosphorothiolate modifications to nucleotides in the structure (labelled in red in Figure 75A). This is similar to the modifications of the six helix bundle nanopore by Howorka et al[212]. The second variation, labelled the "Cholesterol Triangle", uses three cholesterol molecules as lipid anchors in place of the PPT modifications. (Figure 75B) This is similar to a six helix bundle pore published by Howorka et al.[2] The sequence of the triangles was originally designed by Dr Jon Burns.

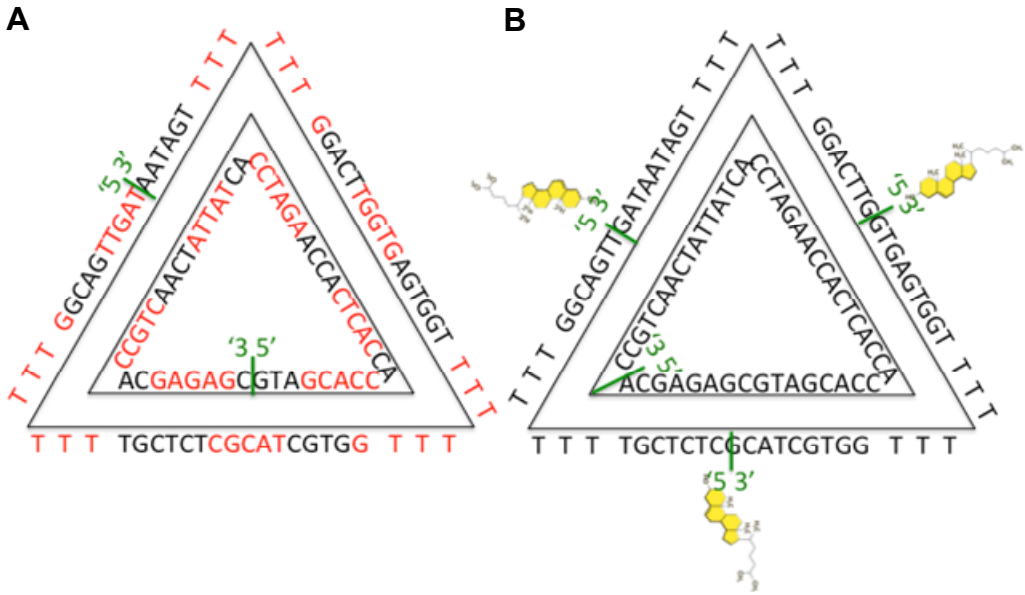

Figure 75 - *A) Sequence design for the "PPT Triangle" - red bases are PPT modified B) Sequence design for the "Cholesterol Triangle" - the 66mer strand is cut at 3 points, cholesterol modifications are added at the 3 prime end of the strands. The nick position of the 48mer is changed so that nicks do not overlap.*

2.2.1 PPT Triangle

The PPT triangle is constructed of two oligonucleotides: a 66 mer, containing 36 phosphorothiolate (PPT) modifications; and a 48 mer, containing 30 PPT modifications (Table 5). PPT modified oligonucleotides are available commercially, with the PPT modified nucleotides incorporated during solid phase synthesis. The thiol moieties can then be reacted with ethyl iodide, via a nucleophilic substation reaction, to produce charged masked alkyl-phosphorothiolates (Figure 76A). The native, negatively-charged oligonucleotide is made more neutral by the addition of the neutral alkyl groups. This provides a hydrophobic region to promote the nanostructure's interaction with a bilayer.

Name	Sequence 5'-> 3' * Indicates phosphorothioate bond	bases	PPT modifications	% modification (2.s.f)
66nt PPT	5- /5Phos/T*A*G* T*T*G ACG G*T*T* T*T*T* T*TG CTC TC*G* C*A*T* CGT GG*T* T*T*T* T*T*T GGT GAG* T*G*G*T*TC AGG* T*T*T* T*T*T* TGA TAA -3	66	36	55
48nt PPT	5- /5Phos/CG*A* G*A*G* CAC* C*G*T* C*AA CTA* T*T*A* T*CA C*C*T* G*A*A CCA C*T*C* A*C*C AC*C* A*C*G*ATG -3	48	30	63

Table 5 *– PPT triangle strands. * indicates a phosphorothioate bond to be reacted with an alkyl group*

Assembly

Native 66 mer and 48 mer strands (1 μM) were quantified and annealed in equimolar conditions, in 12.5 mM $MgCl_2$ 1xTAE buffer using a 48 min protocol. This involved heating to 95°C for 5 min, and cooling at 1°C per 30 sec to 25°C. 10% native PAGE was used to assess the correct assembly of the native triangle (Figure 76B). A single band, at a slower running speed than the 48nt and 66nt strands, was seen in Lane 3. The band sits between the 100 bp and 200 bp marker of the 100 bp DNA ladder. This fits with the theoretical size of the annealed

triangle, which is 114 bp in size. The presence of one band only indicates that only the fully-assembled triangle structure is present in solution, and that the starting concentrations and annealment conditions are correct.

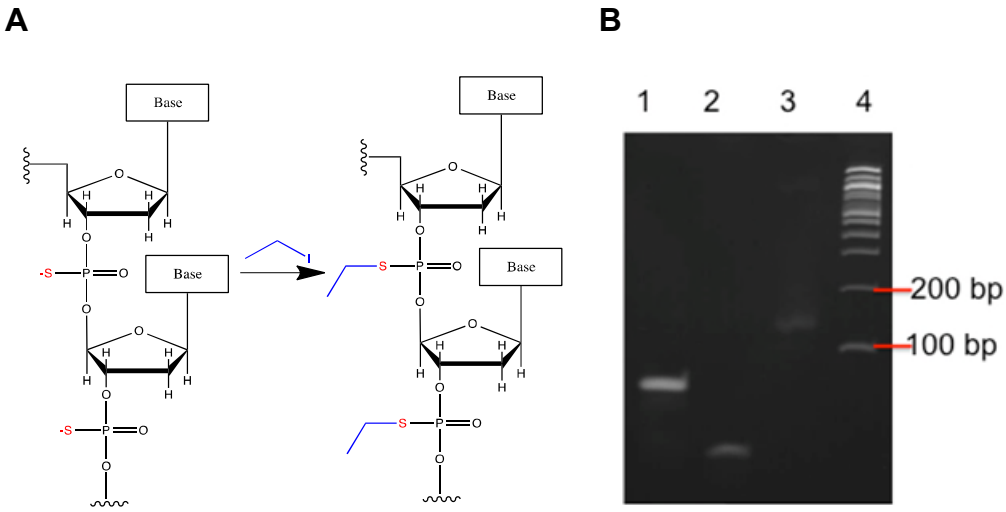

Figure 76 - *A) reaction scheme for ethane capping of the PPT DNA by nucleophilic substitution with iodoethane. B) 10% native PAGE ran for 45 min at 160V. Lane 1 66 nt strand, Lane 2 48 nt strand, Lane 3 native triangle, Lane 4 100 bp ladder.*

Ethyl-Capping

After confirming that the native triangle structure annealed correctly, the PPT modified strands needed to be successfully "ethyl-capped" with ethane, and the ethyl-capped triangle assembled. A protocol for the phosphorothiolate reaction with iodoethane was modified from a protocol by Howorka et al.[212] The protocol was optimised for the 66ntPPT and 48ntPPT strands. Reaction temperature, reaction time, pH and reaction volume were optimised. The reaction extents were monitored using 13% SDS PAGE (Figure 78). The most appropriate reaction conditions were found to be heating at 55ºC for 1hr, in 90%DMF 10% 30mM Tris at pH 8 with constant shaking.

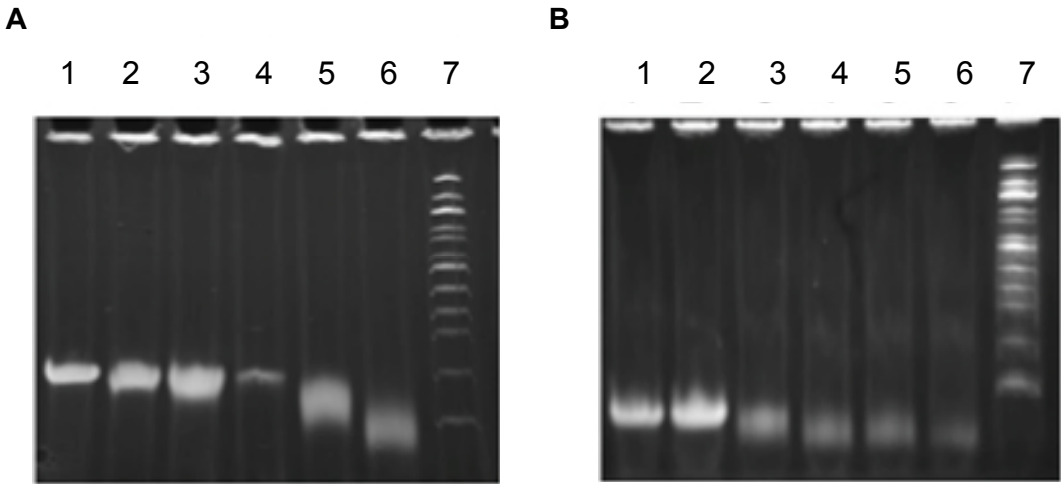

Figure 77 - *13% SDS page gels examples of varying reaction conditions for the 66 and 48 DNA strands. A) 66 PPT strand, lane 1 stock, lane 2 0 min reaction termination by removing solvent under reduced pressure, lane 1 stock, lane 2 0 min, lane 3 15°C 30min, lane 4 15°C 60 min, lane 5 35°C 30 min, lane 6 55°C 30 min, lane 7 100 bp ladder. B) 48 PPT strand, lane 1 stock, lane 2 0 min, lane 3 55°C 30 min, lane 4 55°C 1hr, lane 5 55°C 1hr30min, lane 6 55°C 2hrs, lane 7 100 bp ladder.*

SDS PAGE, instead of native PAGE, provided the best results for visualisation of ethane-containing strands.[212,215] A downwards shift in the SDS gel was seen for both strands after ethane capping. This is consistent with results seen in literature.[212] A second high weight band is seen in the 48PPT ethane lane after reaction (Figure 78, Lane 4). The 48PPT ethane strand contains a higher proportion of ethane-capped residues per strand: 63% of residues in the 48 mer are PPT modified, compared to 55% of residues in the 66PPT strand. The second band in the ethane capped 48 mer lane is most likely a higher order association of hydrophobic regions of the ethane-capped strands in solution.

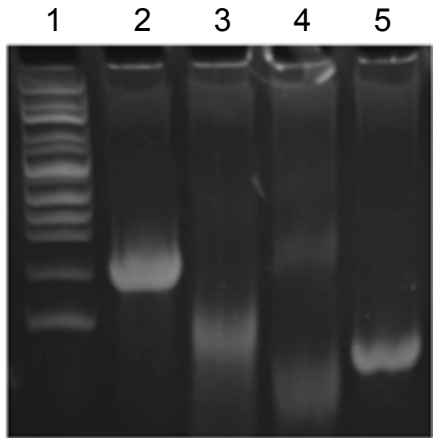

Figure 78 - *13% SDS PAGE Gel showing successful ethane capping of the 66 and 48 strand. Lane 1 100 bp ladder, Lane 2 66ntPPT, Lane 3 66ntPPTethane, Lane 4 48 PPTethane, Lane 5 48 PPT.*

The ethyl capping reaction of the modified PPT triangle was monitored by reverse phase HPLC. (Figure 79) Several solvent combinations and methods were tried. The best results were seen using a 60 min protocol, where the initial buffer gradient at 0 min was 95% 0.1 M TEAA (Triethyl ammonium acetate) buffer/ 5% acetonitrile (ACN). The buffer mixture is slowly moved to 5% 0.1M TEAA/ 95% ACN over 50 min (See Experimental Section). Absorption was monitored at a wavelength of 260 nm.

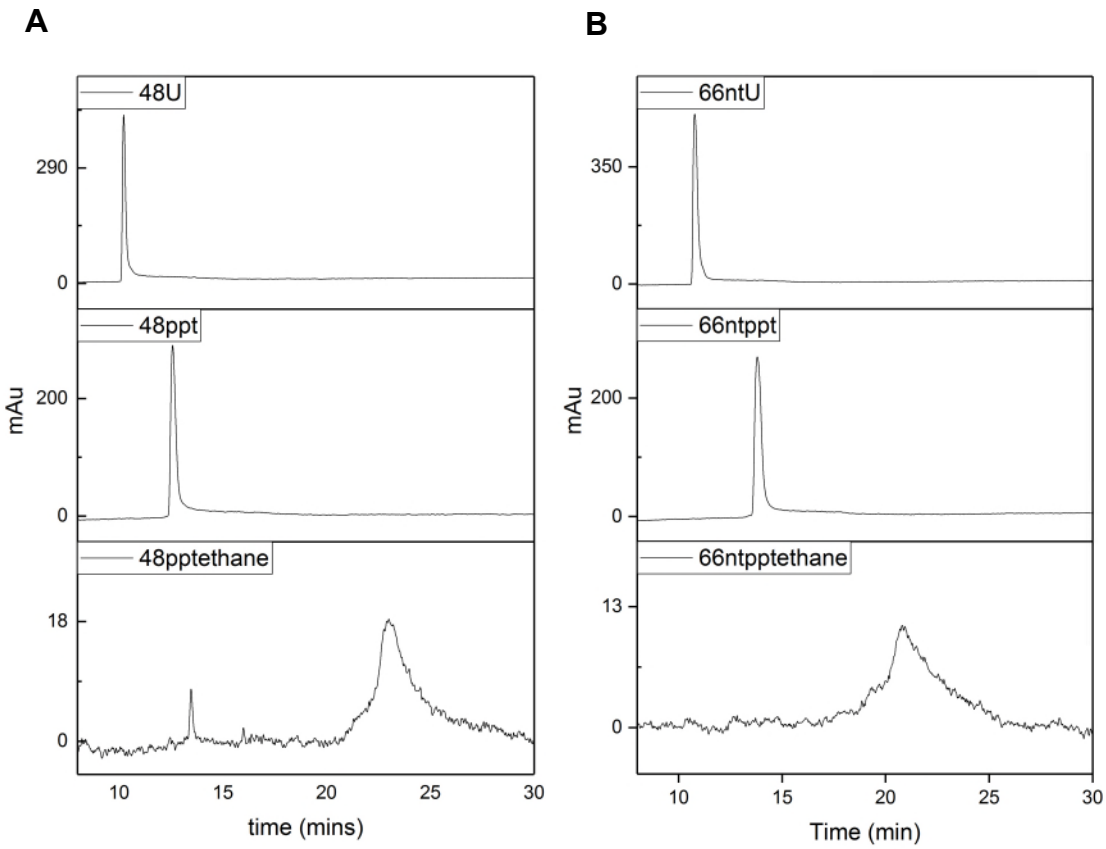

Figure 79 - *HPLC traces comparing the retention time of the DNA strands when native, possessing PPT modification and after ethane capping. An increase in retention time with increasing hydrophobicity of the samples is seen. A) 48nt strand B) 66 nt strand*

The ethane-capped products were expected to associate more strongly with the column, and therefore elute at a later retention time than the native and unreacted PPT strands. By capping a portion of the residues with ethane, the number of negatively-charged residues on the oligos backbone were reduced, and the strand was therefore less polar than its unmodified counterparts. The 48ntU and 66ntU strands showed the lowest retention times, of 10.2 min and 10.7 min. Sulphur is less electronegative than oxygen and, therefore, by replacing the oxygen atom in

the backbone the magnitude of the negative charge on the PPT modified strand's backbone is reduced compared to the native DNA. Therefore, the PPT containing strands show a slight shift to longer retention times, of 12.5 min and 13.7 min. The ethane-capped residues showed a much larger shift in retention time of 23.3 min and 20.7 min for the 66PPTethane and 48PPTethane strands, respectively. The ethane-capped strands show a much lower absorption peak compared to the PPT stock. However, the ethane-capped peaks are much broader. Integrating under the peaks shows a similar total concentration of ethane-capped strand is present compared to the PPT starting material. (Appendix Table 10) The broadness of the peak suggests a range of modification percentages. A small second peak is seen in the ethyl-capped 48 PPT strands spectra at 12.6 min, which corresponds to a small amount of the unreacted 48 PPT strand still present in solution.

Successful ethane capping was further characterised using Mass Spectrometry. (Appendix Figures 99-104) Maldi-Tof was performed on the 66ntU, 66PPT, 66PPTethane, 48U, 48PPT, and 48PPTethane strands. Protocols using HPA, THAP and Sinapinic acid matrices were tried, and both negative and positive modes. The best results were seen using the HPA matrix in negative mode for the unmodified and PPT-containing strands. However, strands capped with ethane, now more neutral, were unable to fly in negative mode. Beck et al.[246] quote successful maldi-Tof of ethane-capped DNA using sinapinic acid in positive mode. This was attempted, but still no significant peaks were detected. The strands used in this experiment are much longer than the maximum 10 bp strands used by Beck et al.

Mass peaks were seen at an average of 20223 ± 123 Da and 14751 ± 81 Da for the 66ntU and 48ntU strands, respectively. These showed a 0.33% and 1.67% percentage difference from the calculated mass values of 19886 Da and 14800 Da. Average mass peak values for the 66PPT and 48PPT strands were found to be 21822 ± 69 Da and 15604 ± 307 Da. These showed a 3.47% and 3.05% percentage difference from the calculated values of 21090 Da and 15141 Da, respectively.

Reacted strands were desalted and purified by NAP-25 column. Fractions containing DNA were re-concentrated under reduced pressure, and quantified by monitoring UV absorption at 260 nm. 48PPTethane (2 μM) and 66PPTethane (2 μM) strands were re-dissolved in 12.5 mM $MgCl_2$ 1xTAE buffer, and annealed using the same 48 min protocol. Assembly was monitored by 13% SDS PAGE (Figure 80). No discrete band was seen in lane 4 for the formation of the PPT ethane triangle, and instead a smear in a section of the lane was seen. DNA objects functionalised with lipid anchors have proven difficult to monitor via PAGE in literature, as the increase in hydrophobic regions affects the running efficiency of the strands[3,215,225]. UV melt analysis was carried out to investigate the triangles' formation. A DNA melt conducted of the PPT triangle prior to capping shows a defined transition, with the first derivative of the melting curve yielding a T_m of 60.7°C (Figure 81A). This indicates that a single DNA object is present.

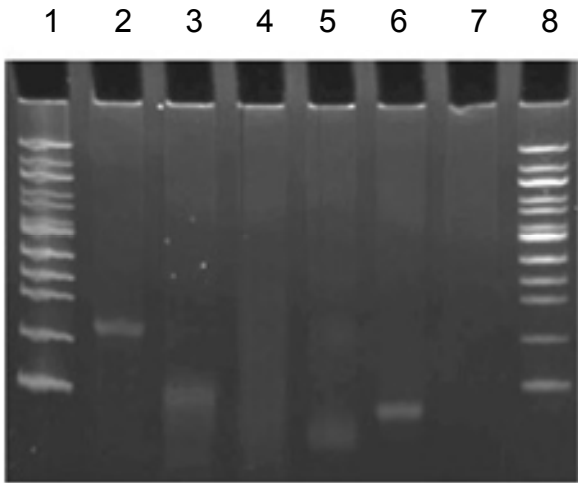

Figure 80 - *13% SDS PAGE gel, comparing the assembled PPT triangle to the unassembled strands. No discrete band was seen for the formation of the PPT triangle. Lane 1/8 100 bp ladder, lane 2 66PPT, lane 3 66PPT ethane, lane 4 assembled PPT triangle, lane 5 48PPTethane, lane 6 48 PPT.*

DNA melting analysis performed for the ethane-capped PPT triangle, with and without the presence of PE PC SUVs (small unimolecular vesicles), showed no defined transitions (n=3). Nanopores possessing ethane-capped PPT residues, assembled by Burns et al., showed greater stability and a higher T_m in the presence of SUVs (as the nanopore was stabilised by the interaction of its hydrophobic belt with the bilayer)[215].

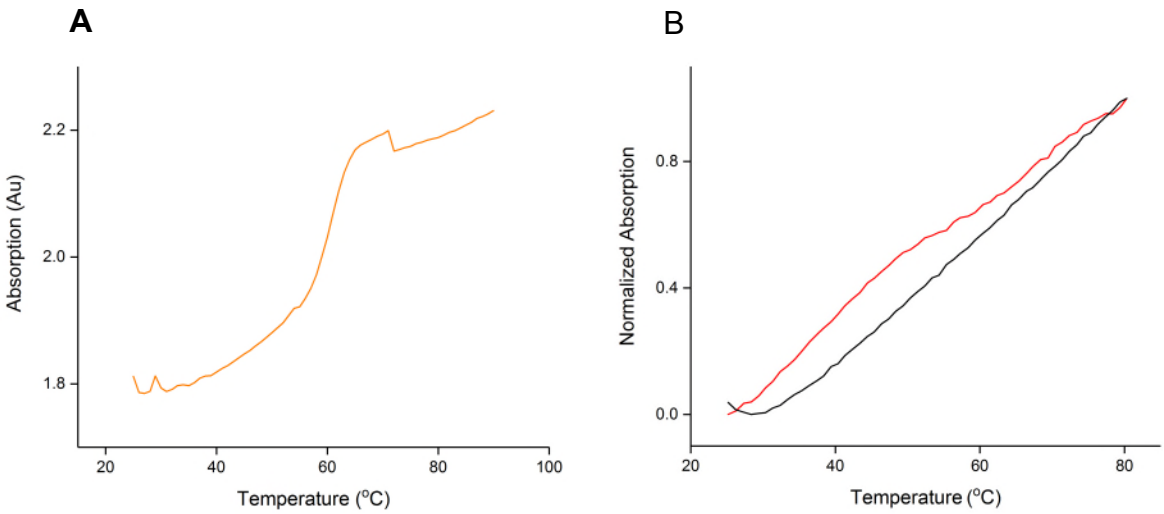

Figure 81 - *DNA melting analysis of the ethane-capped triangle. A) Melting profile of the PPT triangle before ethane modification, showing a melting transition of 60.7°C B) Normalised absorbance curve plotting the 2 curves over each other - no significant difference in the melting with or without vesicles is seen. Red line – without SUV, Black line – with SUV*

No stabilisation effect is seen, and no defined transition is visible for the triangle melted with and without the presence of vesicles (n=3) (Figure 81B). The lack of a defined transition indicates that multiple structures with multiple melting temperatures may be present in solution. A discrete product has not been formed. Due to the difficulty of assembling and quantifying the DNA strands functionalised with ethane, the triangle design was adapted to use cholesterol lipid anchors as an alternative to the PPT-ethane fictionalisations.

2.2.2 Cholesterol Triangle

The cholesterol triangle was formed using the same sequence as the PPT triangle, however, the 66mer strand was split into three shorter oligonucleotides. (Figure 75B, Table 6). This is to allow the addition of cholesterol molecules at the 3 prime end of each of the oligonucleotides. Internal cholesterol modifications are more difficult, and therefore more expensive, to perform by solid phase synthesis. Nick positions, and hence cholesterol molecules, are positioned in the centre of each of the triangle's sides. The nick position of the 48mer was moved to the vertex of the triangle to avoid the overlap of nick positions, which would lead to an opening in the structure. The 48nt strand contains no lipid anchor modifications in this triangle version.

The native version of the triangle, containing no cholesterol strands, was assembled in 12.5 mM $MgCl_2$ 1xTAE buffer with all strands added in equimolar concentrations (5 μM). Samples were annealed using a 48 min protocol. This consists of heating to 95ºC for 5 min, and cooling at 1ºC per 30 sec to 25ºC. Assembly success was monitored with 1.5% agarose gel. Triangle assembly shows a single band, suggesting a single structure is favourably formed. (Figure 82)

Name	Sequence	bases	T_m
48ntU II	/5Phos/CCGTCAACTATTA TCA CCTGAA CCA CTCACC ACCACGATGCGA GAGCA	48	69.5
66nt II Chol. I	/5Phos/TTGACGGTTTTTTTGCTCTCGC/3CholTEG/	22	56.8
66nt II Chol. II	/5Phos/ATCGTGGTTTTTTTGGTGAGTG/3CholTEG/	22	54.1
66nt II Chol. III	/5Phos/GTTCAGGTTTTTTTGATAATAG/3CholTEG/	22	45.6

Table 6 – *Strands for cholesterol triangle. The 66nt strand was split into 3 pieces*

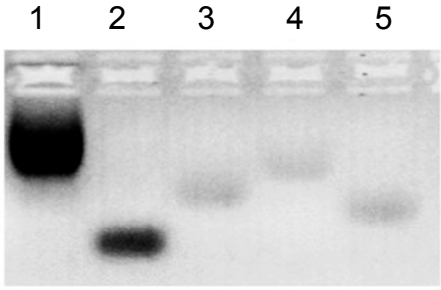

Figure 82 - *Binding study of cholesterol triangle to SUVs. 0.25μM DNA triangle is in each lane, but lipid concentration is varied. Lane 1 0, Lane 2 20μM, Lane 3 35 μM, Lane 4 60μM, Lane 5 100 μM, Lane 6 160 μM, Lane 7 270 μM, Lane 8 450 μM, Lane 9 750 μM.*

The cholesterol version of the triangle, containing cholesterol functionalised strands, was assembled in 12.5 mM $MgCl_2$ 1xTAE buffer with, again, all strands added in equimolar concentrations (5 μM). Samples were annealed using a 48 min protocol, consisting of heating to 95°C for 5 min and cooling at 1°C per 30 sec to 25°C.

Melting Analysis

Assembly of the cholesterol functionalised triangle was analysed using DNA melting analysis. A defined transition was seen with, and without, the presence of vesicles. (Figure 83) The average melting temperature without vesicles was 44.7 ± 4. 1 °C, and with vesicles 47.3 ± 0 °C (n=3). The average melting temperature for the triangle is 2.5°C higher in the presence of vesicles. A much sharper transition can be seen for the triangle after incubation with vesicles. This is consistent with the DNA associating with the membrane, as DNA anchored to surfaces is known to have sharp melting transitions.[247,248] There is an enthalpy gain due to the favourable interaction of the cholesterol modifications with the bilayer, but also an entropy cost as the DNA is tethered to the vesicle and is orientationally restricted.[247] This leads to the sharper melting transition observed. The entropy and enthalpy changes for the nanopore, with and without vesicles, were estimated using the experimental melting curves and the Van't Hoff equation.

The Van't Hoff equation links the change in temperature to the change in the equilibrium constant (K_{eq}). The formula of the equation is:

$$\ln K_{eq} = -\frac{\Delta H}{R\left(\frac{1}{T}\right)} + \frac{\Delta S}{R}$$

Equation 3 *- The Van't Hoff equation*

During a DNA melting experiment the two strands of DNA duplexes become dissociated as the temperature is increased. The aromatic bases of DNA absorb light at 260 nm. When the DNA strands become dissociated the aromatic bases of the duplex unstack allowing the bases to absorb more light. This means that the dissociation of a DNA duplex can be monitored using UV-vis spectroscopy. The fraction of unfolded DNA can be calculated by normalising the absorbance between its highest and lowest value. The equilibrium constant of a DNA melting reaction can be defined as:

$$K_{eq} = \frac{[ssDNA]}{[dsDNA]}$$

Equation 4 *- The equilibrium constant for the dissociation of DNA*

Therefore, the Keq at different temperatures can be calculated using a DNA melting experiment.

Plotting of a Van't Hoff plot, where ln Keq is plotted against 1/T, allows the determination of the entropy change (ΔS) and the enthalpy change (ΔH) of the reaction from the intercept and gradient of the plot respectively.

Without vesicles, enthalpy and entropy change values were calculated to be -487 ± 133 kJ/mol and -1412.3 ± 416 J/mol/K, and with vesicles values were -1463 ± 1018 kJ/mol and -4438 ± 3177 J/mol/K. There are significant increases in the estimated values for both the enthalpy and entropy when the triangle is melted in the presence of vesicles, supporting the triangle's association.

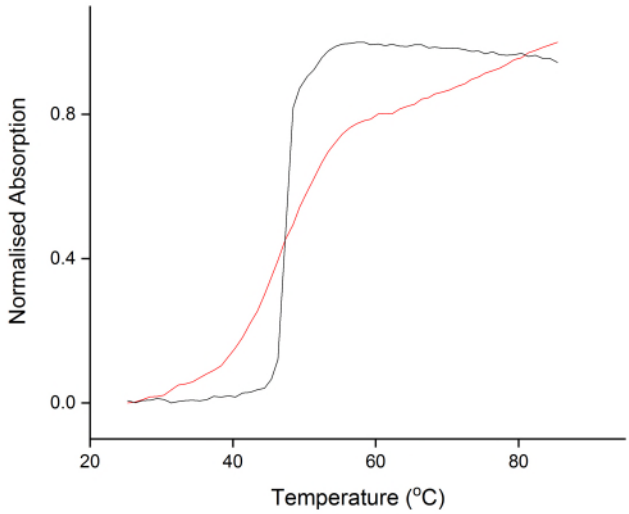

Figure 83 - *Normalised melting profiles for the cholesterol triangle with and without SUVs. Red line – without SUV, Black line – with SUV*

A preliminary binding study of the pore to PE PC 0.3:0.7 SUVs (small, unilamellar vesicles) were performed, using 2% agarose gel to characterise. The annealed cholesterol triangle was added to the wells in the presence of varying concentrations of SUVs, and run at 40 V for 2 hrs. (Figure 84) As the concentration of lipid is increased from 20 µM to 750 µM the presence of the 0.25 µM DNA band is reduced, as higher proportions of the nanopores become associated with the vesicles.

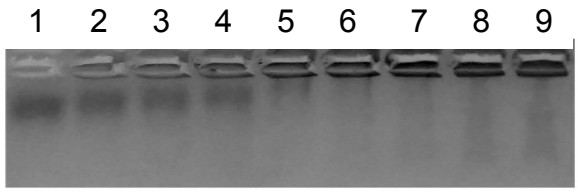

Figure 84 - *Binding study of cholesterol triangle to SUVs. 0.25µM DNA triangle is in each lane, but lipid concentration is varied. Lane 1 0, Lane 2 20µM, Lane 3 35 µM, Lane 4 60µM, Lane 5 100 µM, Lane 6 160 µM, Lane 7 270 µM, Lane 8 450 µM, Lane 9 750 µM.*

The results so far support an association of the nanopore with the bilayer, but not necessarily its insertion. Some fluorophore release studies were conducted with Carboxyfluorosene (CF) and Sulphur rhodamine B (SRB)[2], with the help of Dr Jon Burns. PE PC SUVs were formed in the presence of the fluorophores, and then purified by Nap-25 column to remove un-encapsulated fluorophore. After an equilibrium period of three hours, different concentrations of cholesterol triangle

nanostructure were combined with the vesicles' solutions. Both fluorophores are self-quenched at high concentrations. Insertion of pores into the vesicles allows the fluorophore to be released through the pore. The fluorophore released into solution emits a stronger fluorescence signal, as the dye is no longer self-quenched.

It would be expected that a proportional relationship should be seen between an increase in nanopore concentration and the increase in fluorescence. However, the nanopores' anchors are cholesterol molecules. Cholesterol can increase the rigidity of a bilayer and increases its capacity to sustain "severe shear stress"[249]. Therefore, adding increasing amounts of cholesterol can stabilise the vesicles against rupturing. This opposing effect influences the results collected.

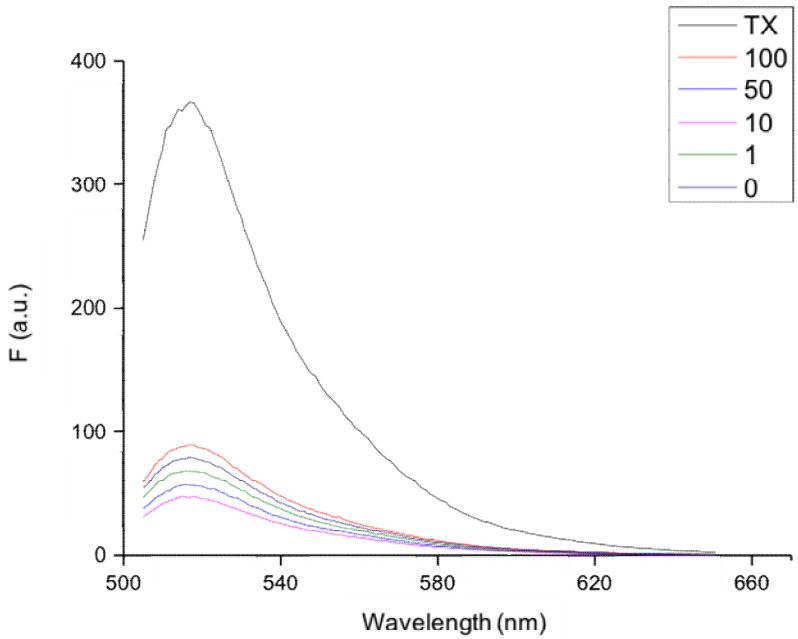

Figure 85 - *CF release study, quantities of 5μM DNA nanopore were varied from 1-100 μL in a 400 μL solution. TX indicates popping of the vesicle with Triton-X detergent*

The results for CF showed a reduction in fluorescence emission at 520 nm with small amounts of nanopore. This can be explained by the stabilisation of the vesicles by the cholesterol anchors. However, an increase in emission was seen after a threshold concentration of nanopore was passed. (100 μL 5 μM Cholesterol triangle) (Figure 86). The maximum emission was shown by bursting the vesicles with Triton-X detergent (labelled TX in figure 86 & 87).

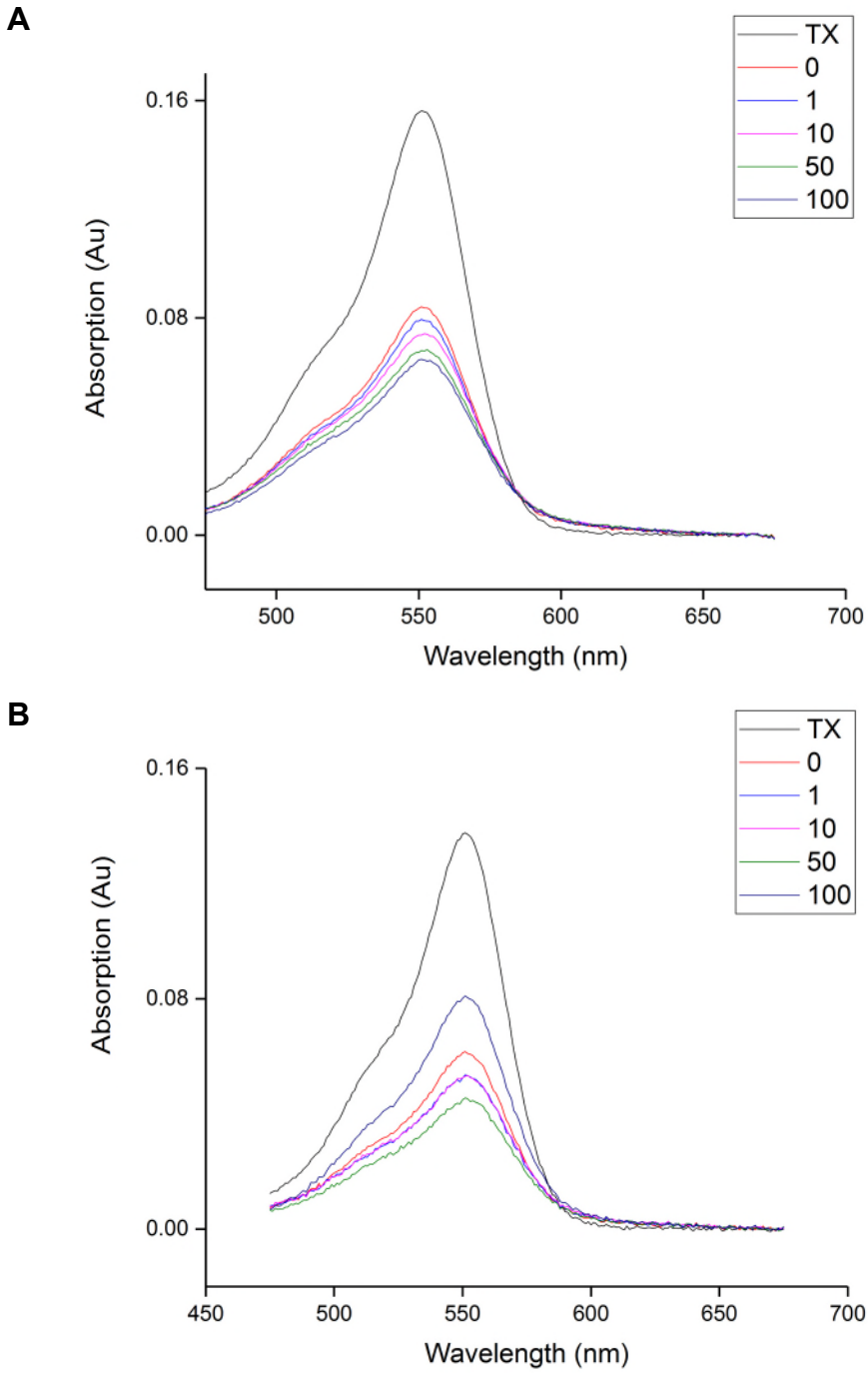

Figure 86 – *SBR release study, quantities of 5 µM DNA nanopore were varied from 1-100 µL in a 400 µL solution. TX indicates popping of the vesicle with Triton-X detergent. A) SRB release study with DNA triangle B) SRB release study with control strands.*

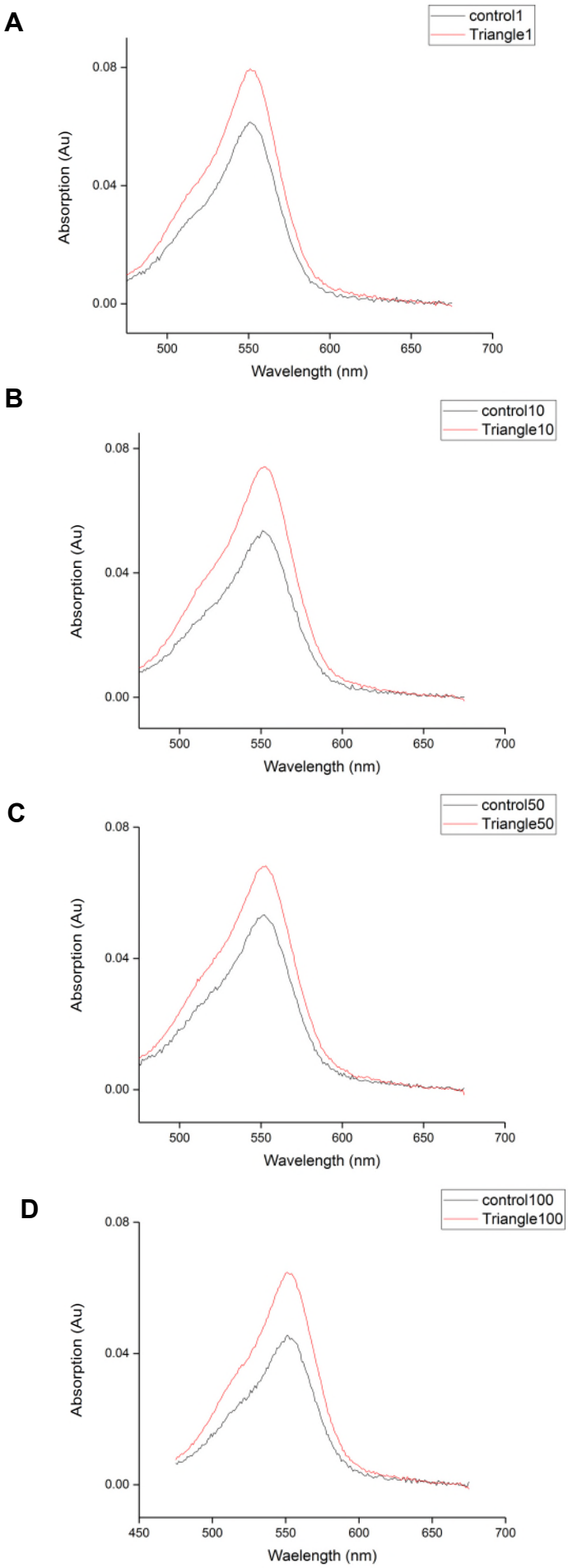

Figure 87 - *Comparison of absorption peak at 560nm for samples incubated with equal concentrations of cholesterol triangle and control strands. A) 1μL B) 10 μL C) 50 μL D) 100 μL*

For the study with the SRB different results were seen; UV absorption at 565nm was reduced consistently with increased nanopore concentration. (Figure 86) A control was run using the three cholesterol modified strands in solution; as the complementary 48mer was not present the cholesterol triangle is unable to form. The same effect was seen - a reduction in absorption signal with increasing strand concentration. However, when comparing control strands of the same concentration to the formed triangle, a larger absorption was seen (Figure 87). This suggests that although there is a stabilisation effect due to pore insertion, dye is still being released more readily in the presence of the nanopore compared to control strands. This suggests that some fluorophore is being released through the inserted nanopore, or the nanopore at least leads to a degree of disruption of the membrane.

Nanopore recordings with the cholesterol triangle did not lead to distinctive current steps, although destabilisation of the lipid bilayer was seen after addition of the triangle to the cis chamber of the Orbit 16 (Figure 88). This suggests that the triangle associates with, and disrupts, the lipid bilayer but does not lead to the formation of a stable, membrane-spanning nanopore.

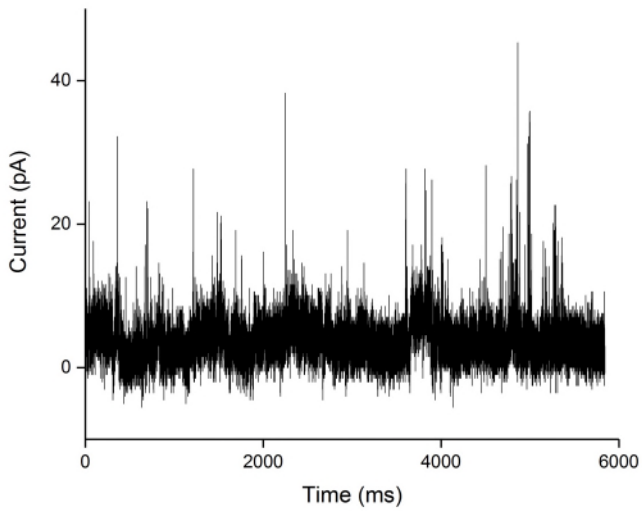

Figure 88 - *Current trace shows the destabilisation of the membrane by the addition of the cholesterol triangle to the cis side of the bilayer.*

AFM imaging was performed of the cholesterol DNA triangle structure associated with a lipid bilayer (PE:PC:Chol 1:1:1 molar ratio) (Figure 89 – AFM operated by Dr Alice Pyne). The AFM imaging showed structures with a width of 4-5 nm as expected, and a height approximately 2.5nm above the membrane. Given the idealised height of the B-DNA duplex is 2.5 nm, this suggests the DNA duplex sits above the membrane, instead of forming a membrane-spanning nanopore. The duplex's cholesterol anchors, however, must disrupt the lipid bilayer membrane, which led to the release of dye in the release experiments and the membrane disruption in single channel current recordings. The structures also do not appear triangular in the AFM images. Membrane pressure likely deforms the flexible, single duplex triangle when it is associated with the bilayer. Additionally, the resolution of the small sized DNA objects above the bilayer in the AFM images is not good, so it is difficult to fully elucidate the shape of the structures present. More AFM images need to be collected to confirm the positioning of the DNA structures in the membrane.

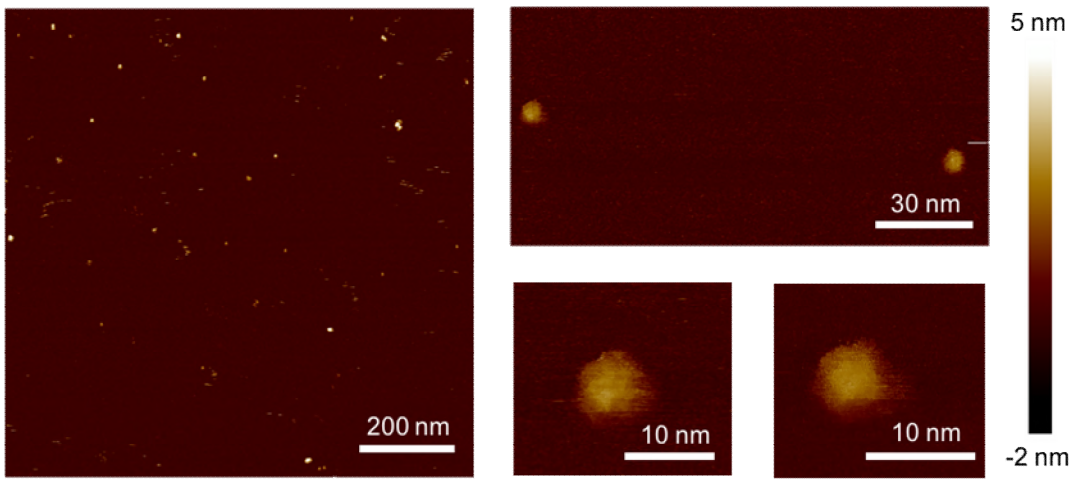

Figure 89 - *AFM imaging of triangle nanostructure nanopore performed by Dr Alice Pyne. Structures were seen with widths of 4-5 nm and heights of approx. 2.5 nm*

2.2.3 Section Conclusion

The findings of this project indicate that the DNA duplex triangle produced in this project did associate with lipid bilayers but did not span the planar lipid bilayers in a fashion which would allow stable channel recordings and the detection of analytes. The formation of a single PPT triangle product was shown successfully. The 48mer and 66mer strands that made up the single duplex nanopore were then shown to be successfully ethane capped by reacting the strands with iodoethane. The formation of the PPT-ethane triangle however proved difficult to characterise, due to the hydrophobicity of the strands and likely aggregation this caused. No single structure could be imaged using gel electrophoresis and no significant melting transition was seen when the PPT-ethane triangle was incubated with SUVs, suggesting that a single duplex structure was not formed.

The triangle nanopore was then functionalised with cholesterol lipid anchors as an alternative. The reduction in anchor number meant that the triangle could be characterised more successfully. Gel electrophoresis experiments and DNA melting profiles showed stabilisation of the triangle structure when it was in association with SUVs. Dye release experiments suggested that the cholesterol triangle led to release of dye from vesicles and potential insertion of the duplex into the bilayer. However, single channel current recordings did not lead to stable insertion steps, and AFM imaging showed a duplex height indicating that the triangle nanopore sat on top of the bilayer instead of inserting into the bilayer to form a stable pore.

2.2.4 Future Work

The results for the cholesterol triangle indicate that it does not span the lipid bilayer. Experimental techniques such as the addition of some detergent or using different lipid compositions could potentially be tried to stimulate the DNA pore to span the bilayer.

The cholesterol anchors are attached to the DNA backbone via an 18 atom TEG linker. It is possible therefore that the cholesterol triangle nanopore may arrange itself so that the cholesterol anchors are embedded in the bilayer, but with the DNA duplex associated with the hydrophilic lipid heads of the bilayer instead of spanning the bilayer. Functionalisation of the triangle with cholesterol strands with a non-standard, shorter linker may lead to better bilayer spanning characteristics.

Alternatively, the PPT-ethyl capped reaction leads to direct ethyl functionalisation of the DNA backbone. The PPT-ethyl triangle may have better lipid bilayer spanning characteristics if the aggregation and experimental difficulty of using the ethyl capped strands can be improved. Reducing and optimising the number of ethyl capped residues could lead to better results.

2.3 DNA Origami Ring

During a placement in the group of Professor Chenxiang Lin at Yale a project was conducted involving the adaption of DNA origami rings[5], designed and previously published by the group for use as an origami nanopore. In the original publication by Yang et al. single stranded "handle" sticky ends hybridised with DNA "anti-handles" were chemically conjugated to DOPE (1,2-Dioleoyl-sn-glycero-3-phosphoethanolamine). These handles were then used as nucleation points to grow unilamellar vesicles of a specific, sub-100 nm templated size. It was hypothesised that by using anti-handles chemically conjugated with cholesterol, the origami could be adapted for use in a nanopore sensing set up.

2.3.1 Origami Ring Assembly

Two ring structures were investigated - a 46 nm diameter ring, and a 29 nm diameter pore. (Figure 90) Both rings were composed of a continuous loop of six helices of DNA in a honeycomb arrangement. Several versions of the 46 nm ring were assembled. Different versions varied the position of handles, which hybridised to cholesterol anti-handles, around the helix bundle. Rings were assembled with handles at helix 0 (H0) extending out of the ring, helix 3 (H3) extending into the rings, and helix 4 (H4) at a 45° angle from the plane of the ring. (Figure 91) Each ring possessed 12 handles, and therefore 12 cholesterol lipid anchors after hybridisation with the anti-handles. 46 nm rings with multiple handles, and therefore a greater proportion of lipid anchors, were also investigated. These rings were assembled with 36 lipid anchors each.

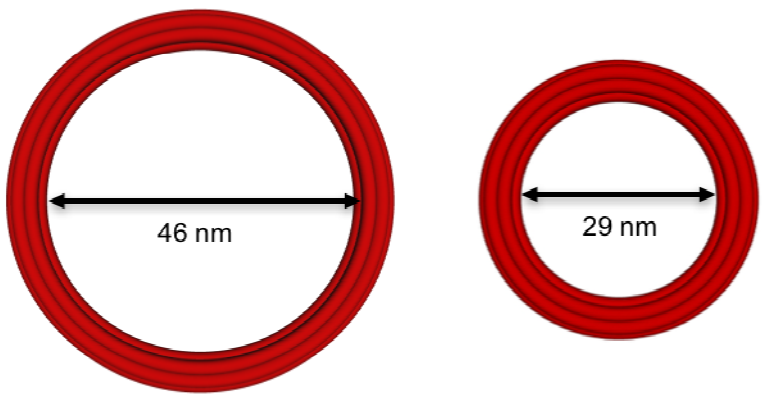

Figure 90 - *Two ring sizes were investigated, a 46 nm diameter ring and a 29 nm diameter ring. Each ring was a continuous loop of six helices.*

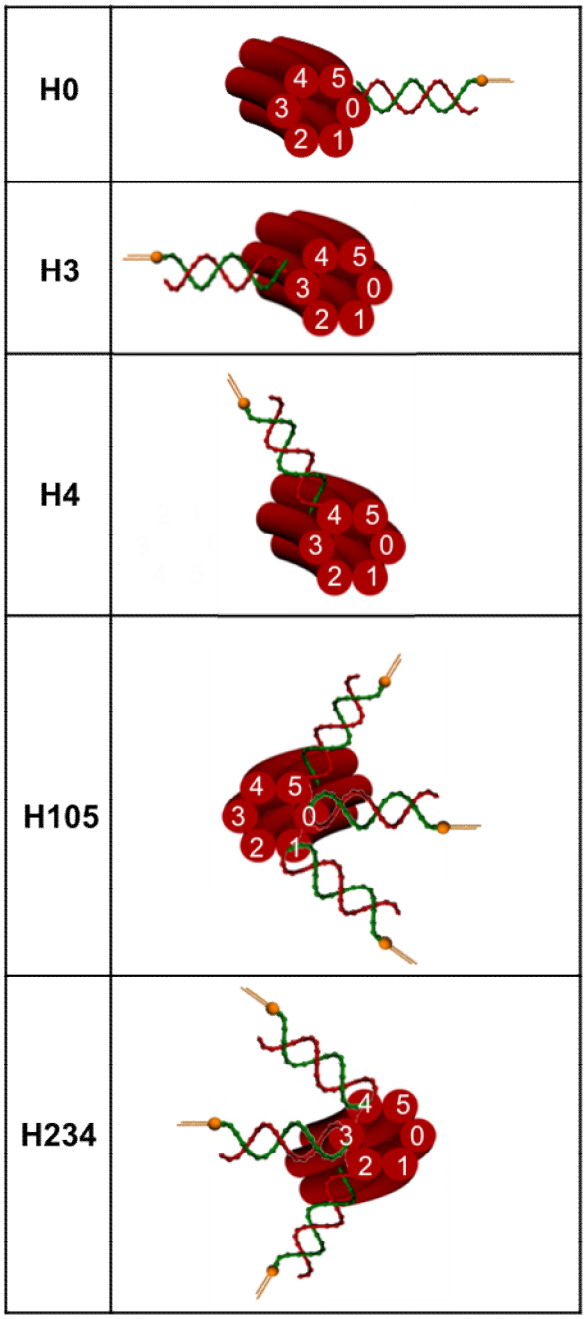

Figure 91 - *The rings helices are labelled 0 to 6. Helix 0 sits on the outside of the ring in the plane of the ring. Helix 3 sits in the plane of the ring on the inside of the ring. 5 46 nm ring variations were looked at with lipid anchors on: H0, H3, H4, H1,0,5. and H2,3,4*

The 46 nm origami rings were assembled from a 3024 nt scaffold strand (50 nM), and a pool of staple strands (300 nM) in a 5 mM Tris–HCl, 1 mM EDTA and 10 mM $MgCl_2$, pH 8 buffer using a two hour magic fold protocol. The correct origami ring structures were separated from staples and multimeric structures by a "rate-zonal centrifugation" protocol, developed and published by the Lin group.[250] Folded origami was added to the top of a centrifuge tube containing a pre-prepared 15%-45% glycerol gradient in 5 mM Tris–HCl, 1 mM EDTA, 10 mM $MgCl_2$

buffer, and centrifuged at 50 000 rpm for three hours at 4°C. 24 equal volume fractions were collected from the top to the bottom of the centrifuge tube, and aliquots were run on a 1.5% agarose gel for 90 min at 60V. (Figure 92) Fractions containing the monomer origami ring were combined and reconstituted in 5 mM Tris–HCl, 1 mM EDTA 10 mM $MgCl_2$ buffer, using spin filtration to a concentration of 5 nM, and examined using TEM analysis. (Figure 94 A&B)

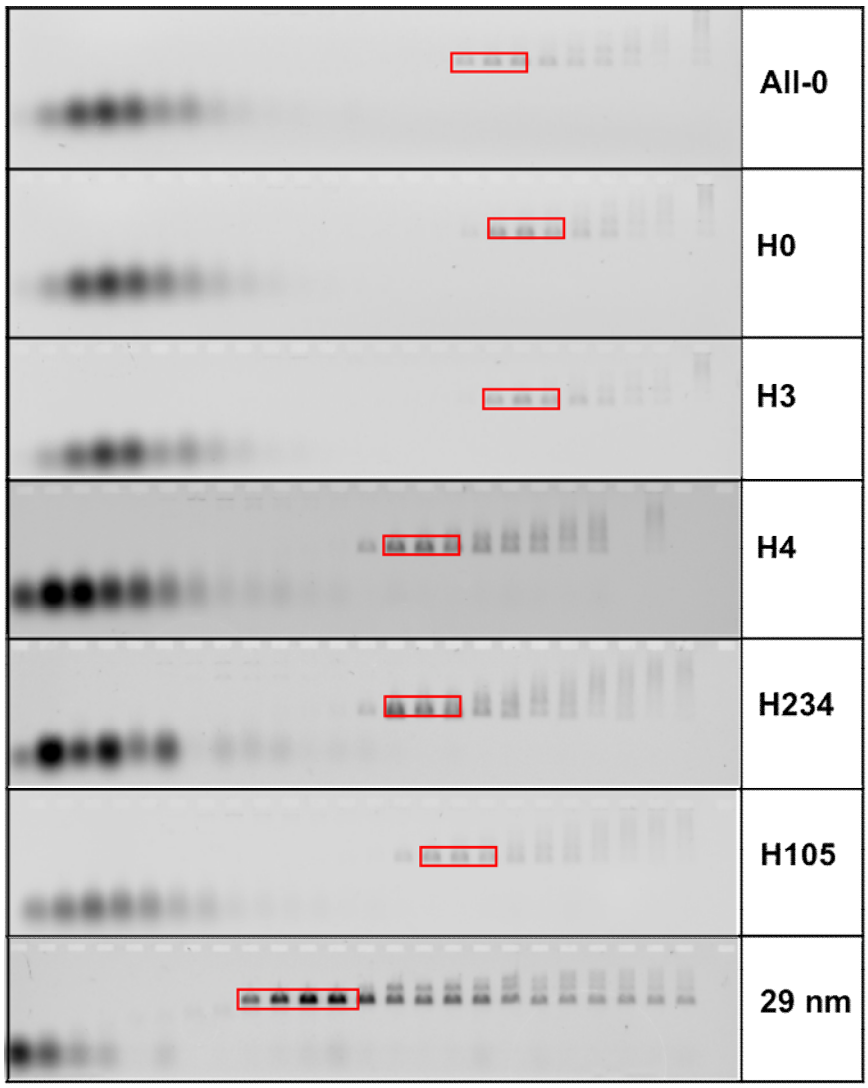

Figure 92 - *1.5% agarose gel run at 60 V for 90 min. 24 fractions were collected from rate-zonal centrifugation protocol and aliquots run on the agarose gel. The lightest structures are seen in earlier fractions. Fractions containing the monomer (lighter than aggregates, heavier than excess staple strands) were combined and purified.*

The origami rings were incubated for an hour at 37°C, with 1.5x to 3x equivalents of cholesterol anti-handles. The binding characteristics of the anti-handles were examined using 1.5% agarose gel electrophoresis. (Figure 93) Little difference was seen in the gel bands produced with either of the levels of equivalents. 1.5x equivalents was chosen to be used in subsequent experiments to minimise aggregation of samples over time. Adding 0.05% SDS to the agarose gel changed the resolution of the bands seen in the agarose gels, however, it did not reduce the band streaking seen for every structure. The streaking was increased with SDS addition for the 29 nm ring.

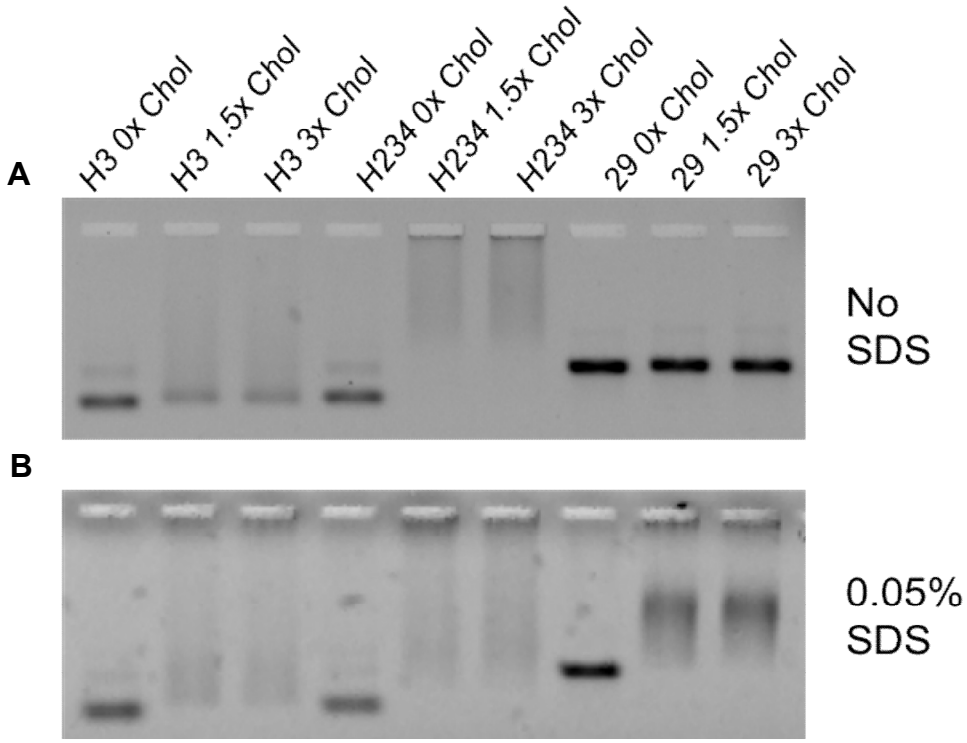

Figure 93 - *1.5% agarose gel. Run at 60V for 90min. The cholesterol handle attachment and ratio was investigated for H3, H234, and the 29nm rings. A) No SDS in gel B) 0.05% SDS in gel and run buffer.*

The structural integrity of the rings, with and without the attachment of the cholesterol functionalised anti-handles, was examined using TEM analysis. (Figure 92) Well-formed ring structures were seen, with a few rings interlinking or twisting on the TEM grid. Cholesterol functionalised rings showed no significant structural differences under TEM compared to the cholesterol free rings.

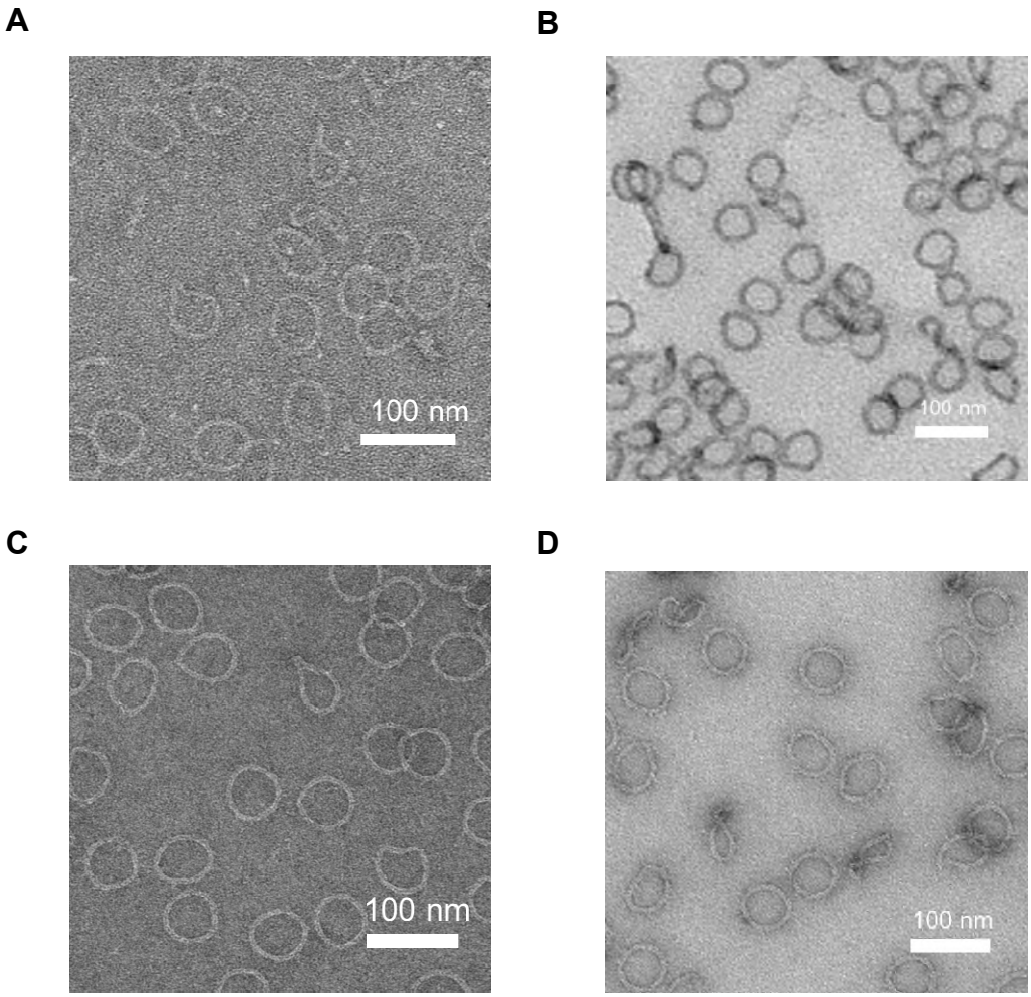

Figure 94 - *TEM images of origami rings in regions of both positive and negative staining. No difference in ring fidelity was seen before and after cholesterol handle addition A) H3 with no cholesterol, B) H234 with no cholesterol, C) H0 with 1.5x cholesterol D) H105 with 1.5x cholesterol.*

Rings with cholesterol anti-handles hybridised to the structures (5 nM) were then incubated with 50 nM of liposomes at 35ºC for two hours. Binding of the rings to the liposomes was examined with TEM imaging. All versions of the 46 nm rings with 12 anchors could be visualised associated to area of liposome, confirming binding. For 46 nm rings with 36 lipid anchors, at the same concentration of liposome, large aggregates of lipid and DNA were formed. This is likely due to the larger hydrophobicity of the origami structures, with a larger number of anchors. (Figure 95)

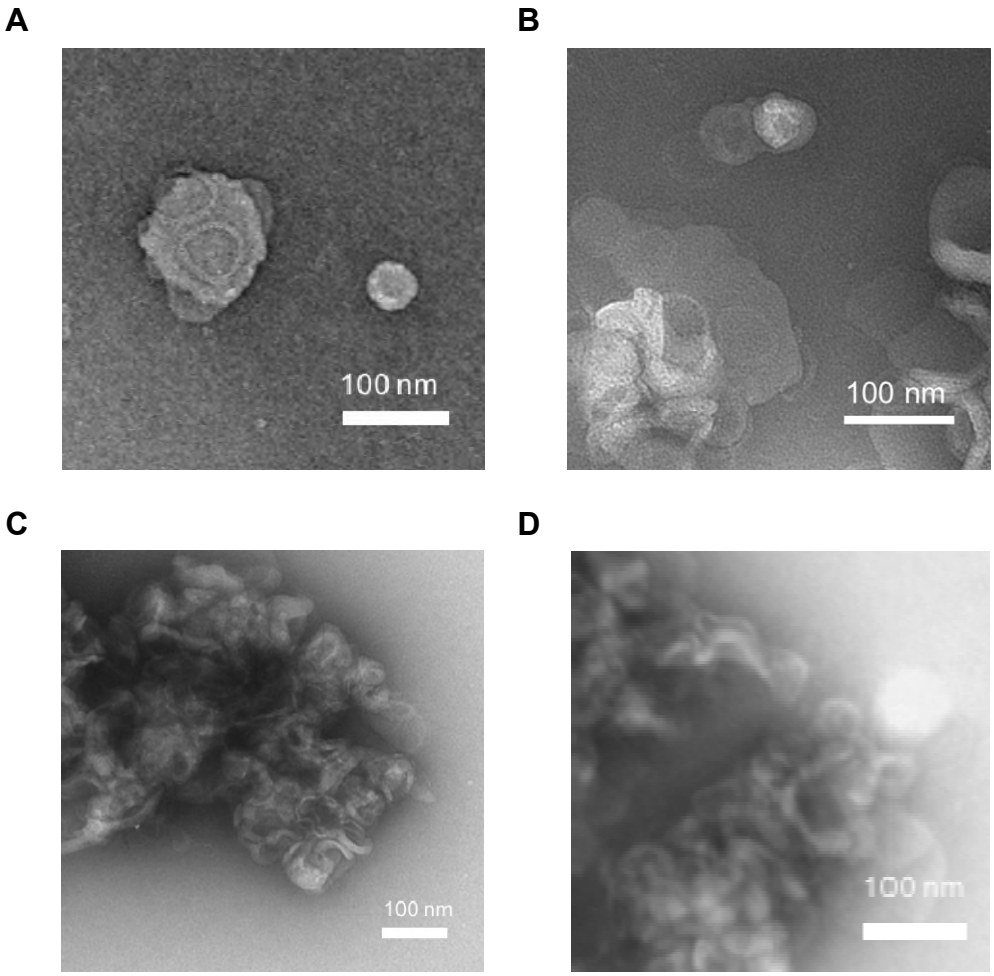

Figure 95 - *5 nM Rings with either 12 or 36 cholesterol anti-handles were incubated with 50 nM of liposomes and then imaged with TEM. A) H0, B) H3, C) H235, D) H105. Structures with more cholesterol anti-handles lead to increased aggregation.*

The 29 nm ring (Figure 96) was assembled and purified using the same protocols as the 46 nm ring. The 29 nm ring possessed 16 handles and, therefore, 16 corresponding cholesterol functionalised anti-handles, which sat inside the ring in the plane of the ring. The rings formed well with few defects seen in the TEM images. No structural changes were seen when the cholesterol anti-handles were added to the rings. TEM imaging also confirmed association of the ring structures with liposomes for the 29 nm ring. (Figure 96C)

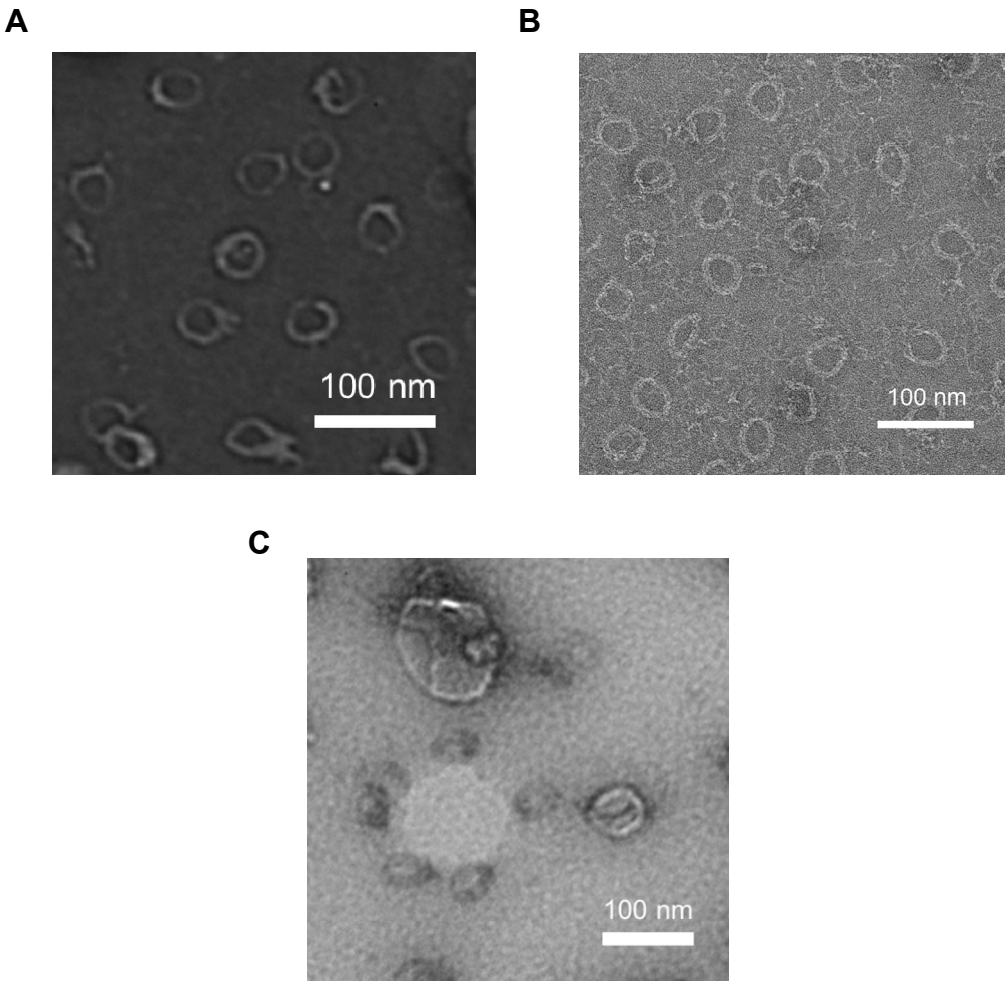

Figure 96 - *TEM images of the 29nm ring. A) ring with no cholesterol, B) ring with 1.5x cholesterol C) cholesterol ring incubated with liposomes.*

2.3.2 Origami Ring Nanopore Recordings

Nanopore recordings for the origami ring were conducted with the use of a portable "MiniOrbit" device from Nanion Technologies. This set uses a 4 channel MECA (multi-electrode-cavity-array) chip and is much smaller compared to the Orbit-16 device. 150 µL of a standard electrolyte solution of 1 M KCl and 10 mM HEPES, pH 8.0 was added to, and stimulated to enter, the channels using a "micro-plunger". DPhPC lipid membranes were manually painted over the four channels of the MECA chip. Successful membrane formation was seen by the reduction of the current passage to 0 pA when a ± 5 pA protocol was applied. A 1.22 kHz sampling rate was used.

A set of five protocols were applied sequentially to systematically examine and optimise the insertion of the origami rings into the bilayer (Table 7). Protocols were first run with the ring only, and subsequently with a 2:1 (ring: 0.5% OPEO) mix. Control experiments showed no insertion as expected. Potential insertion events were only seen with the H0 46 nm ring. The H0 ring had handles which were positioned on the outer helix of the ring, in the ring's plane.

Protocol Number	*Protocol*	*Time (min)*	*Sample Addition (uL)*
1	30 mV Hold	30	8
2	50 mV Hold	30	8
3	100 mV Hold	30	8
4	IV Protocol	30	8
5	Voltage Ramp	30	8

Table 7 - *Protocols applied sequentially to stimulate and characterise the insertion of rings into the bilayer.*

For all experiments a very low insertion rate was seen. Approximately one event every two hours was seen for active samples; this is likely due to the x4 reduction in channel number compared to the orbit 16 equipment and therefore the lower chance of insertion events occurring. With the orbit-mini, membranes are also manually painted instead of spread automatically by a magnetic stirrer bar which can lead to variation in the thickness and viability of the membrane compared to

the automatically spread bilayer. Figure 97 shows two insertion steps in the painted Dphpc bilayer. Insertion events occurred when the voltage was held at +50mV. After a first insertion step it became more favourable to have multiple additional pore insertion steps. The disruption by the insertion of one pore likely leads to the exposure of defect points in the bilayer which additional DNA structure can associate with. The insertion steps in Figure 97 led to current increases of 34.6 pA and 36.8 pA; this corresponded to conductances of 0.69 nS and 0.74 nS respectively. The current reduction spikes seen are likely due to the passage of excess staple strands through the perforation caused in the membrane.

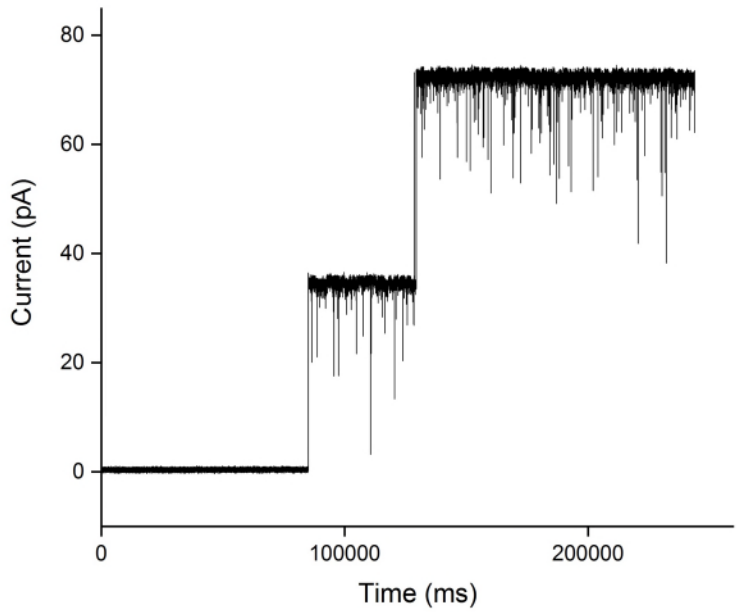

Figure 97 - *Single channel current characterisation for the H0 ring. Current insertion steps were observed during hold protocols (50 mV)*

Figure 98 shows the characteristics observed when an IV protocol and a voltage ramp protocol were applied after a successful insertion event. The IV protocol applied to the nanopore in Figure 98A was: 0 mV (1 sec), ± 20 mV (1 sec), ± 40 mV (1 sec), ±60 mV (1 sec), ±80 mV (1 sec), ± 100 mV (1 sec), ± 120 mV (1 sec), (V_{fp}=20, V_{step}=20 T_{pu}=1, T_{pe}=12, N=6)

The voltage ramp protocol applied to the pore in Figure 98B was: -100 mV to +100 mV, with a 0.8 mV voltage step every 20 ms. (V_{fp}=-100, V_{step}=0.8 T_{pu}=0.02 V_{max}=100).

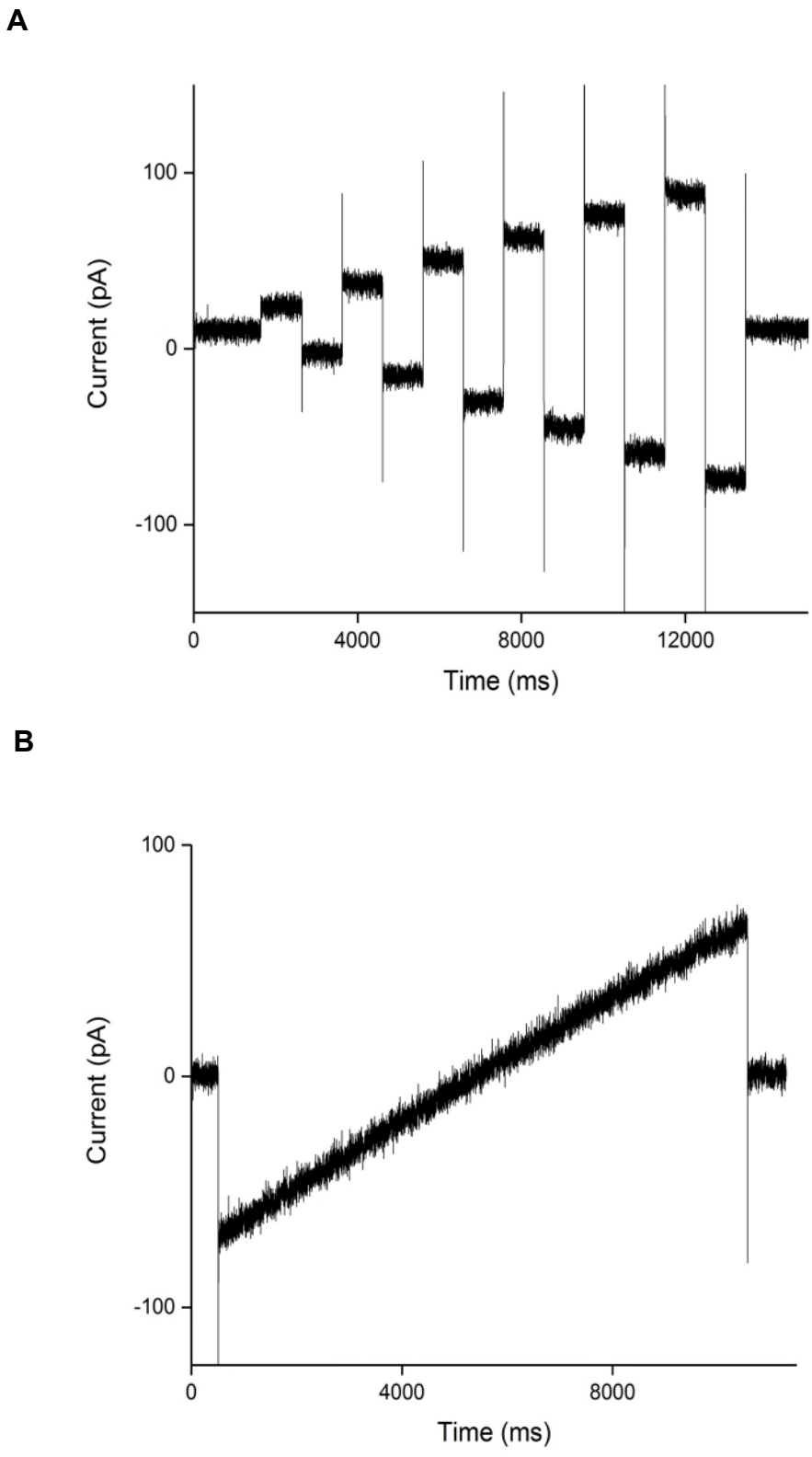

Figure 98 - *A) IV curves showed little gating, B) Voltage ramp showed ohmic characteristics.*

The insertion events seen had ohmic behaviour and did not appear to show any gating characteristics at high voltages. However, the sample set collected was very small (5 pores) so the characteristics of the pore can not be fully elucidated by the data set.

Five insertion events were observed for the H0 ring, giving an average conductance of 0.71 nS. This is a very low conductance compared to what would be expected for a structure of this lumen diameter. Conductance of this range is seen for nanopores with much smaller lumens, such as the six helix bundle used by Burns et al.[212] These results suggest that the H0 origami ring leads to perforation of the bilayer but not the full insertion of the ring. The perforation allows a current flow, but not the formation of a large aperture in the membrane

2.3.3 Section Conclusion

The origami rings designed in the study associated well with the lipid bilayers and led to some perforation of the bilayer, but did not appear to lead to the formation of a channel with an area equivalent to the area of the inside of the DNA ring.

Several different variations of the 46 nm ring and 29 nm ring were synthesised and characterised successfully. These were all shown to associate well with lipid bilayers. However, after extensive characterisation, only one ring variation was shown to lead to events in single channel current recordings. The best results were seen when the lipid anchors were positioned on the outside of the origami rings, however, single channel current records revealed only very low conductances. This suggests that the association of the ring with the bilayer does not lead to the formation of a large membrane hole, although some form of uniform perforation is caused by the insertion of the ring.

2.3.4 Future Work

The results suggest that the nanopore does associate with the bilayer but whether it causes a perforation of a consistent size is hard to confirm with a sample set of this size. Measurements taken on a larger, higher throughput orbit 16 device may help characterise this further. The results suggest that the nanopore does associate. Given the results showing that anchors on H0 lead to the best recording characteristics, varying the number of lipid anchors on H0 may improve the association and potentially the conductances seen.

3. Final Conclusions

The main project of this thesis has described the rational design and construction of a structurally defined nanopore built using the DNA origami technique. This multi-layered DNA origami nanopore was shown to reproducibly sense the translocation of protein analytes. It therefore represents a step change compared to existing DNA nanopores, and demonstrates the effectiveness of DNA as a viable alternative building material to expand the scope of nanopore sensing. Nanopores were characterised by gel electrophoresis, TEM and AFM imaging, and the sensing characteristics of the nanopore were demonstrated and assessed using single channel current recordings.

The secondary project describes two forms of a simplistic triangle nanopore. The triangle nanopore was formed of a single duplex, functionalised with either ethane residues or cholesterol molecules. Successful ethane modification via phosphorothioate residues was confirmed with gel electrophoresis. Assembly of the cholesterol triangle was demonstrated by gel electrophoresis, and its bind to lipid vesicles was demonstrated by UV melting profiles and a gel binding study. The cholesterol triangle showed activity when added to a planar lipid bilayer during single channel current recording, though no consistent current steps were seen.

The third project, a collaboration project with the Lin group, showed the formation and characterisation of several variations of a 46 nm ring and a 29 nm ring, with cholesterol anchors distributed around the ring's six helix bundle structure. All ring types were shown to form correctly and bind to vesicles using gel electrophoresis and TEM imaging. The H0 ring was shown to lead to some insertion events when added to a planar lipid bilayer in a portable single channel current recording device. These events showed a low conductance, which indicates that a channel the size of the ring's inner lumen area is not formed.

In this PhD project, several different DNA nanopore designs have been investigated as alternatives to more standard nanopore structures used in sensing

applications. The project has shown that structures designed out of DNA can be programmed to self-assemble with relative ease. Structures built from DNA have also been shown to be both physically and chemically versatile.

However, at this stage of development DNA nanopores have not overtaken established nanopore structures in the race to facilitate the production of reliable, commercial sensing devices. A major potential benefit of nanopores constructed out of DNA origami, compared to solid-state and protein nanopores will be the possibility to fabricate large, stable nanopores with atomically precise size. However, current nanopore designs, including those presented in this thesis, are susceptible to gating and structural changes at voltages used for sensing applications due to the significant negative charge on the DNA backbone and the effects of membrane pressure. This leads to variation in the size of the current which passes through each of the DNA nanopores, as shown in project one of this thesis. Until DNA nanopore gating can be reduced, the significant advantages of using DNA nanopores cannot be fully realised.

The high negative charge of the DNA backbone can also lead to a selectivity in the analytes which are able to be sensed. This reduces the breadth of analytes which can be detected using the DNA nanopores. However, the selectivity of the nanopore for particularly charged analytes could also be advantageously manipulated for applications where a more positively charged analyte is required to be selectively transported in the presence of a more negatively charged analyte[2]. Some potential solutions, as well as continued development of origami structure design, could include the variation of the composition of lipid membranes used in sensing set ups to those more compatible with DNA structures, such as lipids with amphiphilic domains or the addition of specific levels of detergent to bilayers to relieve some membrane pressure.

The benefit of a structure design with DNA origami is that any additional functionalisation only needs to be attached to a single staple strand, which can then be attached to a single-stranded region of the larger origami structure. Therefore, the addition of a molecular receptor to a structure, such as that described in the main project of this thesis, should be relatively simple to

accomplish. A molecular receptor such as a DNA aptamer or a nanobody (a single variable antigen binding domain (VHH) derived from the camelidae family with no light chain and a small size of 15 kDa)[251] would allow the selective detection of analytes in the presence of serum proteins.

DNA nanopores may also have future applications away from that of a sensing set up. Burns et al. demonstrated that cell death could be accomplished by the addition of a cholesterol functionalised nanostructure nanopore to cancer cells[215]. DNA origami pores which could favourably insert into bilayers may also potentially have uses as synthetic antibiotics if they are able to disrupt currents across bacterial membranes.[252,253] This thesis has shown that nanopores for transport of proteins can be successfully designed using DNA, and has showcased the potential for DNA nanopores to lead to the development of versatile biosensing devices.

The versatility and adaptability of the DNA origami technique has shown DNA to be a promising building material for artificial nanopores. However, there is still significant work to be done in the field to improve the rigidity of synthetic DNA nanopore designs and to improve the resilience of DNA nanopore structure to changes in potential. DNA nanopores will only be able to be used as effective sensing tools if these characteristics can be controlled. Additionally, DNA nanopores will need to be selective for specific analytes to achieve their full potential. Considering the relative simplicity of adding functionality to DNA staple strands using solid phase synthesis, it is likely that the goal of producing nanopores with selectivity for specific analytes could be realised in the near future.

4. Experimental

4.1 Materials

UCL

Native and cholesterol-labelled DNA oligonucleotides with a tri(ethylene glycol)(TEG) linker were purchased from Integrated DNA Technologies (Leuven, Belgium) or ATDbio (Southampton, United Kingdom) on a 1 μmole scale with desalting or HPLC purification, respectively. 1,2-dioleoyl-sn-glycero-3-phosphoethanolamine (DOPE), 1,2-dioleoyl-sn- glycero-3-phosphocholine (DOPC) and 1,2-diphytanoyl-sn-glycero-3-phosphocholine (DPhPC) was procured from Avanti Polar Lipids (Alabaster, AL). M13mp18 DNA was obtained from New England Biolabs (Ipswich, United Kingdom). All other reagents and solvents were purchased from Sigma-Aldrich unless stated.

Yale

DNA oligonucleotides for the ring were purchased from Bioneer Inc. Alameda, CA, USA). The p8064 and p3024 scaffold strands were cloned and amplified in-house following standard protocols.[254] Ultracentrifuge tubes and adaptors for rate-zonal centrifugation were purchased from Beckman-Coulter Inc. (Miami, FL, USA). Amicon filters were purchased from Millipore (Billerica, MA, USA). All other reagents and solvents were purchased from Sigma-Aldrich, unless stated.

4.2 Multi-layered DNA Origami Nanopores

4.2.1 Design of Multi-layered DNA Origami Nanopores

The DNA origami nanopores were designed using the square-lattice version of the CadNano software.[154] Several cycles of strand routing with CadNano and CanDo modelling to assess rigidity were used in designing the structure. The 7249 nt-long, m13mp18 single stranded (New England Biolabs inc. Ipswich) was chosen as a scaffold for the box and funnel assemblies.[152]

The rendering of DNA nanopore and the 2D DNA map highlighting the scaffold in blue and staple strands in red is shown in Appendix Figure 97 and 98, respectively. In the design, lipid anchors are attached to the pore via DNA oligonucleotides that carry cholesterol at the 5 prime or 3 prime termini. These cholesterol-modified anchor strands hybridize via adaptor oligonucleotides to the nanopore designs. The use of this adaptor method limited the number of expensive cholesterol modified strands to two. The DNA sequences for the Box and Funnel nanopores and the cholesterol anchor modified strands are shown in Appendix Table 9 and 10

4.2.2 Assembly

Box

The box was assembled with the full scaffold strand and with a 4204 region of the scaffold strand. DNA staple oligonucleotide strands (Appendix Table 10) were prepared by solid-phase chemical synthesis (Integrated DNA Technologies, Leuven, Belgium) with desalting purification. Objects were annealed in a one-pot reaction containing scaffold (20 µg, 4.2 nM) and 77 staples (130 nM) and 12-26 mM $MgCl_2$ 1xTAE buffer. Solutions were annealed using protocol 1 (12 hours) and 2 (24 hours) in a BIO-RAD T100 Thermal Cycler. (Table 8).

Funnel

The funnel nanopore uses all regions of the scaffold strand. DNA staple oligonucleotide strands (Appendix Table 10) were prepared by solid-phase chemical synthesis (Integrated DNA Technologies, Leuven, Belgium) with desalting purification. Objects were annealed in a one-pot reaction containing scaffold (20 µg, 4.2 nM), staples (100 nM) in 12-26 mM $MgCl_2$ 1xTAE buffer. Samples were initially annealed using protocols 2 and 3.

Further annealment protocols were used when optimising the origami folding procedure. Magic folds (Protocol no. 5 to 6) held the DNA at a fixed temperature for the fold time period. Ramp folds were also investigated. (Protocols no. 7 to 9)

Protocol No.	Protocol Length	Steps
1	12.1 hours	1) 80°C-70°C at 1°C per min 2) 70°C-50°C at 1°C per 10 min 3) 50°C-20°C at 1°C per 15 min 4) 20°C-4°C at 1°C per 4 min
2	24 hours	1) 90°C-70°C at 1°C
3	7 days	1) 80°C-60°C at 1°C per 5 min 2) 60°C-20°C at 1°C per 300 min
4	48 min	1) 95°C for 5 min 2) 95°C-25°C at 1°C per 0.5 min
5	Magic Fold 8 hours	1) Hold temperature (48°C to 38°C) for 8hrs 2) 4°C infinite hold
6	Magic Fold 32 hours	1) Hold temperature (48°C to 38°C) for 32hrs 2) 4°C infinite hold
7	15 hr Ramp	1) 80°C-65°C at 1°C per 5 min 2) 64°C-24°C at 1°C per 20 min 3) hold at 4°C
8	3 day Ramp	1) 80°C-65°C at 1°C per 5 min

		2) 64°C-24°C at 1°C per 120 min 3) hold at 4°C
9	4 day Ramp	1) 80°C-65°C at 1°C per 5 min 2) 64°C-24°C at 1°C per 150 min 3) hold at 4°C

***Table 8** – Fold protocols*

Scaffold Digestion

The 7249bp scaffold strand was cut at BsrBI, SnaBI, DarI, BamIH-HF restriction sites. The scaffold was fragmented into the 4202bp desired fragment for folding; the remaining 3045bp fragment was cut further to 305bp, 343bp, 796bp, 690bp, 532bp and 280bp fragments which were more easily removed from solution by SEC. Scaffold (100 µL, 20 ng) and DNA oligo "primers" for the 7 digestion sites (1 nmole) were combined in 1X Cutsmart buffer (New England Biolabs). The solution was heated at 95°C for 5 min and then cooled for 10 min at 8°C. BsrBI, SnaBI, DarI, BamIH-HF (200 units per cut site) were added and the mixture was incubated at 37°C for 10 min- 24 hours. The best results were seen for an incubation time of 3 hours.

Scaffold Fragment Purification

The 4202bp digested scaffold fragment (4.2 nM) was visualised and purified using an ÄKTA purifier 100/10 fitted with a Superdex 200 10/300 GL column (GE Healthcare), using a flow rate of 0.5 ml per minute at 8 °C. Elution was monitored via UV-vis absorption at 260, 280 and 395 nm. The 4202bp fragment of scaffold strand was re-concentrated by centrifuging with 3K centrifuge spin filters (Vivaspin 500, Sartorius, Gloucestershire)

Cholesterol Strand Addition

To form the cholesterol funnel nanopore the nanopore was incubated with the cholesterol strands for 30 min at 30°C. Several equivalence ratios were investigated. The optimised equivalence ratio was found to be 1:1.1 Funnel to

cholesterol strands (per binding site at the pore, up to 24 sites)

Structure Purification

The assembled box and funnel structures were visualised and purified from excess staples by size exclusion chromatography (SEC) using an ÄKTA purifier 100/10 fitted with a Superdex 200 10/300 GL column (GE Healthcare), using a flow rate of 0.5 ml per minute at 8 °C. Elution was monitored via UV-vis absorption at 260, 280 and 295 nm. Fractions containing the DNA box or funnel were pooled, and the rest of the fractions were discarded.

Freeze 'N Squeeze Gel Band Purification

Gel bands to be imaged were cut with a razor blade from ethidium bromide stained agarose gels during ultraviolet illumination and placed in an eppendorf tube (Eppendorf, Hamburg, Germany). The gel band was then crushed with a plastic pestle. The bottom of the eppendorf was cut off and added, inverted, to the filter cup of a Quantum Prep Freeze 'N Squeeze DNA gel extraction spin column. (Bio-Rad Laboratories, California, United States). The column was centrifuged at 13,000g for 3 min at room temperature and the solution in the dolphin tube collected.

4.2.3 Characterisation

UV-Vis Melting Point Analysis

Melting point analysis was performed using a Varian Cary 100 Bio UV-vis Spectrophotometer equipped with a Peltier element with a 1 cm path length quartz cuvette. The purified DNA box and funnel in 14mM $MgCl_2$ 1xTAE were heated at 0.5 ^oC per minute to 90^oC. Absorbance was monitored at 260 nm and 350 nm.

Gel Electrophoresis

Gel electrophoresis separates particles depending on their size and charge. Gel electrophoresis is run by placing a gel (in this study either poly acrylamide or agarose) in a buffer filled box and applying a potential difference between the two ends of the gel. When an electric field is applied, negatively charged DNA will migrate through the porous gel matrix towards the positive terminal. Smaller, more highly charged or more compact DNA objects will travel more easily through the gel matrix and will therefore move faster. Differently sized DNA molecules and structures will move at different speeds leading to separation of distinct bands in the gel. Polyacrylamide gels are used to separate DNA strands from 1-1000 base pairs in length. Agarose gels are used to separate larger structures in the size range of 50-50000 base pairs.[255]

The assembly of box and funnel structures was analysed using 1.5 % - 2% agarose gel electrophoresis in standard 1xTAE buffer, run at 70 V for 1hr at 8 °C. or at 60 V for 1hr30min. DNA (10 μL) was mixed with 2 μL of 6× gel loading dye and then added to the wells (New England Biolabs). A 1000-base-pair marker (New England Biolabs) was used as the reference standard. DNA bands were visualized by staining with ethidium bromide solution and ultraviolet illumination. SDS containing gels were washed with deionized water for 20 min prior to staining.

SUV binding assays were run in the same way as described above, except that gels were run at 40 V. Pores (15 μL, 1 μM, 14 mM MgCl2,1xTAE) were incubated with SUVs (15 μL, 1 mM, 0.3 M KCl, 15 mM Tris, pH 8.0) for 30 min at 37 °C.

Blue loading dye (6x, no SDS, 10 µL) was added to the mixture and loaded onto the gel (30 µL).

SUV Formation

To analyze the interaction of the funnel with lipid membranes, SUVs (small unilamellar vesicles) were formed. Chloroform solutions of DOPE (0.3 mmol, 22.3 µL) and DOPC (0.7 mmol, 110 µL) were mixed, and added to an oven-dried round bottom flask (10 mL), followed by removal of the solvent under vacuum using a rotary evaporator for 30 min. To form vesicles, a solution of 0.3 M KCl, 15 mM Tris, pH 8.0 (1 mL) was added, and the suspension was sonicated for 30 min at RT. SUV preparations were stored at 4ºC and used within one week. Before experimentation, the SUV solution was vortexed for 2 s.

AFM

Atom force microscopy (AFM) is a type of scanning probe microscopy. Using AFM a topographical image of a surface can be generated by measuring both repulsive and attractive interaction between a nanometer range sharp tip, mounted on a cantilever, and the surface. While the sharp tip moves over the sample surface, the interactions between the tip and the surface are monitored by deflection of a laser focused on the top end of the cantilever[256].

The forces between a surface and the AFM tip are dependent on the distance of the tip from the surface and can be defined by the Lennard-Jones potential.

$$V(d) = 4\varepsilon \left(\left(\frac{\sigma}{d}\right)^{12} - \left(\frac{\sigma}{d}\right)^{6}\right)$$

Equation 5 *- The Lennard-Jones potential*

Where V is the potential, d is the distance between the tip and the sample, ε is the potential well depth and σ is the distance at which the force is zero.

The Lennard-Jones potential has a short-range repulsion term (when the tip and surface are very close) and a longer-range attraction term (when the distance

between the tip and the surface are greater).

AFM imaging is performed in different modes depending on the application. These can generally be divided into two categories: static modes (contact) and dynamic modes (non-contact or tapping mode).

In contact mode, a constant bend of the cantilever is maintained and measurements are taken at distances where the short-range repulsive term of the lennard-Jones potential is dominant. When the AFM tip is repelled from the surface the cantilever is bent, allowing the generation of an image of the surface topology.

In dynamic modes, the cantilever is oscillated at a frequency instead of being kept static. In tapping mode (used in this study) the amplitude and frequency of oscillation is kept constant. Scanning is performed at a distance where long range attractive interactions (such as dipole–dipole forces, van der Waals forces and electrostatic forces) are dominant. The attractive forces of the surface lead to changes in the amplitude of oscillation of the cantilever when they interact with the sharp tip. In non-contact mode, the tip makes no contact with the surface and long range attractive forces act to reduce the resonance frequency of the cantilever. Changes in the oscillation of the cantilever can then be used to generate a topographical image of the surface[257].

DNA origami shapes were imaged using tapping mode in liquid, using Multimode VIII AFM equipped with a type E scanner (Veeco Instruments, Santa Barbara, USA) and silicon tipped nitride (Bruker, Camarillo, USA) cantilevers. Freshly cleaved mica was incubated with SEC purified DNA funnel solution (100 µL) for 5 min, liquid was then wicked off and replaced with 100 µL 14mM $MgCl_2$ 4 mM $NiCl_2$ 1xTAE buffer.

TEM Without Vesicles

2% uranyl formate stain was prepared by adding 20 µg of solid uranyl formate to 1000 µl of boiling distilled water. The mixture was then shaken for 4 min. 5µL of 5M NaOH was next added to the solution and mixed. The solution was then

filtered with a syringe filter (0.2 µm) to remove any remaining precipitate. 5 µL of the funnel sample was added onto glow discharge-treated TEM grids (Electron Microscopy Sciences) and stained with 2% uranyl formate. TEM imaging was performed using a JEOL JEM-1400 Plus microscope operated at 80kV.

TEM With Vesicles

The folded and cholesterol-modified DNA funnel was incubated at a final concentration of ~1 nM with pre-formed SUVs (total lipid concentration ~10 uM, DOPC/DOPE= 7 : 3) in 1X TAE buffer containing 0.3 M NaCl for 30 min at room temperature. After the incubation, 5 µL of the funnel sample was added onto glow discharge-treated TEM grids (AGS147-3, Agar Scientific) and stained with 0.5% Uranyl Acetate solution. TEM observations were then performed on a JEM-2100 electron microscope (JEOL) operated at 200 kV, and the images were acquired with a Orius SC200 camera.

4.2.4 Single Channel Current Recordings

For planar lipid bilayer electrophysiological current measurements, an integrated chip-based, parallel bilayer recording setup (Orbit 16, Nanion Technologies, Munich, Germany) with multielectrode-cavity-array (MECA) chips (IONERA, Freiburg, Germany) was used.[2,239] Bilayers were formed using a magnetic stirring bar coated with DPhPC dissolved in octane or hexane (10 mg mL^{-1}) which spread the lipid over the MECA chips cavities. The electrolyte solution was 1 M KCl and 10 mM HEPES, pH 8.0. For pore insertion, a 2:1 mixture of cholesterol-anchored DNA nanopores and 0.5% OPOE (n-octyloligooxyethylene, in 1 M KCl, 10 mM HEPES, pH 8.0) was added to the *cis* side of the bilayer. A positive voltage of +30 mV was applied to facilitate pore insertion. Successful incorporation was observed by detecting the current steps. The current traces were Low Pass Filtered at 3.0744 kHz and acquired at 20 kHz with an EPC-10 patch-clamp amplifier (HEKA Elektronik, Lambrecht/Pfalz, Germany) Single-channel analysis was performed using Clampfit (Molecular Devices, Sunnyvale, CA, USA). Trypsin solution (5 µL) was added to the *cis* side of the bilayer and mixed with no voltage applied. Voltage protocols were then applied Figure 62 and the results recorded.

4.3 Small DNA Nanostructure Nanopores

Design for the DNA triangle nanopore was provided by Dr Jon Burns.
Conventional and phosphorothioate-modified DNA oligonucleotides were purchased from Integrated DNA Technologies (Leuven, Belgium) on a 1 μmole scale with HPLC purification. DNA stock solutions were quantified using Varian Cary 100 Bio UV/Vis spectrophotometer. Absorbance at λ = 260 nm was measured and the concentration calculated using the Beer Lamberts law, based on their calculated extinction coefficients (Integrated DNA Technologies' OligoAnalyzer 3.1)

4.3.1 Ethane-Capping Protocol

Protocol's adapted from Burns et al.[212]
H_2O from stock solution of Phosphorothioate DNA oligonucleotides (2 nanomoles, PAGE-purified, IDT-DNA, Coralville, IO;) was removed under reduced pressure. Oligonucleotides were re-dissolved in 90 % DMF and 10 % 30 mM Tris-HCl pH 8.0 (20 μL), or 90 % DMF and 10 % 30 mM BisTris-HCl pH 6.0 Iodoethane (5 μL) was added to the solution. The mixture was divided into 5 μL aliquots and heated to temperatures of 15 °C-75oC for 15 min-3 hr in Eppendorf Snap-Cap Microcentrifuge Safe-Lock Tubes, after which the solvent was removed under reduced pressure. The resulting dry solid was dissolved in H_2O or 0.1 M EDTA pH 8.0 (20 μL) by heating to 90 °C for 5 minutes with vigorous stirring.

For the final optimised protocol oligonucleotides were re-dissolved in 90 % DMF and 10 % 30 mM Tris-HCl pH 8.0 (20 μL). Iodoethane (5 μL), was added to the solution. The mixture was divided into 5 μL aliquots and heated to 55 ^oC for 1 hr in Eppendorf Snap-Cap Microcentrifuge Safe-Lock Tubes, after which the solvent was removed using reduced pressure. The resulting dry solid was dissolved in 0.1 M EDTA pH 8.0 (20 μL) by heating to 90 °C for 5 minutes with vigorous stirring.

4.3.2 Ethane-Capped Strand Purification and Quantification

The DNA was desalted with a NAP-25 column (GE Healthcare). Fractions containing DNA were visualised by measuring absorption at λ = 260 nm using a UV/Vis spectrophotometer (Varian Cary 100 Bio UV/Vis spectrophotometer) and then concentrated under reduced pressure. Samples were quantified by measuring the absorbance at λ = 260 nm and calculating the concentration using Beer Lamberts law, based on their calculated extinction coefficients (Integrated DNA Technologies' OligoAnalyzer 3.1)

HPLC Analysis

The ethane-capped strands were purified by reversed phase HPLC using a Varian ProStar system with a Model 210 solvent delivery module and a Model 320 UV detector. The purification was performed using a Varian C18 column (250 x 4.6 mm, 5 μm beads, flow rate of 1mL/min) using the following gradient: at 0 min 95% triethyl ammonium acetate buffer (TEAA) pH 8.0 / 5% acetonitrile (ACN); from 0.1 to 40 min, 70% TEAA/ 30% ACN; from 40.1 to 50 min, 5% TEAA/ 95% ACN; from 50.1 to 53 min 5% TEAA/ 95% ACN; from 53.1 to 60 min, 95% TEAA/ 5% ACN.

Mass Spectrometry

Equivalent amounts of crude reaction mixture and matrix solutions 1-3 (2 μL each) were mixed. 3 μL of mix was then applied to the maldi plate.
Matrix solutions:
(1) 0.03722 g THAP & 0.045 g ammonium citrate in 50% aqueous acetonitrile (2mL)
(2) 0.01 g HPA in 1 mL methanol
(3) 2% solutions of sinapinic acid in 50% aqueous acetonitrile (1 mL).
Solvents and volatile alkylating agents (CH_3I) evaporated with matrix formation while the product remained embedded in the matrix. Mass spectra were recorded on a MALDI micro MX mass spectrometer (Micromass UK Limited, Manchester England) Spectrums were recorded in the 4000-30 000 Da range.

4.3.3 Assembly

The native, PPT containing and ethane-capped forms of the PPT Triangle were assembled by heating an equimolar mixture of the 48 nt and 66 nt strands (2 μM) dissolved in 12.5 mM $MgCl_2$ 1xTAE buffer at 95 °C for 5 minutes, and followed by cooling to 16 °C at a rate of 0.5 °C min^{-1} in a PCR machine. (Table 11)

The native form of the Cholesterol Triangle was assembled by heating an equimolar mixture of the 48ntU II, 66nt II I, 66nt II II, 66nt II III strands (5 μM) dissolved in 12.5 mM MgCl2 1xTAE buffer at 95 °C for 5 minutes, and followed by cooling to 16 °C at a rate of 0.5 °C min^{-1} in a BIO-RAD T100 Thermal Cycler. For the cholesterol modified form of the Cholesterol triangle the same protocol was followed for an equimolar mixture of the 48ntU II, 66nt II chol I, 66nt II chol II, 66nt II chol III strands. (Table 12)

4.3.4 Characterisation

Gel Electrophoresis

The assembled native DNA Triangle structure was analysed under native conditions using 10 % polyacrylamide gel electrophoresis in 1xTBE buffer, run at 160 V for 45 minutes at 8 °C. DNA (10 μL) was mixed with 2 μL of 6× gel loading dye and then added to the wells.

The progress of the ethane-capped DNA strands' reaction and the assembly of the ethane-capped DNA triangle was analysed in the presence of SDS. 13 % polyacrylamide gel and running buffer 25 mM Tris pH 8.8 supplemented with 0.1 % SDS showed the best results. DNA (10 μL) was mixed with 2 μL of 6× gel loading buffer and added to the wells. The electrophoresis conditions were 160 V, 50 minutes, and 8 °C. The bands were staining with ethidium bromide solution and then visualised using UV illumination. SDS containing gels were washed with deionized water for 20 min prior to staining.

The assembled native DNA Triangle structure was analysed under native conditions using 2 % agarose gel electrophoresis in 1xTBE buffer, run at 160 V for 45 minutes at 8 °C.

UV Melting Analysis

UV melting point analysis was conducted at 260 nm. Samples with a concentration of 1-2 μM were dissolved in 0.3 M KCl, 15 mM Tris pH 8.0 and were heated at a rate of 1 °C per minute in the spectrophotometer.

The vesicles were prepared using sonication of a lipid solution containing cholesterol and DPhPC. DPhPC (11.1 mM, 2.65 mL) was added to cholesterol (10 mM, 0.295 mL) in a 20 mL round bottom flask. The solution was dried under vacuum with a rotary evaporator for 1 hr. Deionized water (500 μL) was added to the thin film, and the suspension was sonicated for 10–20 minutes.

Release Experiments

Performed with the help of Dr Jon Burns.
A solution of lipids PE (0.3mmol, 50 μl) and PC (0.7 mmol, 550 μl) in chloroform was added to a 10 mL round bottom flask. The solvent was then removed using a rotary evaporator to yield a thin film, which was subsequently dried under vacuum for 40min. The lipid was re-suspended in a solution of 0.3M KCL 1.5 mM Tris containing either CF or SRB at a concentration of 50mM (1mL). The solution was sonicated for 20–30 min at room temperature and then purified using a NAP-25 column (GE Healthcare) filled with 0.3 M KCL 1.5 nM Tris. SUVs were left to equilibrate for 3 h.

The suspension was gently re-suspended 2 s before use. UV–vis absorbance and fluorescence spectroscopy on a small aliquot confirmed that the encapsulated dyes were self-quenching and did not leak out of the vesicles before rupturing them with the detergent triton-X 100. DNA triangle nanopore (final concentration 1 μM) was added to a volume of 1 mL SUV suspension. Nanopore-mediated release was monitored by measuring absorption at 564 nm for SRB and emission at 515

nm for CF. Experiments were conducted at room temperature, and total release values were measured after 1 h incubation at 30°C

4.3.5 Single Channel Current Recordings

For planar lipid bilayer electrophysiological current measurements, an integrated chip-based, parallel bilayer recording setup (Orbit 16, Nanion Technologies, Munich, Germany) with multielectrode-cavity-array (MECA) chips (IONERA, Freiburg, Germany) was used. Bilayers were formed by spreading via a magnetic stirring bar coated with DPhPC dissolved in hexane (10 mg mL^{-1}). The electrolyte solution was 1 M KCl and 10 mM HEPES, pH 8.0. For pore insertion 5 µL aliquots of the DNA Nanopore was added to the cis side of the bilayer. A positive voltage of +30 mV was applied to facilitate pore insertion. The current traces were Low Pass Filtered at 3.0744 kHz and acquired at 20 kHz with an EPC-10 patch-clamp amplifier (HEKA Elektronik, Lambrecht/Pfalz, Germany) Single-channel analysis was performed using Clampfit (Molecular Devices, Sunnyvale, CA, USA).

4.4 DNA Origami Ring

4.4.1 Assembly

DNA staple oligonucleotide strands were prepared by solid-phase chemical synthesis (Integrated DNA technologies Leuven, Belgium). Origami rings were annealed in a one-pot reaction containing scaffold (50 nM) and staples (300 nM) in 5 mM Tris–HCl, 1 mM EDTA and 10 mM $MgCl_2$, pH 8 buffer. Structures were annealed using a 2hr magic fold protocol.

4.4.2 Purification

Rate-zonal Centrifugation

Purification was performed by the "rate-zonal centrifugation" following the previously published protocol[250]. A linear glycerol gradient (15–45%, v/v) was prepared. Two layers of glycerol solution in 5 mM Tris–HCl, 1 mM EDTA and 10 mM $MgCl_2$, pH 8 buffer, 1.4 mL per layer, were carefully laid into a 3.5 mL (Beckman #349622) ultracentrifuge tube. 45% glycerol solution was place at the bottom of the tube and 15% glycerol solution laid on top. The tube was then laid flat slowly over 2 hrs. The tube was then returned to its vertical position and centrifuged at 50 000 rpm for three hours at 4^{o}C.

Folded origami was added to the top of a centrifuge tube containing a pre-prepared 15%-45% glycerol gradient. The centrifuge tubes were then placed inside the centrifuge buckets, suspended on a swinging-bucket rotor (Beckman SW 55 Ti) and spun at 50 000 rpm (~300 000*g* max) for 3hrs at 4°C. After centrifugation was complete 24 equal-volume fractions were collected from top to bottom of the centrifuge tube using longneck gel-loading tips.

Gel Electrophoresis

Aliquots of each fraction from the rate-zonal centrifugation procedure (10 µl per fraction) were loaded into separate wells of a 1.5% agarose gel containing 5 µL ethidium bromide in 0.5× TBE buffer (45 mM Tris-borate, 1 mM EDTA, pH 8.3) containing 10 mM $MgCl_2$ for 1.5 h at room temperature and run at 60 V. The gels were then scanned on a Typhoon FLV 9000 laser scanner.

Concentration

From the rate-zonal centrifugation procedure, fractions containing the ring monomer were combined and reconstituted into native folding buffer (5 mM Tris–HCl, 1 mM EDTA and 10 mM $MgCl_2$) using Amicon Ultra-0.5 mL centrifugal filters (MWCO 30 kDa) and spun at 7500 rpm for 7 min. 400 µL of ring sample were added to centrifuge filter and spun for 7 minutes. 3x 400 µL of the native fold buffer were then added to the centrifuge filter and spun for 5 minutes per addition.

Cholesterol Functionalisation

The origami rings were incubated for an hour at 37^{o}C, with 1.5x to 3x equivalents of cholesterol anti-handles. The binding characteristics of the anti-handles was examined using 1.5% agarose gel electrophoresis

4.4.3 Characterisation

TEM Imaging

2% uranyl formate stain was prepared by adding 20 µg of solid uranyl formate to 1000 µl of boiling distilled water and then shaking for 4 min. 5 µL of 5 M NaOH was then added to the solution and mixed. The solution was then filtered with a syringe filter (0.2um) to remove any remaining precipitate. 5 µL of the ring samples was added onto glow discharge-treated TEM grids (Electron Microscopy Sciences) and staining with 2% uranyl formate solution. For DNA ring-liposome

images. ring samples (5 nM) were incubated with 50 nM of liposomes at 35^{o}C for 2 hrs before uranyl formate staining. TEM imaging was then performed using a JEOL JEM-1400 Plus microscope operated at 80kV.

4.4.4 Single Channel Current recordings

Single-channel recording was performed using the portable Orbit-mini planar bilayer system, (Nanion Technologies, Munich, Germany) DPhPC dissolved in hexane (10 mg mL^{-1}) was painted over the four apertures in the multielectrode-cavity-array (MECA) chips (IONERA, Freiburg, Germany) manually using a brush until coverage was indicated to have been achieved by the reducing in observed current flow seen ± 5 mV voltage protocol was applied. The electrolyte solution was 1 M KCl and 10 mM HEPES, pH 8.0. For pore insertion, a list of protocols was applied until insertion events were seen (Table 7). In some protocols a 2:1 mixture of cholesterol-anchored origami ring and 0.5% OPOE (n-octyloligooxyethylene, in 1 M KCl, 10 mM HEPES, pH 8.0) was added to the *cis* side of the bilayer. The current traces were acquired at 1.22 kHz. Single-channel analysis was performed using Clampfit (Molecular Devices, Sunnyvale, CA, USA).

5. References

1. Ashton, P. M. *et al.* MinION nanopore sequencing identifies the position and structure of a bacterial antibiotic resistance island. *Nat. Biotechnol.* **33,** 296–300 (2014).
2. Burns, J. R., Seifert, A., Fertig, N. & Howorka, S. A biomimetic DNA-based channel for the ligand-controlled transport of charged molecular cargo across a biological membrane. *Nat. Nanotechnol.* **11,** 152–156 (2016).
3. Burns, J. R. *et al.* Lipid-Bilayer-Spanning DNA Nanopores with a Bifunctional Porphyrin Anchor. *Angew. Chemie Int. Ed.* **52,** 12069–12072 (2013).
4. Seifert, A. *et al.* Bilayer-Spanning DNA Nanopores with Voltage-Switching between Open and Closed State. *ACS Nano* **9,** 1117–1126 (2014).
5. Yang, Y. *et al.* Self-assembly of size-controlled liposomes on DNA nanotemplates. *Nat. Chem.* **8,** 476 (2016).
6. Clark, L. C. JR.(1956). Monitor and control of blood and tissue oxygen tensions. *Trans. Am. Soc. Artif. Intern. Organs* **2,** 41
7. Turner, A. P. F. Biosensors: sense and sensibility. *Chem. Soc. Rev.* **42,** 3184–3196 (2013).
8. Erickson, J. S. & Ligler, F. S. Home diagnostics to music. *Nature* **456,** 178 (2008).
9. Terry, L. A., White, S. F. & Tigwell, L. J. The Application of Biosensors to Fresh Produce and the Wider Food Industry. *J. Agric. Food Chem.* **53,** 1309–1316 (2005).
10. Edelstein, R. L. *et al.* The BARC biosensor applied to the detection of biological warfare agents. *Biosens. Bioelectron.* **14,** 805–813 (2000).
11. Wang, J. Electrochemical Glucose Biosensors. *Chem. Rev.* **108,** 814–825 (2008).
12. Gubala, V., Harris, L. F., Ricco, A. J., Tan, M. X. & Williams, D. E. Point of Care Diagnostics: Status and Future. *Anal. Chem.* **84,** 487–515 (2012).
13. Ahmed, M. U., Saaem, I., Wu, P. C. & Brown, A. S. Personalized diagnostics and biosensors: a review of the biology and technology needed for personalized medicine. *Crit. Rev. Biotechnol.* **34,** 180–196 (2014).
14. Ronkainen, N. J., Halsall, H. B. & Heineman, W. R. Electrochemical biosensors. *Chem. Soc. Rev.* **39,** 1747–1763 (2010).
15. Wang, X. & Wolfbeis, O. S. Fiber-Optic Chemical Sensors and Biosensors (2013–2015). *Anal. Chem.* **88,** 203–227 (2016).
16. Fogel, R., Limson, J. & Seshia, A. Acoustic biosensors. *Essays Biochem.* **60,** 101–110 (2016).
17. Grieshaber, D., MacKenzie, R., Vörös, J. & Reimhult, E. Electrochemical Biosensors - Sensor Principles and Architectures. *Sensors (Basel).* **8,** 1400–1458 (2008).
18. Eggins, B. R. *Chemical Sensors and Biosensors*. (2008).
19. Thévenot, D. R., Toth, K., Durst, R. A. & Wilson, G. S. Electrochemical biosensors: recommended definitions and classification1International Union of Pure and Applied Chemistry: Physical Chemistry Division, Commission I.7 (Biophysical Chemistry); Analytical Chemistry Division, Commission V.5 (Electroanalytical. *Biosens. Bioelectron.* **16,** 121–131 (2001).
20. Castañeda, M. T., Merkoçi, A., Pumera, M. & Alegret, S. Electrochemical

genosensors for biomedical applications based on gold nanoparticles. *Biosens. Bioelectron.* **22,** 1961–1967 (2007).
21. Dutra, R. F. & Kubota, L. T. An SPR immunosensor for human cardiac troponin T using specific binding avidin to biotin at carboxymethyldextran-modified gold chip. *Clin. Chim. Acta* **376,** 114–120 (2007).
22. Centi, S., Bonel Sanmartin, L., Tombelli, S., Palchetti, I. & Mascini, M. Detection of C Reactive Protein (CRP) in Serum by an Electrochemical Aptamer-Based Sandwich Assay. *Electroanalysis* **21,** 1309–1315 (2009).
23. Dell'Atti, D. *et al.* Development of combined DNA-based piezoelectric biosensors for the simultaneous detection and genotyping of high risk Human Papilloma Virus strains. *Clin. Chim. Acta* **383,** 140–146 (2007).
24. Wilson, M. S. & Nie, W. Multiplex Measurement of Seven Tumor Markers Using an Electrochemical Protein Chip. *Anal. Chem.* **78,** 6476–6483 (2006).
25. Mascini, M. & Tombelli, S. Biosensors for biomarkers in medical diagnostics. *Biomarkers* **13,** 637–657 (2008).
26. Daniels, J. S. & Pourmand, N. Label-Free Impedance Biosensors: Opportunities and Challenges. *Electroanalysis* **19,** 1239–1257 (2007).
27. Atkinson, A. J. *et al.* Biomarkers and surrogate endpoints: Preferred definitions and conceptual framework*. *Clin. Pharmacol. Ther.* **69,** 89–95 (2001).
28. Prensner, J. R., Rubin, M. A., Wei, J. T. & Chinnaiyan, A. M. Beyond PSA: the next generation of prostate cancer biomarkers. *Sci. Transl. Med.* **4,** 127rv3 (2012).
29. Ziegler, A., Koch, A., Krockenberger, K. & Großhennig, A. Personalized medicine using DNA biomarkers: a review. *Hum. Genet.* **131,** 1627–1638 (2012).
30. Rifai, N., Gillette, M. A. & Carr, S. A. Protein biomarker discovery and validation: the long and uncertain path to clinical utility. *Nat. Biotechnol.* **24,** 971 (2006).
31. Luo, X. & Davis, J. J. Electrical biosensors and the label free detection of protein disease biomarkers. *Chem. Soc. Rev.* **42,** 5944–5962 (2013).
32. Sang, S. *et al.* Progress of new label-free techniques for biosensors: a review. *Crit. Rev. Biotechnol.* **36,** 465–481 (2016).
33. Mehrabani, S., Maker, A. J. & Armani, A. M. Hybrid integrated label-free chemical and biological sensors. *Sensors* **14,** 5890–5928 (2014).
34. Bilitewski, U. Protein-sensing assay formats and devices. *Anal. Chim. Acta* **568,** 232–247 (2006).
35. Haque, F., Li, J., Wu, H.-C., Liang, X.-J. & Guo, P. Solid-state and biological nanopore for real-time sensing of single chemical and sequencing of DNA. *Nano Today* **8,** 56–74 (2013).
36. Coulter, W. H. Means for counting particles suspended in a fluid. (1953).
37. Coulter, W. H. High-speed automatic blood cell counter and size analyzer. *Prelim. Draft a talk Present. before Natl. Electron. Conf. Chicago* (1956).
38. Hladky, S. B. & Haydon, D. A. Discreteness of Conductance Change in Bimolecular Lipid Membranes in the Presence of Certain Antibiotics. *Nature* **225,** 451 (1970).
39. Neher, E. & Sakmann, B. Single-channel currents recorded from membrane of denervated frog muscle fibres. *Nature* **260,** 799 (1976).
40. de la Escosura-Muñiz, A. & Merkoçi, A. Nanochannels for electrical biosensing. *TrAC Trends Anal. Chem.* **79,** 134–150 (2016).
41. Howorka, S. & Siwy, Z. Nanopore analytics: sensing of single molecules.

Chem. Soc. Rev. **38,** 2360–2384 (2009).
42. Makra, I. & Gyurcsányi, R. E. Electrochemical sensing with nanopores: A mini review. *Electrochem. commun.* **43,** 55–59 (2014).
43. Bayley, H. & Martin, C. R. Resistive-Pulse SensingFrom Microbes to Molecules. *Chem. Rev.* **100,** 2575–2594 (2000).
44. Hume, R. I., Role, L. W. & Fischbach, G. D. Acetylcholine release from growth cones detected with patches of acetylcholine receptor-rich membranes. *Nature* **305,** 632 (1983).
45. Bezrukov & Kasianowicz. Current noise reveals protonation kinetics and number of ionizable sites in an open protein ion channel. *Phys. Rev. Lett.* **70,** 2352–2355 (1993).
46. Kasianowicz, J. J. & Bezrukov, S. M. Protonation dynamics of the alpha-toxin ion channel from spectral analysis of pH-dependent current fluctuations. *Biophys. J.* **69,** 94–105 (1995).
47. Nardin, C., Thoeni, S., Widmer, J., Winterhalter, M. & Meier, W. Nanoreactors based on (polymerized) ABA-triblock copolymer vesicles. *Chem. Commun.* **15,** 1433–1434 (2000).
48. Bayley, H. & Cremer, P. S. Stochastic sensors inspired by biology. *Nature* **413,** 226 (2001).
49. Bayley, H. Nanopore Sequencing: From Imagination to Reality. *Clin. Chem.* **61,** 25–31 (2015).
50. Hall, A. R. *et al.* Hybrid pore formation by directed insertion of [alpha]-haemolysin into solid-state nanopores. *Nat. Nanotechnol.* **5,** 874–877 (2010).
51. Bell, N. A. W. & Keyser, U. F. Nanopores formed by DNA origami: a review. *FEBS Lett.* **588,** 3564–3570 (2014).
52. Shi, W., Friedman, A. K. & Baker, L. A. Nanopore Sensing. *Anal. Chem.* **89,** 157–188 (2017).
53. Miles, B. N. *et al.* Single molecule sensing with solid-state nanopores: Novel materials, methods, and applications. *Chem. Soc. Rev.* **42,** 15–28 (2013).
54. Wanunu, M. *et al.* Rapid electronic detection of probe-specific microRNAs using thin nanopore sensors. *Nat. Nanotechnol.* **5,** 807–814 (2010).
55. Firnkes, M., Pedone, D., Knezevic, J., Döblinger, M. & Rant, U. Electrically Facilitated Translocations of Proteins through Silicon Nitride Nanopores: Conjoint and Competitive Action of Diffusion, Electrophoresis, and Electroosmosis. *Nano Lett.* **10,** 2162–2167 (2010).
56. Song, L. *et al.* Boron Nitride Nanopores: Highly Sensitive DNA Single-Molecule Detectors. *Adv. Mater.* **25,** 4549–4554
57. Uram, J. D., Ke, K. & Mayer, M. Noise and Bandwidth of Current Recordings from Submicrometer Pores and Nanopores. *ACS Nano* **2,** 857–872 (2008).
58. Tabard-Cossa, V. in *Engineered Nanopores for Bioanalytical Applications* (eds. Edel, J. B. & Albrecht, T.) 59–93 (William Andrew Publishing, 2013). doi:https://doi.org/10.1016/B978-1-4377-3473-7.00003-0
59. Gurnev, P. A. & Nestorovich, E. M. Channel-Forming Bacterial Toxins in Biosensing and Macromolecule Delivery. *Toxins (Basel).* **6,** 2483–2540 (2014).
60. Bayley, H. Piercing insights. *Nature* **459,** 651 (2009).
61. Dekker, C. Solid-state nanopores. *Nat. Nanotechnol.* **2,** 209–215 (2007).
62. Coloma, M. J. & Morrison, S. L. Design and production of novel tetravalent bispecific antibodies. *Nat. Biotechnol.* **15,** 159 (1997).
63. Braha, O. *et al.* Simultaneous stochastic sensing of divalent metal ions. *Nat. Biotechnol.* **18,** 1005 (2000).

64. Oukhaled, G. *et al.* Unfolding of Proteins and Long Transient Conformations Detected by Single Nanopore Recording. *Phys. Rev. Lett.* **98,** 158101 (2007).
65. Rotem, D., Jayasinghe, L., Salichou, M. & Bayley, H. Protein detection by nanopores equipped with aptamers. *J. Am. Chem. Soc.* **134,** 2781–2787 (2012).
66. Stoddart, D., Heron, A. J., Mikhailova, E., Maglia, G. & Bayley, H. Single-nucleotide discrimination in immobilized DNA oligonucleotides with a biological nanopore. *Proc. Natl. Acad. Sci.* **106,** 7702–7707 (2009).
67. Purnell, R. F. & Schmidt, J. J. Discrimination of Single Base Substitutions in a DNA Strand Immobilized in a Biological Nanopore. *ACS Nano* **3,** 2533–2538 (2009).
68. Kasianowicz, J. J., Brandin, E., Branton, D. & Deamer, D. W. Characterization of individual polynucleotide molecules using a membrane channel. *Proc. Natl. Acad. Sci.* **93,** 13770–13773 (1996).
69. Siwy, Z. S. & Howorka, S. Engineered voltage-responsive nanopores. *Chem. Soc. Rev.* **39,** 1115–1132 (2010).
70. Howorka, S., Cheley, S. & Bayley, H. Sequence-specific detection of individual DNA strands using engineered nanopores. *Nat. Biotechnol.* **19,** 636 (2001).
71. Astier, Y., Braha, O. & Bayley, H. Toward Single Molecule DNA Sequencing: Direct Identification of Ribonucleoside and Deoxyribonucleoside 5‘-Monophosphates by Using an Engineered Protein Nanopore Equipped with a Molecular Adapter. *J. Am. Chem. Soc.* **128,** 1705–1710 (2006).
72. Manrao, E. A. *et al.* Reading DNA at single-nucleotide resolution with a mutant MspA nanopore and phi29 DNA polymerase. *Nat. Biotechnol.* **30,** 349 (2012).
73. Quick, J., Quinlan, A. R. & Loman, N. J. A reference bacterial genome dataset generated on the MinION^{TM} portable single-molecule nanopore sequencer. *Gigascience* **3,** 22 (2014).
74. Siwy, Z. *et al.* Protein biosensors based on biofunctionalized conical gold nanotubes. *J. Am. Chem. Soc.* **127,** 5000–5001 (2005).
75. Bell, N. A. W. & Keyser, U. F. Nanopores formed by DNA origami: A review. *FEBS Lett.* **588,** 3564–3570 (2014).
76. Movileanu, L., Howorka, S., Braha, O. & Bayley, H. Detecting protein analytes that modulate transmembrane movement of a polymer chain within a single protein pore. *Nat. Biotechnol.* **18,** 1091–1095 (2000).
77. Howorka, S. *et al.* A Protein Pore with a Single Polymer Chain Tethered within the Lumen. *J. Am. Chem. Soc.* **122,** 2411–2416 (2000).
78. Wang, Y. *et al.* Nanopore Sensing of Botulinum Toxin Type B by Discriminating an Enzymatically Cleaved Peptide from a Synaptic Protein Synaptobrevin 2 Derivative. *ACS Appl. Mater. Interfaces* **7,** 184–192 (2015).
79. Kukwikila, M. & Howorka, S. Nanopore-Based Electrical and Label-Free Sensing of Enzyme Activity in Blood Serum. *Anal. Chem.* **87,** 9149–9154 (2015).
80. Rosen, C. B., Rodriguez-Larrea, D. & Bayley, H. Single-molecule site-specific detection of protein phosphorylation with a nanopore. *Nat. Biotechnol.* **32,** 179 (2014).
81. Nivala, J., Mulroney, L., Li, G., Schreiber, J. & Akeson, M. Discrimination among Protein Variants Using an Unfoldase-Coupled Nanopore. *ACS Nano* **8,** 12365–12375 (2014).
82. Pastoriza-Gallego, M. *et al.* Dynamics of Unfolded Protein Transport through

an Aerolysin Pore. *J. Am. Chem. Soc.* **133,** 2923–2931 (2011).
83. Payet, L. *et al.* Thermal Unfolding of Proteins Probed at the Single Molecule Level Using Nanopores. *Anal. Chem.* **84,** 4071–4076 (2012).
84. Li, J. *et al.* Ion-beam sculpting at nanometre length scales. *Nature* **412,** 166–169 (2001).
85. Storm, A. J., Chen, J. H., Ling, X. S., Zandbergen, H. W. & Dekker, C. Fabrication of solid-state nanopores with single-nanometre precision. *Nat. Mater.* **2,** 537–540 (2003).
86. Yuan, J. H., He, F. Y., Sun, D. C. & Xia, X. H. A Simple Method for Preparation of Through-Hole Porous Anodic Alumina Membrane. *Chem. Mater.* **16,** 1841–1844 (2004).
87. Park, S. R., Peng, H. & Ling, X. S. Fabrication of nanopores in silicon chips using feedback chemical etching. *Small* **3,** 116–119 (2007).
88. Fleischer, R. L., Price, P. B. & Walker, R. M. *Nuclear tracks in solids: principles and applications*. (Univ of California Press, 1975).
89. Li, N., Yu, S., Harrell, C. C. & Martin, C. R. Conical Nanopore Membranes. Preparation and Transport Properties. *Anal. Chem.* **76,** 2025–2030 (2004).
90. Lepoitevin, M., Ma, T., Bechelany, M., Janot, J.-M. & Balme, S. Functionalization of single solid state nanopores to mimic biological ion channels: A review. *Adv. Colloid Interface Sci.* **250,** 195–213 (2017).
91. Romano-Rodríguez, A. & Hernández-Ramírez, F. Dual-beam focused ion beam (FIB): A prototyping tool for micro and nanofabrication. *Microelectron. Eng.* **84,** 789–792 (2007).
92. Larkin, J. *et al.* Slow DNA Transport through Nanopores in Hafnium Oxide Membranes. *ACS Nano* **7,** 10121–10128 (2013).
93. Liu, K., Feng, J., Kis, A. & Radenovic, A. Atomically Thin Molybdenum Disulfide Nanopores with High Sensitivity for DNA Translocation. *ACS Nano* **8,** 2504–2511 (2014).
94. Garaj, S. *et al.* Graphene as a subnanometre trans-electrode membrane. *Nature* **467,** 190 (2010).
95. Merchant, C. A. *et al.* DNA Translocation through Graphene Nanopores. *Nano Lett.* **10,** 2915–2921 (2010).
96. Crick, C. R., Sze, J. Y. Y., Rosillo-Lopez, M., Salzmann, C. G. & Edel, J. B. Selectively Sized Graphene-Based Nanopores for in Situ Single Molecule Sensing. *ACS Appl. Mater. Interfaces* **7,** 18188–18194 (2015).
97. Garaj, S., Liu, S., Golovchenko, J. A. & Branton, D. Molecule-hugging graphene nanopores. *Proc. Natl. Acad. Sci.* **110,** 12192–12196 (2013).
98. Schneider, G. F. *et al.* Tailoring the hydrophobicity of graphene for its use as nanopores for DNA translocation. *Nat. Commun.* **4,** 2619 (2013).
99. Banerjee, S. *et al.* Slowing DNA Transport Using Graphene–DNA Interactions. *Adv. Funct. Mater.* **25,** 936–946 (2015).
100. Li, W. *et al.* Single Protein Molecule Detection by Glass Nanopores. *ACS Nano* **7,** 4129–4134 (2013).
101. Plesa, C. *et al.* Fast Translocation of Proteins through Solid State Nanopores. *Nano Lett.* **13,** 658–663 (2013).
102. Pedone, D., Firnkes, M. & Rant, U. Data Analysis of Translocation Events in Nanopore Experiments. *Anal. Chem.* **81,** 9689–9694 (2009).
103. Nir, I., Huttner, D. & Meller, A. Direct Sensing and Discrimination among Ubiquitin and Ubiquitin Chains Using Solid-State Nanopores. *Biophys. J.* **108,** 2340–2349 (2015).

104. Wang, C. *et al.* Atomic Layer Deposition Modified Track-Etched Conical Nanochannels for Protein Sensing. *Anal. Chem.* **87,** 8227–8233 (2015).
105. Sze, J. Y. Y., Ivanov, A. P., Cass, A. E. G. & Edel, J. B. Single molecule multiplexed nanopore protein screening in human serum using aptamer modified DNA carriers. *Nat. Commun.* **8,** 1552 (2017).
106. Bell, N. A. W. & Keyser, U. F. Digitally encoded DNA nanostructures for multiplexed, single-molecule protein sensing with nanopores. *Nat. Nanotechnol.* **11,** 645 (2016).
107. Ali, M. *et al.* Metal Ion Affinity-based Biomolecular Recognition and Conjugation inside Synthetic Polymer Nanopores Modified with Iron–Terpyridine Complexes. *J. Am. Chem. Soc.* **133,** 17307–17314 (2011).
108. Fanzio, P. *et al.* Selective protein detection with a dsLNA-functionalized nanopore. *Biosens. Bioelectron.* **64,** 219–226 (2015).
109. Howorka, S. & Siwy, Z. S. Nanopores as protein sensors. *Nat. Biotechnol.* **30,** 506–507 (2012).
110. Wei, R., Gatterdam, V., Wieneke, R., Tampé, R. & Rant, U. Stochastic sensing of proteins with receptor-modified solid-state nanopores. *Nat. Nanotechnol.* **7,** 257–263 (2012).
111. van den Hout, M. *et al.* Controlling nanopore size, shape and stability. *Nanotechnology* **21,** 115304 (2010).
112. Geng, J. *et al.* Stochastic transport through carbon nanotubes in lipid bilayers and live cell membranes. *Nature* **514,** 612 (2014).
113. Mayer, M. & Yang, J. Engineered Ion Channels as Emerging Tools for Chemical Biology. *Acc. Chem. Res.* **46,** 2998–3008 (2013).
114. Montenegro, J., Ghadiri, M. R. & Granja, J. R. Ion channel models based on self-assembling cyclic peptide nanotubes. *Acc. Chem. Res.* **46,** 2955—2965 (2013).
115. Thomson, A. R. *et al.* Computational design of water-soluble α-helical barrels. *Science (80-.).* **346,** 485–488 (2014).
116. Joh, N. H. *et al.* De novo design of a transmembrane Zn2+-transporting four-helix bundle. *Science (80-.).* **346,** 1520–1524 (2014).
117. Howorka, S. Building membrane nanopores. *Nat. Nanotechnol.* **12,** 619 (2017).
118. Spruijt, E., Tusk, S. E. & Bayley, H. DNA scaffolds support stable and uniform peptide nanopores. *Nat. Nanotechnol.* (2018). doi:10.1038/s41565-018-0139-6
119. Henning-Knechtel, A., Knechtel, J. & Magzoub, M. DNA-assisted oligomerization of pore-forming toxin monomers into precisely-controlled protein channels. *Nucleic Acids Res.* **45,** 12057–12068 (2017).
120. Watson, J. D. & Crick, F. H. C. Molecular structure of nucleic acids. *Nature* **171,** 737–738 (1953).
121. Hong, F., Zhang, F., Liu, Y. & Yan, H. DNA Origami: Scaffolds for Creating Higher Order Structures. *Chem. Rev.* **117,** 12584–12640 (2017).
122. Hunter, C. A. & Sanders, J. K. M. The nature of .pi.-.pi. interactions. *J. Am. Chem. Soc.* **112,** 5525–5534 (1990).
123. Drew, H. R. *et al.* Structure of a B-DNA dodecamer: conformation and dynamics. *Proc. Natl. Acad. Sci. U. S. A.* **78,** 2179–2183 (1981).
124. Rothemund, P. W. K. Folding DNA to create nanoscale shapes and patterns. *Nature* **440,** 297–302 (2006).
125. Nanthakumar, A., Pon, R. T., Mazumder, A., Yu, S. & Watson, A. Solid-phase oligonucleotide synthesis and flow cytometric analysis with microspheres encoded with covalently attached fluorophores. *Bioconjug. Chem.* **11,** 282–288

(2000).
126. Seeman, N. C. Nucleic acid junctions and lattices. *J. Theor. Biol.* **99,** 237–247 (1982).
127. Holliday, R. A mechanism for gene conversion in fungi. *Genet. Res.* **5,** 282–304 (1964).
128. Holthausen, J. T., Wyman, C. & Kanaar, R. Regulation of DNA strand exchange in homologous recombination. *DNA Repair (Amst).* **9,** 1264–1272 (2010).
129. Chan, S. N., Vincent, S. D. & Lloyd, R. G. Recognition and manipulation of branched DNA by the RusA Holliday junction resolvase of Escherichia coli. *Nucleic Acids Res.* **26,** 1560–1566 (1998).
130. Wang, Y. L., Mueller, J. E., Kemper, B. & Seeman, N. C. Assembly and characterization of five-arm and six-arm DNA branched junctions. *Biochemistry* **30,** 5667—5674 (1991).
131. Wang, X. & Seeman, N. C. Assembly and Characterization of 8-Arm and 12-Arm DNA Branched Junctions. *J. Am. Chem. Soc.* **129,** 8169–8176 (2007).
132. Seeman, N. C. Nanomaterials based on DNA. *Annu. Rev. Biochem.* **79,** 65–87 (2010).
133. Seeman, N. C. DNA in a material world. *Nature* **421,** 427 (2003).
134. Chen, J. & Seeman, N. C. Synthesis from DNA of a molecule with the connectivity of a cube. *Nature* **350,** 631–633 (1991).
135. Seeman, N. C. DNA nanotechnology: novel DNA constructions. *Annu. Rev. Biophys. Biomol. Struct.* **27,** 225–248 (1998).
136. Goodman, R. P., Berry, R. M. & Turberfield, A. J. The single-step synthesis of a DNA tetrahedron. *Chem. Commun.* 1372–1373 (2004).
137. Mitchell, N., Ebner, A., Hinterdorfer, P., Tampé, R. & Howorka, S. Chemical Tags Mediate the Orthogonal Self-Assembly of DNA Duplexes into Supramolecular Structures. *small* **6,** 1732–1735 (2010).
138. Nangreave, J., Han, D., Liu, Y. & Yan, H. DNA origami: a history and current perspective. *Curr. Opin. Chem. Biol.* **14,** 608–615 (2010).
139. Kuzuya, A. & Komiyama, M. DNA origami: fold, stick, and beyond. *Nanoscale* **2,** 309–321 (2010).
140. Tørring, T., Voigt, N. V, Nangreave, J., Yan, H. & Gothelf, K. V. DNA origami: a quantum leap for self-assembly of complex structures. *Chem. Soc. Rev.* **40,** 5636–5646 (2011).
141. Fu, T. J. & Seeman, N. C. DNA double-crossover molecules. *Biochemistry* **32,** 3211–3220 (1993).
142. Andersen, E. S. *et al.* Self-assembly of a nanoscale DNA box with a controllable lid. *Nature* **459,** 73–6 (2009).
143. Qian, L. *et al.* Analogic China map constructed by DNA. *Chinese Sci. Bull.* **51,** 2973–2976 (2006).
144. Andersen, E. S. *et al.* DNA Origami Design of Dolphin-Shaped Structures with Flexible Tails. *ACS Nano* **2,** 1213–1218 (2008).
145. Douglas, S. M. *et al.* Self-assembly of DNA into nanoscale three-dimensional shapes. *Nature* **459,** 414–418 (2009).
146. Han, D. *et al.* DNA origami with complex curvatures in three-dimensional space. *Science* **332,** 342–346 (2011).
147. Han, D., Pal, S., Liu, Y. & Yan, H. Folding and cutting DNA into reconfigurable topological nanostructures. *Nat. Nanotechnol.* **5,** 712 (2010).
148. Endo, M., Hidaka, K., Kato, T., Namba, K. & Sugiyama, H. DNA prism

structures constructed by folding of multiple rectangular arms. *J. Am. Chem. Soc.* **131,** 15570–15571 (2009).
149. Ke, Y. *et al.* Scaffolded DNA origami of a DNA tetrahedron molecular container. *Nano Lett.* **9,** 2445–2447 (2009).
150. Ke, Y. *et al.* Multilayer DNA origami packed on a square lattice. *J. Am. Chem. Soc.* **131,** 15903–8 (2009).
151. Dietz, H., Douglas, S. M. & Shih, W. M. Folding DNA into Twisted and Curved Nanoscale Shapes. *Science* **325,** 725–730 (2009).
152. Castro, C. E. *et al.* A primer to scaffolded DNA origami. *Nat. Methods* **8,** 221–229 (2011).
153. Ke, Y., Bellot, G., Voigt, N. V, Fradkov, E. & Shih, W. M. Two design strategies for enhancement of multilayer-DNA-origami folding: underwinding for specific intercalator rescue and staple-break positioning. *Chem. Sci.* **3,** 2587–2597 (2012).
154. Douglas, S. M. *et al.* Rapid prototyping of 3D DNA-origami shapes with caDNAno. *Nucleic Acids Res.* **37,** 5001–5006 (2009).
155. Kim, D.-N., Kilchherr, F., Dietz, H. & Bathe, M. Quantitative prediction of 3D solution shape and flexibility of nucleic acid nanostructures. *Nucleic Acids Res.* **40,** 2862–2868 (2012).
156. Iinuma, R. *et al.* Polyhedra Self-Assembled from DNA Tripods and Characterized with 3D DNA-PAINT. *Science (80-.).* **344,** 65 LP-69 (2014).
157. Wenyan, L., Hong, Z., Risheng, W. & C., S. N. Crystalline Two-Dimensional DNA-Origami Arrays. *Angew. Chemie Int. Ed.* **50,** 264–267
158. Wang, P. *et al.* Programming Self-Assembly of DNA Origami Honeycomb Two-Dimensional Lattices and Plasmonic Metamaterials. *J. Am. Chem. Soc.* **138,** 7733–7740 (2016).
159. Woo, S. & Rothemund, P. W. K. Programmable molecular recognition based on the geometry of DNA nanostructures. *Nat. Chem.* **3,** 620 (2011).
160. Tikhomirov, G., Petersen, P. & Qian, L. Programmable disorder in random DNA tilings. *Nat. Nanotechnol.* **12,** 251 (2016).
161. Yan, H., LaBean, T. H., Feng, L. & Reif, J. H. Directed nucleation assembly of DNA tile complexes for barcode-patterned lattices. *Proc. Natl. Acad. Sci.* **100,** 8103–8108 (2003).
162. Gerling, T., Wagenbauer, K. F., Neuner, A. M. & Dietz, H. Dynamic DNA devices and assemblies formed by shape-complementary, non-base pairing 3D components. *Science (80-.).* **347,** 1446–1452 (2015).
163. Saminathan, R., Georg, K., Guido, G., Michael, S. & Adrian, K. Cation-Induced Stabilization and Denaturation of DNA Origami Nanostructures in Urea and Guanidinium Chloride. *Small* **13,** 1702100
164. Wei, X., Nangreave, J., Jiang, S., Yan, H. & Liu, Y. Mapping the Thermal Behavior of DNA Origami Nanostructures. *J. Am. Chem. Soc.* **135,** 6165–6176 (2013).
165. Lee Tin Wah, J., David, C., Rudiuk, S., Baigl, D. & Estevez-Torres, A. Observing and Controlling the Folding Pathway of DNA Origami at the Nanoscale. *ACS Nano* **10,** 1978–1987 (2016).
166. Sobczak, J.-P. J., Martin, T. G., Gerling, T. & Dietz, H. Rapid Folding of DNA into Nanoscale Shapes at Constant Temperature. *Science (80-.).* **338,** 1458–1461 (2012).
167. Fu, Y. *et al.* Single-Step Rapid Assembly of DNA Origami Nanostructures for Addressable Nanoscale Bioreactors. *J. Am. Chem. Soc.* **135,** 696–702 (2013).

168. Song, J. *et al.* Direct Visualization of Transient Thermal Response of a DNA Origami. *J. Am. Chem. Soc.* **134,** 9844–9847 (2012).
169. Martin, T. G. & Dietz, H. Magnesium-free self-assembly of multi-layer DNA objects. *Nat. Commun.* **3,** 1103 (2012).
170. Dunn, K. E. *et al.* Guiding the folding pathway of DNA origami. *Nature* **525,** 82 (2015).
171. Dannenberg, F. *et al.* Modelling DNA origami self-assembly at the domain level. *J. Chem. Phys.* **143,** 165102 (2015).
172. Funke, J. J. & Dietz, H. Placing molecules with Bohr radius resolution using DNA origami. *Nat. Nanotechnol.* **11,** 47 (2015).
173. Martin, T. G. *et al.* Design of a molecular support for cryo-EM structure determination. *Proc. Natl. Acad. Sci.* **113,** E7456--E7463 (2016).
174. Sharma, J. *et al.* Control of Self-Assembly of DNA Tubules Through Integration of Gold Nanoparticles. *Science (80-.).* **323,** 112–116 (2009).
175. Kumar, A., Hwang, J.-H., Kumar, S. & Nam, J.-M. Tuning and assembling metal nanostructures with DNA. *Chem. Commun.* **49,** 2597–2609 (2013).
176. Huang, D., Freeley, M. & Palma, M. DNA-Mediated Patterning of Single Quantum Dot Nanoarrays: A Reusable Platform for Single-Molecule Control. *Sci. Rep.* **7,** 45591 (2017).
177. Rahman, M., Neff, D. & Norton, M. L. Rapid, high yield, directed addition of quantum dots onto surface bound linear DNA origami arrays. *Chem. Commun.* **50,** 3413–3416 (2014).
178. Doane, T. L., Alam, R. & Maye, M. M. Functionalization of quantum rods with oligonucleotides for programmable assembly with DNA origami. *Nanoscale* **7,** 2883—2888 (2015).
179. Maune, H. T. *et al.* Self-assembly of carbon nanotubes into two-dimensional geometries using DNA origami templates. *Nat. Nanotechnol.* **5,** 61 (2009).
180. Stein, I. H., Steinhauer, C. & Tinnefeld, P. Single-molecule four-color FRET visualizes energy-transfer paths on DNA origami. *J. Am. Chem. Soc.* **133,** 4193–4195 (2011).
181. Voigt, N. V *et al.* Single-molecule chemical reactions on DNA origami. *Nat. Nanotechnol.* **5,** 200–203 (2010).
182. Linko, V., Eerikäinen, M. & Kostiainen, M. A. A modular DNA origami-based enzyme cascade nanoreactor. *Chem. Commun.* **51,** 5351–5354 (2015).
183. Barbara, S. *et al.* Orthogonal Protein Decoration of DNA Origami. *Angew. Chemie Int. Ed.* **49,** 9378–9383 (2010).
184. Lyumkis, D. *et al.* Cryo-EM structure of a fully glycosylated soluble cleaved HIV-1 Env trimer. *Science* **342,** 1484–1490 (2013).
185. Bai, X., Martin, T. G., Scheres, S. H. W. & Dietz, H. Cryo-EM structure of a 3D DNA-origami object. *Proc. Natl. Acad. Sci.* **109,** 20012–20017 (2012).
186. Ketterer, P. *et al.* DNA origami scaffold for studying intrinsically disordered proteins of the nuclear pore complex. *Nat. Commun.* **9,** 902 (2018).
187. Fisher, P. D. E. *et al.* A Programmable DNA Origami Platform for Organizing Intrinsically Disordered Nucleoporins within Nanopore Confinement. *ACS Nano* **12,** 1508–1518 (2018).
188. Tan, S. J., Campolongo, M. J., Luo, D. & Cheng, W. Building plasmonic nanostructures with DNA. *Nat. Nanotechnol.* **6,** 268–276 (2011).
189. Ozbay, E. Plasmonics: Merging Photonics and Electronics at Nanoscale Dimensions. *Science (80-.).* **311,** 189–193 (2006).
190. Mirkin, C. A., Letsinger, R. L., Mucic, R. C. & Storhoff, J. J. A DNA-based

method for rationally assembling nanoparticles into macroscopic materials. *Nature* **382,** 607–609 (1996).
191. Rosi, N. L. *et al.* Oligonucleotide-modified gold nanoparticles for intracellular gene regulation. *Science* **312,** 1027–1030 (2006).
192. Yang, J., Lee, J. Y., Deivaraj, T. C. & Too, H.-P. Single Stranded DNA Induced Assembly of Gold Nanoparticles. (2004).
193. Ding, B. *et al.* Gold nanoparticle self-similar chain structure organized by DNA origami. *J. Am. Chem. Soc.* **132,** 3248–3249 (2010).
194. Pal, S., Deng, Z., Ding, B., Yan, H. & Liu, Y. DNA-Origami-Directed Self-Assembly of Discrete Silver-Nanoparticle Architectures. *Angew. Chemie* **122,** 2760–2764 (2010).
195. Kuzyk, A. *et al.* DNA-based self-assembly of chiral plasmonic nanostructures with tailored optical response. *Nature* **483,** 311–314 (2012).
196. Liu, W. *et al.* Diamond family of nanoparticle superlattices. *Science (80-.).* **351,** 582 LP-586 (2016).
197. Ellington, A. D. & Szostak, J. W. In vitro selection of RNA molecules that bind specific ligands. *Nature* **346,** 818 (1990).
198. Rinker, S., Ke, Y., Liu, Y., Chhabra, R. & Yan, H. Self-assembled DNA nanostructures for distance-dependent multivalent ligand–protein binding. *Nat. Nanotechnol.* **3,** 418–422 (2008).
199. Douglas, S. M., Bachelet, I. & Church, G. M. A Logic-Gated Nanorobot for Targeted Transport of Molecular Payloads. *Science (80-.).* **335,** 831–834 (2012).
200. Yoshina-Ishii, C. & Boxer, S. G. Arrays of Mobile Tethered Vesicles on Supported Lipid Bilayers. *J. Am. Chem. Soc.* **125,** 3696–3697 (2003).
201. Baldelli Bombelli, F. *et al.* Closed nanoconstructs assembled by step-by-step ss-DNA coupling assisted by phospholipid membranes. *Soft Matter* **5,** 1639–1645 (2009).
202. Perrault, S. D. & Shih, W. M. Virus-Inspired Membrane Encapsulation of DNA Nanostructures To Achieve In Vivo Stability. *ACS Nano* **8,** 5132–5140 (2014).
203. Johnson-Buck, A., Jiang, S., Yan, H. & Walter, N. G. DNA–Cholesterol Barges as Programmable Membrane-Exploring Agents. *ACS Nano* **8,** 5641–5649 (2014).
204. Jonathan, L., Michael, W. & C., S. F. Hydrophobic Actuation of a DNA Origami Bilayer Structure. *Angew. Chemie Int. Ed.* **53,** 4236–4239 (2014).
205. Aleksander, C. *et al.* Amphipathic DNA Origami Nanoparticles to Scaffold and Deform Lipid Membrane Vesicles. *Angew. Chemie Int. Ed.* **54,** 6501–6505 (2015).
206. Kocabey, S. *et al.* Membrane-Assisted Growth of DNA Origami Nanostructure Arrays. *ACS Nano* **9,** 3530–3539 (2015).
207. Franquelim, H. G., Khmelinskaia, A., Sobczak, J.-P., Dietz, H. & Schwille, P. Membrane sculpting by curved DNA origami scaffolds. *Nat. Commun.* **9,** 811 (2018).
208. Howorka, S. Changing of the guard. *Science (80-.).* **352,** 890–891 (2016).
209. Zhang, Z., Yang, Y., Pincet, F., Llaguno, M. C. & Lin, C. Placing and shaping liposomes with reconfigurable DNA nanocages. *Nat. Chem.* **9,** 653 (2017).
210. Pugh, G. C., Burns, J. R. & Howorka, S. Comparing proteins and nucleic acids for next-generation biomolecular engineering. *Nat. Rev. Chem.* **2,** 113–130 (2018).

211. Yuanchen, D. *et al.* Cuboid Vesicles Formed by Frame-Guided Assembly on DNA Origami Scaffolds. *Angew. Chemie Int. Ed.* **56,** 1586–1589 (2017).
212. Burns, J. R., Stulz, E. & Howorka, S. Self-assembled DNA nanopores that span lipid bilayers. *Nano Lett.* **13,** 2351–2356 (2013).
213. Gopfrich, K. *et al.* Ion channels made from a single membrane-spanning DNA duplex. *Nano Lett.* **16,** 4665–4669 (2016).
214. Bell, N. A. W. *et al.* DNA origami nanopores. *Nano Lett.* **12,** 512–517 (2011).
215. Burns, J. R., Al-Juffali, N., Janes, S. M. & Howorka, S. Membrane-spanning DNA nanopores with cytotoxic effect. *Angew. Chem. Int. Ed. Engl.* **53,** 12466–70 (2014).
216. Göpfrich, K. *et al.* DNA-tile structures induce ionic currents through lipid membranes. *Nano Lett.* **15,** 3134–3138 (2015).
217. Messager, L. *et al.* Biomimetic Hybrid Nanocontainers with Selective Permeability. *Angew. Chemie - Int. Ed.* **55,** 11106–11109 (2016).
218. Burns, J. R. & Howorka, S. Defined Bilayer Interactions of DNA Nanopores Revealed with a Nuclease-Based Nanoprobe Strategy. *ACS Nano* **12,** 3263–3271 (2018).
219. Birkholz, O. *et al.* Multi-functional DNA nanostructures that puncture and remodel lipid membranes into hybrid materials. *Nat. Commun.* **9,** 1521 (2018).
220. Maingi, V., Lelimousin, M., Howorka, S. & Sansom, M. S. P. Gating-like Motions and Wall Porosity in a DNA Nanopore Scaffold Revealed by Molecular Simulations. *ACS Nano* **9,** 11209–11217 (2015).
221. Maingi, V. *et al.* Stability and dynamics of membrane-spanning DNA nanopores. **8,** 14784 (2017).
222. Wei, R., Martin, T. G., Rant, U. & Dietz, H. DNA Origami Gatekeepers for Solid-State Nanopores. *Angew. Chemie* **124,** 4948–4951 (2012).
223. Hernández-Ainsa, S. *et al.* DNA origami nanopores for controlling DNA translocation. *ACS Nano* **7,** 6024–6030 (2013).
224. Plesa, C. *et al.* Ionic permeability and mechanical properties of DNA origami nanoplates on solid-state nanopores. *ACS Nano* **8,** 35–43 (2013).
225. Langecker, M. *et al.* Synthetic lipid membrane channels formed by designed DNA nanostructures. *Science* **338,** 932–936 (2012).
226. Krishnan, S. *et al.* Molecular transport through large-diameter DNA nanopores. *Nat. Commun.* **7,** (2016).
227. Nakajima, K., Utsumi, H., Kazama, M. & Hamada, A. Alpha-tocopherol-induced hexagonal HII phase formation in egg yolk phosphatidylcholine membranes. *Chem. Pharm. Bull. (Tokyo).* **38,** 1–4 (1990).
228. Anke, K. *et al.* Lipid-Anchored Oligonucleotides for Stable Double-Helix Formation in Distinct Membrane Domains. *Angew. Chemie Int. Ed.* **45,** 4440–4444 (2006).
229. Göpfrich, K. *et al.* Large-Conductance Transmembrane Porin Made from DNA Origami. *ACS Nano* **10,** 8207–8214 (2016).
230. Selnihhin, D. & Andersen, E. S. Computer-aided design of DNA origami structures. *Methods Mol. Biol.* **1244,** 23–44 (2015).
231. Method for cloning and producing the SnaBI restriction endonuclease and purification of the recombinant SnaBI restriction endonuclease. (2000).
232. Wei, H., Therrien, C., Blanchard, A., Guan, S. & Zhu, Z. The Fidelity Index provides a systematic quantitation of star activity of DNA restriction endonucleases. *Nucleic Acids Res.* **36,** e50–e50 (2008).
233. Ali, A. R., Tobias, P., B., S. M., Anna, K. & C., S. F. Surface-Assisted Large-

Scale Ordering of DNA Origami Tiles. *Angew. Chemie Int. Ed.* **53,** 7665–7668 (2014).
234. Murray, M. N. *et al.* Atomic force microscopy of biochemically tagged DNA. *Proc. Natl. Acad. Sci. U. S. A.* **90,** 3811–3814 (1993).
235. Schmied, J. J. *et al.* DNA origami–based standards for quantitative fluorescence microscopy. *Nat. Protoc.* **9,** 1367 (2014).
236. Edwardson, T. G. W., Carneiro, K. M. M., McLaughlin, C. K., Serpell, C. J. & Sleiman, H. F. Site-specific positioning of dendritic alkyl chains on DNA cages enables their geometry-dependent self-assembly. *Nat. Chem.* **5,** 868 (2013).
237. Goyal, P. *et al.* Structural and mechanistic insights into the bacterial amyloid secretion channel CsgG. *Nature* **516,** 250–253 (2014).
238. Baaken, G., Ankri, N., Schuler, A.-K., Rühe, J. & Behrends, J. C. Nanopore-Based Single-Molecule Mass Spectrometry on a Lipid Membrane Microarray. *ACS Nano* **5,** 8080–8088 (2011).
239. del Rio Martinez Juan M., Ekaterina, Z., Sönke, P., Gerhard, B. & C., B. J. Automated Formation of Lipid Membrane Microarrays for Ionic Single-Molecule Sensing with Protein Nanopores. *Small* **11,** 119–125 (2015).
240. Rosenbusch, J. P. The critical role of detergents in the crystallization of membrane proteins. *J. Struct. Biol.* **104,** 134–138 (1990).
241. Hille, B. *Ion channels of excitable membranes*. (Sinauer Associates, Inc, 2001).
242. Bayley, H. *et al.* Droplet interface bilayers. *Mol. Biosyst.* **4,** 1191–1208 (2008).
243. Renner, S., Geltinger, S. & Simmel, F. C. Nanopore translocation and force spectroscopy experiments in microemulsion droplets. *Small* **6,** 190–194 (2010).
244. Howorka, S. DNA Nanoarchitectonics: Assembled DNA at Interfaces. *Langmuir* **29,** 7344–7353 (2013).
245. Göpfrich, K. *et al.* Ion Channels Made from a Single Membrane-Spanning DNA Duplex. *Nano Lett.* **16,** 4665–4669 (2016).
246. Gut, I. G. & Beck, S. A procedure for selective DNA alkylation and detection by mass spectrometry. *Nucleic Acids Res.* **23,** 1367–1373 (1995).
247. Beales, P. A. & Vanderlick, T. K. DNA as membrane-bound ligand-receptor pairs: duplex stability is tuned by intermembrane forces. *Biophys. J.* **96,** 1554–65 (2009).
248. Rogers, P. H. *et al.* Selective, controllable, and reversible aggregation of polystyrene latex microspheres via DNA hybridization. *Langmuir* **21,** 5562–9 (2005).
249. Liu, D.-Z., Chen, W.-Y., Tasi, L.-M. & Yang, S.-P. Microcalorimetric and shear studies on the effects of cholesterol on the physical stability of lipid vesicles. *Colloids Surfaces A Physicochem. Eng. Asp.* **172,** 57–67 (2000).
250. Lin, C., Perrault, S. D., Kwak, M., Graf, F. & Shih, W. M. Purification of DNA-origami nanostructures by rate-zonal centrifugation. *Nucleic Acids Res.* **41,** e40 (2013).
251. Muyldermans, S. Nanobodies: natural single-domain antibodies. *Annu. Rev. Biochem.* **82,** 775–797 (2013).
252. Antoszczak, M. & Huczynski, A. Bioconjugation of Ionophore Antibiotics: A Way to Obtain Hybrids with Potent Biological Activity. *Mini-Reviews in Organic Chemistry* **14,** 258–271 (2017).
253. Hernández-Ainsa, S. & Keyser, U. F. DNA origami nanopores: Developments, challenges and perspectives. *Nanoscale* **6,** 14121–14132 (2014).
254. Douglas, S. M., Chou, J. J. & Shih, W. M. DNA-nanotube-induced alignment of membrane proteins for NMR structure determination. *Proc. Natl. Acad. Sci.*

104, 6644–6648 (2007).
255. Drabik, A., Bodzoń-Kułakowska, A. & Silberring, J. in *Proteomic Profiling and Analytical Chemistry (Second Edition)* (eds. Ciborowski, P. & Silberring, J.) 115–143 (Elsevier, 2016).
256. Seo, Y. & Jhe, W. Atomic force microscopy and spectroscopy. *Reports Prog. Phys.* **71,** 16101 (2007).
257. Binnig, G., Quate, C. F. & Gerber, C. Atomic force microscope. *Phys. Rev. Lett.* **56,** 930 (1986).
258. Rafferty, J. B. *et al.* Crystal structure of DNA recombination protein RuvA and a model for its binding to the Holliday junction. *Science* **274,** 415–421 (1996).

6. Appendix

6.1 Box Scaffold Plan

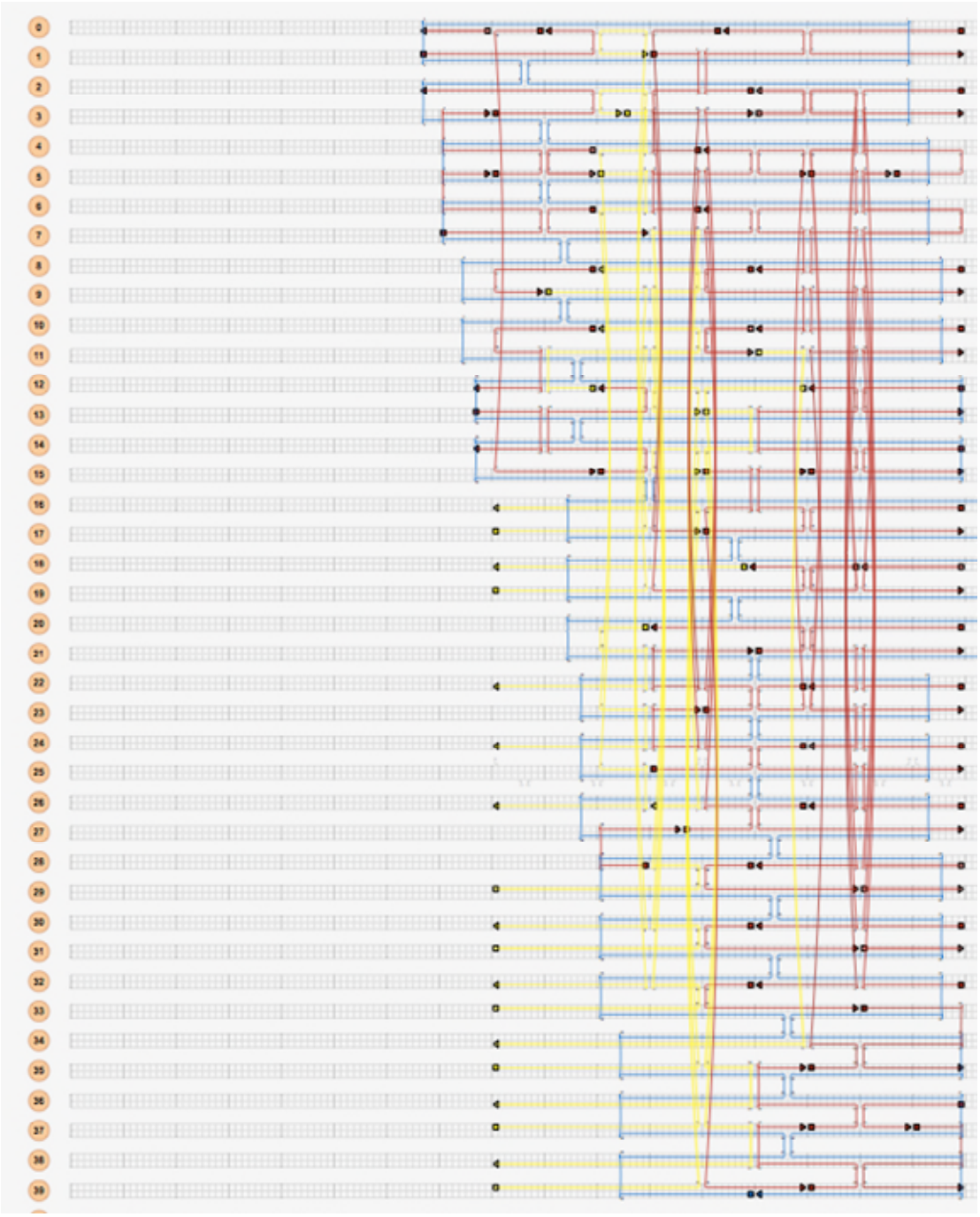

Figure 99 - *Box Scaffold Plan. The scaffold strand is shown in blue, staple strands are labelled in red and strands which hybridise to cholesterol strands are shown in yellow.*

6.2 Box Staple Sequences

0[135]	AAAAAAAATTTTTTTTATTCGCGTCTGGCCTTAACGCCATCAAAAATATTTTTTTTAAAAAAAA
2[135]	AAAAAAAATTTTTTTTACAGGAAGTGACCATAAATCAAAA
5[125]	ACAAAGTTTTTTTTTTGCTATCAGGTCCCCCAAAATTTTTTTTAAAAAAAA
28[135]	AAATTTAAAGATTCATCAGTGTGTAGGTAATTTTTTTTTTAGATTCAAAAGGATCT
8[135]	AAATTTAACATTATGACCCTGTAATACCTGAGTAATTGAGATTTAGGATTA
30[135]	AAATTTGAAAAATCTACGTCGGTTGTACCAAAAAATTT
10[135]	AAATTTTCAATTCTACTAATAGTAGTAAGCTAAATTAATAAAACGAACTGG
32[135]	AAATTTACCTTATGCGATTTGAAAAGGTGGCAAAATTT
24[135]	AAAAATTTTTTCGTTTACCAGTTGCAAAAGAAAAAAATTTTT
26[135]	AAAAATTTTTACATAACGCCATATCATAACCCAAAAATTTTT
29[120]	TTATTACAGGTAGAAATTT
31[120]	AGGACGTTGGGAAAAATTT
4[79]	GGTAATCGCCGTTCTA
0[71]	ACAACCCGTACGCCAGCTGGCGAA
10[103]	ATCCAATATATATTTT
15[96]	AGGTCAGGACCAGACCGTCTATCAGTACAGAC
23[96]	ATACGAGCGCTGTTTCTACCCCGG
13[61]	TTGGGAAGGGCGGCCTCTTCGC
5[112]	TTTTGAGAGGTGAGAAAGGCCGGATGCAATGCTTTTGCGG
30[103]	TTTTTCTTCTTCACCGCCTCATTATACCAGTC
8[103]	GAGAAGCCAAGCCTCAGAGCATAAGCATTAAC
28[87]	GCGGGGAGGTCGGGAAACCTG
3[64]	TGGTGTAGTAAAACTATGTTAAAATTCGATTGACCGTAATGGG
32[103]	CCTGAGAGCAGCAGGCGAAAATTTCAACTTTA
14[135]	AAGAGGTCATTTTTGCAATTGCTCCTTTTGAT
25[88]	TGAGCTAACTCACATTCGGAAGCACGGAGAGGGAGCAAAC
1[53]	GTGGGAACAAACGGCGGCATTAAATTTAGCGAGTA
17[96]	GTTTTGATTGCATCAACAAAGCGAATTAGAGA
15[112]	GTACCTTTGGATGGCTTAGAGCTTCGGTGTCTGGAAGTTTGAACGAGT
2[103]	TTTAAATTTTTTTTAACCAATAGGCCTGTAGCCAGCT
6[95]	AATCACCAATTAATGCTAAAGTGTCACACAAC
10[79]	CAAAGGGTGCCGGAAACGCCATTCCTGCGCAACTG
18[119]	TATAGTCAAACGAGAAATTGTATACAGAAAAGATTGCCTGAGAGGCTTACGACGAT
21[104]	TGTTTAGAAAATGCTTTAAGGTCGACTCTAGA
22[111]	TAGTAAAAAAATAGCGAGAGTCTGGTAGCTAT
16[135]	AATATCGCGTTTTAATTCGAGCTTAAAGATTAAGAGGAAGCCCGAAAG

7[56]	GTATCGGCCTCAGGAATGAGGGGACGACGACACGTGCATC
18[135]	TCTTTACCCTGACTAT
28[103]	ATGAATCGGGGCGCCAGGGTAACGGAACAACA
37[112]	ATTCATTATGAATAAGGCTATAGCAAAGATGC
12[135]	TGATTCCCAATTCTGCCATTCCATATAACAGT
27[93]	TCGTGCCAGCTAATTGCGTATTTTAAAGACAGTCA
24[111]	AAAAACCAATAGTAAGAGCAACACAAAGGAAT
0[63]	TCGGATTCTCC
6[79]	ATATTCAAGATAAATTTTTAGAAC
39[112]	CAGGCGCAGACAAGAACCGTTAAACACTAGAT
15[80]	AGGGGGATGCTGTAGCTCAGTGCGGATCGACATGTTTTAAATTTCGCA
3[104]	TTGATAATAGCAAATA
8[79]	GATAACGCACTCCAGCGCACCGCT
20[135]	ATAAATATTCATTGAATCCCCCTCCTGGATAGGGGGGTAA
1[88]	TCAGCTCAGTAAACGTTTGCATGCCTGCAACAGTTCAGAAGAAGCAAAG
5[64]	TGCCAGTTATGGGCGCATCGTAACGGTCACGT
37[128]	AACGTAACCATCAAGAGTAATCTTTAGGCTGGCTGACCTT
33[120]	ATCATTGTGAATTTTTTAGTAAATTGGGCTTGGAAACACCAGAACGAG
0[98]	TTCATCAACATACGCCAGG
35[112]	CCTGACGAAGATGGTTGCGCGAGCTTAAGAACTGGCTGGC
4[95]	AAGAGAATATCATATGCTGTGTGACGTAATCATGGTCATA
5[80]	GCTGATAATCAATATGCTAATGAGCTGCCCGCTTTTTGCTACGTCAGC
3[84]	GTCACGATGAACCACAATTCAAAGCCTGGGGTTGCTACGTCAGC
12[79]	AATTCAGGGCCATGGTCAATAACCCAAGCGGTTTTTTGCTACGTCAGC
13[96]	CTAAAGTAAATTGCTGCAAGAGTCGAACGTGGACTCCAACGTCAATTTTTTTTGCTACGTCAGC
9[72]	TCTAATTAGCAAAATTTGAGACGGTTTTTGCTACGTCAGC
12[111]	AGATTTAGTTTGACCAATAAATCACCGAGATAGGGTTGAGTGTTGGCTACGTCAGC
11[104]	CATTTGGGTAATCCTGTTTGATGGTGGTTCCGAAATCTTTTTTTTGCTACGTCAGC
18[102]	CGCCCAGTCACGACGTTGTAAAACGACGGCTACGTCAGC
20[87]	GGATCCCCCTCGAATTAATTGTTATCCTTGCTACGTCAGC
39[64]	CTCCGTCTATCTTTTTTTTAGGGCGAAAAACCGGAAGCAAGTGCTGCAAGGCGGCTACGTCAGC
35[64]	CTCCGTCTATCTTTTTTTTGGCAAAATCCCTTTTAGATACATATGCAA
29[64]	CTCCGTCTATCTTTTTAGGCGGTTTGCGTATTGCCAACGCCCTCATATTGCGCTCA
33[64]	CTCCGTCTATCTTTTTCCACGCTGGTTTGCCCAGTTGCAGTGTTTAGCAATCATACAGGCAAGG
19[64]	CTCCGTCTATCGCCAGTGCCAAGCTAATATTTGCAT

31[64]	CTCCGTCTATCTTTTTGCAACAGCTGATTGCCTTCACCAGAAGCAATATTTATTTCAACGCAAG
17[64]	CTCCGTCTATCATTAAGTTGGGTATAAATGTGTTGTTAAA
37[64]	CTCCGTCTATCTTTTTTTTTTCCAGTTTGGAAAATATAATACTCCAAC
Cholesterol 3 prime	GATAGACGGAG/3CholTEG/
Cholesterol 5 prime	5chol/GCTGACGTAGC

Table 9 – *Box DNA sequences. Staples are shown in green. Staples which hybridise to cholesterol strands are shown in yellow, with regions that hybridise to cholesterol strands shown in green and red. Cholesterol strands are shown in orange.*

6.3 Funnel Scaffold Plan

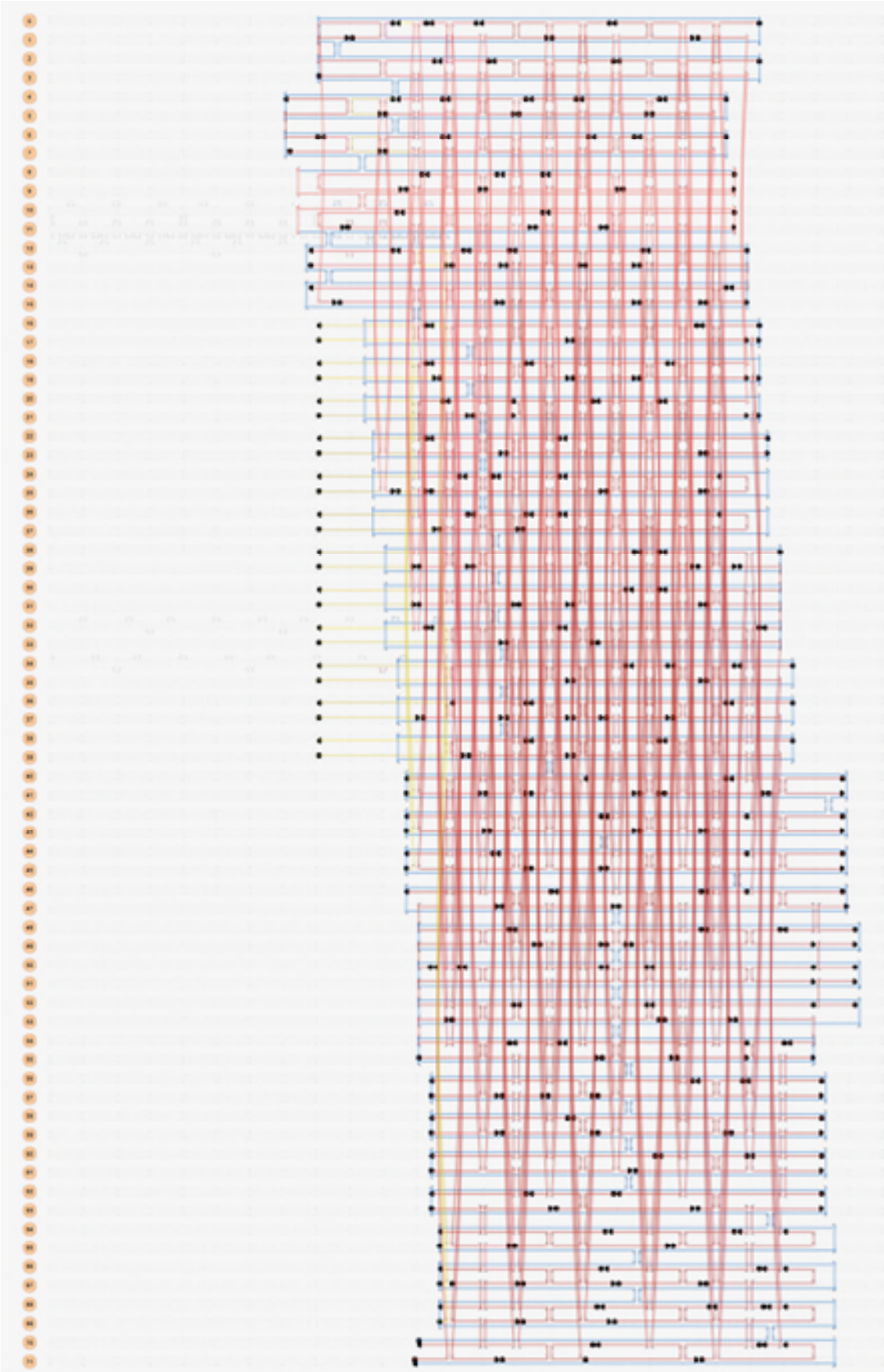

Figure 100 - *Funnel Scaffold Plan. The scaffold strand is shown in blue, staple strands are labelled in red and strands which hybridise to cholesterol strands are shown in yellow.*

6.4 Funnel Staple Sequences

Name	Sequence
47[136]	GGAACAAATCATATATCCCACAAGCTTACCGAAGCTTGATTTCGGTCG
71[156]	AAATGTTACAAAATCGCGCAAAA
35[125]	TAACACCACCAGAGCCACC
44[190]	GAAGGGTTAGAACCTTATACTTCTGAATAA
45[115]	CATTAAGTAAGCATGAGCGCTCCCTGAACTCTGG
0[102]	CCAAGCGTTGAGCCAAGGTGAATGTCA
33[109]	GTGCATTAATTAGCTCGAATTCGTAATC
52[111]	AAAATTCGAACCAATACTCCCGACAAAGCACTC
62[135]	ACGGCCAGTAGCTGTTTCCTGTGTGAAATTGTTAT
65[149]	CTCAAGTGTAAGAATCATAACCGAGTAAAAGAACG
22[90]	TAAGAAGAAAATCTACAAAGCCGGAGACAGTCAAATCAC
4[94]	GGCTCCATTAATTGTCGAAC
34[164]	TATTTCAGAGCGGATGGTTGCTTTGACGAACGCT
32[122]	GGCTGAATTTAGCCTTGAGT
44[106]	AAAGTTACCAGATAAAAGAGGACTAAAGCGATTATA
48[156]	TGAGTCAGAAGGAGCGGAATTATCATCATATATAATCAGC
57[131]	CGCACTTCCAAGAAGATAAGTGTATAGCCGGATTAGGA
31[125]	AACAACATGTTCAAGAGAACGGAATAGG
25[133]	GATAATTTGCCTTGCTAAAGCGAATAAT
0[82]	AACTAGCAACGGCTACAGAGTC
10[118]	AACAGTGAGACTCCTCAGCTAATGCAGATAAGGCT
56[166]	AGAACCCCCAGTCACACCAATCAATCCT
70[130]	AGAACGTGGACATCAAGTTTTCAATTATTGCTCCTGCT
13[128]	ACCGGAACCAGTAGCGTAATT
31[112]	ATTTAACAAGCTGGCGAACTGTTGGGAAGGGCCGG
20[94]	AGAACTGATAAAGCTAAAGGGTGAGA
2[170]	AACCATCGCCCCACTACGACTTATTACACCAGCGC
43[141]	TTTATTTCGCAATCAATAGGAGGGAGGGCACC
27[113]	ATCGAGAAGATGGGCGGAACAAACGGCGGATTGAC
10[83]	TATTTCGGATAATCTTGACAATTATAT
62[114]	TGCGGGTTTTCCCAGTCACATTACGCCACGCC
12[167]	CCACCCTCAAGACAAAGAGTC
24[122]	CAAATAAGAAAATCGTAAAAAACAAGAGAATC
25[157]	CTAAAGCATCACAATATCTGGTCAGTTGCACTAACGCAGCCTTTACAG
19[141]	GAACGTAGAAATTAAACGGGAATACACT
52[193]	CCACGCTGAGAAAGGAATTG
28[175]	ATGTAGAAACGACCAGAATACCTACATTTTGATTA
1[120]	CATGAGGATGCAGGGACGAGG
66[132]	AACGCGCGGGGAGGCAACAGCCTACCTTTGTCGC
26[114]	AACGGAACGCCGCCAGCTTT
56[185]	CATTCTGGCCTCTTTAAT

20[111]	GATAGCCGATCAGCTTCCGCTT
35[157]	CGCAGAGCCACGCCACCCTCAGAACCGACCAA
13[141]	CCCTCATAGGTAAATGCTGAACAATCGGCC
52[143]	AACCTCAACCACCAGCGTATTCTATATTTTCACCT
32[90]	TGCCTCATTAAATGCCCCCTGCC
19[125]	AAATTAAGAAATGACCCTGTAATA
41[115]	GTAGCGGAAATTAACGGAATAGACCCCCAGACTTTTT
64[164]	AGCCGGAAGCATAGTTAGAATTAGTTAATCCAAT
57[108]	GACAGCCGGAAACCAGGCAAAGCGC
39[125]	GCAATATTGACTCAACATGTTTTAAATATGCA
53[164]	GGCGGTCAGTATTAACACCGGCGCGAA
31[88]	GAATCGTCGACTGGATAAACATGATAGTAC
4[146]	CTAGTCAAAAACGTCTTTCCCCTCAATCCTTGCTG
7[57]	ATGAACGGTGTACAGACTTTGA
37[133]	AATTCAATATAAAATCGG
1[155]	AATGCACGCATAAAGAACTGGAAATAGCATATTTCAAAAA
22[122]	ACAAATATCAGTAATGCCGATTCAACCGTTCTAGC
30[138]	CGACGGCTGGTAATATCCAGAACAATACGCTCAATAAT
54[110]	CATCAACTCTCCGTGGCATCGTAACCGTGCATCTGC
14[162]	TGATAGCGATAAATTACCTTAGCCCGAAGTGTTGTTCCAGTTTCACT
46[120]	TGAGTAATGAATATGATGAGAGGGTA
2[135]	CTGAGGCTAGTTTCCAATACATACTTGTCACAAAT
9[104]	AGAGGCTGCCCGTATATCAGCCAT
45[133]	CTTTTGCGGGAAATAAAGATAACG
8[89]	CGCCACCCTCAGAACAGGCGCATAGGTTCATCAAGAGACCTATTATT
53[96]	CATTTTTTCATTAAATAAAGGAATGAGAT
4[114]	TTGCAATCCAAAATAAACAGAAGATTGATTTTGTT
54[167]	CTAAAACACGCGCCCAAATCAGAT
42[190]	GAGACCCAATTCTGCAGTACCTTTTACATC
61[91]	CGATTAAGTTGGGAATCCCCCTGACCATAAATCA
47[108]	CATCTGTAGGTAAGGGTAAT
0[170]	CACCAACCTAAGAAACGTC
32[170]	ATGAGCAATACAGTGTTTTTATAATCACACAATTCACG
50[132]	CGGTACGATTTTTGAGAATTATCTTAAACAGCCC
12[110]	CCAGCATTGGAAAGCCGTAAAATCAGGTCTTGCCCGCTTGGGCGCCAGGG
38[178]	AATTTCATTTGGCTTAGATGAAA
37[109]	TTCCGGTCCACTTCACCAGT
10[164]	CAGGAGTGTACTGGTAATAAGGGTTTTGCTCTGT
8[107]	ACTCTAGACGCGCCTGTTTACTTCTGGTGTATCGG
15[141]	ATTTACATAAATTTCCCTTCAACCGCCTGGC
68[171]	GCGACCACACCCGCCGCGCTCTACAGGG
24[106]	ATTTTGCGGGACTCATAGTCCACCACCCCGT
37[89]	AAATATCTAGCGCGTTCACCGACCGAAA
29[155]	ATCCCATAATCGGCCGTAACAATAGAAGGCCCAG

16[170]	AGACAAAAGGGAAAATTAAAATAC
64[133]	GCCTAATGAGTGAGGTCGTGCCGGTTTGAATTATA
24[98]	TTAGACGTTAGCAAAAAAAA
60[167]	GAGTAGAAACCGTTGTCGTTATACAAAAAGCCATA
13[109]	CACCGGCAAAAAGATTAAG
17[125]	ATTATAAAGGTACATCCAATAAATTGCGTAGA
15[69]	TGCTCATTCAGTGAATAAGTTTCATCGGCATTTTCGGTCACAACG
48[193]	TAAATCCTTTTTATCAGA
6[129]	AGCATTCCACATGGGATTAGTTA
18[148]	GCAAATACCCAAACCGATATAACCGATAGAACAA
67[113]	GAGACGGAGGCGGTTAGGTTGGGATACCGACGCAG
48[110]	GCTATTTCCTGAGAGAAAGTCAGATTTA
49[139]	TAATATTAGACGGTGTTTAACAAGGAATTCAACTTTC
12[82]	CAGACGATTGGCCTTGCATTA
0[134]	AAAACACCACCAGTAGAAGGTAAAAAGAAGATTATTCAT
6[94]	GATCTAATCTTTCCAGGAATACCGAAAGATTCCGG
59[91]	CATTCGCCATTCAAATGTTTAATAAATATAACAGTTAAGCCAGAATGAC
50[183]	TAAAATATCTTTAGGAGGCAAATCAACAGTTG
71[87]	GGGCGATGGTTTTGCGGATG
4[162]	GAATAGAAAGGTTGCGCCGAAAACAGGTAAGCCCAGTT
18[90]	TGGTGGCATCATAAAGCCTCAG
40[190]	AACGGATTCGCCTGAAACAGTTGATTAACA
37[149]	CCTTATCAAAATCAGAGCCCACCCTCAG
69[135]	CAAAATCCCTTATAAATGGCGCTGGAGAAT
52[183]	AGCCAGCAGCAAATGAAAAATCTACAATTTTATACCAACG
43[157]	CAGTTGCACGTAAAACAGAGAAGCCTTATAGC
50[143]	CCGTCAATATATCAAACAGAGCCTTAGTTGCTACT
29[165]	AATTTACGAGCAGTACCGAAGCCATTGACTTGCCT
31[157]	CAGAAAGTAATTCAGTACCAGGCG
59[108]	GCGCAAAGGGGGATGTGCTGCAAGG
13[62]	CAAATTAGCCCCCTTATTAGCGTTTGCAGGT
55[150]	AGACAATATTTTTGAATG
39[100]	GGATGAGGTCATCCCACTACGTGA
20[130]	TTTCGCAATAAAATCATACAGGCAAGGCAAAGAATAAA
50[91]	TTGAGGCTATCAGGTCATTGTTGAGAGAATCTA
29[88]	TTGCCAGACGAGAGGCACCGCCACATAGTAAGTAA
68[158]	GCGCTAGCAAAAGAATTTTTAATAAGAAAACCGAC
26[100]	GAGGCCCTCAGAGTAGCGTAAC
41[147]	GTACGAACCGATTAAAATTCAAGGCAAAAGTAAAATACGT
46[156]	ATTTTTAGAACCCGAAACCACAACATTATCATTTTGCAGA
23[157]	ATAAACTAATAGATTTAGAAGTATTAGTTTTAAAAATAATAAG
30[146]	CCAAGAAAAATCGTCTGAAATGGAAGCCAGCTTTCGAT
33[131]	AGAATAATTTAATAGCTGCATTAATGGTGCTTTC

19[93]	CTTATGCGAAATTAAGCAAATTCTACTA
48[175]	GTTATTAAACTTTACAAACAATTC
34[138]	CTAAAACACCGAGCCTGGGGT
36[178]	GACGCTGAGAAGAACGCGACGCGT
29[101]	TAAAGGAGGTTAAGTATTA
49[133]	GATTGATAAATAGAGATAATTTAAATGCAATGCC
70[170]	TTGGATAGCCGGCGAACGTGAAGGGAA
42[132]	GGTCAATAACCTGTTTAGCTATAGCATTAGGCAA
67[157]	GCGAGTGAATTTGAAAACAAACCATCGCAAGG
11[116]	TCTCTTAATTGAGAATCTTGTAACGCCACTGCAGGTCGACTCTAGAGGA
23[109]	TCCAAAATCTCTAAATGAA
12[99]	AGGAAAGCGGATTGCATCTTTGCGTATTTCCAGTC
3[64]	TTGTGTCGAAATCCGCAAAGACAGCATATAAAGCCTGCGG
36[162]	AATCGTAACCAAAGGAGCGG
58[124]	CACCGTCAACAATACGGGTATCAGGGATAAGGCG
63[121]	ATGGTCATGCCAAGCGGCGTTAAAGTAG
2[92]	ACCCTCAGCAGCGGACAGCCTAAAGG
71[108]	ACCATCACCCAATCCAACGTACCTTTAAAATAA
67[96]	TTTTTCTTGCTGGTTTGCC
43[105]	ATAGTAGTATTTTCAAAGACACCTTCATTAATTTG
8[164]	GATAAGTGCCGTCGAGAGGGTCCCATGTACTGTC
57[91]	CAGTTTGAGGGGACAAAATAGGGGGG
16[155]	ATTCGTGTCTGGTTTGACCATTAGATACTCAGGTTTTTA
44[167]	AAAATTATATGAATATACAGTAACGAACGAGTCAA
46[190]	GATGGCAATTCATCAATTCCTGAGCCCGAAC
1[72]	AACGAGGGGGAGATTTGTATCATCAAAGC
18[114]	CATAAGGAAACGTTAAAGGGCTTTCGATCACG
42[167]	AGATTTAGAAGTTTCATTCC
11[133]	CCAACCAGAACCTATATGTCTGAGAGATGATTGCC
40[162]	CAACGGAACCCTAAAGGGAGCCCCCGAGACGGGGA
54[122]	GTAATCAAAAATAATTCGCAATTGTAAATCAA
0[90]	CAACGAGTAGTAAATTGCATTTGGGGCAATTGCTG
8[118]	TGTATCACTCATTTTTAAACCAAGTACCAACCGAC
50[193]	GAAGGTTATCGACAACTCGT
6[140]	ACAACAATAGGAATGATATAACCTGAACAGACGA
68[131]	CCTGAGAGAGTTTGGTTCCGTGTGAGTGCCTGA
15[108]	GGAATGCAGCTTCAAAGCGAGCAGGCGAGAAAAACCGTCTATCA
4[126]	AATTTTTGGTGAATTACTGA
5[112]	TTTTCTGTAGACAGCCGGTTTTGATAGCG
15[157]	CCGAACGAAAGTATGGTTTGCAGTATGAACGT
55[132]	CGTAGTCTGGCCGCCGTTTTAGAACGCGGCAAGCCCGCCTGT
63[155]	CCGCTGTGAGGCCATTACTAGAAATTCTTGCTTTTGATGATA
41[172]	ATATTTGCTTTGTTACATTTAAGGG

21[101]	CGTAAGATTCAAAATCGGTTGTACCAATAGCA
71[128]	TTTTGGGGTCGAGGTGCCGTAAAGGGAACAAGCAAACATCGGAAA
5[144]	AACAGTTTCAGTACAAATTTTGCACTTATCCGAGA
57[119]	CCTCAGGAAGTTGGTGTACAAGCAATTCCT
59[163]	CCGCCCAAAAGGTTAATAAGAGAATATAAATCAT
20[146]	TATAATTGAGTGAAGCGCACATTTGAGGATTAGAG
46[167]	CTGGGATACGCAAATTGTTTGGATACCATATCAGA
60[185]	TAATAACATCCAACAGGAAA
56[154]	ACCATCATTACTCGCCATTAAACAGAGGTGA
22[172]	AGAGAATAACATAACAATGACAAACAATGCATGATTA
61[140]	TCTGTCCATCACGCAAATTAGAACTCAACGAGC
37[125]	TATACAGAATCAGCAAAATTCATCTTTAGTTT
41[104]	AATATAATTTTGATAATAGAGAGTCAAAGGGCAAATCCTGT
62[185]	AATCCTGAGATTCTTTGATT
34[148]	ATCTTCATACATGACCAGTATGGCATTTTACTATC
67[136]	CTTCAGTGTAGCGGTCGCACGTATATGCAAATTTC
34[178]	AACTTTTTCAATGTTTAGTACAAACATCACACGGAACGGTACGCC
60[145]	GGCCTTGGCCTCTTCGCTGACGTTGTCGCTCAACATA
66[170]	ACTGAGCTAAACAGGAGGCGATTTTAG
53[147]	AGATAAAAAATACCGAACGAAATGATACGTGGCAC
63[91]	TCCCCGGGTACCGGCGTTGCGCTC
38[114]	CCTTTAGAGCCAAGTTTGCCTTTAGCGAAAAT
28[146]	TTTTCGTAGGATGAAAGCGTAAGAGGATAGGTCACGAT
27[93]	CAGTGAGCGAGAATCAGCT
28[140]	TATCATCCTTATTTACATTGGCAGATTCATTCTG
54[176]	CTGATAGCCGCTATTAGAACAGAGAT
65[111]	GGGAAACCTCTAACTCAATAAATAATTGCA
50[98]	ACCCATCAGTTTAATAAAAATCGGTTTAACATTTTA
6[162]	AGTTTCGTCACCAGCGGAGCTAACGAGTGAAA
13[96]	TCATAATCTCAGACTGGCGTTTTAATTCG
26[122]	TTTAGCCTTAAACGTTAATTATAAGCAAATATTTAGAA
41[141]	ACTGAGGCGAATGATGAAAAGTCCACTATTAA
6[64]	AAGAGGACAGGCGCAGACGGTCAATTACTTAGCCGGAACGA
12[142]	AGCCGCCGTAAGCGTCTGAC
55[88]	TAACAACCCGTCGGATATTAAATGACGACGATTAC
5[80]	AACTGTCGAGTTTCGACAG
49[117]	AGCACTAGCATGTCAATCAAAAAACAGGCCAT
58[185]	CGCTCATGGATAATAAAAGG
59[131]	CGGTGCAATAAACATGTAATTGGGTCAGTCCGTT
16[90]	CCGTAGAGCTTGCGAGCTGAAA
9[137]	TTAGCGGTTTTAACGTAGGCAGAAAAGCCAAAAAG
69[113]	TTGATGGGCAGCAAGTGTAAATCTTAAC
38[146]	CAGACCATTAGATAGCAGCACCGTAATCGCCT
25[91]	CGCCATTTTGTTATAATCAGAAAAGCCCCTATGT

2[105]	TTGCGGGATCGGCTTTGAAACGGGCTTGAGA
36[114]	CTCCGGAACCAGAGCCGCCG
33[64]	CTCCGTCTATCTTTTTGTTCAGAAAACGAGAATCAAA
39[64]	CTCCGTCTATCTTTTTTTTCAAACTCCAACAGTATCA
25[64]	CTCCGTCTATCTTATGACTGACCAACCCGCCA
27[64]	CTCCGTCTATCTTCATAACCCTCGTTTAC
31[64]	CTCCGTCTATCTTTTTATACTGCG
17[64]	CTCCGTCTATCAGAAACACCAGAAAGTAC
19[64]	CTCCGTCTATCTTAATCATTGTGAATTAC
29[64]	CTCCGTCTATCTTTTTAAGAAGTT
37[64]	CTCCGTCTATCTTTTTTTTGACTTC
35[64]	CTCCGTCTATCTTTTTTTTATAGTCAGAAGCAGGTTGAGG CCATCTTT
23[64]	CTCCGTCTATCTTTATCTCCATGTCATAAGGG
21[64]	CTCCGTCTATCGTCAGGACGTTGGCGGAACAACATTTGCT ACGTCAGC
65[93]	ACTTACCCTGACTATTTTTTTTTTGCTACGTCAGC
4[82]	CTGTACAGGTAACATTCAACTATTGCTACGTCAGC
43[85]	AGGTTTAATTTCAACTGCTACGTCAGC
45[85]	AGCGCTCATTATACCAGCTACGTCAGC
41[85]	GCTGCTTGCCCTGACGGCTACGTCAGC
9[85]	CTGAGCGTCCATTTTTGCTACGTCAGC
7[80]	CCCTCAGATTTTGCAATTTTTGCTACGTCAGC
11[71]	TCACAAACAAATAAATCTTTAAACATTTTTGCTACGTCAG C
25[83]	ATACAAGCAACACTATTTGCTACGTCAGC
67[93]	TGGAGGAAGCCCGAAATTTTTTTTGCTACGTCAGC
69[93]	CCAACCAGACCGGAAGTTTTTTTTGCTACGTCAGC
Cholesterol 3 prime	GATAGACGGAG/3CholTEG/
Cholesterol 5 prime	5chol/GCTGACGTAGC

Table 10 - *Funnel DNA sequences. Staples are shown in green. Staples which hybridise to cholesterol strands are shown in yellow, with regions that hybridise to cholesterol strands shown in green and red. Cholesterol strands are shown in orange.*

6.5 Digestion Locations

M13mp18 full sequence with primer annealment regions and cut sites labelled.

AATGCTACTA CTATTAGTAG AATTGATGCC ACCTTTTCAG CTCGCGCCCC AAATGAAAAT 60
ATAGCTAAAC AGGTTATTGA CCATTTGCGA AATGTATCTA ATGGTCAAAC TAAATCTACT 120
CGTTCGCAGA ATTGGGAATC AACTGTTACA TGGAATGAAA CTTCCAGACA CCGTACTTTA 180
GTTGCATATT TAAAACATGT TGAGCTACAG CACCAGATTC AGCAATTAAG CTCTAAGCCA 240
TCCGCAAAAA TGACCTCTTA TCAAAAGGAG CAATTAAAGG TACTCTCTAA TCCTGACCTG 300
TTGGAGTTTG CTTCCGGTCT GGTTCGCTTT GAAGCTCGAA TTAAAACGCG ATATTTGAAG 360
TCTTTCGGGC TTCCTCTTAA TCTTTTTGAT GCAATCCGCT TTGCTTCTGA CTATAATAGT 420
CAGGGTAAAG ACCTGATTTT TGATTTATGG TCATTCTCGT TTTCTGAACT GTTTAAAGCA 480
TTTGAGGGGG ATTCAATGAA TATTTATGAC GATTCCGCAG TATTGGACGC TATCCAGTCT 540
AAACATTTTA CTATTACCCC CTCTGGCAAA ACTTCTTTTG CAAAAGCCTC TCGCTATTTT 600
GGTTTTTATC GTCGTCTGGT AAACGAGGGT TATGATAGTG TTGCTCTTAC TATGCCTCGT 660
AATTCCTTTT GGCGTTATGT ATCTGCATTA GTTGAATGTG GTATTCCTAA ATCTCAACTG 720
ATGAATCTTT CTACCTGTAA TAATGTTGTT CCGTTAGTTC GTTTTATTAA CGTAGATTTT 780
TCTTCCCAAC GTCCTGACTG GTATAATGAG CCAGTTCTTA AAATCGCATA AGGTAATTCA 840
CAATGATTAA AGTTGAAATT AAACCATCTC AAGCCCAATT TACTACTCGT TCTGGTGTTT 900
CTCGTCAGGG CAAGCCTTAT TCACTGAATG AGCAGCTTTG TTACGTTGAT TTGGGTAATG 960
AATATCCGGT TCTTGTCAAG ATTACTCTTG ATGAAGGTCA GCCAGCCTAT GCGCCTGGTC 1020
TGTACACCGT TCATCTGTCC TCTTTCAAAG TTGGTCAGTT CGGTTCCCTT ATGATTGACC 1080
GTCTGCGCCT CGTTCCGGCT AAGTAACATG GAGCAGGTCG CGGATTTCGA CACAATTTAT 1140
CAGGCGATGA TACAAATCTC CGTTGTACTT TGTTTCGCGC TTGGTATAAT CGCTGGGGGT 1200
CAAAGATGAG TGTTTTAGTG TATTCTTTCG CCTCTTTCGT TTTAGGTTGG TGCCTTCGTA 1260

GTGGCATTAC GTATTTTACC CGTTTAATGG AAACTTCCTC ATGAAAAAGT CTTTAGTCCT 1320
CAAAGCCTCT GTAGCCGTTG CTACCCTCGT TCCGATGCTG TCTTTCGCTG CTGAGGGTGA 1380
CGATCCCGCA AAAGCGGCCT TTAACTCCCT GCAAGCCTCA GCGACCGAAT ATATCGGTTA 1440
TGCGTGGGCG ATGGTTGTTG TCATTGTCGG CGCAACTATC GGTATCAAGC TGTTTAAGAA 1500
ATTCACCTCG AAAGCAAGCT GATAAACCGA TACAATTAAA GGCTCCTTTT GGAGCCTTTT 1560
TTTTTGGAGA TTTTCAACGT GAAAAAATTA TTATTCGCAA TTCCTTTAGT TGTTCCTTTC 1620
TATTCTCACT CCGCTGAAAC TGTTGAAAGT TGTTTAGCAA AACCCCATAC AGAAAATTCA 1680
TTTACTAACG TCTGGAAAGA CGACAAAACT TTAGATCGTT ACGCTAACTA TGAGGGTTGT 1740
CTGTGGAATG CTACAGGCGT TGTAGTTTGT ACTGGTGACG AAACTCAGTG TTACGGTACA 1800
TGGGTTCCTA TTGGGCTTGC TATCCCTGAA AATGAGGGTG GTGGCTCTGA GGGTGGCGGT 1860
TCTGAGGGTG GCGGTTCTGA GGGTGGCGGT ACTAAACCTC CTGAGTACGG TGATACACCT 1920
ATTCCGGGCT ATACTTATAT CAACCCTCTC GACGGCACTT ATCCGCCTGG TACTGAGCAA 1980
AACCCCGCTA ATCCTAATCC TTCTCTTGAG GAGTCTCAGC CTCTTAATAC TTTCATGTTT 2040
CAGAATAATA GGTTCCGAAA TAGGCAGGGG GCATTAACTG TTTATACGGG CACTGTTACT 2100
CAAGGCACTG ACCCCGTTAA AACTTATTAC CAGTACACTC CTGTATCATC AAAAGCCATG 2160
TATGACGCTT ACTGGAACGG TAAATTCAGA GACTGCGCTT TCCATTCTGG CTTTAATGAA 2220
GATCCATTCG TTTGTGAATA TCAAGGCCAA TCGTCTGACC TGCCTCAACC TCCTGTCAAT 2280
GCTGGCGGCG GCTCTGGTGG TGGTTCTGGT GGCGGCTCTG AGGGTGGTGG CTCTGAGGGT 2340
GGCGGTTCTG AGGGTGGCGG CTCTGAGGGA GGCGGTTCCG GTGGTGGCTC TGGTTCCGGT 2400
GATTTTGATT ATGAAAAGAT GGCAAACGCT AATAAGGGGG CTATGACCGA AAATGCCGAT 2460
GAAAACGCGC TACAGTCTGA CGCTAAAGGC AAACTTGATT CTGTCGCTAC TGATTACGGT 2520
GCTGCTATCG ATGGTTTCAT TGGTGACGTT TCCGGCCTTG CTAATGGTAA TGGTGCTACT 2580
GGTGATTTTG CTGGCTCTAA TTCCCAAATG GCTCAAGTCG GTGACGGTGA TAATTCACCT 2640
TTAATGAATA ATTTCCGTCA ATATTTACCT TCCCTCCCTC AATCGGTTGA ATGTCGCCCT 2700
TTTGTCTTTA GCGCTGGTAA ACCATATGAA TTTTCTATTG ATTGTGACAA AATAAACTTA 2760
TTCCGTGGTG TCTTTGCGTT TCTTTTATAT GTTGCCACCT TTATGTATGT ATTTTCTACG 2820
TTTGCTAACA TACTGCGTAA TAAGGAGTCT TAATCATGCC AGTTCTTTTG GGTATTCCGT 2880
TATTATTGCG TTTCCTCGGT TTCCTTCTGG TAACTTTGTT CGGCTATCTG CTTACTTTTC 2940
TTAAAAAGGG CTTCGGTAAG ATAGCTATTG CTATTTCATT GTTTCTTGCT CTTATTATTG 3000
GGCTTAACTC AATTCTTGTG GGTTATCTCT CTGATATTAG CGCTCAATTA CCCTCTGACT 3060
TTGTTCAGGG TGTTCAGTTA ATTCTCCCGT CTAATGCGCT TCCCTGTTTT TATGTTATTC 3120
TCTCTGTAAA GGCTGCTATT TTCATTTTTG ACGTTAAACA AAAAATCGTT TCTTATTTGG 3180
ATTGGGATAA ATAATATGGC TGTTTATTTT GTAACTGGCA AATTAGGCTC TGGAAAGACG 3240
CTCGTTAGCG TTGGTAAGAT TCAGGATAAA ATTGTAGCTG GGTGCAAAAT AGCAACTAAT 3300
CTTGATTTAA GGCTTCAAAA CCTCCCGCAA GTCGGGAGGT TCGCTAAAAC GCCTCGCGTT 3360
CTTAGAATAC CGGATAAGCC TTCTATATCT GATTTGCTTG CTATTGGGCG CGGTAATGAT 3420
TCCTACGATG AAAATAAAAA CGGCTTGCTT GTTCTCGATG AGTGCGGTAC TTGGTTTAAT 3480
ACCCGTTCTT GGAATGATAA GGAAAGACAG CCGATTATTG ATTGGTTTCT ACATGCTCGT 3540

AAATTAGGAT GGGATATTAT TTTTCTTGTT CAGGACTTAT CTATTGTTGA TAAACAGGCG 3600
CGTTCTGCAT TAGCTGAACA TGTTGTTTAT TGTCGTCGTC TGGACAGAAT TACTTTACCT 3660
TTTGTCGGTA CTTTATATTC TCTTATTACT GGCTCGAAAA TGCCTCTGCC TAAATTACAT 3720
GTTGGCGTTG TTAAATATGG CGATTCTCAA TTAAGCCCTA CTGTTGAGCG TTGGCTTTAT 3780
ACTGGTAAGA ATTTGTATAA CGCATATGAT ACTAAACAGG CTTTTTCTAG TAATTATGAT 3840
TCCGGTGTTT ATTCTTATTT AACGCCTTAT TTATCACACG GTCGGTATTT CAAACCATTA 3900
AATTTAGGTC AGAAGATGAA ATTAACTAAA ATATATTTGA AAAAGTTTTC TCGCGTTCTT 3960
TGTCTTGCGA TTGGATTTGC ATCAGCATTT ACATATAGTT ATATAACCCA ACCTAAGCCG 4020
GAGGTTAAAA AGGTAGTCTC TCAGACCTAT GATTTTGATA AATTCACTAT TGACTCTTCT 4080
CAGCGTCTTA ATCTAAGCTA TCGCTATGTT TTCAAGGATT CTAAGGGAAA ATTAATTAAT 4140
AGCGACGATT TACAGAAGCA AGGTTATTCA CTCACATATA TTGATTTATG TACTGTTTCC 4200
ATTAAAAAAG GTAATTCAAA TGAAATTGTT AAATGTAATT AATTTTGTTT TCTTGATGTT 4260
TGTTTCATCA TCTTCTTTTG CTCAGGTAAT TGAAATGAAT AATTCGCCTC TGCGCGATTT 4320
TGTAACTTGG TATTCAAAGC AATCAGGCGA ATCCGTTATT GTTTCTCCCG ATGTAAAAGG 4380
TACTGTTACT GTATATTCAT CTGACGTTAA ACCTGAAAAT CTACGCAATT TCTTTATTTC 4440
TGTTTTACGT GCTAATAATT TTGATATGGT TGGTTCAATT CCTTCCATAA TTCAGAAGTA 4500
TAATCCAAAC AATCAGGATT ATATTGATGA ATTGCCATCA TCTGATAATC AGGAATATGA 4560
TGATAATTCC GCTCCTTCTG GTGGTTTCTT TGTTCCGCAA AATGATAATG TTACTCAAAC 4620
TTTTAAAATT AATAACGTTC GGGCAAAGGA TTTAATACGA GTTGTCGAAT TGTTTGTAAA 4680
GTCTAATACT TCTAAATCCT CAAATGTATT ATCTATTGAC GGCTCTAATC TATTAGTTGT 4740
TAGTGCACCT AAAGATATTT TAGATAACCT TCCTCAATTC CTTTCTACTG TTGATTTGCC 4800
AACTGACCAG ATATTGATTG AGGGTTTGAT ATTTGAGGTT CAGCAAGGTG ATGCTTTAGA 4860
TTTTTCATTT GCTGCTGGCT CTCAGCGTGG CACTGTTGCA GGCGGTGTTA ATACTGACCG 4920
CCTCACCTCT GTTTTATCTT CTGCTGGTGG TTCGTTCGGT ATTTTTAATG GCGATGTTTT 4980
AGGGCTATCA GTTCGCGCAT TAAAGACTAA TAGCCATTCA AAAATATTGT CTGTGCCACG 5040
TATTCTTACG CTTTCAGGTC AGAAGGGTTC TATCTCTGTT GGCCAGAATG TCCCTTTTAT 5100
TACTGGTCGT GTGACTGGTG AATCTGCCAA TGTAAATAAT CCATTTCAGA CGATTGAGCG 5160
TCAAAATGTA GGTATTTCCA TGAGCGTTTT TCCTGTTGCA ATGGCTGGCG GTAATATTGT 5220
TCTGGATATT ACCAGCAAGG CCGATAGTTT GAGTTCTTCT ACTCAGGCAA GTGATGTTAT 5280
TACTAATCAA AGAAGTATTG CTACAACGGT TAATTTGCGT GATGGACAGA CTCTTTTACT 5340
CGGTGGCCTC ACTGATTATA AAAACACTTC TCAAGATTCT GGCGTACCGT TCCTGTCTAA 5400
AATCCCTTTA ATCGGCCTCC TGTTTAGCTC CCGCTCTGAT TCCAACGAGG AAAGCACGTT 5460
ATACGTGCTC GTCAAAGCAA CCATAGTACG CGCCCTGTAG CGGCGCATTA AGCGCGGCGG 5520
GTGTGGTGGT TACGCGCAGC GTGACCGCTA CACTTGCCAG CGCCCTAGCG CCCGCTCCTT 5580
TCGCTTTCTT CCCTTCCTTT CTCGCCACGT TCGCCGGCTT TCCCCGTCAA GCTCTAAATC 5640
GGGGGCTCCC TTTAGGGTTC CGATTTAGTG CTTTACGGCA CCTCGACCCC AAAAAACTTG 5700
ATTTGGGTGA TGGTTCACGT AGTGGGCCAT CGCCCTGATA GACGGTTTTT CGCCCTTTGA 5760
CGTTGGAGTC CACGTTCTTT AATAGTGGAC TCTTGTTCCA AACTGGAACA ACACTCAACC 5820
CTATCTCGGG CTATTCTTTT GATTTATAAG GGATTTTGCC GATTTCGGAA CCACCATCAA 5880
ACAGGATTTT CGCCTGCTGG GGCAAACCAG CGTGGACCGC TTGCTGCAAC TCTCTCAGGG 5940
CCAGGCGGTG AAGGGCAATC AGCTGTTGCC CGTCTCGCTG GTGAAAAGAA AAACCACCCT 6000
GGCGCCCAAT ACGCAAACCG CCTCTCCCCG CGCGTTGGCC GATTCATTAA TGCAGCTGGC 6060
ACGACAGGTT TCCCGACTGG AAAGCGGGCA GTGAGCGCAA CGCAATTAAT GTGAGTTAGC 6120
TCACTCATTA GGCACCCCAG GCTTTACACT TTATGCTTCC GGCTCGTATG TTGTGTGGAA 6180
TTGTGAGCGG ATAACAATTT CACACAGGAA ACAGCTATGA CCATGATTAC GAATTCGAGC 6240
TCGGTACCCG GGGATCCTCT AGAGTCGACC TGCAGGCATG CAAGCTTGGC ACTGGCCGTC 6300
GTTTTACAAC GTCGTGACTG GGAAAACCCT GGCGTTACCC AACTTAATCG CCTTGCAGCA 6360
CATCCCCCTT TCGCCAGCTG GCGTAATAGC GAAGAGGCCC GCACCGATCG CCCTTCCCAA 6420
CAGTTGCGCA GCCTGAATGG CGAATGGCGC TTTGCCTGGT TTCCGGCACC AGAAGCGGTG 6480
CCGGAAAGCT GGCTGGAGTG CGATCTTCCT GAGGCCGATA CGGTCGTCGT CCCCTCAAAC 6540
TGGCAGATGC ACGGTTACGA TGCGCCCATC TACACCAACG TAACCTATCC CATTACGGTC 6600
AATCCGCCGT TTGTTCCCAC GGAGAATCCG ACGGGTTGTT ACTCGCTCAC ATTTAATGTT 6660
GATGAAAGCT GGCTACAGGA AGGCCAGACG CGAATTATTT TTGATGGCGT TCCTATTGGT 6720
TAAAAAATGA GCTGATTTAA CAAAAATTTA ACGCGAATTT TAACAAAATA TTAACGTTTA 6780
CAATTTAAAT ATTTGCTTAT ACAATCTTCC TGTTTTTGGG GCTTTTCTGA TTATCAACCG 6840
GGGTACATAT GATTGACATG CTAGTTTTAC GATTACCGTT CATCGATTCT CTTGTTTGCT 6900
CCAGACTCTC AGGCAATGAC CTGATAGCCT TTGTAGATCT CTCAAAAATA GCTACCCTCT 6960
CCGGCATTAA TTTATCAGCT AGAACGGTTG AATATCATAT TGATGGTGAT TTGACTGTCT 7020
CCGGCCTTTC TCACCCTTTT GAATCTTTAC CTACACATTA CTCAGGCATT GCATTTAAAA 7080
TATATGAGGG TTCTAAAAAT TTTTATCCTT GCGTTGAAAT AAAGGCTTCT CCCGCAAAAG 7140
TATTACAGGG TCATAATGTT TTTGGTACAA CCGATTTAGC TTTATGCTCT GAGGCTTTAT 7200
TGCTTAATTT TGCTAATTCT TTGCCTTGCC TGTATGATTT ATTGGATGTT

6.6 Triangle Sequences

Name	Sequence 5'-> 3' * Indicates phosphorothioate bond	bases	T_m
66nt PPT	5- /5Phos/T*A*G* T*T*G ACG G*T*T* T*T*T* T*TG CTC TC*G* C*A*T* CGT GG*T* T*T*T* T*T*T GGT GAG* T*G*G*T*TC AGG* T*T*T* T*T*T* TGA TAA -3	66	68.7
48nt PPT	5- /5Phos/CG*A* G*A*G* CAC* C*G*T* C*AA CTA* T*T*A* T*CA C*C*T* G*A*A CCA C*T*C* A*C*C AC*C* A*C*G*ATG -3	48	68.7
66nt U	5- /5Phos/TAGTTG ACG GTTTTTTTG CTC TCGCATCGT GGTTTTTTT GGT GAGTGGTTC AGGTTTTTTTGA TAA -3	66	68.7
48ntU	5- /5Phos/CGA GAGCACCGTCAACTATTA TCA CCTGAA CCA CTCACC ACCACGATG -3	48	68.7

Table 11 – *ppt triangle strands*

Name	Sequence	bases	T_m
48ntU II	/5Phos/CCGTCAACTATTA TCA CCTGAA CCA CTCACC ACCACGATGCGA GAGCA	48	69.5
66nt II Chol. I	/5Phos/TTGACGGTTTTTTTGCTCTCGC/3CholTEG/	22	56.8
66nt II Chol. II	/5Phos/ATCGTGGTTTTTTTGGTGAGTG/3CholTEG/	22	54.1
66nt II Chol. III	/5Phos/GTTCAGGTTTTTTTGATAATAG/3CholTEG/	22	45.6
66nt II I	/5Phos/TTGACGGTTTTTTTGCTCTCGC	22	56.8
66nt II II	/5Phos/ATCGTGGTTTTTTTGGTGAGTG	22	54.1
66nt II III	/5Phos/GTTCAGGTTTTTTTGATAATAG	22	45.6

Table 12 - *cholesterol triangle strands*

6.7 HPLC Integration

Strand	Peak area
48PPT	95.5776
48PPTethane	47.66645
66PPT	102.68322
66PPTethane	32.91572

Table 13 – *Integration of HPLC peaks*

6.8 PPT Triangle – Maldi Toff Mass Spectrums

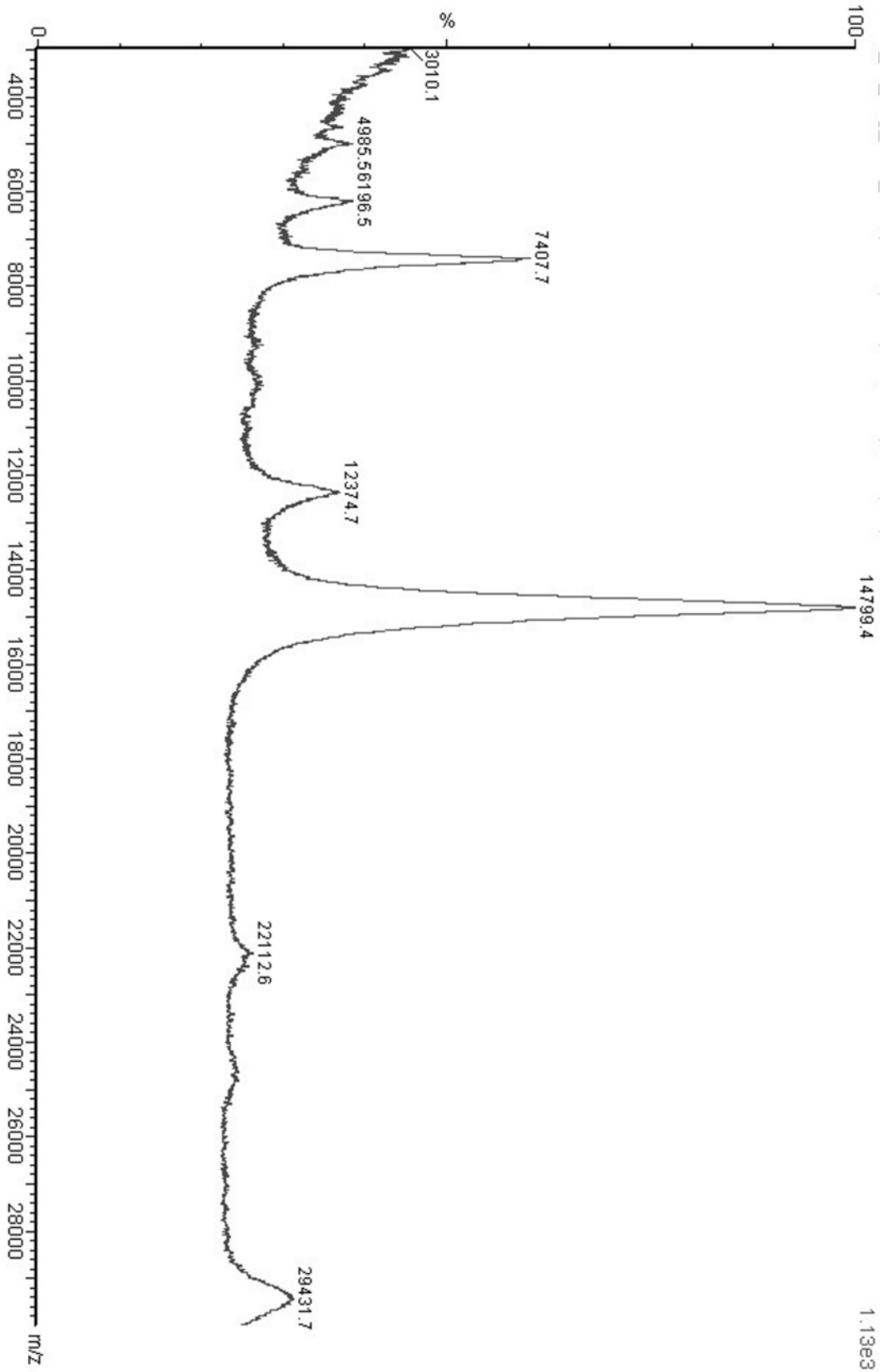

Figure 101 - *Maldi Toff spectrum of 48U strand*

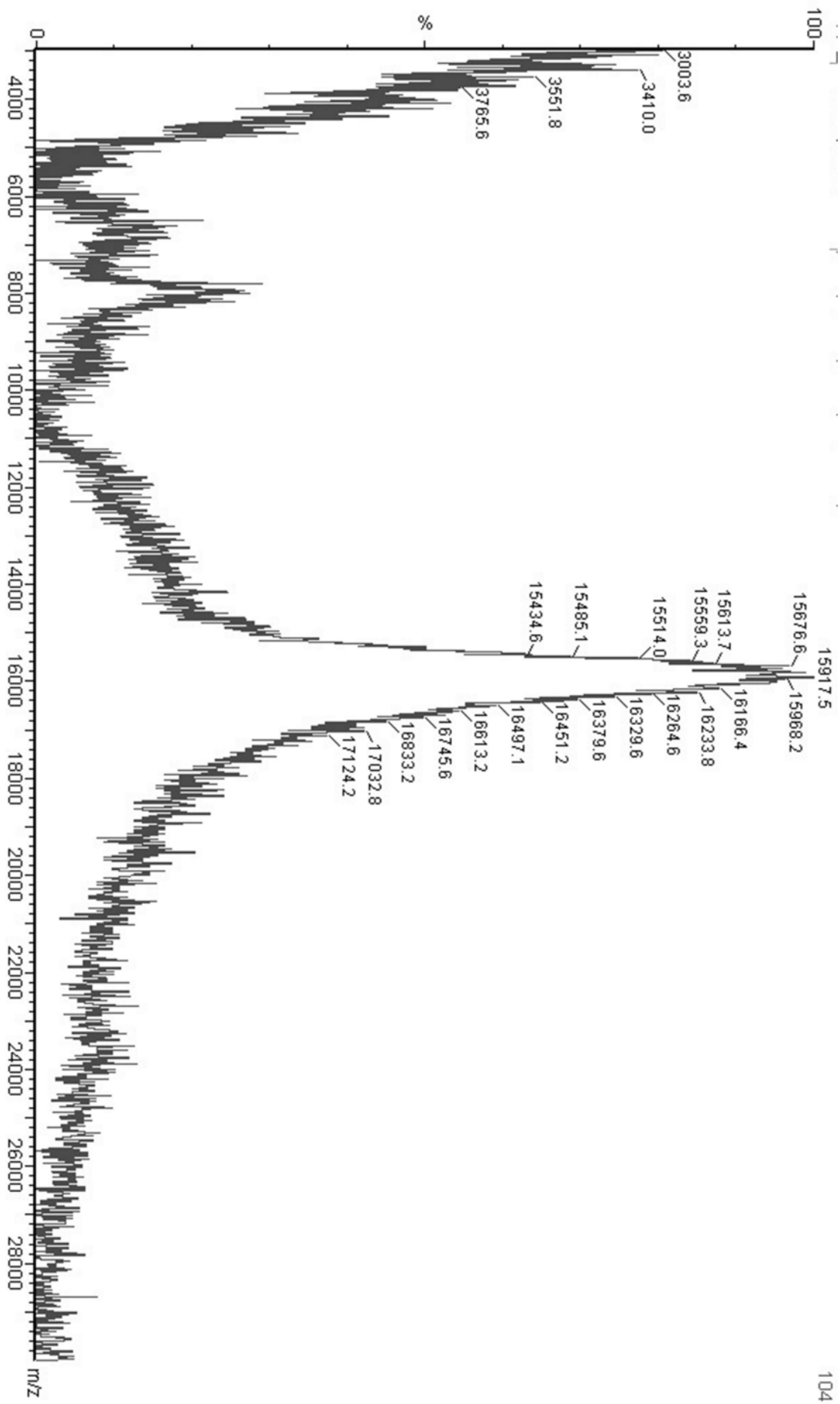

Figure 102 - *Maldi Toff spectrum of 48PPT strand*

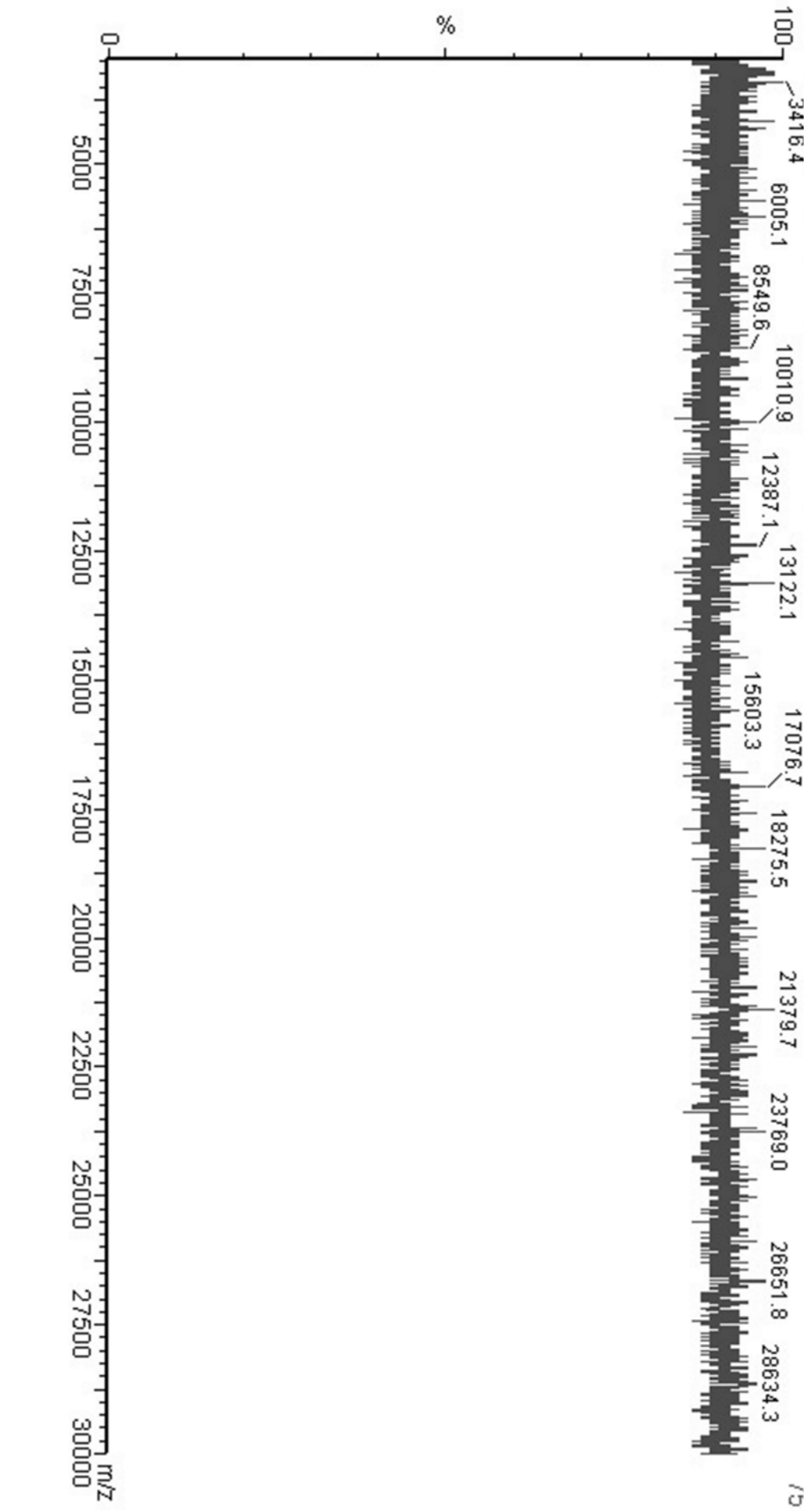

Figure 104 *- Maldi Toff spectrum of 48PPTethane strand*

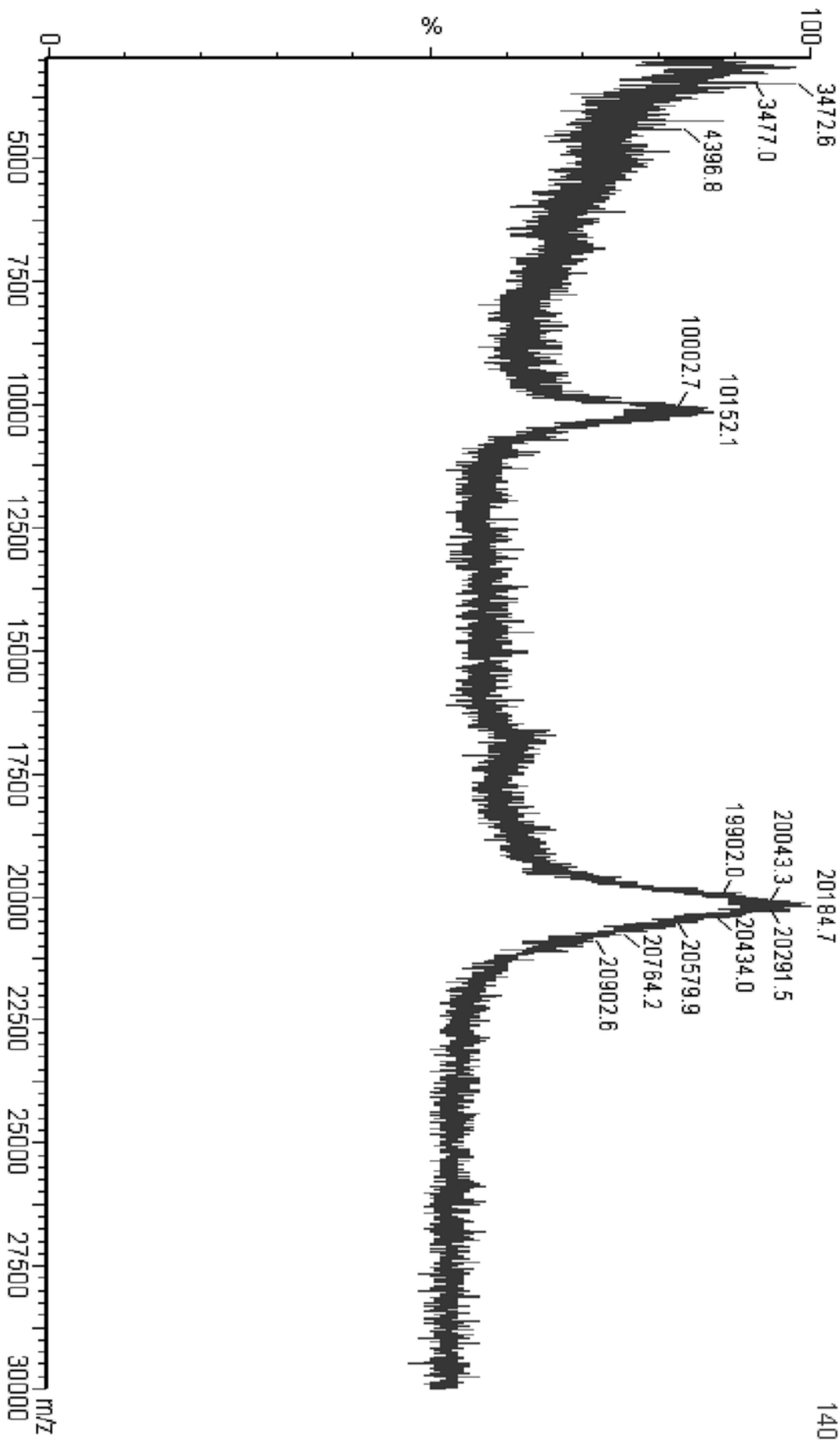

Figure 105 - *Maldi Toff spectrum of 66U strand*

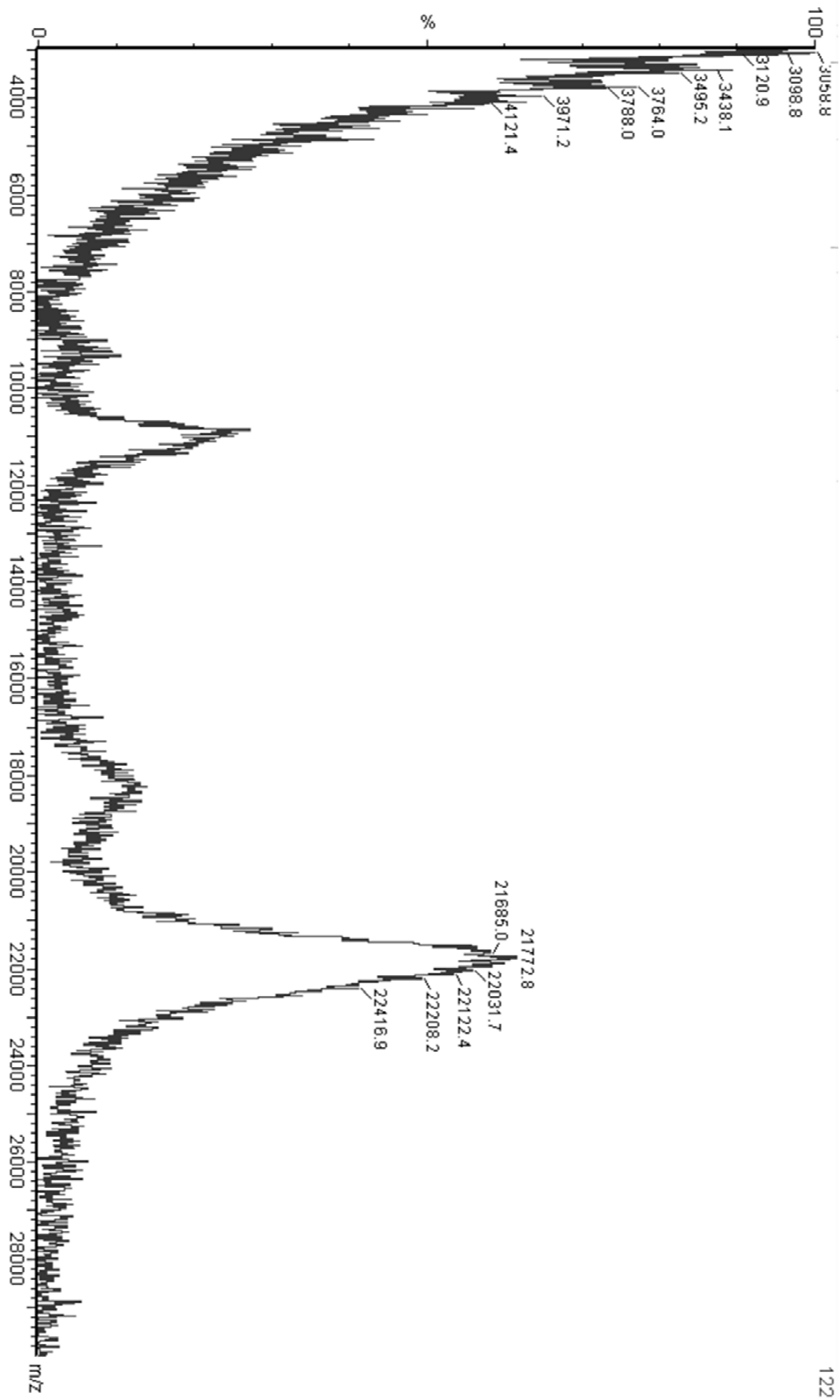

Figure 106 - *Maldi Toff spectrum of 66PPT strand*

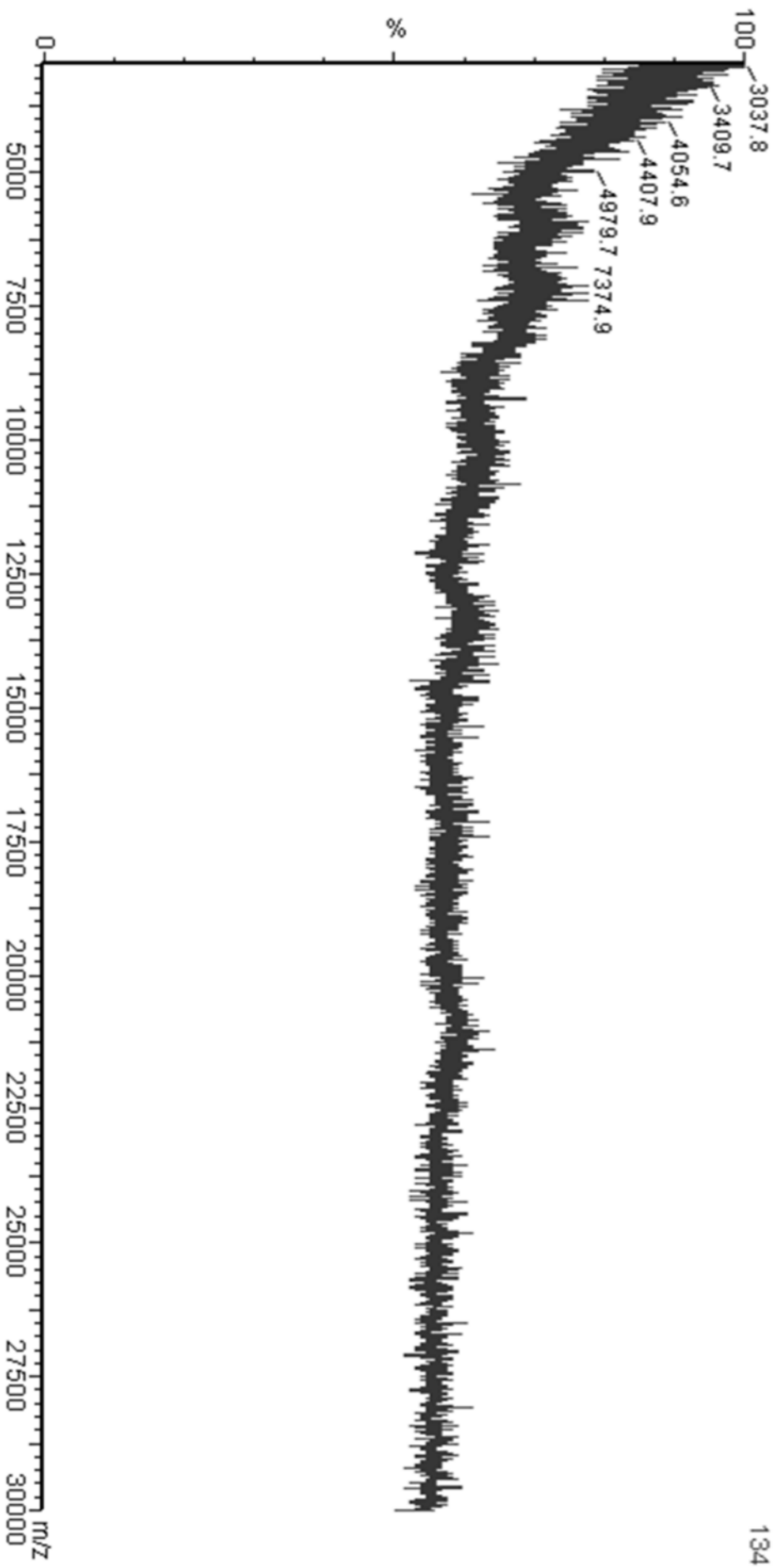

Figure 107 - *Maldi Toff spectrum of 66PPT ethane strand*

6.9 Figure List

6.10 Table List

6.11 Equation List